High Brightness Electron Beam Diagnostics and their Applications to Beam Dynamics in a Superconducting Energy-Recovering Free-Electron Laser

Ph. Piot,
Thomas Jefferson National Accelerator Facility,
Accelerator Division, Free-Electron Laser Team
12000, Jefferson Ave., Newport News VA 23606, USA
and
Université Joseph-Fourier-Grenoble-I, Sciences et géographie
Domaine Universitaire de Saint Martin d'Hère
38000, Grenoble, France

February 8, 2000

This Work has been prepared under the US-DOE contract number DE-AC05-84ER40150, the Office of Naval Research, the Commonwealth of Virginia and the Laser Processing Consortium.

corresponding electronic address: philippe.piot@desy.de

Abstract

A high power infrared free-electron laser (IRFEL) facility driven by a recirculating superconducting accelerator has been built and commissioned at Thomas Jefferson National Accelerator Facility. The system is principally composed of a 10 MeV photoinjector capable of delivering a high charged (60 pC) short bunch (1 ps) electron beam which is injected in a superconducting linac and accelerated up to 48 MeV prior to the lasing system consisting in a planar wiggler whose spontaneous radiation is amplified with a resonant cavity.
The present report details the diagnostics that have been developed and implemented in the IRFEL driver-accelerator for characterizing both transverse and longitudinal phase space. We also report on the use of the developed instrument and related techniques to study and try to understand some Beam Dynamics problems in the driver-accelerator. When possible, we have tried to benchmark measurements with numerical simulations.

Keywords: Electron beam dynamics, Phase space, Emittance, High-brightness beam, Free-electron laser, Bunch length characterization, Coherent radiation, Optical transition radiation.

Résumé

Un laser à électrons libres infrarouge (IRFEL) utilisant un accélérateur supraconducteur avec système de recupération d'énergie a été construit et récemment mis en route à Thomas Jefferson National Accelerator Facility. Le système se compose principalement d'un injecteur, dont la source d'électrons est basée sur l'effet photoélectrique. Cette source peut produire des paquets d'électron fortement chargés (60 pC) ultra-court (1 ps), ayant une énergie de l'ordre de 10 MeV. Ces électrons sont ensuite injectés dans un accélérateur linéaire où ils sont accélérés jusqu'à une énergie pouvant atteindre 48 MeV. Le système de production de lumière se compose d'un onduleur plan dont l'émission spontanée est amplifiée grâce à une cavité optique résonnante.
Le présent rapport décrit les diagnostics qui ont été developpés afin de caractériser les espaces de phase transversaux et longitudinal du faisceau d'électron de l'accélérateur. Nous décrivons aussi les applications de ces diagnostics à quelques problèmes de dynamique de faisceau. Quand cela fut possible nous avons tenté de comparer les résultats de nos mesures avec des simulations numériques.

Mots-Clefs: Dynamique de faisceau d'electrons, Espace de phase, Emittance, Faisceau d'électrons à forte brillance, Laser à électrons libres, Mesure de la longueur de paquets d'électrons, Rayonnement cohérent, Rayonnement de transition optique.

Acknowledgments

It has required many people to achieve the work that constitutes part of this thesis. First I wish to thanks the three people that have chronologically directed my work at Jefferson Lab: Jean-Claude Denard, Geoffrey Krafft, and Courtlandt Bohn. Jean-Claude Denard offered me to come at CEBAF as a phD student and with him I worked on the development of non-interceptive diagnostics such as transition and diffraction radiation for the CEBAF accelerator. Geoffrey Krafft confided me to work on one of his favorite topics: the characterization of ultra-short beam, he also gave many advices in Beam Dynamics. Court Bohn offered me a position in the FEL department to experimentally characterize bunch self interaction due to coherent synchrotron radiation.

In France this work was directed by Jean-Marie Loiseaux, I thank him for letting me total freedom in my research work and I am grateful for his total confidence and advises. I would like to express my gratitude to Pascal Elleaume from ESRF and Louis Rinolfi from CERN, both of them have accepted the role of referee for the present report, their careful reading, suggestions and comments have made this manuscript clearer. Many thanks also to Fernand Merchez who chaired the examination committee, but also for his interest and encouragement for the present work.

Next I wish to thanks the colleagues from Jefferson Lab who spent time to educate me in various area of Beam Physics: David Douglas, Dave Kehne, Peter Kloeppel, Robbert Legg, Lia Merminga, Byung Yunn have provided general Accelerator Physics help and insights. Rui Li has shared her work on CSR and I have freely borrow some passage of her publications in the present manuscript. George Neil and Michelle Shinn have taught me the few things I know about Free-electron lasers. Steve Benson helped me understanding the impact of electron beam parameters on the FEL photon beam. Thanks to Jinhu Song who initiated me to the world of EPICS and MEDM but who also made many contribution, he especially coded the data reduction algorithm for the multislit so that we could have results on-line. Uwe Happek and Michael James built the interferometers that are used for bunch length measurement. Thanks to Hongxiu Liu for letting me use his customized version of the PARMELA code. Alicia Hofler and Albert Grippo made many contributions to the data acquisition and diagnostics control system. Sue Witherspoon help setting up the model server and fixed the problems I encoutered very efficiently.
I would like to express my gratitude to Kevin Jordan and his team (Rich Hill and Rich Evans), Karel Capek, and Erich Feldl for their excellent technical support, without them most of the work presented in this manuscript could not have happened. I ought a lot to Timothy Siggins, "The Creator" (of electrons): despites many "event" we encountered with the electron source, he and Joe Gubeli were able to provide "good-enough-photocathode" to run high enough charge electron beam; without electrons this manuscript won't exist!

My special thanks also go to Dik Oepts, visitor from FOM instituut voor Plasmafysica Rijnhuizen for many helpful comments and suggestions he made on the off-line analysis code of the polarizing interferometer, and Peter Michel from the Forschungszentrum Rossendorf e.V. for his help debugging and troubleshooting diagnostics (and seating many shifts with me!).

I thank the CEBAF machine operators, with whom I shared endless nights in the machine control center" they have taught me how to be a "smooth operator".

Michèle Blanc from ISN took care of all the administrative paperwork at Université Joseph Fourier; her kind help is greatly appreciated. I also would like to thank Kate Ross, from CERN, for providing english syntax and grammar corrections.

Lastly, I would like to thank my fellow graduate students with whom I spent many enjoyable times in the United States. I apologize for those that I have not explicitly mentioned here and of course I also thank them !

This work was sponsored by US tax payers via the Department of Energy grant number DE-AC05-84ER40150, the Office of Naval Research, the Commonwealth of Virginia and the Laser Processing Consortium.

Contents

List of Tables

List of Figures

Chapter 1

Introduction

In recent years, there has been a growing interest in coherent light sources driven by electron (or positron) accelerators. Such light sources have proven to be capable of generating photon in deep UV domain and are planned to generate X rays. They have found many applications ranging from fundamental sciences (biology, crystallography, etc...) to industrial applications (e.g. nano-electronics).
The generic configuration consists of, e.g., an electron beam accelerator that generates and prepares (i.e. accelerates, bunches and transversely shapes) the electron beam before sending it in a periodic magnetic field created by an undulator magnet which causes the electrons to oscillate transversally. As an electron bunch oscillates, it creates a (spontaneous) synchrotron radiation pulse that mirrors its characteristics (i.e bunch length, shape,..). Two schemes are generally used for such light sources: the storage ring and the free-electron laser (FEL). In the former case, the particle beam is stored in a ring and periodically goes through an undulator magnet, while in the latter case the beam is generated by a linac and passes though the undulator once. The free-electron laser has generated much more interested in the recent years because of their unequaled ability to produce high brightness photon beam compared to storage ring. Furthermore brightness of storage ring tends to worsen at low energy, due to Touschek intra-beam collision, and high energy because of the importance of quantum fluctuations. In a resonator-based FEL the undulator magnet is inserted between two mirrors which constitutes a resonant optical cavity that recirculates the photon pulse coincidently with the next incoming electron bunch. It ideally generates a photon pulse coherently superimposed to the former photon pulse. In such an oscillator FEL the mechanism is quite similar to conventional laser, the "free" electrons acts as medium that amplifies a spontaneous radiation created via synchrotron emission. In a SASE (self amplified spontaneous emission) FEL, the undulator is made long enough so that lasing arise "naturally" from self amplification of the incoherent synchrotron emission. This latter type of FEL is especially suited to generate ultra-short wavelength (e.g. X-rays) coherent light since for such wavelengths a mirror might not be available thereby preventing the resonator configuration. A main feature of the FEL-based light source is their ability to provide laser light over a continuous tunable range of wavelength, that can be substantial, by varying the magnetostatic field of the undulator or the energy of the incoming electron beam.

Generally the driver accelerator consists in room temperature cavities that do not allow simultane-

ously high accelerating gradient and high electron bunch repetition rate. Hence the common light source can produce high peak power because of the high charge that can be stored in a bunch, but cannot easily produce high average power light needed by certain application such as power beaming, micro-machining, etc... An alternative scheme, that has been used in the driver-accelerator considered throughout this thesis, is to use superconducting accelerating cavities which offer low wall losses via Joules effect thereby allowing the operating of the cavities at high continuous wave (cw) gradient. A comparison of the average power that can be produced by such superconducting linear accelerators (e.g. the IRFEL from Jefferson Lab), with conventional high average power source generally used (e.g. excimer and carbon lasers) is depicted in Figure 1.1. A maximum output power of the order of 2 kW can be expected from the Jefferson Lab superconducting free-electron laser, and recently we achieved 1.7 kW experimentally.
Another concern that has arisen, especially in our project where the main motivation is to develop a light source for industrial application, is cost efficiency. This cost is mainly impacted by the input power demand to accelerate the beam. This demand was reduced in the JLAB IRFEL by recirculating and decelerating the beam using the same linac. The deceleration-induced voltage in the cavity directly supplements the input power provided by the klystron to accelerate higher average current electron beam for a given beam energy thereby reducing the demand on input power from klystron.

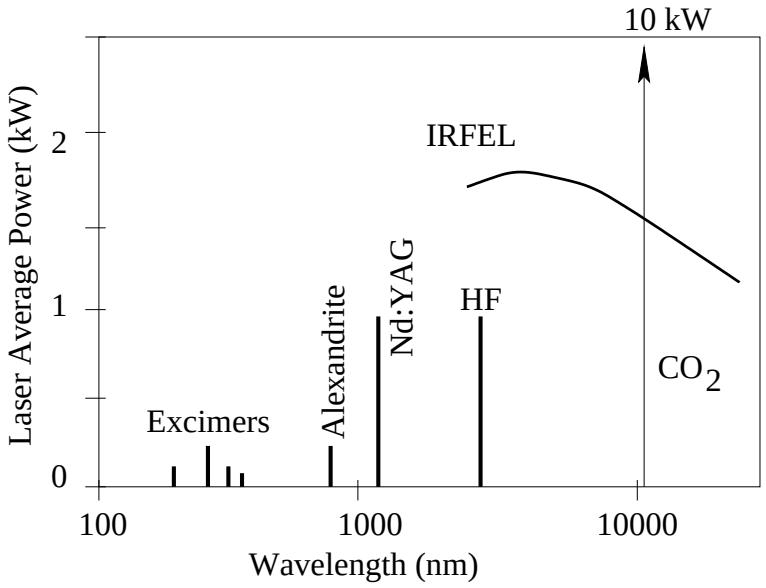

Figure 1.1: Comparison of the expected power of the IR cw free-electron laser of Jefferson Lab with common high average power source.

The superconducting FEL that served as experimental platform for this thesis is dedicated to study the possible application of high-power cw FEL's. It is an infrared demo FEL capable of providing continuous photon beams in the infrared spectrum (3 μm-6 μm) with high-average power of approximately 1 kW. Though this FEL is an user-oriented facility, it is also devoted to study the technologies required for high-power free-electron lasers especially the beam dynamics aspects in the driver-accelerator.
The driver-accelerator needs to provide a high-brightness, ultra-short bunch, low transverse-emittance, electron beam. Because of the high-charge concentrated in the bunch of electrons, effect such as

space-charge in the low energy regime, and wakefield (for short bunch) can lead to beam instability. Another potential problem that can arise with such beam parameters is the self interaction of a bunch via coherent synchrotron radiation (CSR) emitted as the bunch passes through dipoles. CSR leads to an increase in energy spread which in turn couple via dispersion to the transverse phase-space yielding an emittance growth in the bending plane.

The beam parameters we need to measure acurately are: the bunch length, the beam transverse density, the transverse emittance and the beam energy spread. The present report deals with several aspects concerning the development of the Beam Instrumentation required to properly characterize the electron beam and perform some Beam Physics studies in the Jefferson Lab IRFEL. In Chapter Two we will review radiations emitted by electrons and explain the principle of FEL oscillator by using as an example the IRFEL and try to understand what are the specification on the IRFEL electron beam parameters. Chapter Three presents the FEL-driver accelerator along with some optical lattice characterization that were crucial for understanding and setting up the energy recovery scheme. In Chapter Four, we describe the transverse phase space instrumentation we have developed to characterize beam in both emittance and space-charge-dominated regime. The Chapter Five presents our work for characterizing ultra-short (sub-picosecond) bunch. In Chapter Six we will present some beam dynamics studies of the injector, and in the recirculator with an attempt to measure the emittance growth in the recirculation arc of the IRFEL. We will then conclude in a Chapter Seven.

Chapter 2

Electron Radiation and Free-Electron Lasers

2.1 Introduction

There are many processes among which electrons can emit radiation. Most of them are due to change in the electron environment. To name few of them, synchrotron, transition, Smith-Purcel, and diffraction radiations have been widely studied in literature. Though these types of radiation can be used to generate intense light pulse over large domain of wavelength, they can also be used to infer certain characteristics of the electron beam that produced them. In the present Chapter we will recall few properties of the two types of radiation that will be considered in this report: synchrotron and transition radiation. We will then discuss undulator radiation and its amplification in free-electron lasers such as the one used as experimental platform in the report. In a last section we will present the required electron beam parameter to drive the desired FEL.

2.2 Single Particle and Multi-particle Emission

In this section we derive the expression for the total radiation emitted by an ensemble of particle and introduce the bunch form factor.

Radiation emitted by electrons depends on the electron's density distribution. For pure continuous beam (DC), no radiation is theoretically emitted (the field Fourier transform $\int E(t)\exp(-i\omega t)dt$ is zero). Indeed, experimentally there is an incoherent radiation resulting from Schottky noise that induces temporal fluctuation dependence on the electron motion. In high energy particle accelerator, acceleration is provided by radio-frequency wave: the beam must consist of a series of bunches and therefore electromagnetic waves can be radiated.
When an electromagnetic field is radiated by a collection of electron, the total field detected by an observer located in P (see figure 2.1) is the superposition of the field at this point generated by

each electron [2, 3] [1]:

$$\overrightarrow{E}_T(P) = \sum_{j=1\ldots N} \frac{\overrightarrow{k_j} \wedge (\overrightarrow{k_j} \wedge \overrightarrow{V_j})}{|\overrightarrow{k_j} \wedge (\overrightarrow{k_j} \wedge \overrightarrow{V_j})|} |\overrightarrow{E}_{1e}(k)| e^{-i\overrightarrow{k_j}\overrightarrow{X_j}}, \tag{2.1}$$

where k_j V_j and X_j are respectively the wavevector of the electric field emitted by the j-electron, $\overrightarrow{V}_j$ its the velocity, and $\overrightarrow{X}_j$ is the position vector that locates the j-th electron with respect to the bunch center.

Under the far-field approximation, we can, without significantly changing the results, replace the

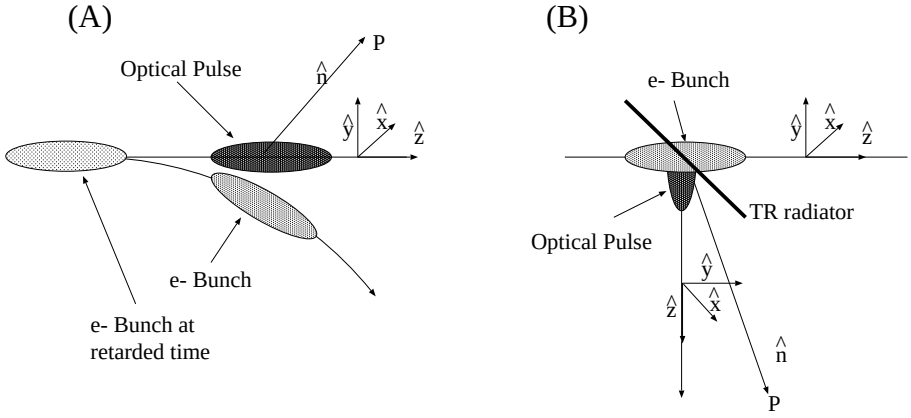

Figure 2.1: Geometry of the problem. In the case of synchrotron emission **(A)**, the optical pulse reference coordinate are the one of the electron bunch at the retarded time. For backward transition radiation **(B)**, the reference coordinates are the specular reflection of the electron bunch coordinate as it stroke the aluminum radiator.

wave vector k_j by $2\pi\widehat{n}/\lambda = \omega/c$ where λ (resp. ω) is the wavelength (resp. frequency) of observation and $\widehat{n}$ is the unit vector pointing from the center of the charge distribution toward the point of observation P. Introducing the normalized velocity, β_j, the former equation takes the form:

$$\overrightarrow{E}_T(P) = \sum_{j=1\ldots N} \frac{\widehat{n} \wedge (\widehat{n} \wedge \overrightarrow{\beta_j})}{|\widehat{n} \wedge (\widehat{n} \wedge \overrightarrow{\beta_j})|} E_{1e}(k) e^{-i\overrightarrow{k_j}\overrightarrow{X_j}} \tag{2.2}$$

The total density power radiated at the location P is then $E_T E_T^*$; it writes:

$$\frac{d^2P(\omega)}{d\omega d\Omega} = E_{1e}(\omega)E_{1e}^*(\omega) \left\{ N + \sum_{j,k=1\ j<k} \frac{\widehat{n} \wedge (\widehat{n} \wedge \overrightarrow{\beta_j})}{|\widehat{n} \wedge (\widehat{n} \wedge \overrightarrow{\beta_j})|} \times \frac{\widehat{n} \wedge (\widehat{n} \wedge \overrightarrow{\beta_k})}{|\widehat{n} \wedge (\widehat{n} \wedge \overrightarrow{\beta_k})|} e^{-\frac{i\omega}{c}\widehat{n}(\overrightarrow{X_j}-\overrightarrow{X_k})} \right\} \tag{2.3}$$

The first term, proportional to the number of particle in the bunch, is the incoherent contribution to the power. It can be written as the product $N \times d^2P/(d\omega d\Omega)|_{1e}$ where $d^2P/(d\omega d\Omega)|_{1e}$ is the power spectrum generated by a single electron. The second term describes the coherent contribution. Henceforth, we shall only concentrate on this latter "coherent" contribution that we will designate as coherent power. Let's introduce the function ψ of the reduced velocity: $\overrightarrow{\psi}(\overrightarrow{\beta_j}) = \frac{\widehat{n}\wedge(\widehat{n}\wedge\overrightarrow{\beta_j})}{|\widehat{n}\wedge(\widehat{n}\wedge\overrightarrow{\beta_j})|}$,

[1] In this report the vectorial product is designated with $\wedge$ symbol

then the coherent power simply rewrites as:

$$\frac{d^2P(\omega)}{d\omega d\Omega} = \left[\frac{d^2P(\omega)}{d\omega d\Omega}\right]_{1e} \sum_{j=1\ldots N} e^{-\frac{i\omega}{c}\hat{n}\overrightarrow{X}} \overrightarrow{\psi}(\beta)\delta(\overrightarrow{X}-\overrightarrow{X_j})\delta(\beta-\beta_j) \times \sum_{k=1\ldots N,k<j} e^{-\frac{i\omega}{c}\hat{n}\overrightarrow{X'}} \overrightarrow{\psi}(\beta')\delta(\overrightarrow{X'}-\overrightarrow{X_k})\delta(\beta'-\beta_k) \quad (2.4)$$

where we have used the properties of the Dirac δ-functions. Let's consider the spatial and angular distributions respectively $S(\overrightarrow{X}) = (1/N)\sum_{j=1\ldots N}\delta(X-X_j)$ and $A(\overrightarrow{\beta}) = (1/N)\sum_{j=1\ldots N}\delta(\beta-\beta_j)$. Using these definitions, we can rewrite the previous expression for the coherent power as an integral over the continuous extension of S and A. Therefore the ratio $\Xi(\omega,\hat{n})$ of coherent power over single particle emission power is:

$$\Xi(\omega,\hat{n}) = \frac{\frac{d^2P(\omega)}{d\omega d\Omega}}{\left[\frac{d^2P(\omega)}{d\omega d\Omega}\right]_{1e}} = N(N-1)\left|\int_{-\infty}^{+\infty} S(\overrightarrow{X})e^{-\frac{i\omega}{c}\hat{n}\overrightarrow{X}}d\overrightarrow{X}\right|^2 \left|\int_{-\infty}^{+\infty} A(\overrightarrow{\beta})\overrightarrow{\psi}(\overrightarrow{\beta})d\overrightarrow{\beta}\right|^2 \quad (2.5)$$

This latter equation defines the bunch form factor (BFF): $f(\omega,\hat{n}) \stackrel{def}{=} \Xi(\omega)/(N(N-1))$. It is worthwhile to mention the two limits of $\Xi(\omega,\hat{n})$ assuming that the factor $|\int_{-\infty}^{+\infty} A(\overrightarrow{\beta})\psi(\overrightarrow{\beta})d\overrightarrow{\beta}|^2$ is unity[2]:

$$\lim_{\omega\to 0}\Xi(\omega,\hat{n}) = N(N-1) \stackrel{(N\gg 1)}{\simeq} N^2, \text{ and, } \lim_{\omega\to+\infty}\Xi(\omega,\hat{n}) = 0 \quad (2.6)$$

Hence the coherent power is proportional to N^2 for practical number of electron in a bunch, and coherent enhancement is observable in the high frequency limit. In this coherent regime, the bunch radiates as a "particle" of charge Ne. Using the above notation we can write the total power emitted by a collection of electrons with a continuous density distribution $S(\overrightarrow{r})$ is:

$$\left[\frac{d^2P(\omega)}{d\omega d\Omega}\right]_{\text{total}} = \left[\frac{d^2P(\omega)}{d\omega d\Omega}\right]_{1e} \times (N + N(N-1)f(\omega,\hat{n})) \quad (2.7)$$

This formula was first introduced by Nodvick and Saxon [4].

2.3 Transition Radiation

Transition radiation is used throughout this report to measure different properties of an electron beam. We briefly remind the essential properties of this radiation in the present section. Transition radiation (TR) is produced when uniformly moving charged particles experience a discontinuity of dielectric constant of the surrounding environment, e.g. when crossing a boundary between two media with different electric properties. TR was first predicted and first studied by Ginsburg and Frank [5]. The use of transition radiation as particle beam diagnostic was first demonstrated by Warsky [6] to measure beam transverse distribution and beam energy. Qualitatively transition radiation is emitted because the electric fields in the two different media have different properties, and somewhere, i.e. at the interface, the electric field needs to reorganize.
For the most general case, i.e. the emission of transition radiation as an electron crosses the

[2] this assumption will be discussed when we will treat the longitudinal phase space characterization in Chapter 5.

boundary between vacuum and a medium of relative dielectric permittivity $\epsilon = \epsilon_{absolute}/\epsilon_0$ (where ϵ_0 is the vacuum electric permittivity), the problem consists of solving the scalar and vector potential equation

$$\nabla^2 \left[\begin{array}{c} \Phi \\ \overrightarrow{A} \end{array} \right] - \frac{1}{c^2}\frac{\partial}{\partial t} \left[\begin{array}{c} \Phi \\ \overrightarrow{A} \end{array} \right] = -\frac{1}{\epsilon\epsilon_0} e \left[\begin{array}{c} \delta(\overrightarrow{r},t) \\ \overrightarrow{\beta}\,\delta(\overrightarrow{r},t) \end{array} \right] \tag{2.8}$$

in the two media i.e. vacuum (by letting $\epsilon = 1$) and in the media with permittivity ϵ. The homogeneous solution of the latter equation gives the radiation field (Φ_{photon}, $\overrightarrow{A}_{photon}$). The obtained electromagnetic field solution of Eqn.(2.8) must be matched with the proper boundary condition at the media interface: the following components of the electromagnetic field must have continuity: $E_{\|}$, $B_{\perp}$, $H_{\|}$, and $D_{\perp}$ ("$\|$" and "$\perp$" corresponds to the components parallel and perpendicular to the interface surface). Moreover the electric field solution of the homogeneous equation (i.e. the radiation potentials) must satisfy $\nabla.\overrightarrow{E}_{radiation} = 0$ everywhere. When solving this problem two types of radiation are found: a forward radiation which is emitted in the direction centered around the direction of motion of the electron, and a backward radiation emitted around the specular axis of reflection of the interface. The most general expression for the transition radiation emitted in the backward direction by an electron moving from vacuum to a medium of permittivity ϵ with an angle of incidence ψ (defined in the plane $x-z$) with respect to the interface normal direction is [7]:

$$\begin{aligned} \frac{d^2W_{\|}}{d\omega d\Omega} &= \frac{Z_0 e^2 \beta_z^2 \cos^2(\theta)|\epsilon-1|^2}{4\pi^3\left[(1-\beta_x^2\cos^2(\theta_x))^2 - \beta_x^2\cos^2(\theta)\right]^2\sin(\theta)} \times \\ &\quad \left|\frac{\left(1-\beta_z^2+\beta_z\sqrt{\epsilon-\sin^2(\theta)}-\beta_z^2-\beta_x\cos(\theta_x)\right)\sin^2(\theta)-\beta_x\beta_z\cos(\theta_x)\sqrt{\epsilon-\sin^2(\theta)}}{\left(1+\beta_z\sqrt{\epsilon-\sin^2(\theta)}-\beta_x\cos(\theta_x)\right)\left(\epsilon\cos(\theta)+\sqrt{\epsilon-\sin^2(\theta)}\right)}\right|^2 \end{aligned} \tag{2.9}$$

$$\begin{aligned} \frac{d^2W_{\perp}}{d\omega d\Omega} &= \frac{e^2\beta_x^2\beta_z^4\cos^2(\theta_y)\cos^2(\theta)|\epsilon-1|^2}{4\pi^3\left[(1-\beta_x\cos(\theta_x))^2-\beta_z^2\cos^2(\theta)\right]\sin^2(\theta)} \times \\ &\quad \frac{1}{\left|\left(1-\beta_z\sqrt{\epsilon-\sin^2(\theta)}-\beta_x\cos(\theta_x)\right)\left(\sqrt{\epsilon-\sin^2(\theta)}+\cos(\theta)\right)\right|^2} \end{aligned} \tag{2.10}$$

$Z_0 = 120\pi\ \Omega$ is the vacuum free space impedance, and the different angles are presented in figure 2.2. The dependence on ψ is in $\beta_x = \beta\sin(\psi)$ and $\beta_z = \beta\cos(\psi)$ and $\theta_{x,y}$ are the angles between the direction of observation and the x or y axis. These angles are defined by $\cos(\theta_x) = \sin(\theta)\cos(\phi)$ and $\cos(\theta_y) = \sin(\theta)\sin(\phi)$, ϕ is the azimuthal angle in the x-y plane and ψ is the incidence angle referenced w.r.t. the z axis.
A priori transition radiation spectrum has no direct dependence on the frequency ω of observation; in reality this dependence is coming from the electric permittivity $\epsilon = \epsilon(\omega)$.

Under normal incidence, i.e. $\psi = 0$ ($\beta_x = \beta_y = 0$), only the "$\|$" component remains, and the spectral energy distribution emitted in the backward direction via transition radiation reduces to:

$$\frac{d^2W}{d\omega d\Omega} = \frac{e^2\beta^2\sin^2(\theta)\cos^2(\theta)}{\pi^2 c(1-\beta^2\cos^2(\theta))^2}\left|\frac{(\epsilon-1)\left(1-\beta^2+\beta\sqrt{\epsilon-\sin^2(\theta)}\right)}{\left(1+\beta\sqrt{\epsilon-\sin^2(\theta)}\right)\left(\epsilon\cos(\theta)+\sqrt{\epsilon-\sin^2(\theta)}\right)}\right|^2 \tag{2.11}$$

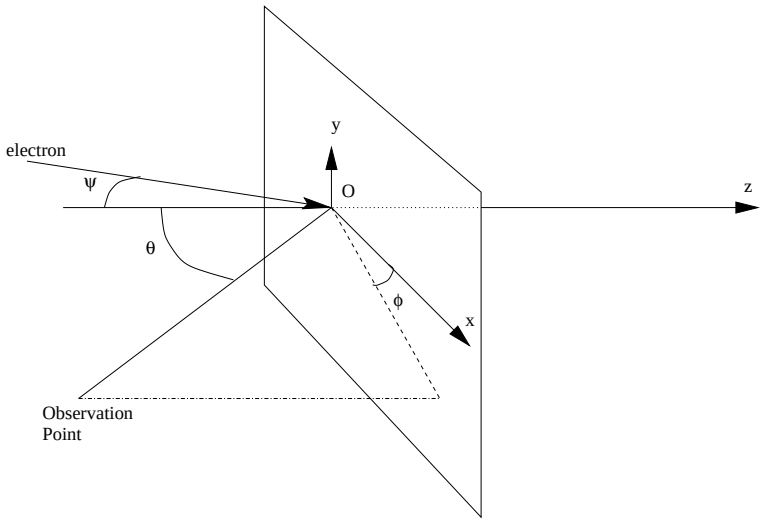

Figure 2.2: Definition of the angles used in equations (2.9) and (2.10).

This case is of importance for our discussion on the elaboration of a non interceptive TR-based density measurement where we used carbon to produce transition radiation.

Finally, another important case is the one of a perfect conductor (i.e. $\epsilon(\omega) \to \infty$, $\forall\omega$). For such class of material, and under normal incidence, the latter Eqn.(2.11) reduces to the well known relation [3]:

$$\frac{d^2W}{d\omega d\Omega} = \frac{Z_0 e^2 \beta^2 \sin^2(\theta)}{4\pi^4 c(1-\beta^2\cos^2(\theta))^2} \overset{(\gamma\gg 1, \theta \ll 1)}{\to} \frac{Z_0 e^2}{4\pi^3}\frac{\theta^2}{(\gamma^{-2}+\theta^2)^2} \tag{2.12}$$

The Eqn.(2.12), in the limit of an ultra-relativistic electron (i.e. $\gamma \to \infty$) is also valid in the case where the electron incomes on the interface with a 45 deg incidence; the angle θ, in this case, being referenced with respect to the specular axis.

The configuration generally used to generate transition radiation in a particle accelerator is to intercept the electron beam with very thin foil. In our case, the foil is made of aluminum or carbon. This type of configuration allows to generate both backward (at the vacuum-to-aluminum interface) and forward (at the aluminum-to-vacuum interface) transition radiation. A typical angular distribution of backward TR, for the case of an aluminum interface, generated by an electron under normal incidence is presented in figure 2.3(A) for three different values of the Lorenz factor γ. As the electron energy increase, the maximum of the angular distribution get larger and occur at smaller angle since it is $1/(\beta\gamma)^2$. In the extreme case where $\gamma = \sqrt{2}$ the maximum occurs at angle of 90 deg w.r.t. the specular axis. In figure 2.3(B), we compare the renormalized (compared to its maximum value) TR angular distribution emitted by in the forward direction by an electron normally incident on a carbon and aluminum foil. Typical radiation pattern are presented in the antenna diagram in figure 2.4 for the case of normal and 45 deg incidence of the electron beam on the foil. In the case of normal incidence, the pattern is symmetric with respect to the electron axis.

[3] In fact this relation can be derived directly, without solving the wave equation, by using the method of image charge usually use to render easier the treatment of boundary values problem. In the present case, the problem of an electron moving toward an infinite perfectly conducting plane can be reduce to an electron and its electromagnetic image traveling toward each other. The passage from the electron into the perfect conductor is then equivalent to the collision of the electron with its image, formalism to treat such "collapsing dipole" is readily available (see reference [8] Chap.(15)).

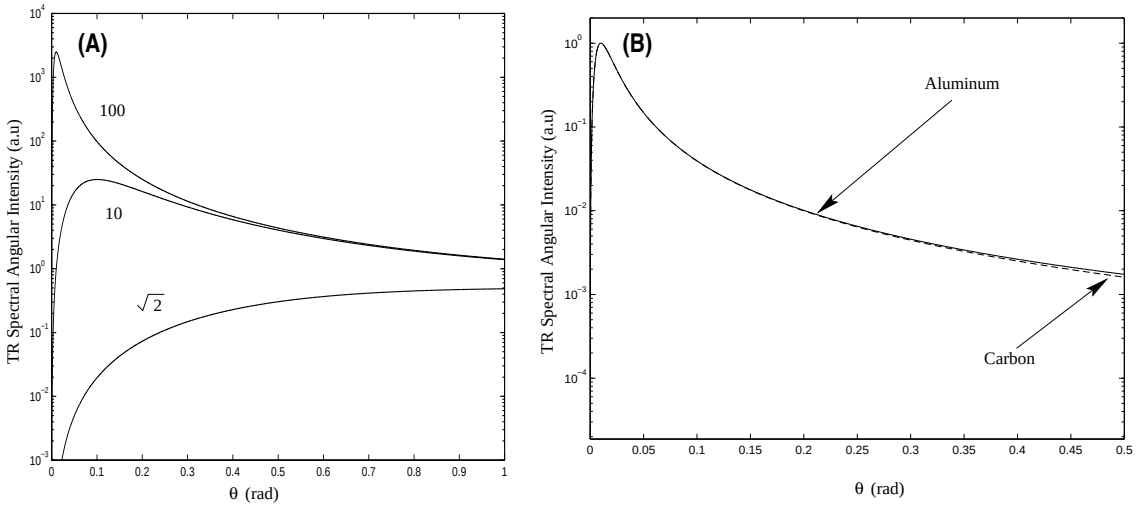

Figure 2.3: Distribution of forward TR radiation for different value of γ (mentioned close to the appropriate curve) as an electron passes from the interface vacuum-aluminum **(A)**. Comparison of the renormalized TR forward angular distribution emitted by an electron passing through a vacuum-aluminum (solid line) and vacuum-carbon (dashed line) interface **(B)**. For carbon the permittivity is assumed to be 5.7. (Carbon or more exactly graphite has two different electric permittivity for its two different crystal direction. The 5.7 value is the smallest permittivity. Private communication from Goodfellow Inc., London, U.K.).

However in the case of non-normal incidence there is a dis-symmetry in the lobes amplitude. This dis-symmetry tends to be reduced as the electron energy is increased, and becomes insignificant, in the case of 45 deg incidence, for ultra-relativistic electrons. Let's study how the radiation, in term of energy, is distributed around its maximum. For such a purpose we need to evaluate the integrals:

$$\begin{aligned}\frac{dW}{d\omega} &= \int d\Omega \frac{d^2W}{d\omega d\Omega} = \int_0^{2\pi} d\phi \int_0^{\theta} d\theta \frac{d^2W}{d\omega d\Omega} \\ &= \frac{-\beta + (1-\beta^2)\mathrm{argtanh}(\beta)}{2\beta} + \\ &\quad \frac{2\beta(\beta^2-1)\cos(\theta) - (1+\beta^2)\mathrm{argtanh}(\beta\cos(\theta))(-2+2\beta^2+\beta^2\cos(2\theta))}{2\beta(-2+\beta^2+\cos(2\theta))} \end{aligned} \tag{2.13}$$

Therefore the total energy radiated in the hemisphere is obtained setting the upper limit of the above angular integral to $\theta = \pi/2$:

$$\left[\frac{dW}{d\omega}\right]_{\mathrm{tot}} = \frac{-\beta + (1+\beta^2) \times 2\log\left(\frac{1+\beta}{1-\beta}\right)}{2\beta} \tag{2.14}$$

Firstly we note that for ultra-relativistic electron the total energy emitted in the hemisphere has a logarithmic dependence on the energy in $\log(4\gamma^2)$.
In figure 2.5(B) we present the dependence of the fraction of the total energy encompassed in the $1/\gamma$-cone versus the energy of the incident electron. We note that for ultra-relativistic electrons, most of the energy is located outside this $1/\gamma$-cone. Despite transition radiation has a sharp maximum located at the $1/\gamma$-cone, its power is not, like for instance for synchrotron radiation,

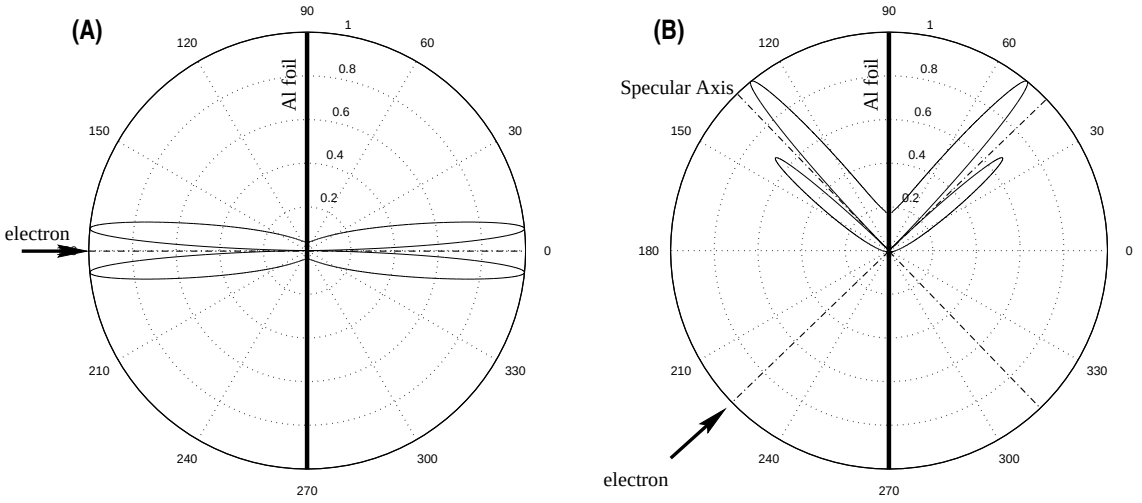

Figure 2.4: Polar plot of the normalized radiation pattern for an aluminum foil with an electron under normal incidence (i.e. $\psi = 0$ deg in Eqns.(2.9) and (2.10)) **(A)** and with a 45 deg incidence **(B)** (i.e. $\psi = 45$ deg in Eqns.(2.9)) and (2.10). For these plots the Lorentz factor was chosen to be $\gamma = 10$ for clarity of the figure, and the equations (2.9) and (2.10) were renormalized to their maximum value.

located within this cone: most of the power is in fact in the tail of the distribution. Therefore we should be careful when detecting transition radiation to optimize the angular acceptance of the detection system as a function of the electrons energy that produce the radiation. For such purpose we have plotted in figure 2.5(A) the fraction of the total energy versus the angular acceptance for the different electron energy we will consider in the present dissertation.

2.4 Synchrotron Radiation

The electromagnetic radiation emitted by a charged particle with non-zero acceleration is historically termed "synchrotron radiation" after its first visual observation nearly fifty years ago in a synchrotron accelerator. Such radiation is typically emitted in presence of a magnetic deflecting field such as the one generated by dipole magnets, because of the centrifugal acceleration associated with uniform circular orbit. Synchrotron radiation (SR) and the associated energy loss has first been known as a limitation to operate circular accelerators above the 100 GeV regime to accelerate electrons. Nowadays it is a common mechanism on which accelerator-based light source are working. Also, since SR is generated "for free" in accelerator, examination of the SR properties emitted by a electron bunch can reveal information on the bunch properties as we will see in Chapter 5. The purpose of this section is to expose few basic properties of SR. Since it has been widely treated in many textbook (e.g. see [8]), we will not derive any of its properties and only reproduce the results we feel necessary for the present discussion.
An important quantity is the spectral angular distribution of the synchrotron radiation which is given by (extended from [8]):

$$\left[\frac{d^2W}{d\omega d\Omega}\right]_{1e} = \frac{3r_c m_e c^2 Z_0 \gamma^2}{16\pi^3 c}\frac{\omega^2}{\omega_c^2} \times (1+\gamma^2\theta^2)^2 \times \left[K_{2/3}^2(\xi) + \frac{\gamma^2\theta^2}{1+\gamma^2\theta^2}K_{1/3}^2(\xi)\right] \tag{2.15}$$

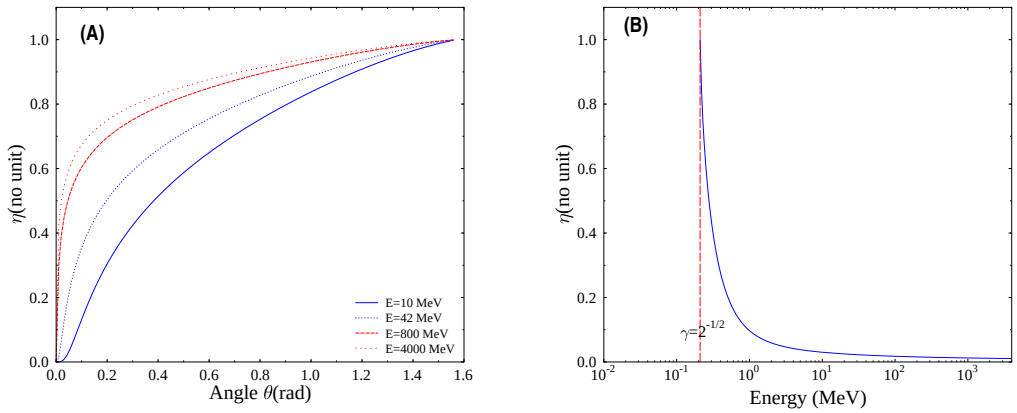

Figure 2.5: Fraction of the total transition power emitted into the hemisphere that is concentrated within a cone of semi-angle θ **(A)** and contains within a cone of semi-angle $1/\gamma$ **(B)**.

where $\xi = 1/2 \times \omega/\omega_c(1+\gamma^2\theta^2)^{3/2}$, ω_c is the critical frequency as defined in the synchrotron radiation formalism ($\omega_c = 2/3 \times c\gamma^3/\rho$), Z_0 is vacuum free space impedance, m_e the electron mass and $r_c = e^2/(4\pi\epsilon_0 m_e c^2)$ is the classical electron radius. The first term in the bracket ($\propto K^2_{2/3}(\xi)$) is the power associated with the σ-polarization of the electric field i.e. the component in the plane of the electron trajectory while the second term ($\propto K^2_{1/3}(\xi)$) corresponds to the π-polarization i.e. the electric field component parallel to the deflecting magnetic field. As one can notice from figure 2.6,

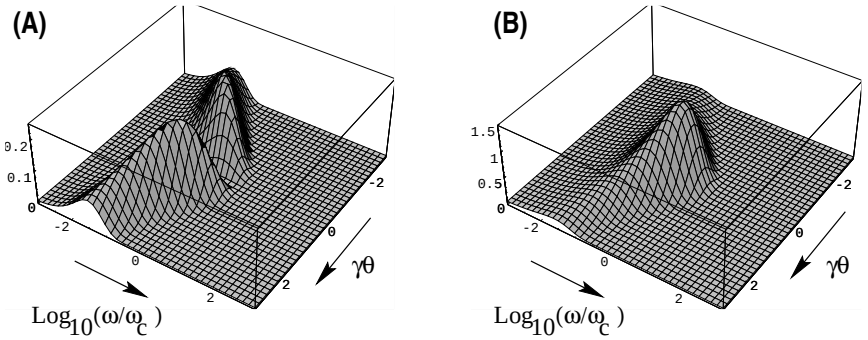

Figure 2.6: Angular and frequency distribution of synchrotron radiation for the π **(A)** and the σ **(B)** polarization.

the angular distribution of the two polarizations very strongly depend on the frequency. For instance the angular opening of the σ-mode radiation gets narrower as the frequency is increased.
Because we generally deal with relativistic beam ($\gamma \gg 1$), i.e. when the radiation is very collimated and therefore when most of the lobe can be captured by a detector, one quantity of interest is the total synchrotron radiation power spectrum integrated over the whole solid angle which is given by [10]:

$$\left[\frac{dP}{d\omega}\right]_{1e} = \frac{P_{tot}}{\omega_c} S(\omega/\omega_c) \tag{2.16}$$

where P_{tot} is the instantaneous total SR power emitted: in practical units (GeV/s), $P_{tot} = 8.8575 \times 10^{-5} cE^4/(2\pi\rho^2)$, where the numerical factor is the Sand's definition of the radiation constant E and ρ are the electron energy in GeV and the radius of trajectory curvature in meters. $S(x)$ in Eqn.(2.16) is the so-called Universal function, $S(x) = \frac{9\sqrt{3}}{8\pi} x \int_x^\infty K_{5/3}(x)dx$, which is plotted in figure 2.7. It is worthwhile to mention that the point $x = 1$ is the mid-total integral point: $\int_0^1 S(x)dx = \int_1^\infty S(x)dx = 1/2 \int_0^\infty S(x)dx$.

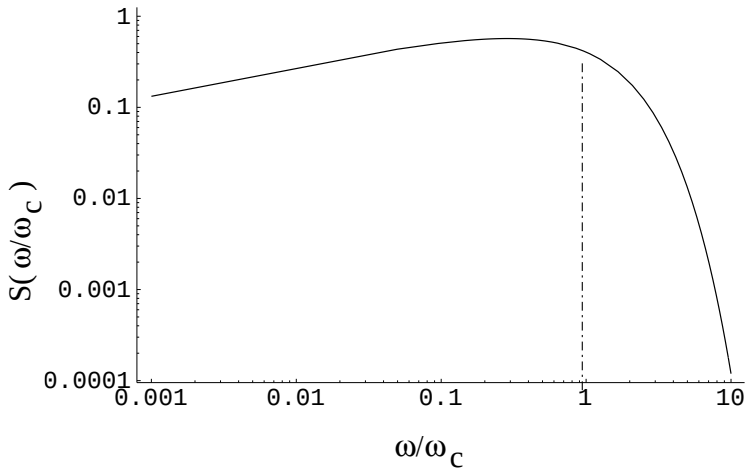

Figure 2.7: Plot of the Universal function $S(\omega/\omega_c)$. The frequency distribution of the total synchrotron radiation is proportional to the Universal function.

2.5 Rudiments on FEL-oscillator Theory

Despite the fact the present report does not specifically deal with the photon beam generated by the IRFEL, we briefly explain the bases of FEL theory since they will enable the reader to understand better the requirements on the driver-accelerator electron beam parameters. First of all, we should note that the word *free* in free-electron laser does not mean that the electrons are free, indeed it means they are unbounded (contrary to conventional laser) but there are confined in a magnetostatic region since the free electrons will not radiate unless they are experiencing some kind of acceleration.
As in a conventional laser, FEL consists in three main processes: (i) a spontaneous emission is provided by synchrotron radiation emitted as electrons wiggle in a magnet; (ii) the so-generated radiation is recirculated in a resonator; (iii) and is amplified as it copropagates with the electron beam (stimulated emission).

2.5.1 Undulator Radiation

In a FEL, the spontaneous emission is generated as the electrons are injected into a wiggler, a magnet that generates a spatially periodic magnetostatic field. In the case of the IRFEL of Jefferson Lab, the undulator is a planar one: it consists in two rows of N_u permanent magnets of opposite polarities stacked together with a period λ_u; the row are separated by a fix gap as

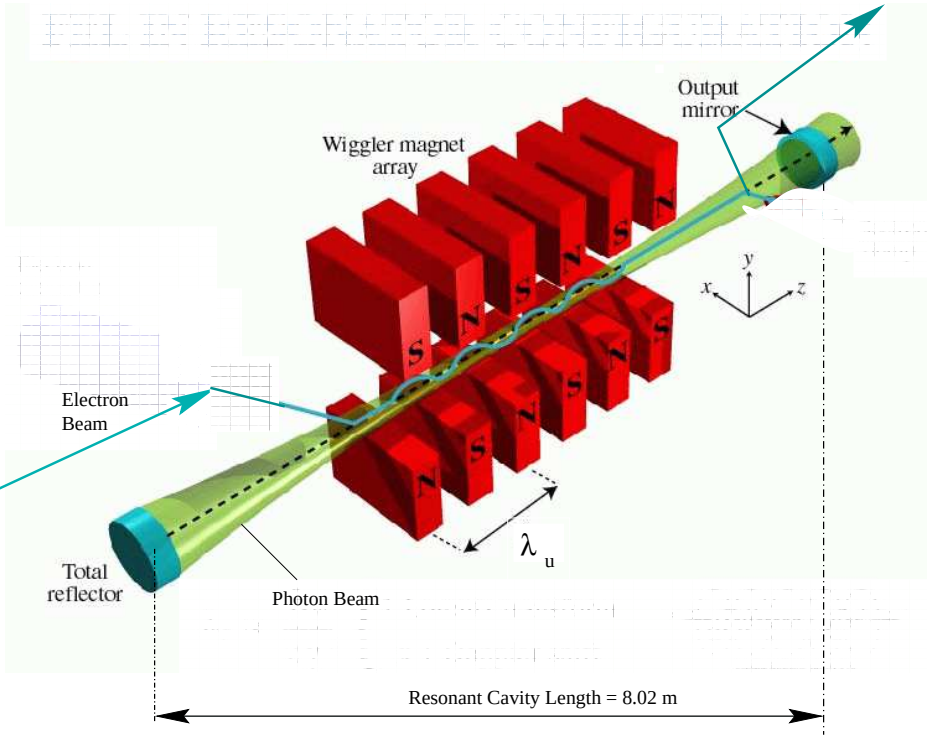

Figure 2.8: FEL-oscillator principle (Courtesy J. Martz, Jefferson Lab).

schematically described in figure 2.8. In such configuration the generated magnetostatic field is transverse with respect to the electron velocity. As electrons travel in the wiggler, they are slightly deflected alternatively up and down (see Figure 2.8) and thereby spontaneously emit synchrotron radiation that is linearly polarized (in the case of a planar wiggler).
In the case of IRFEL, the undulator produces a weak magnetostatic field of typically 0.4 Tesla. The electron trajectory when it is located within the undulator poles is described by:

$$y = -a\cos(2\pi z/\lambda_u) \qquad (2.17)$$
$$\frac{dy}{dz} = \frac{2\pi a}{\lambda_u}\cos(2\pi z/\lambda_u)$$

The force on the electron at the maximum curvature ρ corresponds to the peak value of the magnetic field $\overrightarrow{B}$: $\rho = \gamma m_e \beta c/(eB)$. It is common to characterize the undulator magnet by the so called deflection parameter K defined as $K = \gamma dy/dz|_{\max} = 2\pi\gamma\lambda_u a$. Together with the relation $(2\pi/\lambda)^2 a = eB/(\gamma m_e c)$, K takes the form:

$$K = \frac{eB\lambda_u}{2\pi m_e c} \qquad (2.18)$$

this deflection parameter is the maximum angular excursion of the beam in units of $1/\gamma$. It is interesting to compute the maximum amplitude in the case of the IRFEL: $a = K\lambda_u/(2\pi\gamma) \simeq 60\,\mu$m which is smaller that the electron beam sizes at this location ($\sigma_x \simeq \sigma_y \simeq 200\,\mu$m).
The wavelength of the radiation emitted by the undulator is determined by the time contraction factor $dt/dt' = 1-\beta\cos\theta$, t being the time reference in the moving frame whereas t' is the laboratory (i.e. undulator) time. In the electron rest frame, the electron "sees" the N_u periods of the wiggler

as an N_u counter-propagating radiation field with a Lorentz-contracted wavelength $\lambda'_u = \frac{\lambda_u}{\gamma_u}$. Thus it oscillates N_u times along a vertical line perpendicular to the wiggler axis, thereby emitting a radiation pulse of length $N_u\lambda'_u$. centered on the wavelength $\lambda'_s \simeq \lambda'_u$. In other terms, the electron acts as a relativistic mirror and reflect the incoming radiation via Compton back-scattering. In fact λ'_s is also shifted by the Compton wavelength, but this shift is negligible for relativistic electrons provided we observe wavelength that are larger than the Compton wavelength $\lambda_{Compton} = \frac{hc}{\gamma mc^2}$, a good assumption in the case of IRFEL. Therefore the fundamental wavelength of the undulator radiation is:

$$\lambda_1 = \lambda_u(1 - \langle\beta\rangle\cos\theta) \tag{2.19}$$

where θ is the angle of observation referenced to the axis of the undulator.
Using the average z-velocity $\beta\langle\cos\Psi\rangle = \beta(1 - \frac{K^2}{4\gamma^2} + \mathcal{O}(K^4))$ (Ψ is the trajectory deflection angle), one finds that the fundamental wavelength is:

$$\lambda_1 = \frac{\lambda_u}{2\gamma^2}(1 + \frac{K^2}{2} + \gamma^2\theta^2) \tag{2.20}$$

In fact all the harmonic are also present i.e. the wavelength $\lambda_n = \lambda_1/n$ with $n \in \mathbf{N}$. The wavelength represents the wavelength of the field component that interfere constructively. Other wavelengths are suppressed. If the undulator would have a infinite number of period, the line width will have the limit$\Delta\lambda/\lambda \to 0$ Since the electron only makes N_u oscillations in the undulator the generated radiation contains the same number of wavelengths and therefore the duration of the pulse is $T = N_u\lambda/c$. The Fourier transform of a plane wave truncated after N_u oscillations is sinc-function[4] , hence the frequency spectrum of the spontaneous undulator radiation has the frequency dependence:

$$\frac{d^2W}{d\omega d\Omega} \propto \mathrm{sinc}^2\left(\pi N_u\frac{\omega - \omega_n}{\omega_n}\right) \tag{2.21}$$

Which means the radiation is peaked at the frequency $\omega_n = 2\pi c/\lambda_n$. The width of the spectrum is about $\frac{\Delta\omega}{\omega} = \frac{1}{N_u}$. It is important to note that in the case of the FEL-oscillator, since only the on-axis ($\theta = 0$) component is of interested, i.e. is amplified, the fundamental wawelength reduces to:

$$\lambda_1 = \frac{\lambda_u}{2\gamma^2}(1 + \frac{K^2}{2}) \tag{2.22}$$

Finally we need to elaborate the power density spectrum. We have qualitatively explained the sinc dependence but there are many other properties that have been derived (see for instance reference [9]) and are worth mentioning in the present discussion. The optical wave generated from an undulator can be well approximated, if N_u is large enough, by a pure TE wave. In such case, the on-axis radiation only contains odd harmonic. The power spectral angular distribution is of the form [9]:

$$\frac{d^2W}{d\omega d\Omega} \propto mK^*(1 - K^{*2}/2)\left[J_{(m+1)/2}(mK^{*2}/4) - J_{(m-1)/2}(mK^{*2}/4)\right]^2 \stackrel{def}{=} Q \tag{2.23}$$

with $K^* \stackrel{def}{=} K/\sqrt{1 - K^2/2}$.
The latter equation is plotted in figure 2.9 for the two different values of K that are considered

[4]The cardinal sinus function is defined as: $\mathrm{sinc}(x) = \frac{\sin(x)}{x}$

for the IRFEL operation ($K = 1.00$ and optionally 1.39). In this figure one sees that spontaneous emission associated with the third harmonic can be almost as powerful as the emission at first harmonic with proper choice of the K value which can be set by changing the undulator gap[5]. Such feature is very interesting for producing shorter wavelength light. In the IRFEL operation at the third ($\lambda = \lambda_1/3$) and fifth ($\lambda = \lambda_1/5$) harmonic has been achieved.

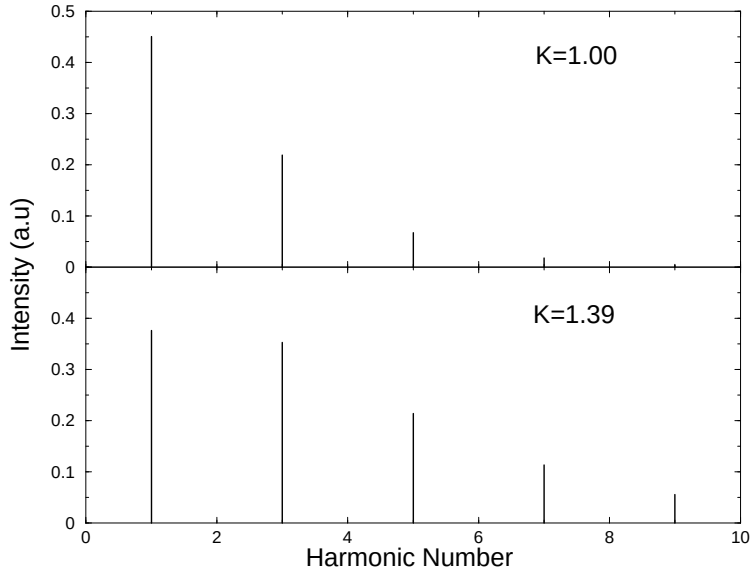

Figure 2.9: Normalized power of the on-axis undulator radiation for the two different value of K considered for the IRFEL.

2.5.2 Amplification of the Spontaneous Undulator Radiation

Once a radiation pulse at the wavelength given in Eqn.(2.22) has been established via the interaction of an electron bunch with the magnetic field of the undulator, it is recirculated in a resonator cavity that consists in two spherical dielectric mirrors. One of them is a total reflector while the other is a partially reflector and out-couple radiation through a small aperture with a diameter of the order of the wavelength. The spacing between the two mirrors is chosen so that the pulse will copropagate with the next incoming electron bunch and therefore the length of the cavity is $L = c/(2\tau)$ (where τ is the temporal spacing between two consecutive electron bunches) and should be a sub-multiple of 8.003 m in the case of the IRFEL. For electrons injected at the resonant energy $\gamma_r = \frac{1}{2}\sqrt{\frac{\lambda_u}{\lambda_s}(1+K^2)}$, the relative phase between the electrons and the copropagating radiation pulse will, in principle, remain constant. Since the electron beam velocity has a non zero component parallel to the optical pulse electron field, the scalar product of an electron velocity and radiation electric field ($\vec{v}.\vec{E}$) is non-zero and slowly varying so that there can be a net exchange of energy between the electron and the radiation. Hence, depending on the value of the relative phase, each electron in the bunch can (i) give energy to the field and decelerate, that is "stimulated emission"; (ii) take energy from the radiation field and accelerate, that is, "absorption". Thus if we consider a bunch of electron whose center energy is resonant energy, we could easily imagine that

[5]The K value dependence on the gap d is of the form $K \propto \exp(-\pi d/\lambda_u)$

half of the electron is decelerated while the other half is accelerated resulting in a null amplification. This is true in the first period of the wiggler but in very short time, the more energetic electrons catch up to the less-energetic, introducing an energy modulation within the electron bunch which, in turn, leads to a longitudinal density modulation or micro-bunching: the electron beam that has an initial distribution depending on the previous dynamics, soon consists in a sub-bunches of electrons spaced at the spontaneous wavelength. It turns out that if the electron energy is slightly higher than the resonant energy it results in a net gain i.e. an amplification of the light pulses.
This simple model assumes that electrons within a bunch do not interact each with other, that is single-particle-dynamics model is valid. When such a model is valid, like in the case of the IRFEL, the FEL is said to operate in the Compton regime.

2.5.3 FEL Gain

The amplification of the spontaneous emission is quantified by the gain that corresponds to the ratio of the energy transmitted by the electron beam to the copropagating electromagnetic wave to the initial energy of the copropagating electromagnetic wave. The gain[6] is defined as:

$$G \stackrel{def}{=} -mc^2 \frac{\Delta\gamma}{W_0} \tag{2.24}$$

where $\Delta\gamma$ is the reduced energy transmitted by the electron beam to the electric field of the optical mode and W_0 is the energy of the optical mode considered (i.e. the one which is supposed to be amplified). The derivation of analytic formula for the FEL gain has been performed in reference [11] and is beyond the scope of this thesis. However it seems worthwhile to study the effects of the electron beam parameters on the FEL-gain by considering the approximate 1D model that has been discussed by S. Benson [12]. The gain can be parametrized as:

$$g = 0.0004 I \gamma Q N_u N_\beta^2 \eta_{\tilde{\varepsilon}} \eta_\gamma \eta_f \eta_\mu \tag{2.25}$$

where γ and I are the electron beam energy and peak current. Q is a factor that has been defined in Eqn.(2.23). The η's coefficients in Eqn.(2.25) represent degradation factors of the gain.
η_γ is the gain degradation due to energy spread and is a result of the non-mono-energetic character of the incoming electron beam: since electrons in a bunch do not all have an energy exactly corresponding to the resonant energy; this factor is defined as:

$$\eta_\gamma = \frac{1}{\left(1 + 4\sqrt{2} h N_u \sigma_\gamma / \gamma\right)^2} \tag{2.26}$$

where σ_γ is the reduced rms-energy spread of the incoming electron bunches, and h, as before, is the harmonic number.
$\eta_{\tilde{\varepsilon}}$ is the degradation due to beam non-zero transverse emittance. This degradation also depends on the η_γ coefficient:

$$\eta_{\tilde{\varepsilon}} = \frac{1}{\sqrt{1 + \eta_\gamma (4\pi^2 \tilde{\varepsilon} N_\beta / \lambda)^2}} \tag{2.27}$$

[6] In this dissertation, gain designates the so-called "small signal gain" in the FEL literature since it is the quantity of importance when considering the startup of FEL interaction, our primary concern in the present section.

Parameter	Value	Unit
N_u	40	–
B_u (rms)	0.28	T
λ_u	2.7	cm
Gap	12	mm
K^2	0.5	–

Table 2.1: Parameters of the chosen wiggler for the IR-Demo FEL.

where $\tilde{\varepsilon}$ is the beam transverse rms-emittance and N_β is the number of betatron oscillations along the wiggler. η_f is the gain reduction due to the filling factor for the optical mode; it simply results from the nonintegral overlap of the electron bunch and the radiation pulse and is approximated by:

$$\eta_f = \frac{1}{1 + 4\pi\tilde{\varepsilon}/\lambda} \tag{2.28}$$

η_μ is the gain reduction due to slippage :

$$\eta_\mu = \frac{1}{1 + \frac{hN_u\lambda}{3\sigma_z}} \tag{2.29}$$

where σ_z is the rms-longitudinal bunch length.
From Eqn.(2.25) we see that the gain is proportional to peak current which in turn is proportional to the charge per bunch and inversely proportional to the longitudinal bunch length. Hence FELs, to be more efficient, require high-charge, ultrashort-bunch electron beam. We now present the beam parameters required to drive the IRFEL.

2.6 Characteristics of the IRFEL driver-accelerator

To discuss the characteristics required for the electron beam generated by the IR-Demo driver accelerator, we list in Table 2.1 the specifications on the wiggler magnet which have been derived from the requirements on photon beam parameters define by the experimentalists. In the JLab FEL IR-demo [15] (see figure 2.11), the charge per bunch was initially chosen to be 60 pC, the maximum value that yields a tolerable emittance growth due to space-charge. The average current should be as high as possible to maximize the average power of the laser. It is a function of the charge per bunch, and the bunch repetition that depends on the photocathode driver-laser which in turn must be a sub-harmonic of the superconducting linac operating frequency (1497 MHz). The maximum bunch repetition rate is 74.85 MHz and it is limited by the electron source. The repetition rate of the electron bunch was indeed initially set to 37.425 MHz which mean the maximum average current that can be reach is approximately 5 mA.
Since the energy does not affect the gain, and its only implication is on FEL wavelength: the IR-demo is foreseen to initially lase in the region 3 μm-6 μm range[7] (later this range will be extended

[7] Theoretically the output wavelength only depends on energy. Hence we could, in the IRFEL operate at any arbitrary wavelength by choosing the proper energy. Experimentally, the output wavelength is limited to a certain range that depends on the FEL-optical cavity mirror. For instance the mirror used to lase at 3 μm are not the same as the one used to lase with an output wavelength of 6 μm

to 100 μm wavelengths); this implies the maximum electron beam energy should be in the range 38-48 MeV.
The transverse normalized emittance specification are set by the wavelength at which we wish to operate the laser: the electron beam emittance should be less than the optical beam emittance:

$$\tilde{\varepsilon}_n < \gamma \frac{\lambda}{4\pi} \tag{2.30}$$

The factor $\lambda/(4\pi)$ is the transverse phase space area of the optical beam assuming it can be well described by Gaussian optics.
For the laser wavelength and energy of operation (i.e. $\lambda_1 \simeq 3\,\mu$m and $\gamma \simeq 77$) the Eqn.(2.30) yields a normalized emittance for both transverse plane that must be smaller than $\tilde{\varepsilon}_n \simeq 19$ mm-mrad to enable the operation of the laser at the fundamental wavelength. In fact this value is an "edge" value: it was assessed from numerical simulation of the FEL gain that the emittance should be less than 8.7 mm-mrad to also enable the laser to produce light at the third harmonic with sufficient gain[8].
The energy spread of the electron beam σ_γ/γ should be less than $\frac{1}{5N_u}$ i.e. $\sigma_\gamma/\gamma < 0.5$ % Using the above parameters as guideline we presents in figure 2.10, typical sensitivity of the small signal gain versus bunch length and transverse emittance.

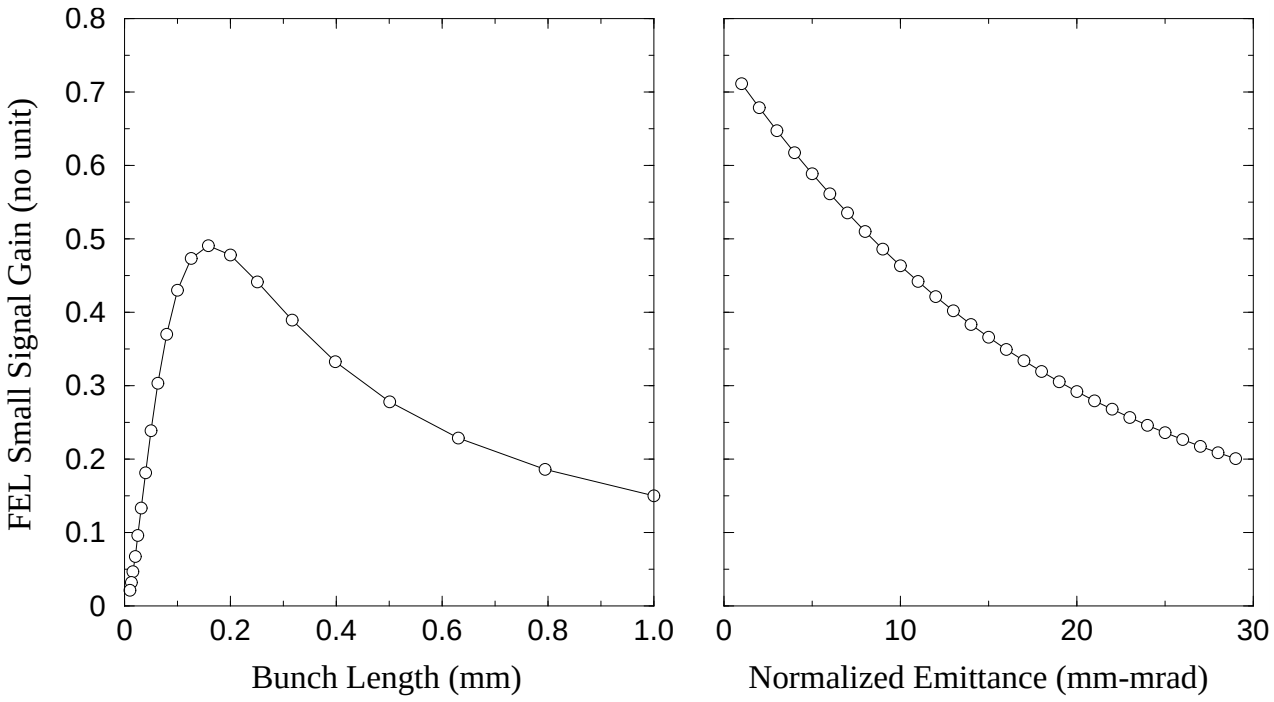

Figure 2.10: An example of variation of the gain versus the bunch length **(A)** and the transverse emittance (both x and y plane) **(B)** (these plots were computed using the very simple 1D model exposed in the previous section).

[8] S. V. Benson, private communication

2.7 The Jefferson Lab IR project

The purpose of the consortium gathered around Jefferson Lab is to develop the technologies needed to realize high-power free-electron laser in a cost effective frame. The long term project is to build a 20 kW infrared free-electron laser As a starting point it was decided to build the IRFEL that is used as experimental platform throughout the present report.

In the built IRFEL (see top view in figure 2.11), the electron beam is generated by a 350 keV photoemission electron gun and accelerated by two superconducting RF CEBAF-type cavities (5-cells cavity operating on π-accelerating mode) mounted as a pair in the so-called "quarter cryounit" which provides a beam energy gain of approximately 10 MeV. The beam is then injected into the main linac which is composed of one cryomodule, containing 8 superconducting CEBAF-type superconducting RF cavities. The linac can currently accelerate the beam up to approximately 48 MeV. This cryomodule is followed by two 4-bends chicanes that bypass the FEL optical cavities and provide additional longitudinal phase space manipulation. The IR undulator (see parameters in Table 2.1) is located between the two aforementioned chicanes. After the FEL interaction, the "spent" beam is recirculated with a quasi-isochronous recirculator with variable momentum compaction and path length up to the entrance of the cryomodule with the proper time of arrival so that the electron bunches are on the decelerating phase of the radio-frequency wave. The secondary beam is thereby decelerated down to 10 MeV and separated from the primary beam before being dumped in the "energy recovery dump" by the mean of the "extraction chicane". The energy recovery scheme allow the recovery of almost all the energy provided to the beam by the main linac during the acceleration phase.
The FEL light is directed in an optical room where it can be diagnosed and sent to one of the six user laboratories. The experiments that have been run to date, include standard pump-probe experiment to measure the gold reflectivity in the IR region, the observation of laser light effect on a plasma, and some preliminary tests in micro-machining.

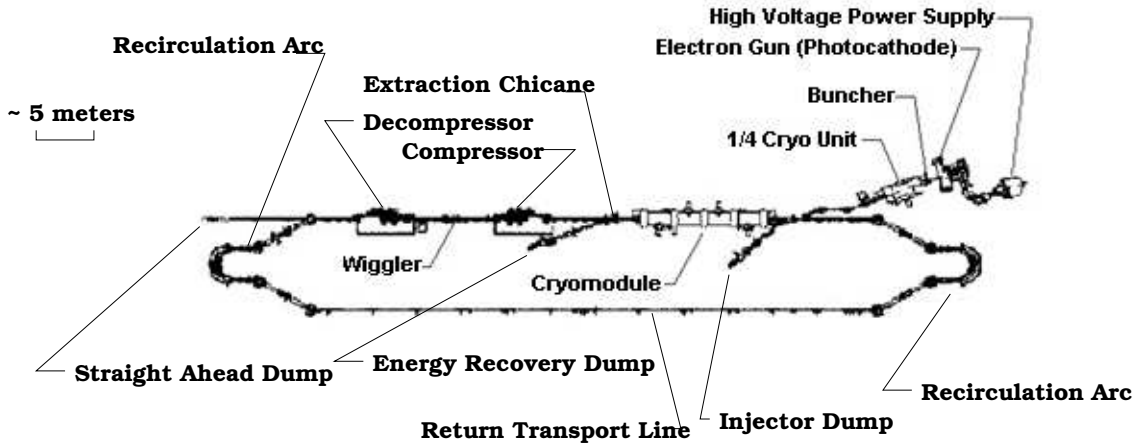

Figure 2.11: An actual top view of the "as built" IRFEL driver accelerator.

The electron source [14] is a DC-photo-emission gun presented in figure 2.12. It consists of a Gallium Arsenide (GaAs) photocathode illuminated by a laser system capable of providing 5 W.

The wavelength is chosen so that the photon energy is above the work function of the GaAs. Once the photoelectrons are extracted from the GaAs crystal they are rapidly accelerated by the high DC electric field (approximately 4 MV/m) applied between the photocathode and the anode which are separated by 14.63 cm. The choice of a photoemission gun was driven by its capability to achieve high current density simultaneously with ultrashort bunch length compared to conventional thermionic electron source.

The cathode illumination system was designed to be flexible so that it can be used to vary several characteristics of the electron beam: the charge of the electron micro-bunches, their frequency and the macropulse frequency and width. The illumination system consists of a mode-locked, frequency doubled, Nd:$YLiF_4$ laser commercially available from Antares© [13] producing a wavelength λ =527 nm. The optical pulse achieved is 23 ps (RMS) at a repetition rate that can be varied up to 74.85 MHz. This frequency corresponds to the 20th sub-harmonic of the fundamental frequency of the linear accelerator radio-frequency system: 1497 MHz; it thereby insures the bunch to bunch acceleration. The maximum power that can be achieved by such photocathode driver laser is approximately 6 Watts. It can be adjusted by modulating the laser beam using two electro-optics crystal. The choice of using simultaneously two electro-optics cell is driven by the desire to achieve a high extinction ratio.

The electron bunch charge can be varied from 0 to 135 pC by attenuating the laser beam thanks to a rotational polarizer located between the two electro-optics cells.

Hence the optical pulse on the photocathode generally consists in a series of 23 ps width "micropulses" occurring at a frequency f_m. The micropulse produced during a certain time t_M constitute a macropulse. Hence the micropulse frequency can only take the value $f_m = 74.85/h$ MHz (with $h \in \mathbf{N}$).

The transverse beam spot on the photcathode can be shaped by using a mask to make it looks more square or gaussian. The former distribution has been shown experimentally to reduce nonlinearities in the space charge forces [14].

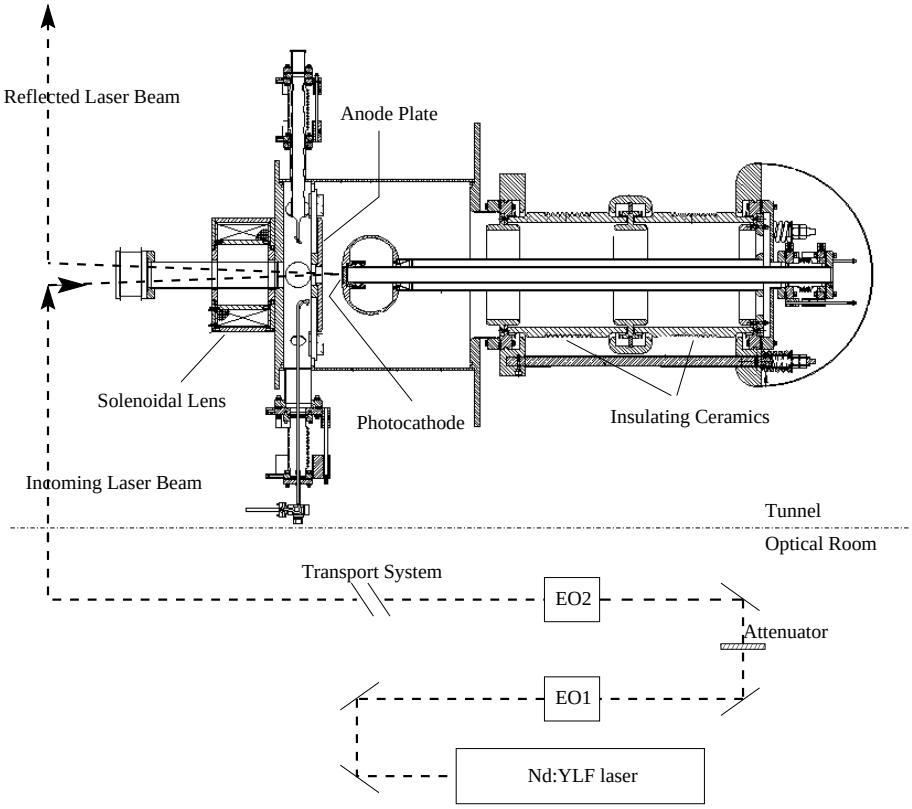

Figure 2.12: Simplified schematic of the electron source: A 527 nm laser beam that can be modulated by two electro-optics cell (EO1 and EO2) and attenuated by a rotational polarizer illuminates the GaAs photocathode. Ejected photo-electrons are accelerated through to the accelerating voltage of nominally 350 kV between the photocathode and the anode.

Chapter 3

The FEL driver accelerator: Lattice Study

3.1 Introduction

The present Chapter deals with the optical lattice of the IRFEL driver-accelerator. After briefly reviewing the accelerator magnetic optics with the help of a numerical model, we present few experimental results obtained as we tried to characterize the lattice and compare it with a numerical model.

3.2 A Brief Overview of the FEL Optical Lattice

In this section we describe the FEL optical lattice for the main accelerator only. It has been designed by D. Douglas and it is also described in numerous reference (see for instance reference [16]). For the purpose of the present discussion, the driver-accelerator can be divided into five parts:

1. A 10 MeV injector and the injection transfer line
2. A 48 MeV superconducting radio-frequency (SRF) linear accelerator (it is used both to accelerate the first pass beam and to decelerate the second pass beam); this linac is also termed "cryomodule" hereafter,
3. A wiggler insertion region,
4. A recirculation ring,
5. A reinjection transfer line.

In this section we will only concentrate on the high energy lattice (E$\simeq$48 MeV) that is items 3, 4, and 5 in the list above.

The first region encountered by the beam at the exit of the SRF linac is a "matching" region. It

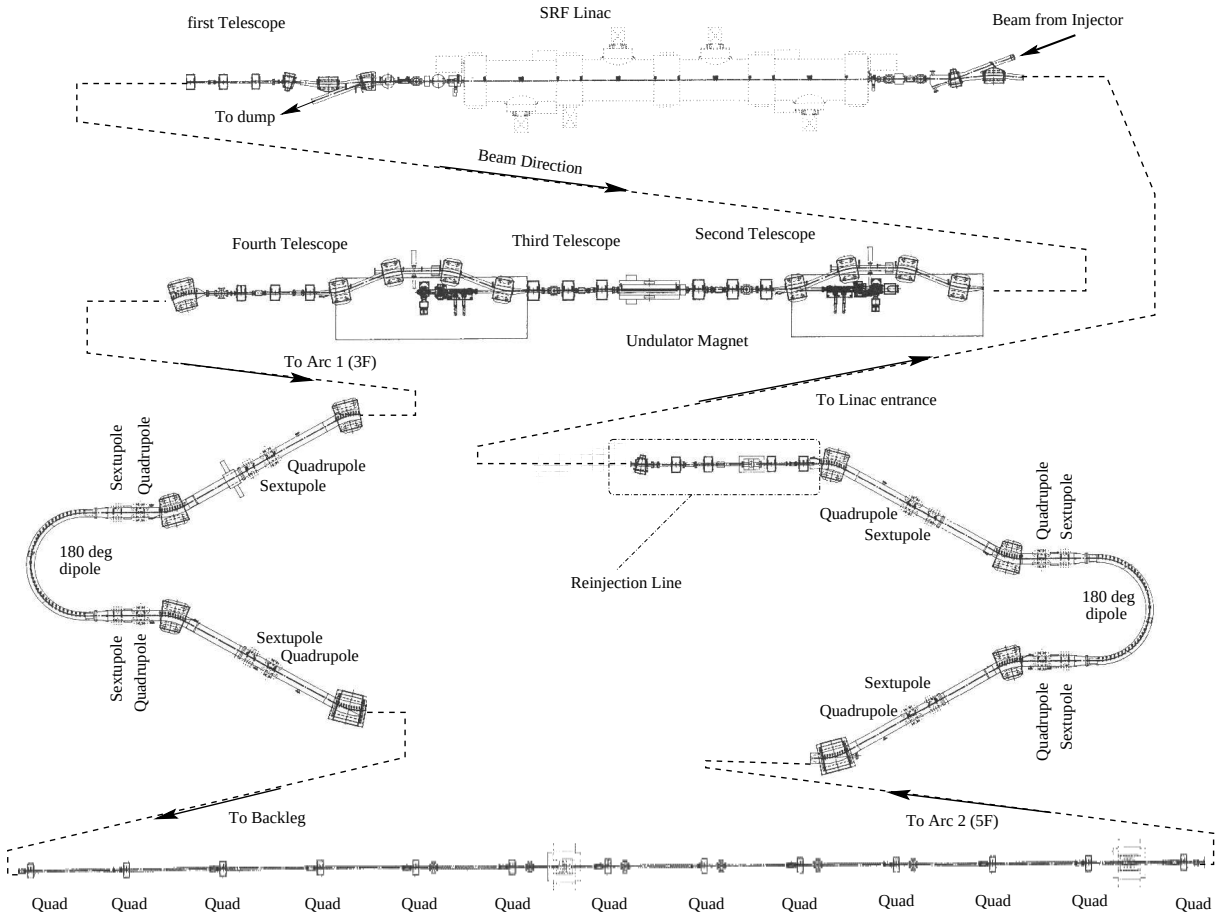

Figure 3.1: Dispersed overview of the main ring of the driver accelerator corresponding to figure 2.11. The path of the electron beam is indicated with arrows.

insures the beam lattice functions are properly matched to the desired value at the undulator center. This region consists of two quadrupole telescopes disposed upstream and downstream an achromatic chicane. The telescopes consist each of three quadrupoles. These two telescopes provide six free parameters (the strength of the quadrupoles) to adjust the four Twiss parameters (α_x, α_y, β_x, β_y) while insuring the beam size can still be contained within the vacuum chamber with acceptably low particle loss via scraping. The α-functions are supposed to be zero at the wiggler center whereas the betatron functions are matched to the wiggler "natural" betatron function eigenvalue of an infinitely long wiggler $\beta_w = \gamma\lambda_w/(2\pi\sqrt{2}K)$, with λ_w the wiggler period and K the undulator parameter (see Chapter 2). The "upstream" by-pass chicane provide further longitudinal phase space rotation because of its non isochronicity (momentum compaction[1] $R_{56} = -28$ cm).
After the wiggler, two additional telescopes each composed of quadrupole triplets are used to match the optical lattice functions to the desired values at the injection point. Longitudinally, further phase space rotation is provided by the "downstream" by-pass chicane which is identical to the upstream chicane.
The recirculation loop is composed of two arcs linked by a straight line section, termed "backleg"

[1]Throughout this report the momentum compaction is defined as the transfer matrix element $R_{56} = \frac{\Delta z}{\Delta E/E}$ in the TRANSPORT formalism. This definition is different from the usual definition (generally for closed orbit accelerator) where it is defined as the ratio of relative path length change for a relative energy change $\alpha = \frac{\Delta L/L}{\Delta E/E}$

Parameter	Value
α_x	-0.178
β_x (m)	8.331
α_y	-0.124
β_y (m)	3.979

Table 3.1: Twiss parameters downstream the cryomodule expected from simulations with the code PARMELA.

that consists of six period of a FODO lattice.
The arcs are based on the MIT-Bates accelerator design [17]; they provide each a total bending angle of 180 deg. They include four wedge-type dipoles, each bending the beam by an angle of $\simeq\pm 28$ deg alternatively, installed in pair symmetrically around a 180 deg dipole. Furthermore providing the desired rotation, the arcs are also used to adjust the total beam path length of the recirculated beam in a such way that the electron bunches have the proper timing to be on the decelerating phase of the SRF linac, a very important parameter for energy recovery. For such a purpose, the arc is instrumented with a pair of horizontal steerers located upstream and downstream the 180 deg dipole to vary the reference orbit path length inside the 180 deg magnet. Two families of quadrupoles (the trim quadrupoles) and sextupoles are installed in the arc to provide both linear and quadratic energy dependent path length variation that are necessary in the "energy-compression" scheme needed to properly energy recover the beam [18] i.e. to precisely adjust the momentum compaction R_{56}[2] (linear dependence of longitudinal position with relative energy) and the nonlinear momentum compaction T_{566} (quadratic dependence). When the quadrupoles and sextupoles are not powered, the arc is operating in a non-isochronous mode ($R_{56} = 13.124$ cm). However under nominal operation, i.e. when the FEL is operating and the linac is in energy recovery mode, because of the need of energy compression, the sextupoles and quadrupoles of one family are excited to proper values in order to provide the required R_{56} between the wiggler exit up to the linac entrance.
The backleg transport line consists of thirteen quadrupoles. Nominally it is operated as a F0D0 lattice with a phase advance per cell $\mu = 90$ deg, but we have demonstrated its operation with a phase advance of $\mu = 60$ deg needed during emittance measurement based on multi-monitor technique. Its total transfer matrix is **-I** for both transverse plane: it images the lattice optical functions at the first arc exit into the first arc entrance accordingly to $\beta \rightarrow \beta$ and $\alpha \rightarrow -\alpha$.
The reinjection line consists of a telescope composed of four quadrupoles that is used to adjust the beam lattice function to achieve reasonable beam envelope at the entrance of the SRF linac.
As the electron bunches go for the second times through the SRF linac, they are decelerated and induce voltage in the cavity via beam loading. This induced-voltage is at the proper mode to serve to accelerate the next bunch in the acceleration phase which is in the neighboring RF bucket. The wasted beam, once decelerated (i.e. at approximately 10 MeV), bifurcates into a dump.

Typical lattice functions, computed with the second order optics code DIMAD, are shown in figure 3.2. The initial conditions (see Table 3.2) that are used, have been computed using the PARMELA code since it include space charge effects in the low energy region and also have a very detailed model of the SRF cavities. For the figure presented, the undulator magnet is installed.

[2] $R_{56}^{s_0 \rightarrow s} = \int_{s_0}^{s} = \frac{R_{16}(x)}{\rho(x)} dx$, where $\rho(x)$ is the local bending radius. So since the presently mentioned quadrupole are located in a dispersive region, i.e. $R_{16} \neq 0$, so that R_{56} can be varied.

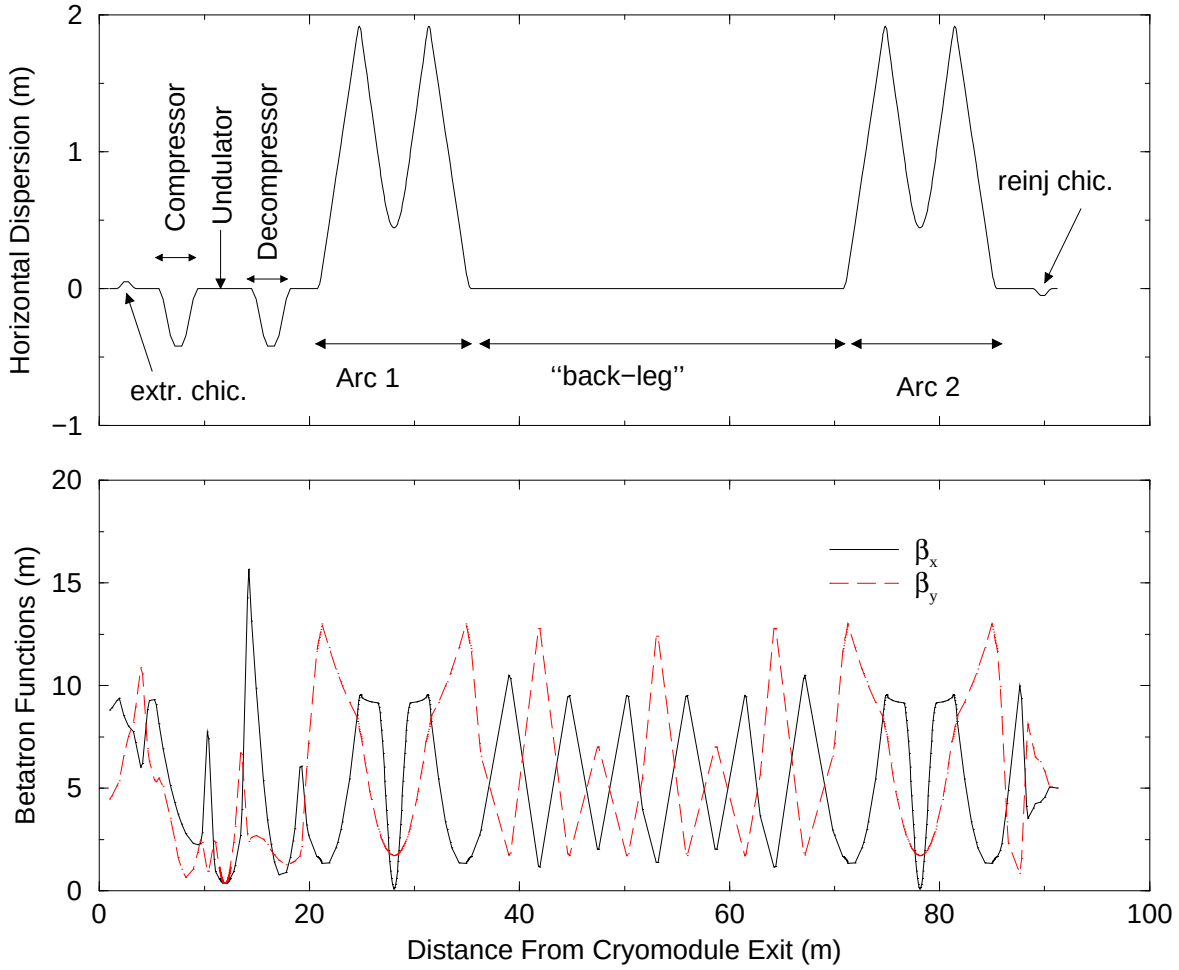

Figure 3.2: Horizontal Dispersion (**top graph**) and transverse betatron functions (**bottom graph**) for the nominal settings of the magnetic optics.

3.3 Measurement of the Transverse Response

Though the driver-accelerator design is essentially specified via numerical simulations, there are many factors that can cause the real machine to be different from the numerical model. Among the causes of these discrepancies, the most usual are alignment errors, magnet disfunctions, etc... Hence it is of prime importance, in the first phase of commissioning of the accelerator, to diagnose these defects and potentially fix or understand them to match as close as possible the numerical model to the "as built" accelerator. In this section we report on measurement of the transverse lattice response of the driver accelerator along the recirculator. In this report, we have only concentrated on two types of measurements: (1) try to verify that the first order transfer matrix used in the model is close to the machine, (2) measure precisely the dispersion (i.e. the transverse position dependence on energy) function in the back-leg transfer line.

3.3.1 Theoretical Background

The purpose of measuring the transverse response of the optical lattice is to get some insights on the first order transport and potentially find out problems with the lattice i.e. magnets corrupted excitation, optical elements misaligned. We have performed two types of measurement: (1) response of the lattice for a given angular excitation by mean of correctors and (2) energy dependence of the lattice i.e. measurement of the dispersion.
In a dispersion-free region, the position and divergence centroid of a beam $(x(0), y(0))$ at an arbitrary position 0, is propagated to another position, under the assumption of first order transport validity, accordingly to:

$$\begin{pmatrix} x(s) \\ x'(s) \end{pmatrix} = \begin{pmatrix} R_{11}^{0\to s} & R_{12}^{0\to s} \\ R_{21}^{0\to s} & R_{22}^{0\to s} \end{pmatrix} \begin{pmatrix} x(0) \\ x'(0) \end{pmatrix} \tag{3.1}$$

The observable that can easily be measured is a beam centroid position at the downstream location $x(s)$. Hence a technique to measure the transverse response is distort the orbit by using a perturbative angular kick on the beam trajectory at the position $x(0)$ i.e. $x'(0) \to x'(0) + \Delta x'$. In such an event, the "perturbed" beam position downstream now writes:

$$x_{perturb}(s) = R_{11}^{0\to s} x(0) + R_{12}^{0\to s}(x'(0) + \Delta x') \tag{3.2}$$

That is the displacement of the beam position at s, $\Delta x(s) \stackrel{\text{def}}{=} x_{perturb}(s) - x(s)$ is only dependent on the angular perturbation at 0:

$$\Delta x(s) = R_{12}^{0\to s} \Delta x' \tag{3.3}$$

Moreover, for a dipole we can relate the angular kick to the beam momentum: $\Delta x' = 1/(3.3356 \times p) \times \int Bdl$ where $\int Bdl$ represents the field integral (in T.m), and p is the beam momentum (in GeV).
Hence a very simple way to check if the "real world" machine is performing as predicted by first order transfer matrix model, is to measure the beam position along the beam line for different perturbations (angular kick values but also position of the kicker magnet used). It is worth mentioning that this technique allows directly to measure the R_{12} transfer matrix element. The measurement of R_{11} requires more elaboration: one needs to create a perturbation that is exactly 90 deg out of betatron phase with respect to the kick intended to measure the R_{12}; in such way one can compute to what position displacement it corresponds.

The other type of measurement is the energy dependence of the optical lattice. This measurement is very similar to the transfer matrix response aforementioned: it is know that after magnetic element systems such as dipoles there can be position dependence on energy, i.e. the position $x(s)$ writes as $x(s) = x_\beta(s) + \eta(s)\delta(0)$, where $x_\beta(s)$ is a pure betatron induced position and the product of $\eta(s)$, dispersion function at s, with $\delta(0)$, energy offset at 0, represent the dispersive contribution to the orbit. Note that $\eta(s) \equiv R_{16}^{0\to s}$. Therefore by varying the energy of the bunch centroid (i.e. $\delta \to \delta + \Delta\delta$) and measuring the associated position change downstream the beamline $\Delta x = \eta \Delta\delta$ we can get an estimate of the dispersion function η.

3.3.2 Experimental Method

To determine experimentally the lattice response due to either kick excitation (pure transverse response) or energy change (dispersion), we only have to measure the beam position, the only observable we can easily access. The beam position is measured by means of electromagnetic pickup called beam position monitors (BPMs) [25]. These BPMs consist of a number of pick-up antennae distributed around the diameter of the vacuum chamber that detect the Coulomb field associated with an electron bunch as it propagates along the beamline. Based on the asymmetry of the signal on each antenna, the beam centroid coordinates can be inferred. Two types of BPMs are installed in the IRFEL accelerator. In the measurement presented hereafter, we have only used the so-called stripline BPMs whose cross section is depicted in figure 3.3. This type of BPM consists of four strip-like pickup antennae oriented at 90 deg from each other. This type of geometry for the pickup antennae has the advantage to minimize the beam quality deterioration because of wakefield. The beam centroid coordinate is a simple function of the electric potential (V_R, V_L, V_D,

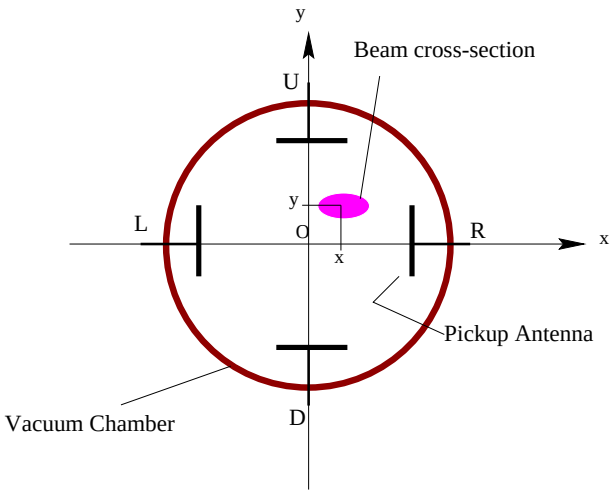

Figure 3.3: schematic cut of a beam position monitor (BPM).

V_U)induced by the beam on each antenna [19] of the BPM (R, L, D, U on figure 3.3):

$$\begin{aligned} x &\propto \frac{V_R - V_L}{V_R + V_L} \\ y &\propto \frac{V_U - V_D}{V_U + V_D} \end{aligned} \tag{3.4}$$

The electronic system used to process the signal is the so-called Switched Electrode Electronics (SEE) [24]. The signal of peripherical electrodes is multiplexed to the same processing electronics system. And the beam position is inferred using the standard technique from this signal. An advantage of this electronic is that it can be used to acquire beam position at very high rate typically 30 Hz to study potential time dependent beam position fluctuation.
The practical method to measure the response of the lattice is as follows: (1) For the nominal condition, measure the beam position on all the desired BPMs $\{x_0, y_0\}_{i=1...N}$ (the subscript i is the BPM index); (2) impress the desired distortion (i.e. energy change for dispersion measurement or angular kick for R_{12} measurement); (3) measure the new beam position on the N BPMs $\{x, y\}_{i=1...N}$ and compute the displacement (or difference orbit) of the beam centroid along the beamline at the

location of each BPMs $\{\Delta x, \Delta y\}_{i=1...N}$:

$$\begin{pmatrix} \Delta x \\ \Delta y \end{pmatrix}_{i=1...N} = \begin{pmatrix} x \\ y \end{pmatrix}_{i=1...N} - \begin{pmatrix} x_0 \\ y_0 \end{pmatrix}_{i=1...N} \tag{3.5}$$

For a transverse response lattice measurement, the transverse matrix elements are numerically computed using the lattice set-up used during the measurement; the beam centroid induced by the angular perturbation are computed using the R_{12} transfer matrix element.

For dispersion measurement, the energy change is impressed using the last pair of cavities in the cryomodule. Unfortunately this method does not provide valuable information (see the experimental section for more explanation) and we had to use another technique to perform such measurement. In the first place dispersion always results in a non-zero local R_{16} transfer matrix element e.g. due to the presence of a dipole magnet. After it has been generated, it can propagate in region with no magnetic field; for instance if at the exit of the dispersion generator the dispersion and its derivative are η_0 and η'_0, then at a downstream location, the dispersion can be computed from the knowledge of the transfer matrix between the dispersion generator exit and the considered location:

$$\eta = R_{11}\eta_0 + R_{12}\eta'_0 \tag{3.6}$$

Note that in the case the dispersion generator is achromatic, we have $\eta_0 = 0$ and $\eta'_0 = 0$ so that $\eta \equiv 0$.
Because in the dispersion generator the beam momentum p is related to the magnetic field of the dipole B ($B\rho = ecp$), we have after differentiation $(\Delta p)/p = (\Delta B)/B$. Hence a transverse offset due to a relative energy change is equivalent to a relative magnetic field variation:

$$\Delta x(s) = \eta(s) \left[\frac{dp}{p}\right]_0 \equiv \eta(s) \left[\frac{dB}{B}\right] \tag{3.7}$$

where the subscript 0 indicate the energy changed is impressed before the magnetic system, and the $\left[\frac{dB}{B}\right]$ is the relative magnetic field variation of the magnetic system downstream which the dispersion is measured.

3.3.3 Results on Transverse Response

From the aforementioned technique to assess whether the optical lattice is performing accordingly to the model, we need to have an accurate knowledge of the angular excitation provided by a corrector magnet. In order to estimate such angular kick and since all the corrector magnets are of the same type, we have use a corrector located in the backleg transport line with the next upstream beam position monitor. The quadrupoles in between these two elements were not powered. So the transfer matrix between the element is the one of a drift space of length 2.80 m. For different corrector excitation, we measured the beam position as presented in figure 3.4. The beam position is linearly dependent on the corrector strength in the range in position the BPM was used [-4 mm, +4 mm]. A linear interpolation of the data presented in the figure, along with the knowledge of the transfer matrix between the BPM and the corrector yields an angular kick provided by the corrector magnet of approximately 0.64 mrad/(100 $\times$ Gauss.cm) this value is very close, within 3%,

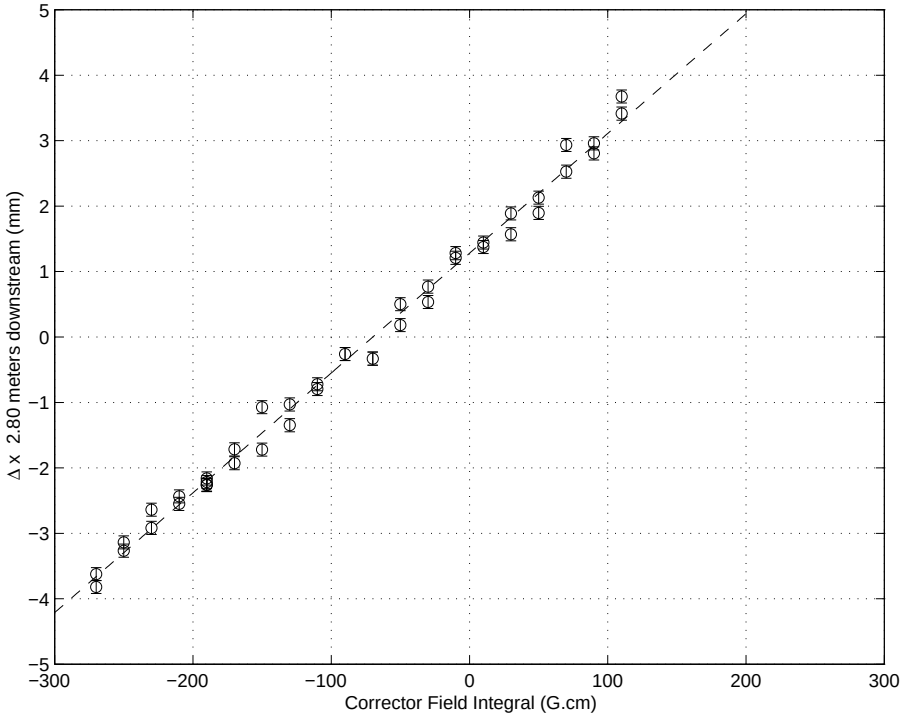

Figure 3.4: Example of calibration of a corrector. The slope of the linear interpolation is 0.0183 mm/(G.cm) which corresponds to an angular deflection of 6.54 μrad/(G.cm)

of the calculated value deduced from the corrector magnetic field map measurement[3] which give a kick of 0.65 mrad/(100 $\times$ Gauss.cm)

Practically, the corrector strength is set *de viso* by looking at the on-line histogram plot of the BPM value along the beam line, in such a way that the kick provide a significant position change along the beam line; typical value used during the acquisition of difference orbit measurement are approximately 100 G.cm. For a given corrector change $B_{nom} + \Delta B$, (B_{nom} is the nominal magnetic excitation of the corrector) all the BPM readbacks along the beamline are acquired three times (to quantify the beam position jitter). Then the corrector is set to the value $B_{nom} - \Delta B$. This latter operation allow to validate the measurement, since for the latter corrector setting, because of linearity of the system, the BPM readback should be the opposite of the one measured for the first measurement. Therefore the computation of the sum of the two measurements should give zero for all the BPMs.
The use of only one corrector to study the response of the lattice is not sufficient since it only "probe" the lattice at location that have a relative betatron phase advance of approximately 90 deg[4]. Hence it is preferable to use at least two correctors separated by the proper phase advance so that they probe different part of the lattice. In our present study, we use six different correctors: three for the horizontal plane (2F00H, 2F04H and 2F08H) and three for the vertical plane (2F00V, 2F04V and 2F08V). The correctors are chosen so that the relative betatron phase advance between

[3] G. H. Biallas, private communication, June 99

[4] In the general Twiss transfer matrix formalism one has: $R_{12}^{s_0 \to s} = \sqrt{\beta(s)\beta(s_0)}\sin(\Delta\mu)$ where $\Delta\mu = \mu(s) - \mu(s_0)$ is the relative betatron phase advance between the points s and s_0.

each other is approximately 60 deg so that one can accurately probe the whole period of the betatron excitation as pictured in figure 3.5. An example of measurement for the six corrector

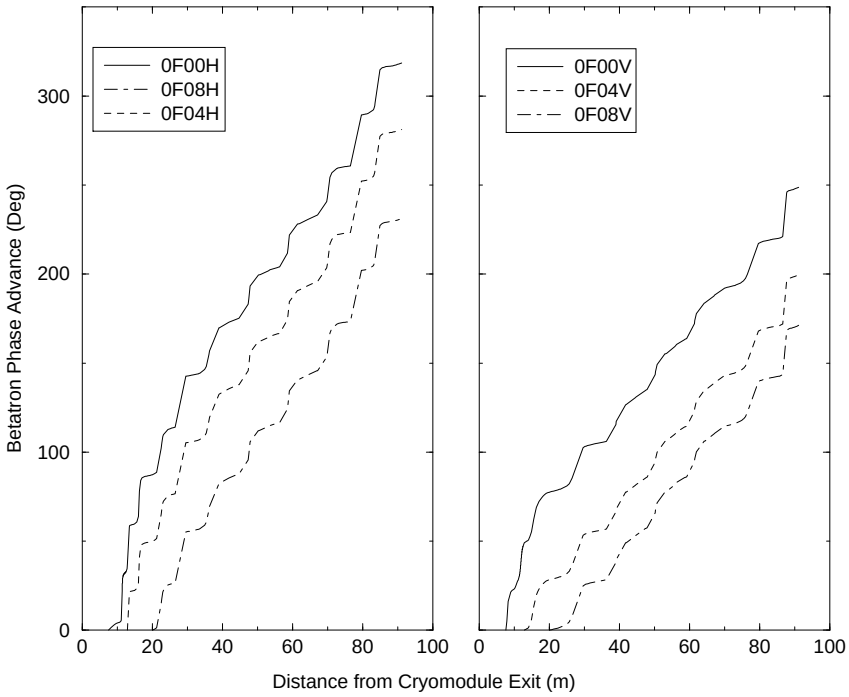

Figure 3.5: Betatron phase advance between each corrector used to perturb the orbit along the lattice in the horizontal (**left plot**) and vertical (**right plot**) plane (100 meters corresponds approximately to the end of the back leg beamline).

aforementioned is presented in figure 3.6. It is experimental response with the lattice and simulated response. Although the two patterns generally match quite well one can see in the case of corrector 2F04H that there are large discrepancies. A technique used to find out the discrepancies is to vary in the model different magnetic elements and try to minimize a χ^2-type quantities defined as: $\chi^2_x = \sum_{i=1}^{N}(\Delta x_i^{measured} - \Delta x_i^{simu})^2$ for the horizontal plane (the same kind of quantity is defined for the vertical plane). In the present case, it was found[5] that one of the quadrupoles was not producing the magnetic gradient that it was set to; the discrepancy between the set gradient and the one effectively produced according to the difference orbit analysis is approximately 10%. After inclusion of this discrepancy in the model, the newly computed pattern (see figure 3.7) are in good agreement with the measurement indicating the model (second order based transfer matrix) can be used to describe accurately the lattice.

3.3.4 Results on Dispersion Measurement

As we have already mentioned, the dispersion measurement theoretically reduces to the measurement of the orbit transverse displacement for a given energy change. The easy way of varying the energy in the accelerator is to change the accelerating gradient or the injection phase of one cavity. Unfortunately, there are transverse fields in the CEBAF cavity that can significantly deflect the

[5]D.R. Douglas first noted this fact

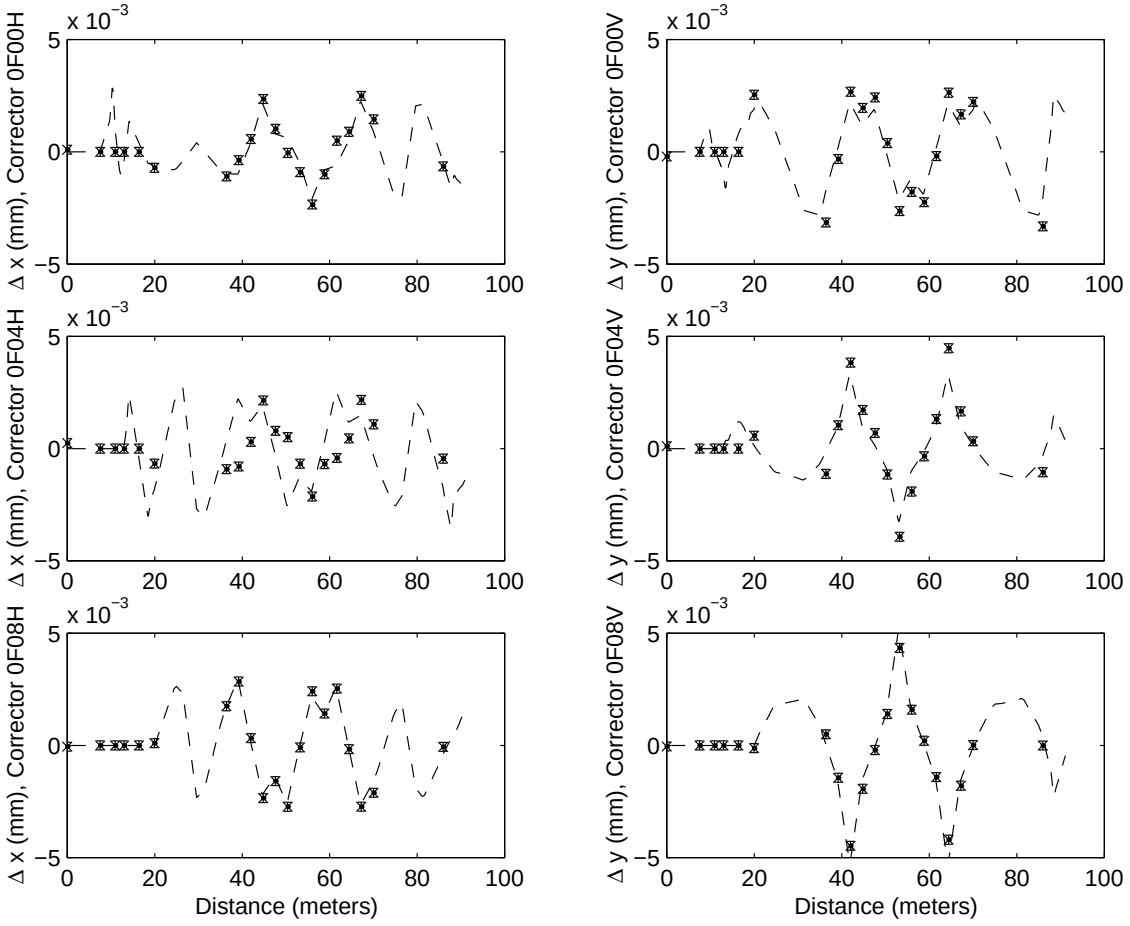

Figure 3.6: Comparison between the measured and simulated lattice response for the six correctors used during the difference orbit measurement (100 meters corresponds approximately to the end of the back leg beamline).

beam[6]. Because this RF-induced deflection is inversely proportional to the beam energy it can be a problem for the operating energies of the IRFEL: simulations indicates the induced deflection due to gradient change is significant and can be of the order of few tens of mrad. We have experimentally verified such result in our preliminary measurement of dispersion in the back-leg transfer line by varying the cavity gradient. We present in figure 3.8 the beam position offset along the beamline and compare it with the case where we operate the cavity at their nominal gradient and used a corrector at the linac exit to simulate potential RF-induced steering: the same type of pattern (which is in fact the R_{12}-induced pattern) is reproduced. This result confirms our suspicion that dispersion measurements performed using RF-gradient variation is not valid. Next we present , in figure 3.9, a measurement of dispersion obtained by varying the magnetic field in all the dipoles of the recirculation arc. We note that the maximum traverse displacement of the beam centroid is approximately $500 \pm 100\,\mu$m for a magnetic field variation of 1% insuring the spurious dispersion is lower than 5 cm in absolute value. This is an important result for emittance measurement as we shall see in Chapter 4.

[6] A detailed study of this effect is presented in Chapter 6

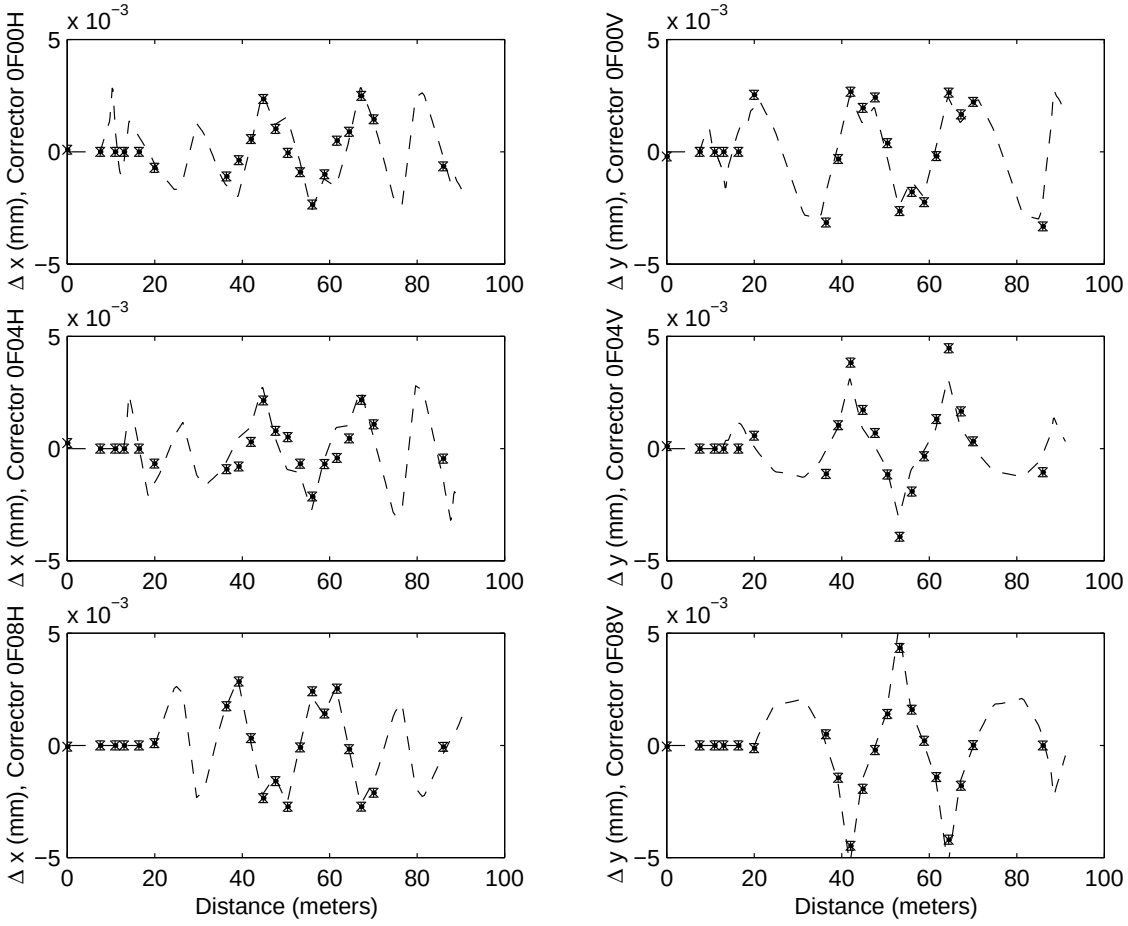

Figure 3.7: Comparison between the experimental data after correction and the simulated lattice response for the six correctors (100 meters corresponds approximately to the end of the back leg beamline).

3.3.5 Summary of the Transverse Response Measurements

We have demonstrated that the numerical model describes with high confidence the transverse properties of the as-built recirculating accelerator. We have measured the dispersion in the backleg transfer line when the trim quadrupoles and sextupoles in arc 1 are not excited and have discovered the spurious dispersion has an amplitude smaller than 5 cm.

3.4 Measurement of the Longitudinal Response

3.4.1 Motivation

It was demonstrated in Reference [18] how important, for energy recovery purpose, the energy compression scheme was. It enables to handle the large momentum spread induced as the laser operates. The basics idea is to set the longitudinal lattice, in the recirculation, in such a way

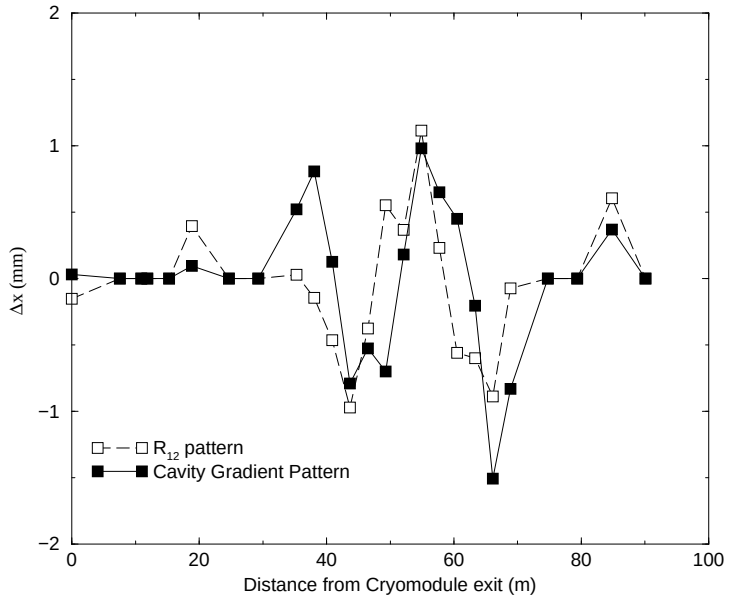

Figure 3.8: Comparison between an energy change induced beam displacement along the lattice and the response to an angular perturbation.

that during the deceleration phase, for energy recovery purpose, the relative momentum spread is reduced. Under the assumption of single dynamics first order optics this is simply because after the linac, the energy offset δ_i for an electron can be written as a function of its energy offset δ_0 and longitudinal position z_0 at the wiggler exit as:

$$\delta_i = R_{65}^{\text{linac}} z_0 + R_{65}^{\text{linac}} R_{56}^{\text{wiggler}\rightarrow\text{linac entrance}} \delta_0 \tag{3.8}$$

The R_{65} transfer matrix element of the linac is generally fixed: since the linac is setup to provide the proper energy for lasing. Therefore the only parameter that can affect the energy spread at the linac exit after energy recovery is the R_{56} of the recirculation from the wiggler exit to the linac entrance. An example of the importance in settings the energy recovery transport is shown in figure 3.10 where we present simulation of the energy recovery scheme: the PARMELA code is used as a skeleton to simulate the acceleration and deceleration of the beam (i.e. RF-induced curvature and phase slippage due to the non-relativistic nature of the beam are taken into account); the recirculation transport is simply simulated by tracking particles using the longitudinal transformation[7].

$$\begin{aligned} z_i &= z_i + R_{56}\delta_i + T_{566}\delta_i^2 + \mathcal{O}(\delta_i^3) \\ \delta_i &= \delta_i \end{aligned} \tag{3.9}$$

For sake of simplicity and in order to expedite numerical simulations, we have turned off space charge routine in PARMELA. The proper phase to achieve the shortest bunch at the wiggler insertion is approximately -8 deg off crest. The beam is recirculated and re-injected $-8 + 180$ deg off crest in the cryomodule so that it is decelerated and the electromagnetic energy stored in the cavity via beam loading is directly used to supplement the available power for the accelerating mode. We present the obtained results in 3.10, the longitudinal phase space at the linac exit (after

[7] In this numerical analysis, neither longitudinal wakefield induced in the accelerating structure and various beamline component, nor space charge collective force are taken into account

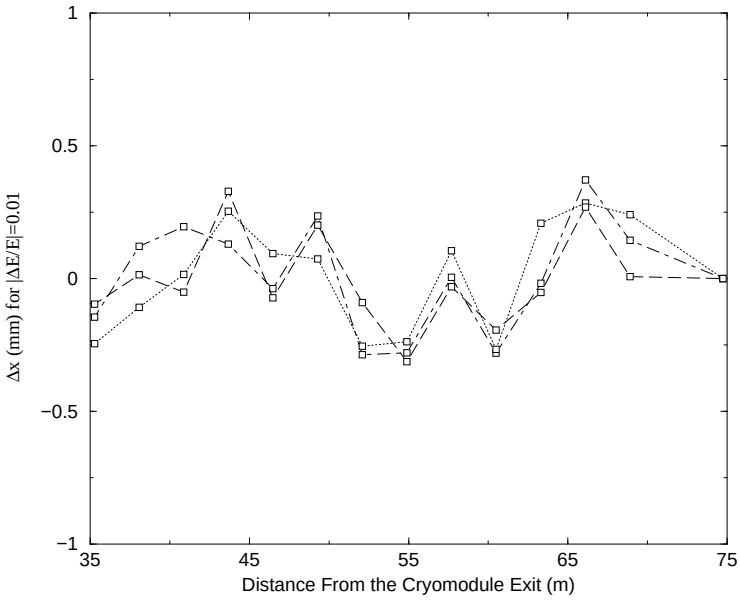

Figure 3.9: Beam displacement in the backleg transport for a relative variation of 1% of the magnetic field of the first recirculation arc.

acceleration), the downstream and upstream the wiggler are presented in the first row. The effect of the wiggler was numerically simulated by generating an energy offset of .5 MeV and the energy spread of the particle was set to: $\delta_i \rightarrow \delta_i + 1/2\Delta E \times rand(-1,1)$ where "rand" randomly generate a number in [-1,1] interval. The longitudinal phase space after the recirculation for different values of R_{56} and T_{566}. The corresponding phase space after the deceleration in the linac are presented in the bottom row. It is seen (bottom right) that with proper choice of R_{56} and T_{566}, the resulting energy spread can be greatly reduced, yielding a beam that can be transported through the dump transfer line.

The optimum point for operation of the linac in terms of both phase and accelerating voltage must be related to the momentum compaction of the transport from the linac exit to the wiggler in order to achieve the right longitudinal phase space slope at the entrance of the linac. In fact the linac voltage and phase are dictated by the fact that one needs to match the longitudinal phase to the R_{56} of the compressor chicane by fulfilling the relation: $\sigma_{56}/\sigma_{55} = -1/R_{56}$ (σ_{56} and σ_{55} are the beam sigma matrix elements). This matching condition is required to insure one can produce the shortest possible bunch length at the point where the FEL-interaction takes place. This minimum bunch length, when the matching condition is verified, is $\sigma_z^{MIN} = R_{56}\tilde{\varepsilon}_z/\sigma_z^0$ where the rms longitudinal emittance $\tilde{\varepsilon}_z$ and the bunch length σ_z^0 are taken at the linac exit.
From PARMELA optimization[8] and recent experimental operation, the linac accelerating voltage is about 38 MeV and is operated at approximately -8 deg off-crest.
The by-pass chicanes have their momentum compaction fixed by design to -28.8 cm and the only free system to adjust the R_{56} are the end-loop arcs of the recirculation transport by varying the trim quadrupoles as we have already mentioned. An example of variation of the momentum compaction of one arc with respect to the second family quadrupoles excitation is shown in figure 3.11. In the figure we also plotted the non linear term T_{566} for the quadrupole but also for different sextupoles

[8]B. C. Yunn, updated PARMELA input files for the IRFEL driver-accelerator, private communications

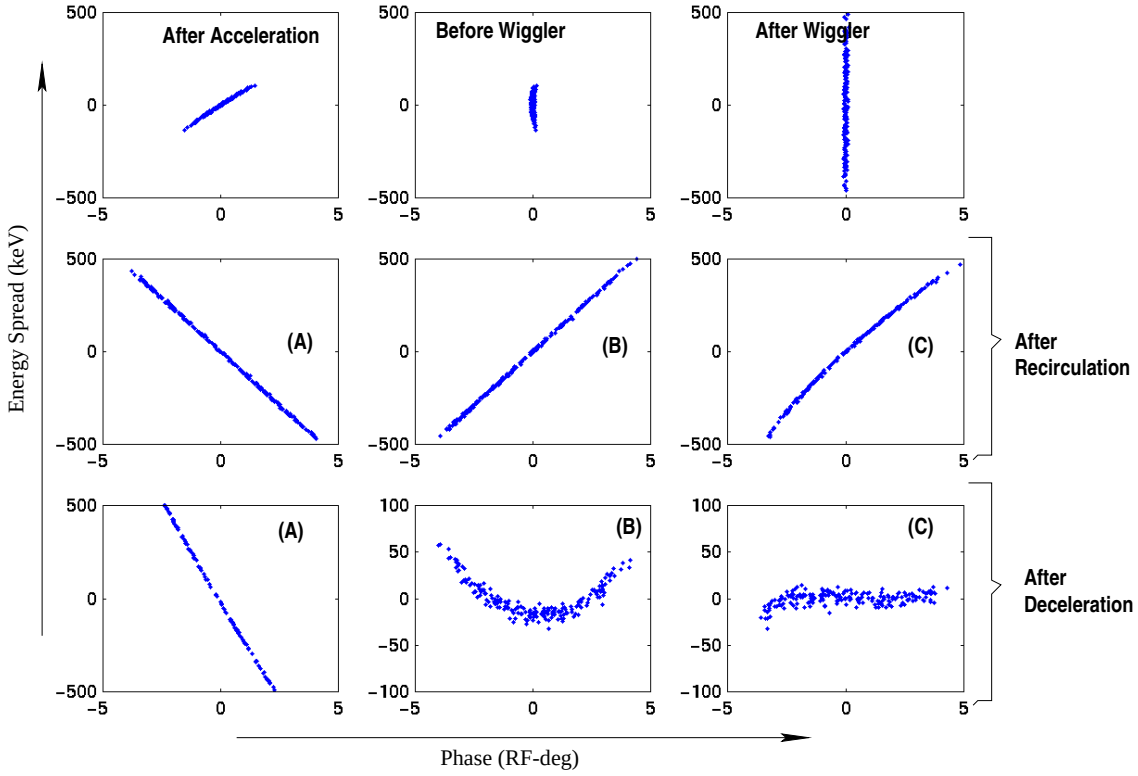

Figure 3.10: Energy compression scheme: The first row (from left to right) presents the longitudinal phase space at the linac exit, after the compression chicane, and just after the wiggler interaction has taken place; the second row show longitudinal phase space at the entrance of the linac just prior to deceleration for three different choice of R_{56} and T_{556} (for (**A**) -0.2 and 0. m, for (**B**) 0.2 and 0 m and for (**C**) 0.2 and 3.0 m). The result for the three cases after deceleration are shown in the third row.

excitation (in this latter case the trim quadrupoles are unexcited). Note that the momentum compaction as a function of the quadrupole strength can be parameterized by a quadratic regression to give the "handy" formula:

$$R_{56}(k_q) = 0.1436 - 0.5496k_q - 0.05255k_q^2 \tag{3.10}$$

Experimentally this formula can be used to quickly check the R_{56} of an arc and compare with measurement.

3.4.2 Theoretical Background

The longitudinal lattice characterization is very similar to the transverse response measurement previously detailed: the method again consists of impressing a known variation of the beam initial condition and measuring the corresponding response downstream the section one wishes to characterize. There are two types of longitudinal measurement that can be done very easily in the IRFEL: the compression efficiency (or phase-phase correlation) and the momentum compaction (or

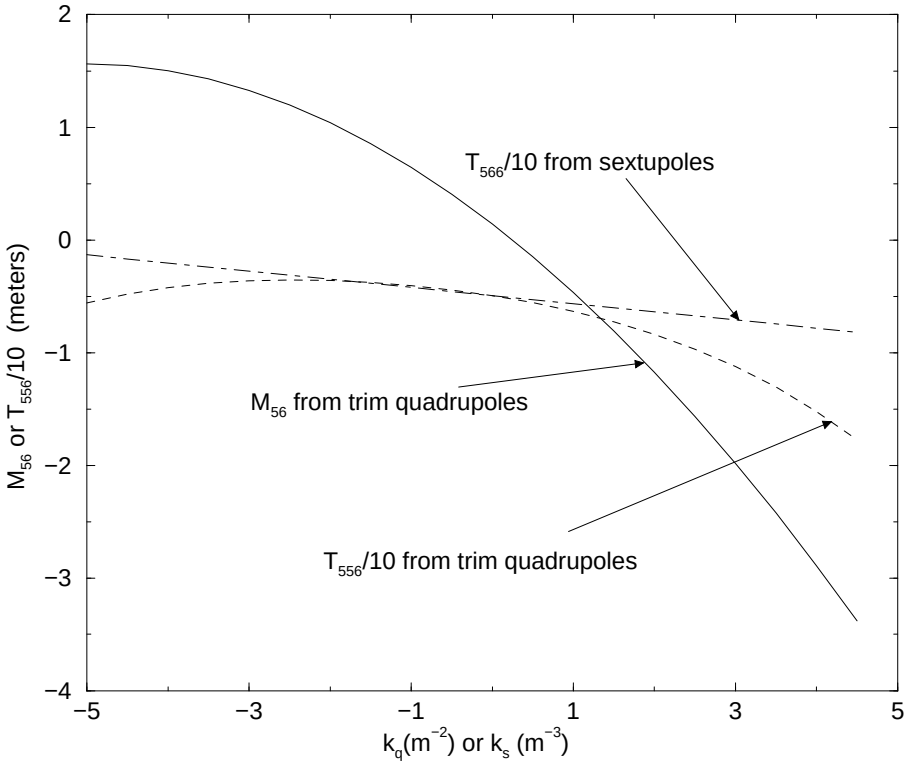

Figure 3.11: Momentum compaction and nonlinear momentum compaction for one arc versus the second family of trim quadrupoles excitation strength (k_q). nonlinear momentum compaction versus the second family sextupoles strength k_s (for this calculation, the trim quadrupoles are unexcited).

phase-energy correlation). In these measurements, the bunch is considered as a macroparticle and the time-of-flight (TOF) of its centroid is measured between the locations where the variation is impressed and a point where the time of arrival can be estimated.

Compression Efficiency

The phase-phase correlation, $\langle \phi_{in} | \phi_{out} \rangle$ requires the measurement of time-of-flight (TOF) of the bunch centroid versus a variation of its "injection phase" in the section we wish to study. In the FEL driver-accelerator, this quantity is only measured starting from the photocathode since it is the only location the "injection phase" ϕ_{in} can be varied orthogonally with respect to the injection energy by varying the phase of the photo-cathode drive laser that illuminates the photocathode with respect to the master oscillator (and all the RF-element settings are kept constant). The phase variation an arbitrary location downstream the photocathode $\delta\phi_{out}$ as a function of the injection phase perturbation $\delta\phi_{in}$ writes:

$$\delta\phi_{out} = \frac{\partial \phi_{out}}{\partial \phi_{in}} \delta\phi_{in} \stackrel{\text{def}}{=} \langle \phi_{in} | \phi_{out} \rangle \delta\phi_{in} \tag{3.11}$$

Therefore by varying in a known fashion the injection phase and measuring the associated response downstream, we obtain the phase-phase response of the section comprised between the perturbation and the measurement station. From this phase, using the standard notation of the TRANSPORT

lattice code[9], we have:

$$\langle\phi_{in}|\phi_{out}\rangle\delta\phi_{in} = (R_{55} + \sum_{k<5} T_{5k5}r_k)\delta\phi_{in} + T_{555}(\delta\phi_{in})^2 + (\text{3rd order terms}) \tag{3.12}$$

where r_k is k-th co-ordinate of the vector $r = (x_{in}, x'_{in}, y_{in}, y'_{in}, \phi_{in}, \delta_{in})$ Therefore, nonlinear fit of this phase-phase transfer map yields the arbitrary order transfer matrix element $\langle\phi_{in}|\phi_{out}\rangle$.

Momentum Compaction

The R_{56} measurement involves the variation of beam energy. Such operation can be performed by varying the gradient of an rf cavity. The beam injected in this cavity must be relativistic to avoid phase slippage effects. If the measurement occurs in a dispersion free point, the same kind of relation as Eqn.(3.12) can be written:

$$\langle\delta_{in}|\phi_{out}\rangle\delta_{in} = (R_{56} + \sum_{k<6} T_{5k6}r_k)\delta_{in} + T_{666}(\delta_{in})^2 + (\text{3rd order terms}) \tag{3.13}$$

Hence again a nonlinear fit of this energy-phase transfer map can theoretically provide informations on the linear and nonlinear terms of the Taylor expansion in the TRANSPORT formalism.

3.4.3 Experimental Method

We have seen that knowing both compression efficiency and momentum compaction relies on the measurement of the time of arrival. Such measurement is performed by detecting the amplitude signal produced by the TM_{010} waves excited as the electron traverses a resonant stainless steel cavity [20, 21] The cavity has a resonant frequency of 1.497 GHz. The principle of the TOF measurement is to measure the phase of beam induced voltage since it is in phase with the bunch. The phase of the RF signal coming from the cavity ($V_{RF}\cos(\omega t + \phi_{RF})$) is mixed with the reference signal phase shifted by means of a programmable phase shifter ($V_0\cos(\omega t + \phi_0)$). The signal at the mixer output, after removal of high frequency component with a low pass filter, is:

$$V_{out} = \frac{V_{RF}V_0}{2}\sin\Delta\phi \tag{3.14}$$

where $\Delta\phi \stackrel{\text{def}}{=} \phi_{RF} - \phi_0$ is a measure of the relative time of flight.
The coefficient $(V_{RF}V_0)/2$ is initially determined during a calibration procedure that consists in varying the phase shifter to find the two zero-crossings of the pickup cavity, i.e. the phase for which the signal V_{out} is zero and measure the dependence of V_{out} for slight variations of$\Delta\phi$ (so that $\sin(\Delta\phi) \simeq \Delta\phi$)). Once the measurement is calibrated, the phase shifter phase ϕ_0 is set so that for the nominal conditions of the machine the cavity is operated at zero-crossing. Hence a change in the TOF induced by varying the phase of the photo-cathode drive laser (for phase-phase map measurement) or by an energy change (for energy-phase map measurement) gives a change of ϕ_{RF} which in turn induces a change of V_{out}. Practically only the change in V_{out} is directly measured but because one knows the coefficient $V_{RF}V_0$ one can infer ϕ_{RF} i.e. the relative TOF of the bunch.

[9] hence forth we refer this notation as TRANSPORT formalism

Experimentally the calibration coefficients are stored in software, the voltage V_{out} is digitized by an ADC card, and a data analysis program directly output the TOF in unit of RF-deg (1 RF-Deg is 556 μm at 1.497 GHz).
In the driver accelerator four cavities have been installed; their locations are shown in figure 3.12. In this section we will only consider measurement performed by the pickup cavities 2, 3, and 4, the measurement from the cavity #1 requiring some deeper analysis as we shall see in chapter 6. It is worth noting that contrary to what we have implicitly assumed in the previous discussion the measurement is not a single bunch measurement. Because of the needed signal to achieve good enough signal over noise in the time of flight measurement, the cavity signal corresponds to a macropulse that consists of 4675 electron bunches (the characteristics of the macropulse used for the measurement are: a width of 250 μsec, a micro-bunch frequency of 18.7 MHz and a macropulse frequency of 60 Hz).

To expedite the measurements, the quantity varied (i.e. laser phase for $\langle\phi_{in}|\phi_{out}\rangle$ transfer map

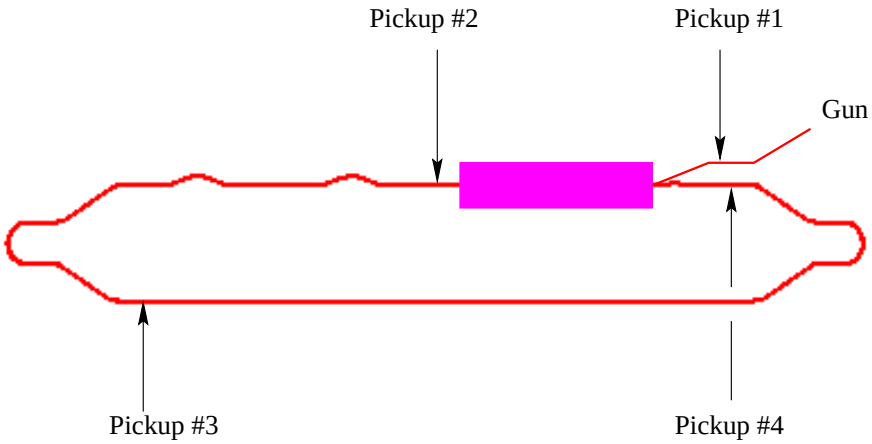

Figure 3.12: Location of the pickup cavities along the transport line in the FEL driver accelerator.

and cavity gradient for $\langle\delta_{in}|\phi_{out}\rangle$ transfer map), is indeed modulated with a frequency of 60 Hz (see again fig. 3.13). The modulation is performed with a triangular waveform generated by a function generator used to vary the proper quantity (phase of the photo-cathode drive laser or cavity gradient). The choice of a triangular modulation was done to uniformly populate the transfer map. Moreover sinusoidal modulation is also planned (but was not used during the work reported hereafter) in order to use the Tchebytchev-polynomial- based analysis that has been developed by G. Krafft for the CEBAF injector [22] at Jefferson Lab.

3.4.4 Simulation of $\langle\phi_{in}|\phi_{out}\rangle$ transfer map

As aforementioned the measurement of phase-phase transfer map provide important information on how the bunching process is performing and can give some insights on the bunch length. Because the map is measured between the photocathode and the pickup cavities (see fig. 3.12 for their locations), we cannot use standard single dynamics relativistic codes such as TLIE or DIMAD but need to use particle tracking code such as PARMELA which include nonrelativistic effects such as phase slippage effects in accelerating cavities. The technique we have used to compare measurement with numerical simulation is as follows.
We use the PARMELA code to generate uniform macroparticle distribution over a given extent in

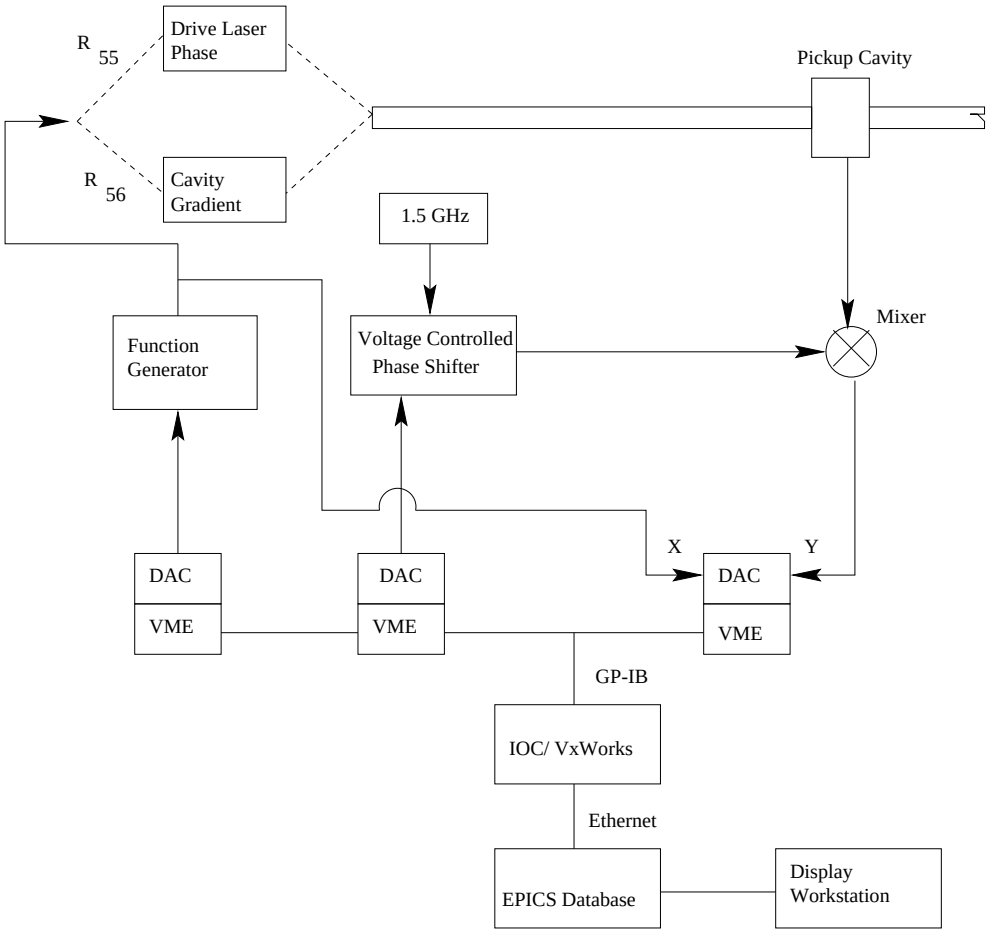

Figure 3.13: Block diagram of the compression efficiency R_{55} and momentum compaction R_{56} measurement.

phase at the photocathode surface. The corresponding phase of emission ϕ^i_{in} of the i-th macroparticle at the photocathode surface is recorded and the macroparticles populating this uniform distribution are "pushed" along the beamlines. During tracking the space charge subroutine in PARMELA is turned off, and each macroparticle is assimilated to a bunch centroid of bunches emitted at different drive-laser phase. We then record the phase of arrival ϕ^i_{out} at the desired pickup cavities in the simulation. The couple $\{\phi^i_{in}, \phi^i_{out}\}_{i=1,\ldots,N}$ gives the phase-phase transfer map and can readily be compared with the experimental data.

3.4.5 Measurement of $\langle \phi_{in} | \phi_{out} \rangle$ transfer map

Nominal Set-up Measurement

We will not treat measurement of phase-phase correlation function in the injector since they will be presented in Chapter 6. The figure 3.14 presents a measurement of phase-phase beam transfer function between the drive laser photocathode and the three different pickup cavities aforemen-

tioned. From the transfer function in Fig. 3.15 we can deduced by performing non-linear fit, an

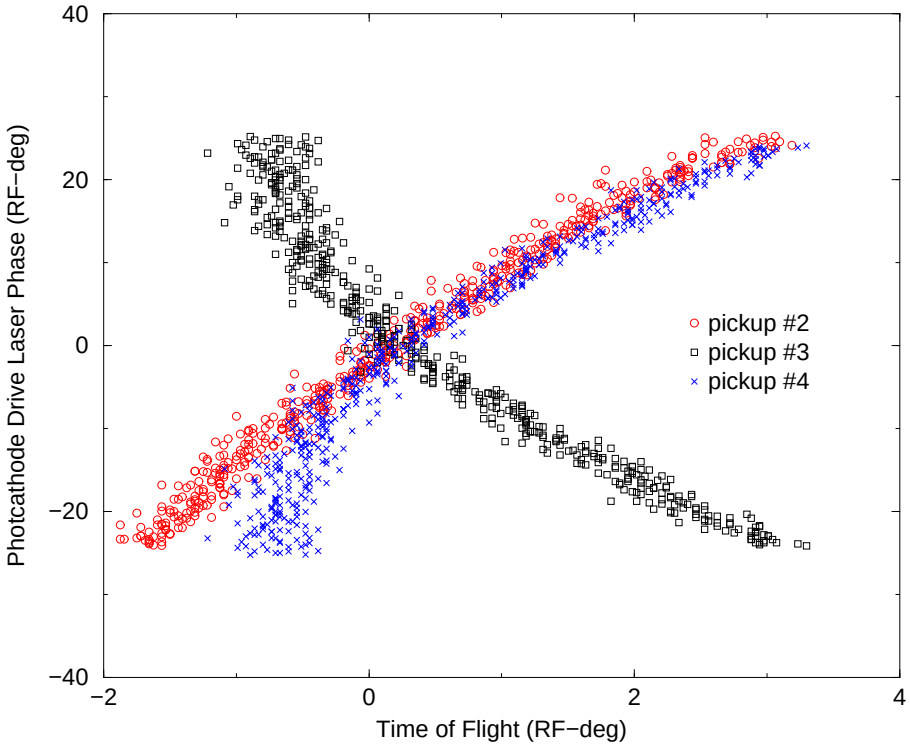

Figure 3.14: phase-phase beam transfer function between the photocathode surface and the three different pickup cavities: pickup #2, #3, and #4.

estimate of the transfer matrix element the results of the non-linear fit are gathered in Table 3.4.5. The measurement of the linear part are in very good agreement with the simulation except for the cavity #4, we believe the discrepancy comes from a bad centering of the electron beam on the magnetic axis of the trim quadrupoles and sextupoles in the arc 2.

Effects of the Quadrupoles

We have experimentally investigated the effects of the second family trim quadrupoles on the phase-phase transfer map. In figure 3.16 we present measurement of the phase-phase correlation for different cases. The study has only been carried out using the pickup cavity #3. For such measurement we have measured the beam phase-phase correlation with the trim quadrupoles set to their nominal values. Then we iterate the measurement for both the trim quadrupoles turned off and with their value opposite to nominal. The measurements are gathered 3.16(A). Since no time was spent to re-measure the transfer map along the linac and iterate the same procedure as before, i.e. set the model such that the same transfer map is achieved at the linac exit, and then use the model to predict the change at cavities #3 and #4, the disagreement is quite important. However, if we look at what is the relative change, i.e. by calculating the difference $\langle\phi_{out}|\phi_{in}\rangle^{\text{Quad Settings}} - \langle\phi_{out}|\phi_{in}\rangle^{\text{Nominal Settings}}$ for both the experiment (see fig. 3.16(C)) and the numerical model (see fig. 3.16(D)) the agreement is satisfactory. Though in the present case the method does not allow to extract quantitative number for R_{55} and T_{555}, it shows that this map does evolve the same way

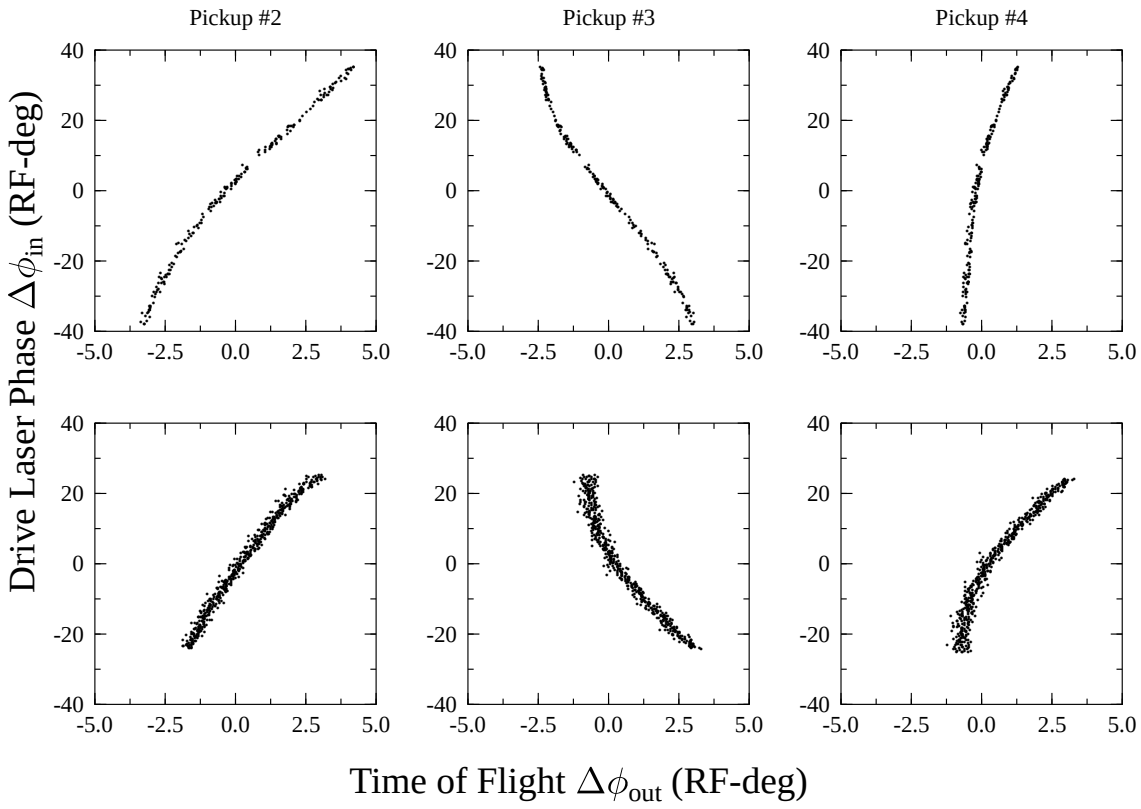

Figure 3.15: Comparison of the phase-phase beam transfer function between the photocathode surface and the three different pickup cavities (pickup #2, #3, and #4) **(bottom row)** with the one simulated using PARMELA **(top row)**.

both experimentally and in the model when we try to perform a perturbation-type measurement. This also suggest that the same "difference orbit" technique we use for the transverse plane could be performed in the present case, if the motivation was not to extract matrix elements.

Effects of the FEL on the Phase-Phase map

Assessing the effect of the FEL on the beam has been studied only experimentally. We will attempt to provide a qualitative explanation. In this experiment we have set the laser phase modulation amplitude to 40 deg, since it corresponds the full bunch length at the cathode surface. Firstly we prevented the laser to run by detuning the optical cavity and recorded the phase-phase transfer function. Then we tuned the optical cavity, i.e. adjust the length to match the time of flight of electron bunches inside the cavity, and recorded the phase-phase transfer map. The other

Pickup	Linear Coefficient	Quadratic Coefficient
Experiment		
# 2	0.1172	0.0008
# 3	-0.0801	0.0016
# 4	0.0911	0.0006
Simulation		
# 2	0.1070	0.0007
# 3	-0.0834	0.0003
# 4	0.0256	0.0004

Table 3.2: Comparison of coefficients obtained from the non-linear fit of the measured and PARMELA-simulated phase-phase transfer map.

measurements were performed at various stages of the detuning curve of the optical cavity. The obtained transfer maps are gathered in figure 3.17. For the case where the laser is turned off (see fig. 3.17 (A)), the transfer map looks as usual, mainly linear with a small parabolic behavior due to T_{555} contribution. However when the laser is turned on (see fig.3.17 (B)), and optimized to extract a maximum output power, the fold-over is substantial, bunches emitted with phase close to the "nominal phase" have a larger time of flight because now they are contributing to the laser process and therefore are less energetic. At various stage of detuning curves the phase-phase map fold-over due to the non-linear effect introduced by the laser interaction is less important. We have succeeded in operating the laser at the limit of its turn-off point by properly adjusting the cavity, in this region, (see fig.3.17 (E)) we can notice that the phase-phase transfer map has two contributions: for bunch centered around the zero-crossing phase (i.e. $-10 < \phi_{in} < +10$ deg), the transfer map has the same fold-over as when the laser is optimized for maximum output power (see fig.3.17 (B)), however for bunches emitted with phases $|\phi_{in}| > 10$ deg, the transfer map has the same behavior has the transfer map measured when the laser interaction is turned off, indicating that in this region, the bunches are no more taking part to the laser interaction. This observation remains to be studied with numerical simulations.

3.4.6 Simulation of $\langle \delta_{in} | \phi_{out} \rangle$ transfer map

Since the $\langle \delta_{in} | \phi_{out} \rangle$ transfer map measurement is only performed in the 48 MeV energy region, we can use relativistic single dynamics code. We computed first and second order transfer matrix elements (R_{56} and T_{556}) using the DIMAD code. In order to generate energy-phase transfer map we have used the arbitrary high order code TLIE [23] code[10]. The energy offsets experimentally achieved when modulating the gradient of the last cavity encountered by the beam during its acceleration is used as input in the TLIE code from which we can generated by using the tracking option the phase of arrival at the desired pickup cavity. The couple $(\{\delta^i_{in}, \phi^i_{out}\}_{i=1,...,N})$ will give the energy-phase correlation and again can be readily compared with the experimentally generated transfer map.

[10]This code is based on Lie differential algebra technique to compute transfer map in an accelerator lattice

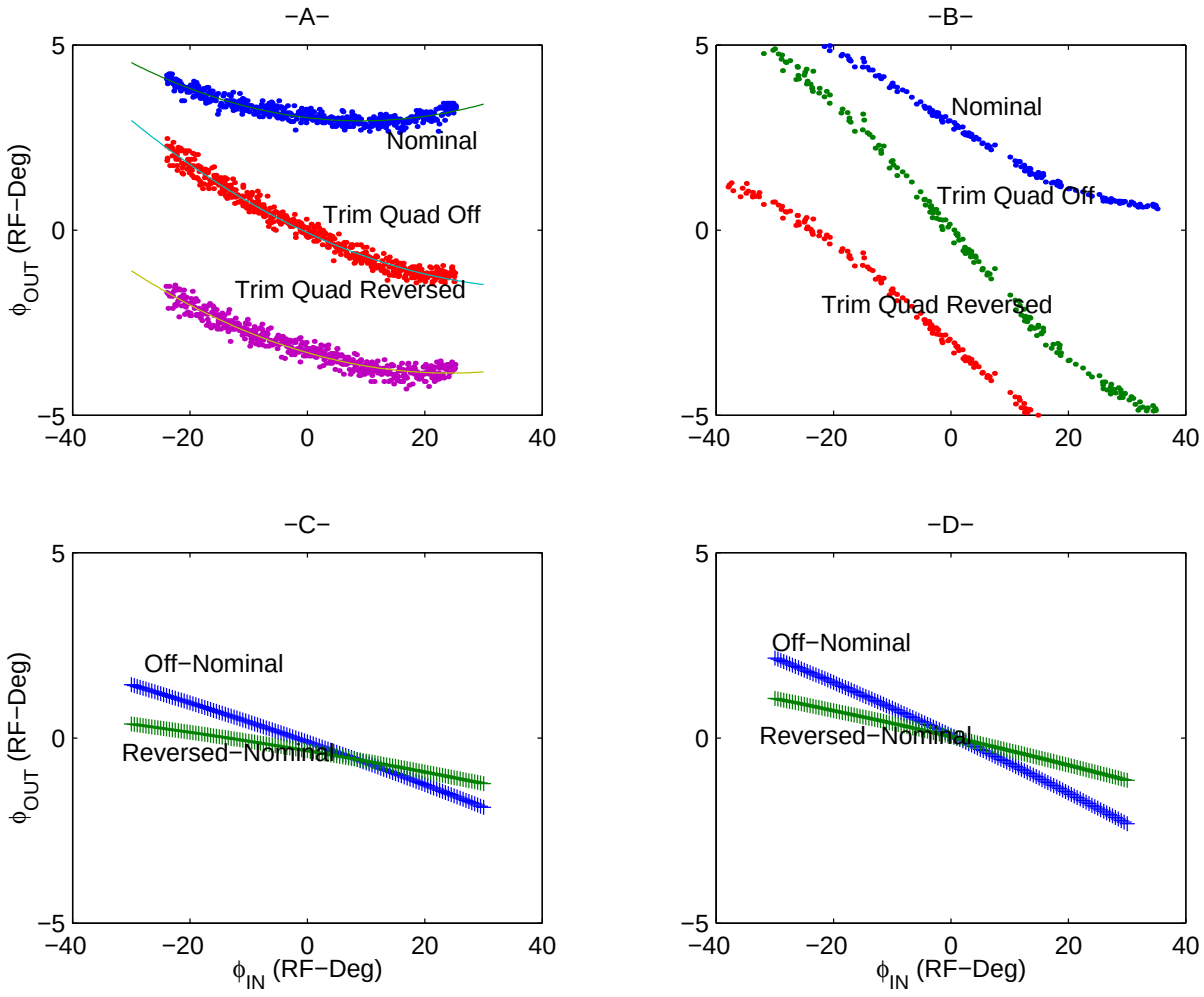

Figure 3.16: Demonstration of longitudinal difference-orbit: phase-phase transfer map measured (**A**) and simulated (**B**) for three different settings of the trim quadrupole. Plot (**C**) and (**D**) correspond to difference of the measured map presented in the top raw for respectively the experiment and the simulation.

3.4.7 Measurement of $\langle \delta_{in} | \phi_{out} \rangle$ transfer map

Effects of the Trim Quadrupoles

The trim quadrupole family has two effects on the energy-phase correlation. Firstly it modifies the momentum compaction, R_{56}. Since the quadrupole introduce a path length variation linearly dependent on the energy offset. Also via its second order coefficient, the trim quadrupoles also introduced a quadratically energy offset dependent path length variation which results in a modification of the nonlinear momentum compaction $T_{566} = \langle \phi_{out} | \phi_0^2 \rangle$.
We have measured, using the nominal optical lattice setup the energy-phase transfer map at both pickup cavities located downstream arc 1 and 2 (pickup cavity #3 and #4) on the figure 3.12. The results are presented in figure 3.18: a linear fit of the measured transfer map has been per-

formed and is compared in this figure with the expected momentum compaction computed using the magnetic optic code DIMAD. We have performed the measurement at both location with the trim quadrupole in arc 1 both powered and turned off. It is seen the level of agreement is excellent. Typical R_{56} measured and expected for the whole recirculation, i.e. from the cryomodule exit up to its entrance is approximately -20 cm for the nominal setup used at that time (February 1999). From these both measurement it is possible to deduce the R_{56} of the by-pass chicanes: Using the nominal settings measurement we find: $R_{56}^{\text{chic}} \simeq -29.60\,\text{cm}$ and $R_{56}^{\text{arc}} \simeq 23.51\,\text{cm}$, again we can note the very good agreement, with 2 cm between the measured R_{56} for the chicanes and its design values of $-28\,\text{cm}$. We have attempted to quantify the R_{56} dependence on the trim quadrupoles excitation by systematically varying the quadrupoles strength and each time measuring the momentum compaction from the linac exit up to the pickup cavity #3. The results are presented in figure 3.19 where we compared the measurement with numerical simulation using the DIMAD code; the code seems to be a very good tool to predict the R_{56} evolution around the recirculation.

Effects of the Sextupoles

We have carried a qualitative study of the sextupole effect on the energy-phase transfer function. The experiment consisted of measuring the $\langle \delta_{in} | \phi_{out} \rangle$ transfer function using the pickup cavity number 3. During the measurement the trim quad are un-powered. In figure 3.20, we present the measured transfer functions. Quantitatively there is some disagreement between the simulated and measured data. However it is seen that the sextupole have the same effect: when turn on they tend to introduced a positive non-linear (quadratic) curvature. Again one can use the same scheme as we used before and compare not the absolute transfer map, but relative transfer map i.e. compare the algebraic difference $\langle \delta_{in} | \phi_{out} \rangle^{on} - \langle \delta_{in} | \phi_{out} \rangle^{off}$ for the simulated and measured set.

3.4.8 Concluding Remarks on the Longitudinal Response Measurement

In this section we have showed that:

1. phase-phase first order map and nonlinearities measured can be rather well reproduced with the PARMELA code. Also it can be used to deduce both the compression rate between the point of measurement (pickup cavity locations) and the photo-cathode surface; of course this is a lattice compression rate, practically, and especially in the low energy region, where the beam is in a space-charge-dominated regime, the compression is strongly influenced by collective space charge force.

2. phase-phase map can be used to set the lattice i.e. to operate in isochronous mode, e.g. by making sure the map before and after a section is approximately the same

3. energy-phase transfer map, can give with fairly good accuracy the momentum compaction of a section. We have measured the momentum compaction of the recirculation to approximately $R_{56} \simeq -12$ cm from the cryomodule exit to the arc 3F. Which give the for the section wiggler to linac entrance $R_{56} \simeq +16$ cm very close to the desired value of 20 cm.

4. energy-phase transfer map can also be used to characterize, with high accuracy the effect of the sextupole on the longitudinal dynamics, also in the present work we were not able

to precisely extract the T_{566} term probably because of mis-centering in the arcs transport, it could be use for such purpose to ease the path length correction required by introducing linear and high order energy chirp.

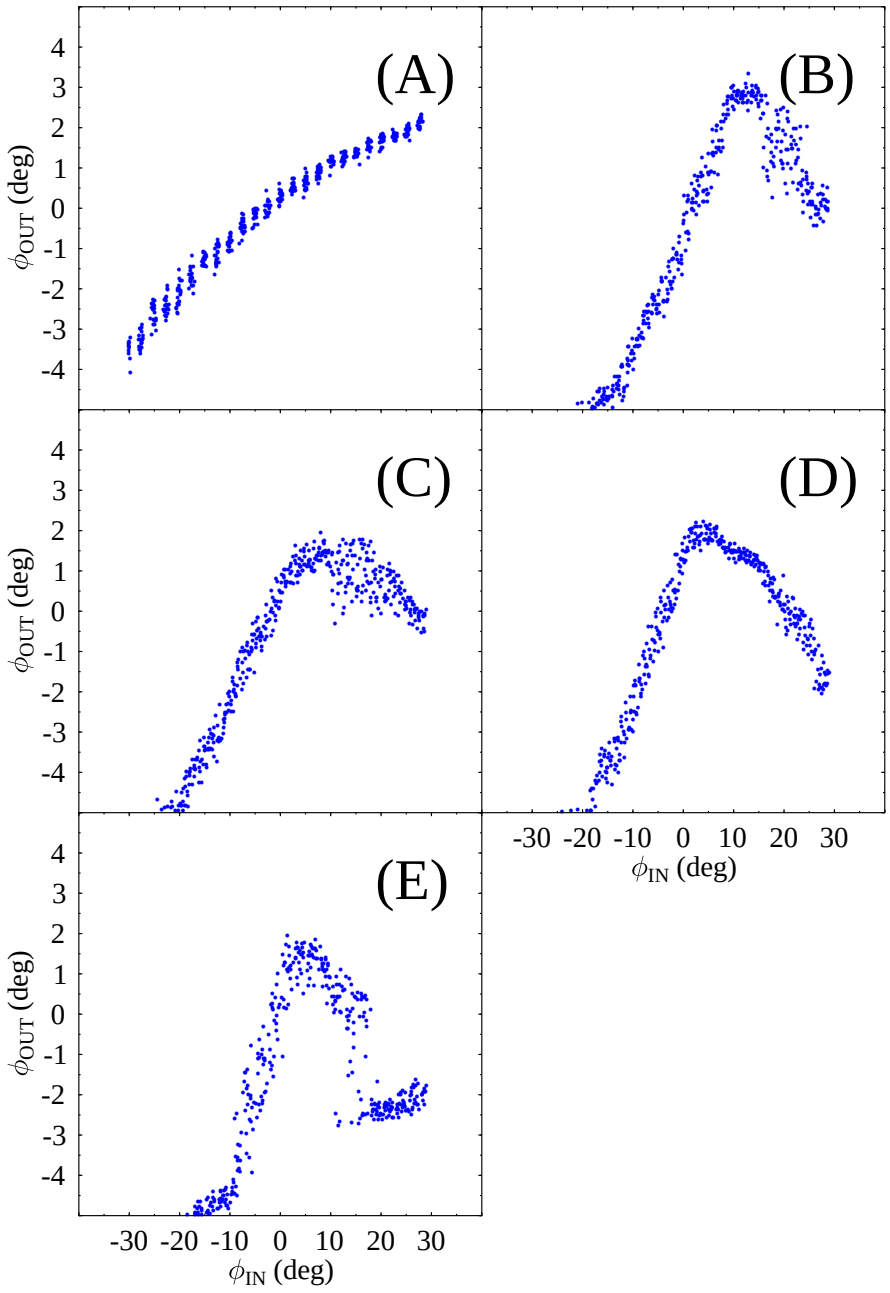

Figure 3.17: Phase-phase transfer functions for different settings of the optical cavity length. In **(A)** the optical cavity is completely detuned so that the laser does not operate. In **(B)** the cavity is precisely tuned to maximize the FEL output power. In **(E)** the cavity is tuned so that the laser operate at the limit of its turn off. In **(C)** and **(D)**, the phase-phase transfer map is measured for different detuning of the optical cavity case **(B)** and **(E)**.

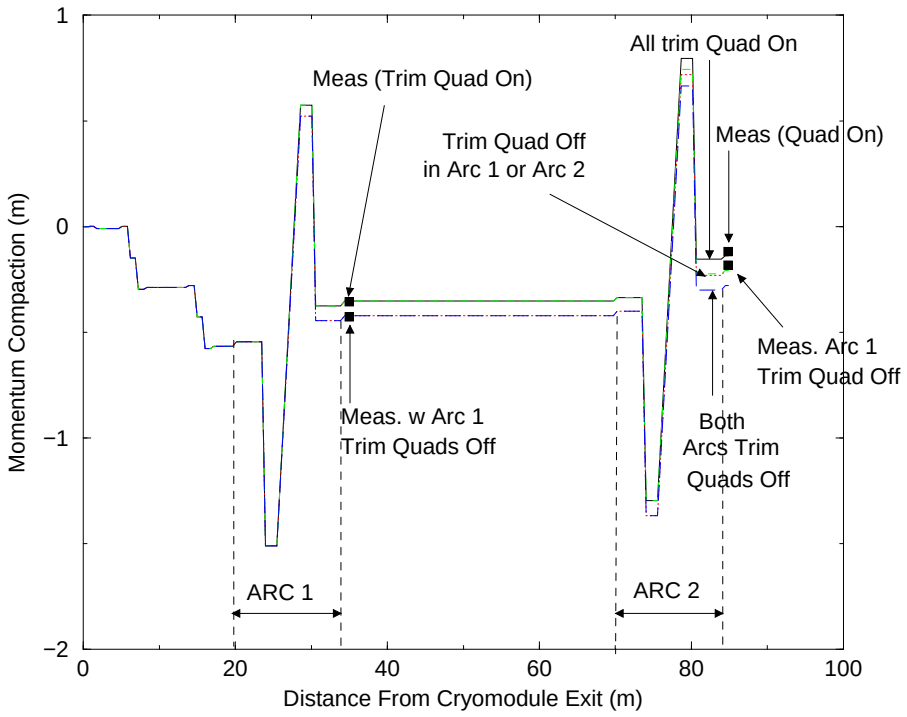

Figure 3.18: Evolution of the R_{56} along the beam transport in the recirculation transport, from the linac exit to arc 3F exit. Measured R_{56} are also presented as filled squares.

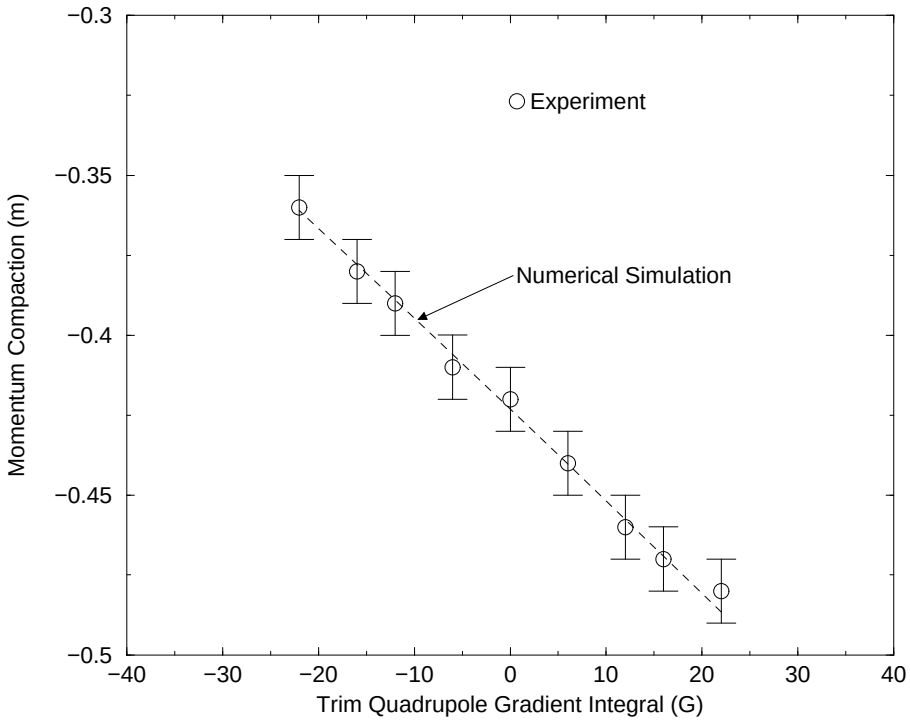

Figure 3.19: Comparison of the linear term extracted by fitting the measured energy-phase transfer map with the expected momentum compaction R_{56} from the DIMAD code, for different trim quadrupoles settings.

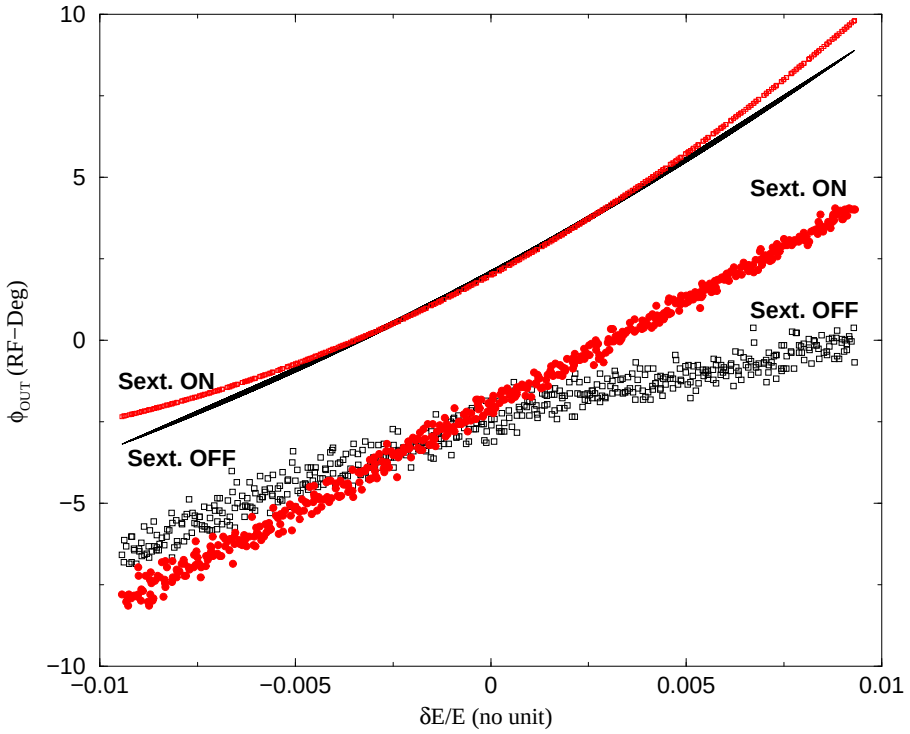

Figure 3.20: Effect of the sextupoles in the Arc 3F on the energy-phase correlation. (Simulations and experimental data are offset for clarity).

Chapter 4

Transverse Phase Space Characterization

4.1 Introduction

The present Chapter is intended to discuss the emittance measurement that we have developed in the IRFEL. Techniques to measure both emittance-dominated[1] and space-charge-dominated [2] beam are described. Because beam profile measurement is an integral part of an emittance measurement we describe the OTR-based beam density monitor that have been installed in the IRFEL. Before discussing in great detail the techniques we use to measure the transverse emittance and phase space parameters, and because of the different definitions that vary from source to source in the contemporary beam dynamics literature, we find it imperative to settle the definition of beam emittance that we will use throughout this dissertation.

4.1.1 Beam, Hamiltonian Dynamics and Liouville's Theorem

By definition, a beam is a collection of particles that are contained within a finite region of the phase space. In the most general case, the phase space is a 6-dimensional space [26] and the particles (assumed to be point-like) are represented by their position vector (x, y, z) and kinetic momentum vector (p_x, p_y, p_z), and occupies a six-dimensional hyper-volume generally referred as Γ_6. This representation concerns the simplest case: in other cases, additional coordinate such as spin, for polarized beams, or charge and mass, for multiple-species beams, might be required. The notion of a beam also entails the existence of a privileged direction, the direction of propagation, along which the kinetic momentum is much greater than the momentum in the two other directions. The choice of (x, y, z) and (p_x, p_y, p_z) as coordinate is simply coming from the Hamiltonian description of the particle system which requires canonically conjugate variables. In the six-dimensional phase

[1] emittance dominated beam means that the beam evolution is driven by external forces (e.g. external focussing)

[2] emittance dominated beam means that space-charge forces dominates the beam evolution (i.e. Coulombian repulsion)

space a beam that consists of N particles, is best described, at a given instant, in terms of a density function $n_6(x, y, z; p_x, p_y, p_z)$. The number of particles in an element of phase space volume $d\tau_6 = dx dp_x dy dp_y dz dp_z$ in the vicinity of the point $(x, y, z; p_x, p_y, p_z)$ is:

$$d^6N = n_6(x, y, z; p_x, p_y, p_z) d\tau_6 \tag{4.1}$$

The total volume in Γ_6 occupied by the beam, at a given instant is:

$$\mathcal{V}_6 = \int\int\int\int\int\int d\tau_6 \tag{4.2}$$

This quantity, generally referred as 6D-hyper-emittance, is well defined provided the density function n_6 is a compact function.

A useful simplification, when describing a beam, occurs when each degree of freedom is independent of the two other degrees of freedom. Then the since Hamiltonian write as the sum of uncoupled sub-hamiltonian corresponding for each of the three degree of freedom, the density distribution factorizes as:

$$n_6(x, y, z; p_x, p_y, p_z) = n_{2,x}(x, p_x) n_{2,y}(y, p_y) n_{2,z}(z, p_z) \tag{4.3}$$

In such case, the beam dynamics can be studied separately in each of the three two-dimension projected phase space. The main properties of the particle trajectories in these planes can be summarized as follow:

- The trajectories depend on the initial values of the coordinate and the time. An important consequence is that two trajectories with different initial condition cannot intersect. Also note that a trajectory at a given time can have several value thereby yielding phase-space bifurcation.
- A boundary in the phase space that enclose a given number of particle at a given time t will map into a boundary at a time t' which enclose the same group of particles.
- In linear phase space transformations, ellipses map to ellipses, straight lines to straight lines. Such geometry might be appropriate to limit phase space density.

Generally the phase space density function, $n_6(x, y, z; p_x, p_y, p_z)$ is Liouvillian i.e. it satisfies Liouville's theorem which states that the density of particle in the appropriate phase space is invariant along the trajectory of any given point. This theorem can also be expressed in terms of the invariance of the phase space hyper-volume enclosing a chosen group of points as they move in the phase space. The ensemble of particle behaves as an incompressible fluid:

$$\frac{d\mathcal{V}}{dt} = 0 \tag{4.4}$$

We should insist that Liouville's theorem applies to conservative Hamiltonian systems i.e. systems in which the forces can be derived from a potential. In the case of charged particle beam, Liouville theorem cannot be applied when:

- Emission of electromagnetic radiation (e.g. synchrotron)
- Non negligible self interaction (e.g. space charge force, coherent synchrotron radiation,...)
- Quantum excitation effect are non negligible

4.1.2 Phase Space and Emittance

Henceforth, we will only concentrate on the transverse phase-space, $x - p_x$ and $y - p_y$ and assume there is no coupling between these two sub phase-spaces. Therefore we will consider the horizontal phase space $x - p_x$, similar discussion is valid for the vertical phase space $y - p_y$.
Firstly it is always preferable to work in the trace space which is the plane $x - x'$ where $x' = p_x/p_z$ is the renormalized horizontal momentum or the particle divergence. The variables x and x' are no more canonically conjugate but the phase space properties exposed previously are still applicable in the trace space. For sake of simplicity, the phase space distribution is generally arbitrarily bounded by ellipses since they have the good properties to map into ellipses under canonical transformation. Such ellipse is generally referred as the phase space ellipse. It can be fully specified with three parameters, the emittance ε, the betatron function β_T and the α_T function; its equation is given by[3]:

$$\gamma_T x^2 + 2\alpha_T x x' + \beta_T x'^2 = \varepsilon \tag{4.5}$$

where γ_T is defined as $\gamma_T = \frac{1+\alpha_T^2}{\beta_T}$. In this previous equation, the emittance is generally named geometric emittance and corresponds to the area of the ellipse:

$$\int_{\text{ellipse}} dx dx' \stackrel{\text{def}}{=} \pi\varepsilon \tag{4.6}$$

The bilinear form expressed in Eqn.(4.5), can be rewritten in a matrix form $\vec{x}\Sigma\vec{x}^T$ with $\vec{x} = (x, x')$ and Σ being the beam matrix:

$$\Sigma \stackrel{\text{def}}{=} \begin{pmatrix} \beta_T\epsilon & -\alpha_T\epsilon \\ -\alpha_T\epsilon & \gamma_T\epsilon \end{pmatrix} \stackrel{\text{def}}{=} \begin{pmatrix} \sigma_{11} & \sigma_{12} \\ \sigma_{12} & \sigma_{22} \end{pmatrix} \tag{4.7}$$

Despite this definition of emittance is the one generally used by experimentalist, it suffers from many problem especially in presence of non-gaussian phase space distribution or when nonlinear effects are present in the transport channel (chromatic aberration, wakefield, space charge,...). These nonlinear processes generally yield non linear distortions of phase space which render the geometric emittance concept difficult to quantify a phase space which shows a great deal of structure (e.g. filamentation).
A convenient way is to statistically characterize the phase space using the first, $\langle x\rangle$, $\langle x'\rangle$ and second order, $\langle x^2\rangle$, $\langle x'^2\rangle$, $\langle xx'\rangle$, moments of the phase space distribution. Then we can define a root mean square emittance [27] as:

$$\tilde{\varepsilon}_x = \left[\langle (x - \langle x\rangle)^2\rangle\langle (x' - \langle x'\rangle)^2\rangle - \langle (x - \langle x\rangle)(x' - \langle x'\rangle)\rangle^2\right]^{1/2} \tag{4.8}$$

It is also common to find in the literature the effective emittance which is the defined as 4 times the rms emittance. Also, most of the time one rather normalized the emittance with respect to the momentum and define the normalized rms emittance as:

$$\tilde{\varepsilon}_x^n = \beta\gamma\tilde{\varepsilon}_x \tag{4.9}$$

[3] In this Section the Twiss parameters are indexed with the subscript $_T$ to avoid confusion with other variables. Later, where confusion cannot occur, we will omit this subscript.

This definition of emittance is practical since it does not vary if the forces are linear.
As for the geometric emittance one can define Twiss parameters from the first and second order moments:

$$\begin{cases} \beta_T = \frac{\langle (x - \langle x \rangle)^2 \rangle}{\tilde{\varepsilon}_x} \\ \alpha_T = -\frac{\langle x x' \rangle - \langle x \rangle \langle x' \rangle}{\tilde{\varepsilon}_x} \\ \gamma_T = \frac{1+\alpha_T^2}{\beta_T^2} \end{cases} \tag{4.10}$$

Introducing the rms beam size, σ_x, and divergence, σ'_x, it is possible to have a simple expression for the rms emittance:

$$\tilde{\varepsilon}_x = \sigma_x \sigma'_x \sqrt{1 - r_{12}^2} = \frac{\sigma_x \sigma'_x}{1 + \alpha^2} \tag{4.11}$$

Where r_{12} is a correlation coefficient defined as $r_{12} = \frac{\langle x x' \rangle}{\sigma_x \sigma'_x}$; it is a measure of the trace space slope.

Therefore, measuring a transverse emittance $\tilde{\varepsilon}_x$ always reduces to the measurement of beam density along x-axis (i.e. beam size measurement) and along x'-axis (i.e. beam divergence measurement). As we will see, both of these measurements indeed reduce to the measurement of a beam transverse density profile. Therefore we shall first concentrate our discussion on this latter type of measurement. We will then discuss the emittance computation.

4.2 Measurement of Beam Profile Using Transition Radiation

As we have seen in the previous section, measurement of transverse trace space generally requires measuring the beam profiles i.e. the transverse particle density along the horizontal or vertical axis. Several techniques are commonly used for such a purpose depending on the beam. For instance in the IRFEL driver-accelerator, the transverse beam distribution are measured by:

- a fluorescent screen: a ceramic plate is inserted in the beam path, and the light emitted via the fluorescence effect is observed with a camera since the fluorescence occurs in the optical region of the spectrum (see fig. 4.1 b). These types of beam profile monitor are usable for quantitative measurement only for extremely low average beam current of typically 10 nA. It is only used as a qualitative beam transverse section measurement in the low energy (350 keV) region of the injector to observe low current beam. The use of these type screens for quantitative measurement of higher average beam current is not possible: the ceramic does not have a linear response and can saturate resulting in erroneous beam density measurements.
- a wire scanner: the beam is intercepted by a thin (20 μm) moving tungsten wire. As the wire scan the beam in the transverse plane, the potential across its ends is proportional to the beam current intercepted. Therefore the measurement of this electric potential versus the position of the wire gives the transverse beam density along the direction perpendicular to the wire (see fig. 4.1 b). Despite this type of technique can achieved very high resolution, depending on the diameter of the wire and the steps of the scan, it as few inconvenient: it is a very slow measurement, because of its generally large diameter (more than 20 μm), the

wire can yields a large loss of particle that can hit the vacuum chamber or other beamline components and potentially damages electronics system.

- several synchrotron radiation monitors: as the beam is bent in dipole magnets, it emits synchrotron radiation. In the IRFEL this radiation is emitted in the infra-red region of the electromagnetic spectrum and is imaged on a very sensitive CCD detector (see fig. 4.1 c). This profile monitor has the advantage of being non-invasive (it does not yield beam degradation) and it can be used to measure beam distribution at very high current. However it is not well suited for emittance measurement: the beam profile is measured in a bend i.e. at a dispersive location and therefore the emittance computation, requires a somewhat tedious analysis since we need to deconvolved the dispersion contribution to the beam profile.

- many transition radiation monitors: thin aluminum foil are inserted into the beam path and transition radiation (see the Introduction chapter) is detected with a CCD detector. Generally the foil makes a 45 deg angle with the beam direction and backward transition radiation is detected (see figure 4.1 d). This configuration requires the foil material to have a good reflection coefficient. Since very thin foil are available, this type of devices can stand high current beam without yielding significant beam degradation.

Among the techniques listed above, transition radiation was chosen to provide the quantitative measurement of transverse distribution required for measuring the emittance in the IRFEL. This choice was principally driven by the reliability, the speed and the low cost of this type of instrument. Before the IRFEL was built we study many aspect of this type of apparatus: what are the average beam current limit, what are the beam transverse phase space degradation after an OTR screen. Such studies, experimentally carried in the CEBAF machine at Jefferson Lab, helped with the choice of the type of screen (aluminum). During these studies we also developed a quasi non-interceptive screen that was used to measure the beam profile of the high power beam of the CEBAF accelerator; also we did not implement this type of monitor in the IRFEL short term plan, it might be sometime implemented to continuously monitor the electron beam quality without significant impact on the beam itself. In the following sections we discuss the limitations of transition radiation-based diagnostics and the development of the non interceptive profile monitor.

4.2.1 The limitation of Transition Radiation Monitor

As we have mentioned in Chapter 2, when we discussed electromagnetic radiation emitted by moving charged particles, that transition radiation can be observed whenever a charged particle experience a discontinuity in the electric properties of its environment. A common way of observing transition radiation is to intercept the beam trajectory with a thin metallic foil (or TR radiator). Such method allows the observation of the TR produced as the beam crosses the boundary vacuum/foil (backward TR) or foil/vacuum (forward TR). As the beam is intercepted by the foil some concerns might arise:
Firstly because of the dE/dx of the material the beam deposits some energy in the TR radiator thereby increasing its temperature. Therefore we must study the thermal effect of the beam on the TR radiator.
Secondly when the electrons that constitute the beam pass through the foil material, they undergo scattering on the nuclei that can potentially degrades the beam emittance and therefore will not result in a non-interceptive diagnostics. On the other hand, the divergence induced via scattering

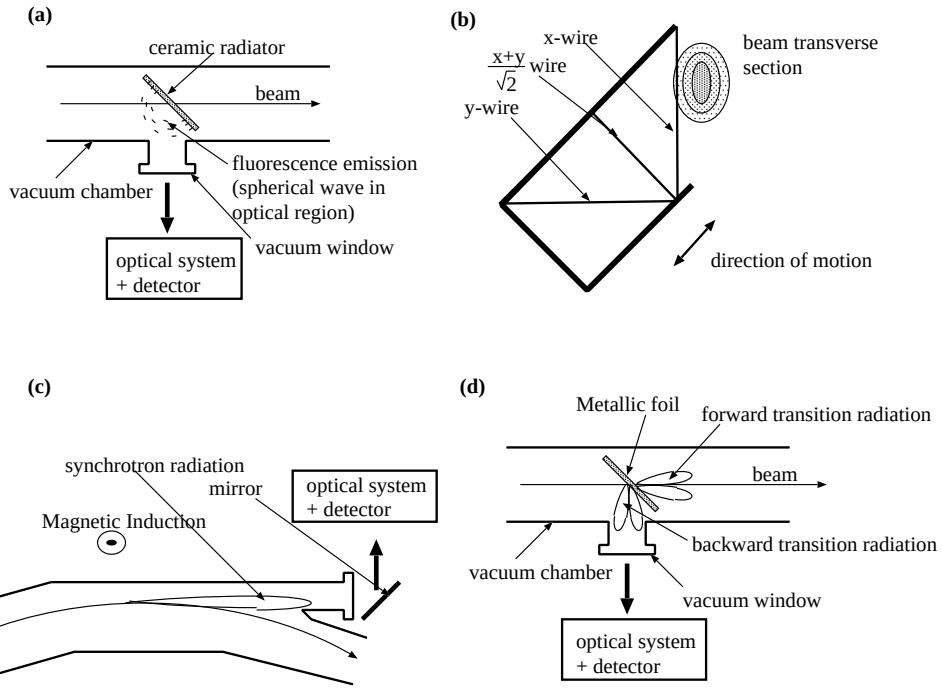

Figure 4.1: Schematics of principle for the different type of beam profile density measurement devices.

can be so large that some of the electron can be lost. If the percentage of lost particles exceeds a certain threshold it can trigger the Machine Protection System (MPS) which will turn off the machine, also even if the MPS is not armed, losing a large fraction of the beam is always a concern. The protection system threshold depends on the machine, and insures that one cannot damage any piece of hardware (vacuum pipe, electronics,...) that is located in the tunnel enclosure. In the following we consider the behavior of three kinds of TR radiator: aluminum, gold and carbon foil.

4.2.2 Thermal Studies

The primary concern, as we previously emphasized, is due to the energy the beam deposits in the foil. The energy deposition is mainly due to ionization losses of the relativistic electrons minus the energy carried on by secondary electrons; it was computed using the EGS4 (Electron and Gamma Shower 4) code[4] distributed by Stanford Linear Accelerator Center. If the only mechanism of heat transfer is conduction, the temperature of a body in which power is deposited is described by the heat transfer equation:

$$\rho c_p \frac{\partial T}{\partial t} - kappa \bigtriangledown^2 T = \frac{\partial P}{\partial V} \tag{4.12}$$

where T is the temperature, ρ the density, c_p, the specific heat, κ the thermal conductivity, V the volume of the body, and the deposited power.
This equation can be numerically integrated by several finite-element program. In the case of body with high emissivity, heat evacuation via radiation is an important mechanism that should be

[4]Private Communication from P. K. Kloeppel, November 1995

incorporated in the computations. Typically for a given deposited power, a temperature gradient will result. A given surface of the body dS whose local temperature is T_s will radiate and lose power at a rate proportional to $T^4 dS$. More precisely, the power radiated is given by Stefan-Bolztman relation:

$$dP_S = 2\sigma\epsilon dS(T_S^4 - T_0^4) \tag{4.13}$$

where σ is the Stefan constant ($\sigma = 5.670 \times 10^{-8}\,\mathrm{Wm^{-2}K^{-4}}$), ϵ is the emissivity of the body, and T_0 is the ambient temperature of the canonical system the body is located in (in our case vacuum at a temperature assumed to be 300 K henceforth).
To compute the temperature rise due to power deposition in the steady state case, we use the following numerical iterative method. Firstly, let's assume (and this is indeed the case) that the TR radiator consists in a circular foil of radius r and thickness t whose normal makes an angle θ with the beam axis. In a such case, the power is evacuated radially via the conduction mechanism. We can divide the foil by a series of annuli of outer and inner radii r_i and r_{i+1} (see fig. 4.2). Therefore the temperature of the ith annulus is related to the temperature of the i-1 th crown by:

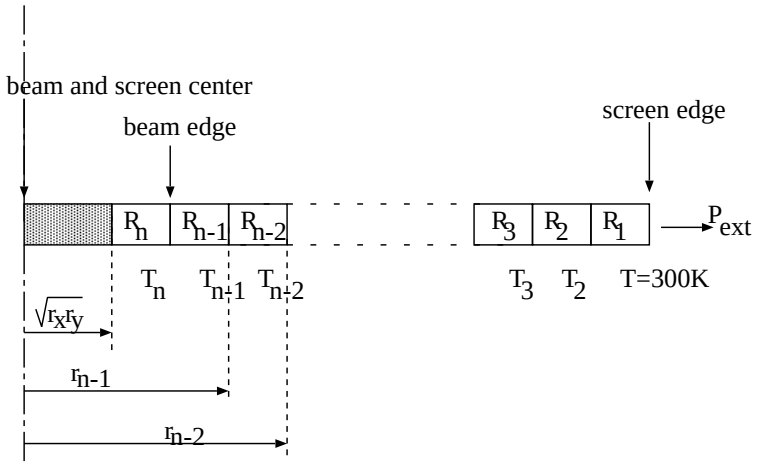

Figure 4.2: Methodology to compute temperature rise in a cylindrically symmetric TR radiator.

$$T_i = T_{i-1} + R_i P_i \tag{4.14}$$

where $R_i = \frac{1}{2\pi\kappa t} \ln\left(\frac{r_{i+1}}{r_i}\right)$ is the thermal resistance (κ is the thermal conductivity of the foil material and t its thickness, and P_i is the total power coming from the i th crown. Part of the power is heat radiated and the remaining is transmitted via conduction to the next element. The radiated power is:

$$P_i = P_{i-1} + 2\pi\sigma(T^4 - 300^4)(r_i^2 - r_{i-1}^2) \tag{4.15}$$

To compute the temperature rise at the beam edge crown, we introduced the parameter P_{ext} that represent the evacuated power. Hence varying the value of this parameter and iterating the Eqns. (4.14) and (4.15) from the edge of the foil up to the edge of the beam allows to determine the temperature at the beam center and the deposited power (from which we can get the beam current) using the equations [29]:

$$T_{center} = T_n + \frac{1}{4\pi\kappa t} P_n \tag{4.16}$$

and

$$I = \frac{P_n}{\Delta E t} \cos\theta \tag{4.17}$$

Eqn. 4.16 relates the temperature at the beam center and the temperature at the beam edge. It is valid under the assumption of a uniformly populated beam. Using this method we have computed

Material	Melting Point (K)	Thermal Conductivity W/m.K	dE/dx eV/μm
Aluminum	933	237	410
Gold	1337	317	6380
Carbon	3700	333	130

Table 4.1: Physical properties of the considered material for OTR screens.

the maximum beam current different foils can stand versus the equivalent beam size defined as $\sqrt{r_x r_y}$ where r_x and r_y are the full beam size respectively in the horizontal and vertical direction. The considered material with their properties are gathered in Table 4.1. The results are presented in the fig. 4.3 which depicts the maximum average current that can be reached for a given beam radius assuming the TR-radiator has a 0.8 μm thickness[5]. For instance, we can see that with the typical beam size expected in the free-electron laser, aluminum foil can easily withstand average current up to 500 μA even with a beam of 300 μm radius. Even in the low-emittance CEBAF accelerator the maximum design of 200 μA can be reached without melting the foil for typical envelope of 200 μm.

Obviously, we can notice in figure 4.3 that carbon is the best choice as far as thermal aspects only are considered. Unfortunately the main drawback of carbon, as we will see later, is its low coefficient of reflection in comparison to aluminum or gold which does not facilitate its use to observe backward TR.

Finally we note that despite its higher thermal melting point compared to aluminum, gold does not stand higher beam average current due to its higher dE/dx coefficient. In figure 4.4 we present the steady state temperature versus the incoming beam average current for different aluminum foil thickness and a beam of 2 mm.

4.2.3 Study of Multiple Scattering in Aluminum foil

We now turn to the study of beam degradation due to scattering in the TR radiator. In this section, we present an experiment devoted to study scattering of a 45 MeV electron beam on very thin aluminum foils. The experiment was performed in the CEBAF injector region (for a description of the injector see Reference [28]). We compared the data with a semi-empirical model and numerical simulations.

[5] this thickness is an optimum value: it corresponds to the thinnest foil we can have (in order to minimize beam degradation) still having a good surface reflection coefficient. Also thickness is limited by the frame on which the foil is mounted: too thin foil could not be mounted on our holding support because they would anymore self-support.

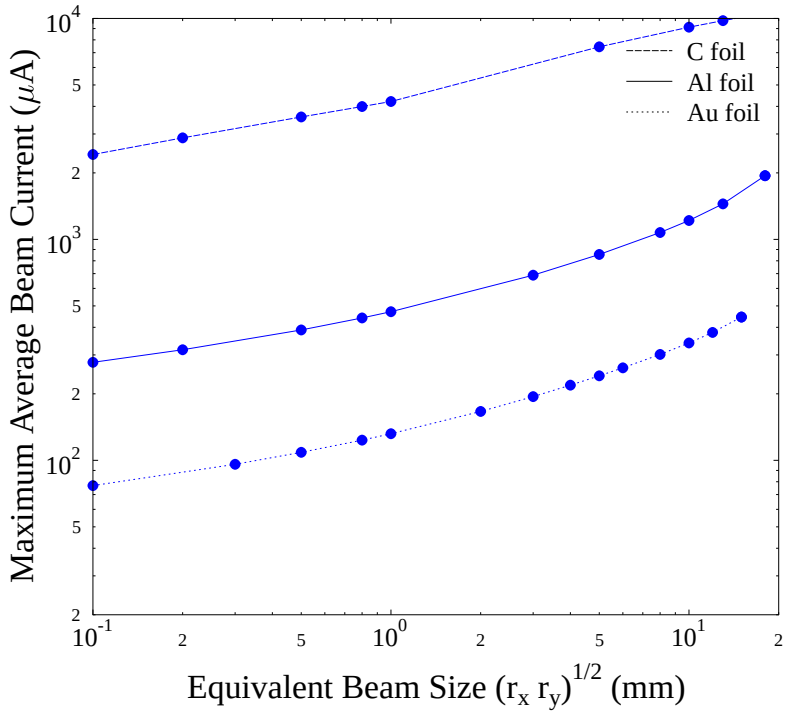

Figure 4.3: Maximum average current that can withstand a TR radiator as a function of the equivalent beam radius. Three types of TR radiator have been considered: Aluminum, Gold and Carbon. The three radiator are 0.8 μm thick.

Experiment

We have performed an experiment in the CEBAF injector at 45 MeV to study scattering effect as the beam pass through aluminum foil of different thickness. The experimental setup is as follow: different aluminum foil are mounted on a support, and can be inserted into the beam path remotely. The scattered beam then drifts through a length of 7.43 m up to a transverse beam profile measurement station: a wire-scanner. All the quadrupole and corrector magnets between the foils and the wire scanner are turned off. In figure 4.5 we compare two typical wire scanner traces obtained with and without a 0.8 μm aluminum foil inserted in the beam path. The wire scanner has three wires (see fig. 4.1 b) that respectively (from right to left in the figure) gives the beam profile along the horizontal, vertical and 45 deg axes. The fact that the beam size in the horizontal direction is much smaller than the vertical direction one is simply due to the optics tune upstream. As one can expect the beam profile is larger as the 0.8 μm foil is inserted. More generally it gets wider as the foil thickness increases. For quantitative analysis of the scattering, we only consider the tail of the beam profile located on the right side of the horizontal profile (right peak) because the other peaks overlap and would yield a tedious deconvolution. We also assume that we have scanned 100 % of the beam. Let $\mathcal{S}(\theta)$ be the function associated to the tail. $\mathcal{S}(\theta)$ is indeed the convolution of the beam profile $\mathcal{B}$ with the foil "scattering transfer function" $\mathcal{T}$ (or scattering

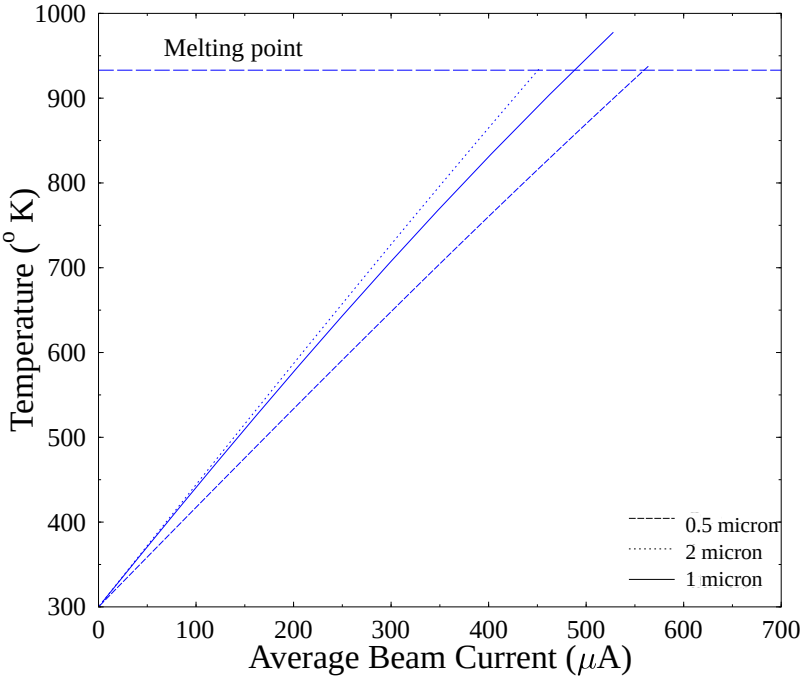

Figure 4.4: Steady state temperature versus average beam current for three different TR radiator thickness and a beam equivalent radius of 2 mm.

distribution):

$$\mathcal{S}(\theta) = (\mathcal{T} * \mathcal{B})(\theta) \tag{4.18}$$

where $*$ is the convolution product.
Rewriting the above equation in the Fourier space yields the scattering distribution function of the foil:

$$\mathcal{T} = \mathcal{F}^{-1}\left(\frac{\mathcal{S}}{\mathcal{B}}\right) \tag{4.19}$$

The $\mathcal{F}^{-1}$ is the inverse Fourier transformation. We have numerically performed this deconvolution, and the calculated scattering functions for three different foil thickness are shown in figure 4.6. From this figure we can see that the larger the thickness is, the larger the rms scattering angle (i.e. variance of the scattering distribution) is.

Comparison with the Theory

It is useful to compare the previous results with the theory, in order to see how accurately we are able to predict the effects of an OTR radiator on the beam. There are several theoretical model

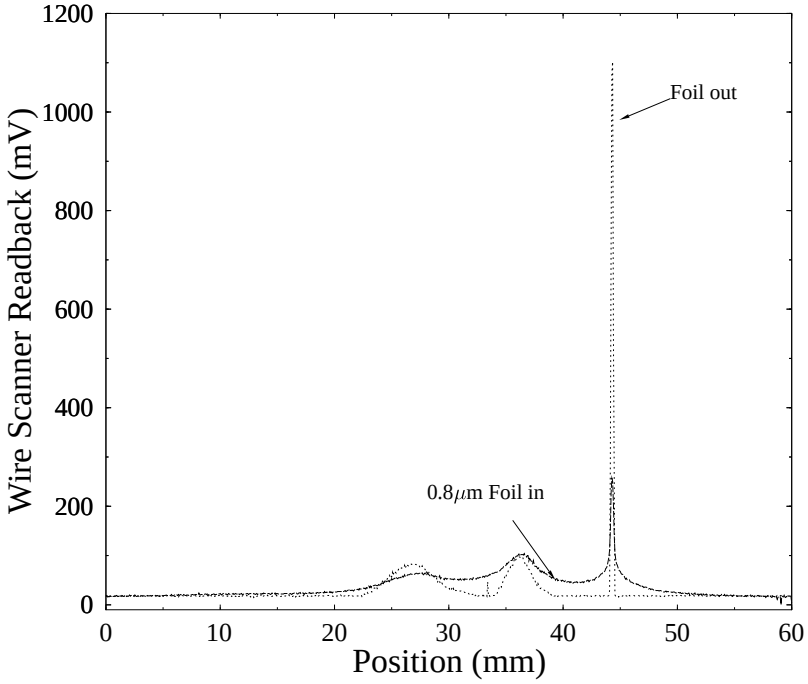

Figure 4.5: An example of the effect of a 0.8 μm thick aluminum foil on the beam profile. The beam is measured using a wire scanner located downstream the foil.

describing scattering inside very thin targets each of them have their own domain of applicability which depends on the mean average of collision Ω an electron experiences as it pass through the foil:

- simple scattering ($\Omega \leq 1$),
- plural scattering ($1 \leq \Omega \leq 20$),
- multiple scattering ($\Omega \geq 20$).

In the case of aluminum foil with thickness thinner than 5 μm, the mean number of collision being less then 20 we are in the plural scattering regime. This type of scattering is well described by the semi-empirical model elaborated by Keil [30] which is an extrapolation of the Moliére model that describes multiple scattering. The detailed study of Keil model is out of the scope of this thesis. In brief, Keil used the Fourier transform of the scattering distribution derived by Molière and only considered the two first terms of this series, a valid approximation if the mean number of collision is below 20. He then empirically calculated the numerical coefficient of the series using the experimental measurements performed by Leisegang [31] as he was experimentally studying scattering through very thin gold foils. The relation that gives the angular scattering distribution

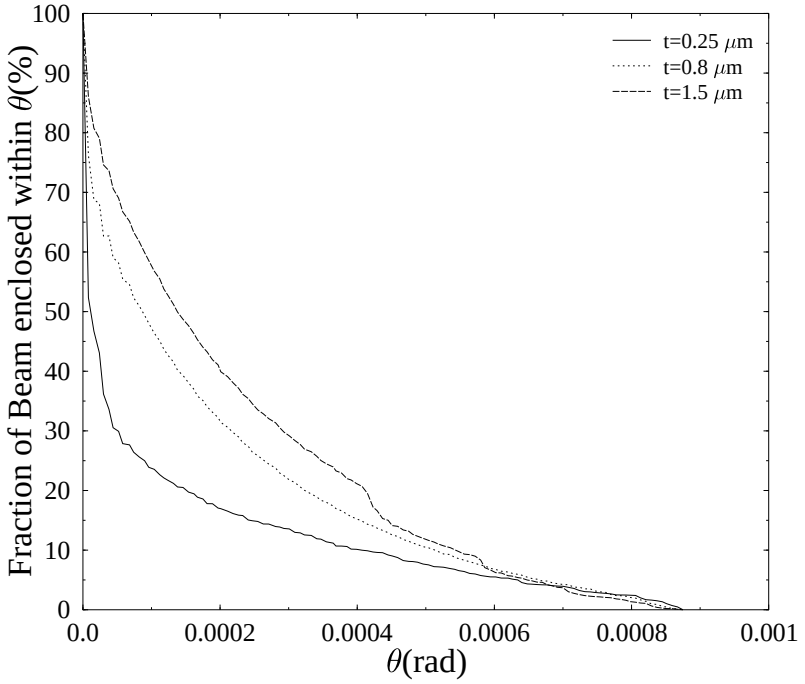

Figure 4.6: Angular scattering distribution experimentally measured for three different thicknesses of Aluminum foil.

for a given mean number of collisions Ω as a function of the reduced angle θ_s is given by:

$$F(\Omega,\theta_s) = e^{-\Omega}\sum_{k=0}^{\Omega}\sum_{l=0}^{m-k} C_m^k C_l^{m-k} \times b_1^k B_2^l \times \frac{lc_1 - kc_2}{((c_1 l + c_2 k)^2 + \theta_s^2)^{3/2}} \tag{4.20}$$

where the coefficents c_1 and c_2 are constant that where determined from experiment. The mean number of collision Ω is a function of the atomic weight A, the atomic number Z, and the thickness of the foil:

$$\Omega = 8.83 \times 10^3 \frac{t}{A}\frac{Z^{4/3}}{\beta^2} \tag{4.21}$$

where β is the reduced velocity.
The reduced angle, θ_s, in the latter equation is related to the projected angle via the relation:

$$\theta_s = \frac{\theta}{\chi_\gamma} \tag{4.22}$$

where the critical angle is defined as $\chi_\gamma = \frac{4.23Z^{1/3}}{E}$, E being the energy of the incident electrons in MeV. It is worthwhile to note that the work of Keil (as Moliére) was to show that the angular scattering distribution in the plural scattering regime does not exactly follow a gaussian distribution

material	Be	C	Mg	Al	Ti	Fe	Cu	Ag	Au
# of collision per μm	7.5	8.7	8.3	13.6	28	51	62	90	127
thinnest foil available	0.25	0.25	0.5	0.5	1	0.5	0.25	0.25	0.1
corresponding Ω	1.9	2.2	4.2	6.8	28	26	15	22.6	22

Table 4.2: Survey of materials commercially available for monitoring intense beams with TR radiators; we excluded the materials with low thermal conductivity and mean number of collision greater than 30 in their smallest thickness.

(since the average number of collision is too low to fulfill the validity of the central limit theorem). The gaussian character of the distribution especially deteriorates at large angle, where large tail tend to develop. It also breaks down for small angle where the scattering distribution has a dirac-like behavior corresponding to the case $k = 0$ and $l = 0$ in the Eqn.(4.20).

Numerical Simulations

To complete are studies, we have performed numerical simulation using the monte-carlo code GEANT from the CERNLIB which is a popular simulation tool in the Particle Physics community. This code has a scattering routine that uses the Molière model. However if the parameters are so that the Moliére model is not applicable, GEANT will simulate a series of single Coulomb scatterings. We have used this code to simulate each of the foils used in the previously described experiment.

A Comparison between Experiment, Theory and Simulation

We summarize the results given by the experiment, the theory and the numerical simulation in figure 4.7 where the different curves show the effect of the foil thickness on the semi-angle containing 70%, 95% of the beam. Clearly, the Keil model and the numerical simulation agree within 50% in the worst case. However both of them are overestimations of the measurement by factor of 5 in the worst case. Therefore it seems we can use the numerical simulations or the Keil model to predict, with a safety margin, the fraction of the beam we may lose as the beam pass through a thin foil of material.

4.3 The Possible Use of Carbon as TR radiator

We have surveyed the commercially available very thin material that may be used as TR radiator. In table 4.3 we gather several material that could be used and can self support on a 10 mm diameter holder, with the corresponding mean number of collision. The best candidates are beryllium and carbon; they are equivalent but we prefer the latter because of the chemical toxicity of beryllium. Another advantage of carbon is its capability of withstanding very high current because of its very high melting temperature. Using the GEANT code we estimated the angular scattering

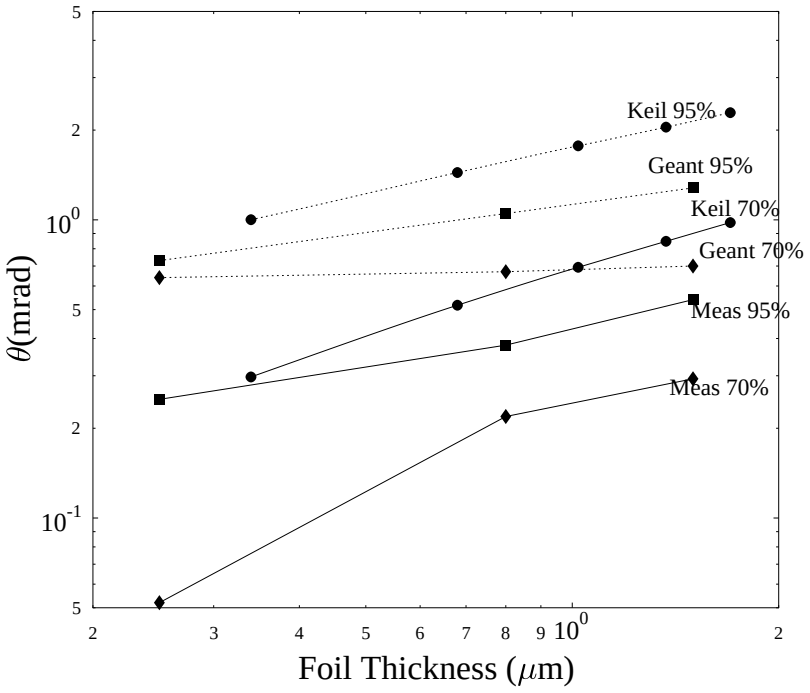

Figure 4.7: Comparative results of experiment with Keil's semi-empirical theory and GEANT computation for thin aluminum foils.

distribution for carbon. In figure 4.8 we present the projected scattering angle (normalized to the energy) containing 70%, 95% and 99.5% of the beam versus the mean number of collision for in the case of relativistic electron traversing very thin foils. Using this plots and knowing the machine dynamics acceptance, we can compute the fraction of the beam we can lose as the foil is inserted into the beam path.

4.3.1 A non-interceptive TR beam profile monitor

In an attempt to check our previous estimations we have developed a prototype for measuring beam profile. The experiment was performed in the CEBAF accelerator and located in one of the transfer lines to one of the nuclear physics experimental end station.

Experimental setup

The backward TR depends on the reflection characteristics of the surface. There are several problems that arise with very thin foils: surface inhomogeneity makes their coefficient of reflection nonuniform, and it is also difficult to stretch them enough to obtain a very flat surface. These

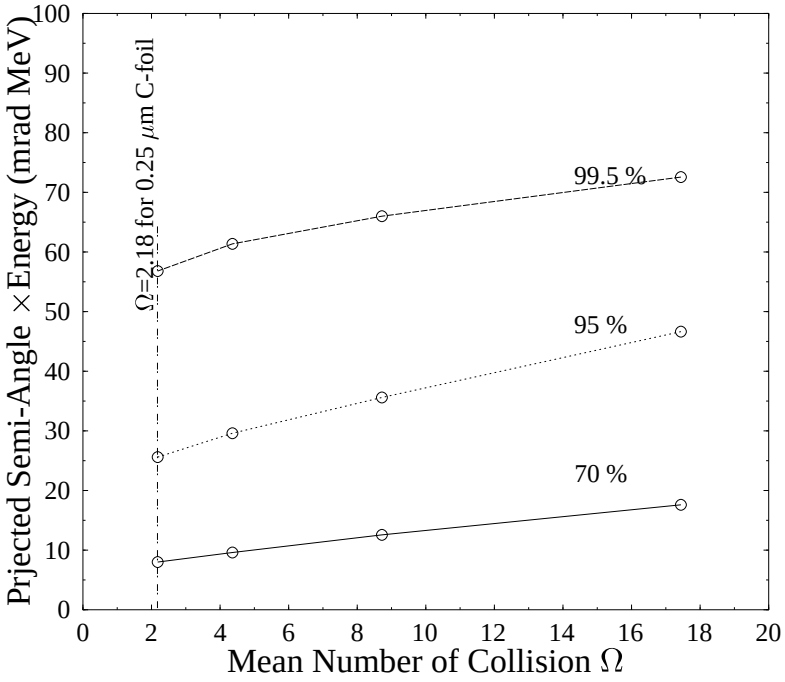

Figure 4.8: GEANT computation for thin carbon foils.

problems disappear with forward TR since it is emitted in cone centered on the beam axis regardless of the angle or reflection properties of the TR radiator. There are two additional advantages to the forward over backward TR with a 45 deg foil: (i) the depth of field effect becomes negligible, (ii) a beam normally incident on the radiator has a shorter path in the material which in turn reduces the scattering angle. Based on these considerations, we built a prototype that uses the forward TR emitted from a 0.25 μm thick carbon foil presented in figure 4.9 (A). The foil is mounted on a support which is U-shaped and open on the side crossing the beam path, so that it can be inserted without obliging the beam to be turned off. A mirror collects part of the TR radiation. With the TR that is strongly directional in a $1/\gamma$ cone, we need to collect the light emitted at small angles from the beam axis. We did this by locating the mirror on the same insertion mechanism as the foil. The mirror is 175 mm downstream from the foil; this insertion mechanism brings its edge 4 mm close to the beam trajectory. The mirror sends the collected light to a charge coupled device (CDD) via two achromatic lenses. The lenses image the foil plane onto the CCD array with a magnification of 1/2 which yields a pixel size of approximately 20 μm in the object plane.

Experimental Results

We tested our prototype at the highest beam current deliverable in CW mode by the CEBAF accelerator: 200 μA at an energy of 3.2 GeV (i.e. beam power of 640 kW). The carbon foil was not

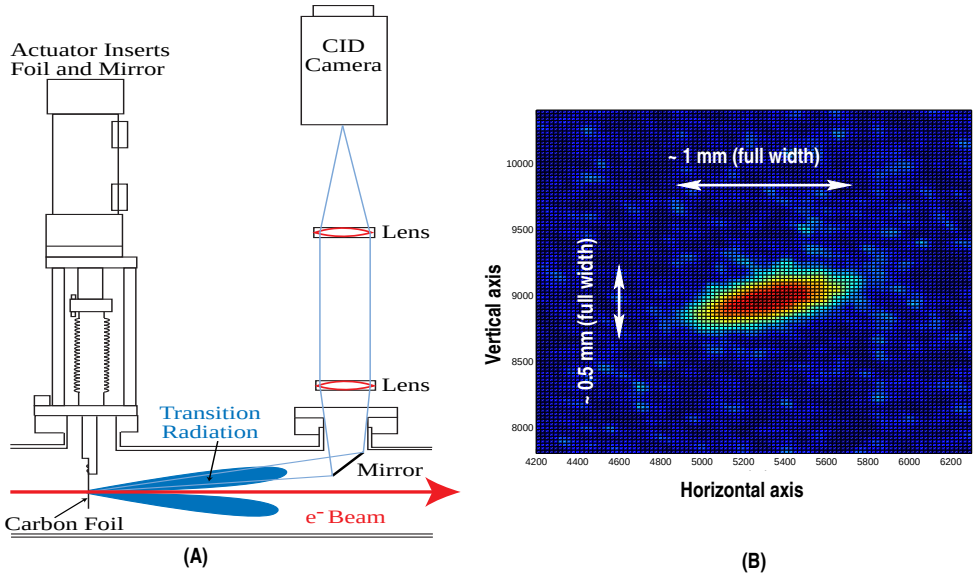

Figure 4.9: Overview of the carbon foil based OTR experiment (Courtesy from S. Spata) **(A)** and a typical beam density measured with such device **(B)**.

damaged, as predicted by our thermal studies.
On figure 4.9 (B) we show typical measured beam density. The beam size (define as the rms value), obtained performing a nonlinear fit of the transverse profiles with a Gaussian distribution, are 255 μm and 130 μm for respectively the horizontal and vertical directions. These values are compatible with the one expected using the magnetic optics code DIMAD. We also compare these rms beam size with the one obtained using the wire scanner in close proximity and obtained the same beam width within the uncertainty tolerance as shown in Table 4.3.1.

To the best of our knowledge this is the first time TR was used to measured beam size of hundreds of microns for an ultra relativistic beam ($\gamma \simeq 6300$). This measurement is the proof of the nonvalidity of a common argument in the beam instrumentation community according to which TR cannot be use to measure micron-sized beam profiles for relativistic beams. The hypothetical limit in resolution that had been claimed was that for a given reduced energy γ the minimum rms beam size that could be resolved by detecting TR at the wavelength λ is of the order of the product $\lambda\gamma/(4\pi)$. In our case such criterion would set, at a wavelength of observation of 500 μm, the smallest rms beam size we could observed to approximately 250 μm rms, i.e. approximately 2 times larger than the smallest beam size we measured. Resolution issues concerning OTR have been discussed in numerous paper [33]. In brief, the aforementioned criterion concerning the minimum rms beam size σ_x we can resolve originates from the diffraction limit which states that the rms divergence σ' of a source and its extent σ are bounded by the relation $\sigma\sigma' > \lambda/(4\pi)$. In the case of TR, the common mistake is to write $\sigma' \simeq 1/\gamma$ which finally yield to the relation $\sigma' < \gamma\lambda/(4\pi)$. Indeed, TR contrary to SR, is not collimated within a $1/\gamma$-cone: for instance the TR emission associated with a 1 GeV electron has only 30% of its total power contained within a cone of $10 \times 1/\gamma$!
In collaboration with the nuclear team of one of the experimental end station we investigated the impact of the foil on the electron beam. The test was aimed to see whether the foil is "transparent" to the nuclear physics detectors. The detector used was the High Resolution Spectrometer (HRS), an electron spectrometer located in one of the hadronic experimental end stations of the CEBAF

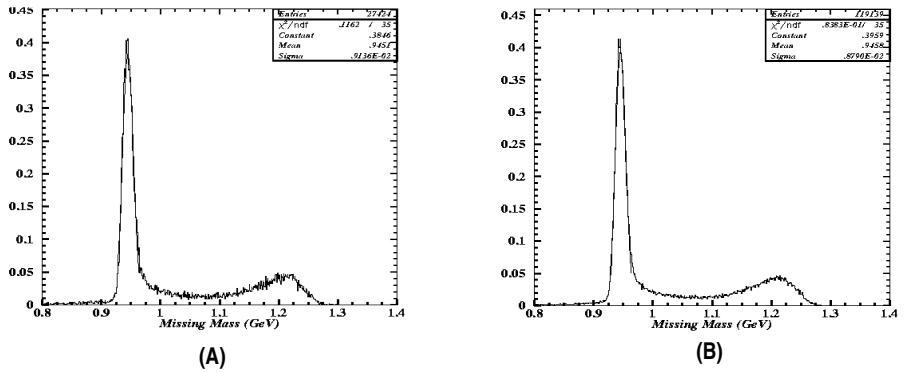

Figure 4.10: Comparison of the Missing mass spectra obtained using one of the experimental hall spectrometer with **(A)** and without **(B)** the beam being intercepted by the carbon foil (Courtesy of P. Guèye, Hampton University, VA USA).

	horizontal direction	vertical direction
wire scanner	0.204 ± 0.050 mm	0.082 ± 0.050 mm
OTR-monitor	0.255 ± 0.060 mm	0.130 ± 0.060 mm
Simulation	0.250 mm	0.114 mm

Table 4.3: Comparison of the profile measurements with the wire scanner and OTR-monitor.

accelerator. The experiment consisted of setting the angle and the dipoles of the spectrometer to observe the recoil electron issued from the scattering of the electron beam on a hydrogen target. Namely we were observing the reaction $e + p \rightarrow e' + p'$ in the elastic scattering. A criterion to determine whether the foil has significant impact on the nuclear physics measurement was to look at the missing mass spectrum. In this missing mass spectrum, we have a peak centered on the proton mass (945 MeV/c). Due to the finite resolution of the detector, the emittance of the incoming electron beam that hits the target, this peaks as a nonzero width. One straightforward experiment with the carbon foil is to determine if the fact of inserting the carbon foil in the beam path downstream the target yield an enlargement of the peak width. Hence two sets of measurements were performed: In a first one we inserted the carbon TR radiator and acquired data with the spectrometer while in a second set data were acquired without inserting the carbon foil. Figure 4.10 shows the missing mass spectra in the two cases. In both cases, the rms width of the elastic peak was similar well within experimental noise. This measurement were performed at 3 GeV. Latter in collaboration with another experimental Hall, the similar experiment was iterated at lower energy 800 MeV yielding a similar conclusion. Therefore, at least at energy higher than 800 MeV, the prototype we built constitutes a noninvasive beam profile monitor.

4.3.2 Profile Monitor Configuration in the FEL

Experimental Setup

Although the carbon foil monitor is very useful as a noninterceptive device, we decided, for the short term, to use as beam density monitor in the FEL driver, aluminum foils in the popular configuration as pictured in figure 4.11. This choice is in part due to the difficulty to reliably mount very thin carbon foil on large support. Also in the case of the FEL, the laser itself can serve to diagnose the beam quality in a continuous and non intrusive fashion.
The system we use consists of 0.8 μm thick aluminum foils mounted on a circular frames of 19 mm diameter that makes a 45 deg angle w.r.t. the beam direction. The foil can be remotely inserted/withdrawn from the beam path by the means of an air cylinder actuator. In this configuration the backward transition radiation emitted at 90 deg with respect to the beam axis shines out of the vacuum chamber through a silica optical window. It is then collected by a planar mirror and sent to an optical system composed of a commercially available telephoto lens (optimized to reduce chromatic and spherical optical aberration) and a high resolution CCD camera whose video output signal is digitized by a VME-based DATACUBE image processing board that can be externally triggered. The system is set to image the foil plane on the CCD array detector with magnification of approximately 1/3. The choice of the magnification ratio is dictated by the need of achieving the highest possible resolution with a reasonable field of view. The circular frame on which the foil is mounted determines the field of view: this 19 mm diameter frame is used to accurately calibrate the image and thereby determine what is the conversion factor between the CCD array pixels and real distances in the foil plane.

To avoid damaging the aluminum foil, and since the beam dynamics is only dominated by sin-

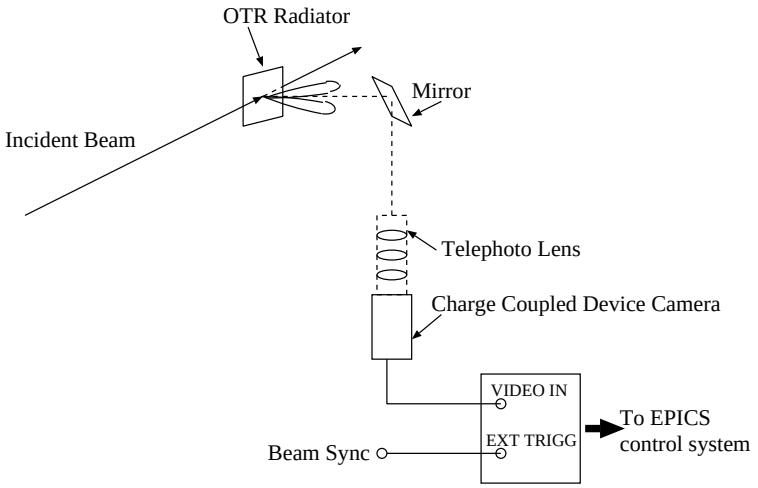

Figure 4.11: Standard configuration of the OTR-based profile monitor in the FEL-driver accelerator.

gle bunch effect, i.e. the beam phase space density only depends on the charge per bunch and not on the bunch repetition rate, the beam average current is decreased to approximately 0.5 μA. There are four independent parameters that can influence the beam average current: the charge per bunch, the bunch repetition rate in a macropulse, the macropulse width and the macropulse repetition rate. Since only the charge per bunch affects the phase space and consequently the beam

density profile, by acting on the other three parameters it is possible to reduce the beam current without affecting on the phase space distribution. Naturally the fact we have to use a reduced beam current during the measurement of the beam parameter impacts on the FEL operation and subsequent experiments. Therefore such a measurement is invasive. As we have seen in Chapter 2,

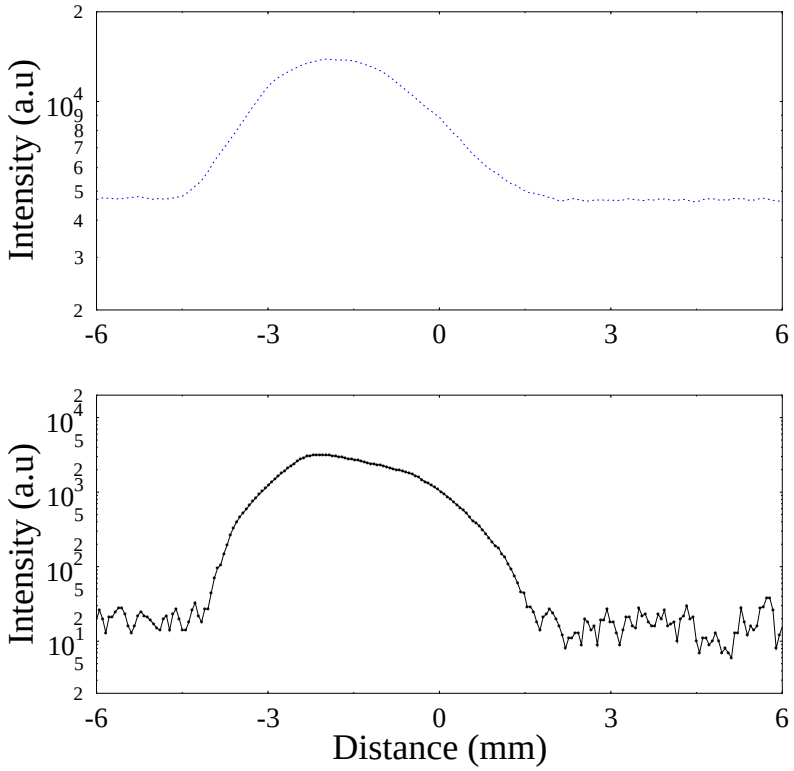

Figure 4.12: Raw data beam profile (top graph) and beam profile after processing (background subtracted, ghost pulse contribution removed,...).

each macropulse contains bunches (whose charge can be arbitrary varied from 0 pC to 135 pC [6]) at a repetition rate up to 74.85 MHz. All the beam structure is generated by a master oscillator which also synchronously generate a 5 V rectangular pulse whose width and repetition rate are the replica of the macropulse. Such signal called the "beam sync" is available from the control system to trigger data acquisition systems.
In the present case, we trigger the image processing board to grab only the video frame that contains the beam image. For such a purpose we use the following setup: the "beam sync" is delayed by 0.435 ms before being sent to the "external trigger" input of the image processing board. The delay is set so that the digitizer is triggered at the next incoming pulse.
The digitized data stream at the image board output consists of a 660×484 array matrix, $I(x, y)$. Some primary operations on this data stream can be directly performed by the CPU of the image processing board in real time [39]. Such operations include the calculation of:

[6] In the results presented in this report the maximum charge used is approximately 60 pC

- the beam centroid position defined as $x_0 = \int x dx I(x,y)$
- the beam spot the rms width defined as $\sigma = \int (x - x_0)^2 I(x,y) dx$
- and the Hough transforms (i.e. projection) along horizontal and vertical axis (i.e. $P(x) = \int I(x,y) dy$)

Along with these implemented operations, some signal processing functions such as filtering, background subtraction, etc..., are available.
During our preliminary measurements we have noticed that directly computing the variance of the beam profile computed on the raw data matrix was yielding erroneous values for the rms beam size. This was traced back to be due to the so-called "ghost pulse" effect: along with the main macropulse that contains a series of electron bunches, whose transverse density is the quantity of interest for our measurement, there are parasitic bunches called "ghost bunches" that consists of photo-electron emitted as the drive laser pulse if off. These "ghost bunches" are indeed due to the inability to have a perfect extinction ratio of 0 between drive laser pulse that serve to create "real" bunches. Physically this is due to the electro-optics cell that are used to switch the laser pulse on and off on the photocathode. Therefore we modified our acquisition algorithm to take into account this effect by using the following steps during a measurement:

1. reduce macropulse width to 100 ns to only detect "ghost" pulses,
2. acquire the pixel matrix M_{ghost} and store it in a memory buffer,
3. increase the macropulse to the appropriate width
4. acquire the pixel matrix $M_{\text{beam+ghost}}$ and store it in the current buffer
5. mathematically perform the operation $M_{\text{beam}} = M_{\text{ghost}} - M_{\text{beam+ghost}}$
6. compute parameter using the matrix M_{beam}

The results of this operation is graphically shown in Figure 4.12. We have also verified that this method yields reasonable results.
In the above step **3**, we need to clarify the meaning of "appropriate" macropulse duration: it depends on the beam size, and it is experimentally determined by insuring the CCD array is still operated in its linear domain. Typically the power surface density, dP/dS, on the pixel array, scales with the transverse rms beam size image, σ_x and σ_y, and with the power of the emitted radiation, P, according to the relation:

$$\frac{dP}{dS} \propto P \times \frac{1}{\sigma_x \sigma_y} \tag{4.23}$$

During our experiments, for each measurement station, the macropulse width was experimentally determined for typical beam size on each of the beam profile measurement station. It is then automatically recalled when a measurement is performed. Also to accommodate potential operating condition changes we can use the scaling law of the latter equation to re-adjust the macropulse width dynamically.

Resolution of beam size measurement

It is very important to have a precise knowledge of the systematic error on a beam size measurement since we will have to include these errors and propagate them to find the error bar due to systematic errors on the transverse emittance computation.
There are principally two types of effects that enter in the resolution of this type of imaging devices system we use: optical resolution and electronic response. The former effect can be evaluated in our case since our system is optimized to minimize spherical and chromatic aberration, the optical degradation of resolution is essentially due to the depth of field effect that results because the plane we are imaging, the foil, makes a 45 deg angle with respect to the CCD array. The best way to characterize the resolution of the whole system i.e. including optical and electronic transfer function, is to image via this system a sharp edge [43]. For such a purpose a target image that consists of an sharp edge between an optically black and optically white region is positioned at TR radiator location. The derivative of the corresponding digitized image will provide information on the impulse response of the system and its width can be used to quantify the resolution of the system. Typical resolution measured were at maximum 1.5 times the pixel size in the object plane. For typical magnification we use, the pixel size in the object plane is about 40 μm which gives a typical rms resolution of 60 μm well below the typical beam size measured (of the order of approximately 1 mm rms).

4.4 Measurement of Emittance in the 38+ MeV Region

4.4.1 General Considerations

The method to measure emittance in the high energy region of the FEL is the usual envelope fitting technique. It assumes that the beam can be first order transport, that there is no coupling between the horizontal and vertical planes, and that the dispersion is negligible at the location of the measurement. If the latter assumptions are fulfilled then one can use TRANSPORT formalism to find the relation between beam parameters at two different locations in the beamline knowing the transfer matrix between them R

$$\Sigma^{(i)} = R\Sigma^{(0)}R^T \tag{4.24}$$

Expanding the above matrix relation (recall Σ is the beam matrix) we can relate the RMS beam size at the location i with the RMS divergence, beam size and beam correlation of the beam at the location 0. Hence varying the transfer matrix for a given set of initial values in 0, provides different beam size at the station location i. Therefore one can easily get a (generally over determined) system of N equations (corresponding to N different transfer matrices) with only 3 unknowns. Such system is traditionally inverted by the means of the least square method: Given the N squared-beam size measurements, one needs to find the set of parameter ($\sigma_{11}^{(0)}$, $\sigma_{12}^{(0)}$, $\sigma_{22}^{(0)}$) that minimizes the χ^2:

$$\chi^2 = \sum_{i=1}^{N} \frac{\left[\sigma(i) - (R_{11}^2(i)\sigma_{11}^{(0)} + R_{12}^2\sigma_{22}^{(0)} + R_{11}R_{12}\sigma_{12}^{(0)})\right]^2}{\delta(i)^2} \tag{4.25}$$

where δ_i is the error on the i^{th} beam size measurement.
It is well known [40] that the value of σ_0 that minimized the χ^2 satisfies:

$$\begin{pmatrix} \sum_{i=1}^{N} \frac{R_{11}^2(i)\sigma(i)}{\delta^2(i)} \\ \sum_{i=1}^{N} \frac{2R_{11}(i)R_{12}(i)\sigma(i)}{\delta^2(i)} \\ \sum_{i=1}^{N} \frac{R_{12}^2(i)\sigma(i)}{\delta^2(i)} \end{pmatrix} = \begin{pmatrix} \sum_{i=1}^{N} \frac{R_{11}^4(i)}{\delta^2(i)} & \sum_{i=1}^{N} \frac{2R_{11}^3(i)R_{12}(i)}{\delta^2(i)} & \sum_{i=1}^{N} \frac{R_{11}^2(i)R_{12}^2(i)}{\delta^2(i)} \\ \sum_{i=1}^{N} \frac{2R_{11}^3(i)R_{12}(i)}{\delta^2(i)} & \sum_{i=1}^{N} \frac{4R_{11}^2(i)R_{12}^2(i)}{\delta^2(i)} & \sum_{i=1}^{N} \frac{2R_{11}(i)R_{12}^3(i)}{\delta^2(i)} \\ \sum_{i=1}^{N} \frac{R_{11}^2(i)R_{12}^2(i)}{\delta^2(i)} & \sum_{i=1}^{N} \frac{2R_{11}(i)R_{12}^2(i)}{\delta^2(i)} & \sum_{i=1}^{N} \frac{R_{12}^4(i)}{\delta^2(i)} \end{pmatrix} \begin{pmatrix} \sigma_{11}^{(0)} \\ \sigma_{12}^{(0)} \\ \sigma_{22}^{(0)} \end{pmatrix}$$

$$c \Leftrightarrow b = \mathcal{C}\sigma_0 \tag{4.26}$$

The 3x3 matrix is named curvature matrix. The solution for σ_0 is obtained inverting the previous matrices equation. It is worth (for software implementation) to note that the curvature matrix has the following form:

$$\mathcal{C} = \begin{pmatrix} A & 2B & C \\ 2B & 4C & 2B \\ C & 2B & E \end{pmatrix} \tag{4.27}$$

which yields a very tractable form for its inverse, the error matrix:

$$\mathcal{E} = \frac{1}{|\mathcal{C}|} \begin{pmatrix} 4(CE - D^2) & -2(BE - CD) & 4(BD - C^2) \\ -2(BE - CD) & (AE - C^2) & -2(AD - BC) \\ 4(BD - C^2) & -2(AD - BC) & 4(AC - B^2) \end{pmatrix} \tag{4.28}$$

where $|\mathcal{C}|$ denotes the determinant of C:

$$|\mathcal{C}| = 4(ACE - AD^2 - B^2E + 2BCD - C^3) \tag{4.29}$$

The elements of the error matrix are the variance and covariance numbers on the computed $\Sigma(0)$ matrix element namely:

$$\begin{cases} \Delta_{\sigma_{11}} = \sqrt{E_{11}} \\ \Delta_{\sigma_{12}} = \sqrt{E_{22}} \\ \Delta_{\sigma_{22}} = \sqrt{E_{33}} \\ \Delta_{\sigma_{11},\sigma_{12}} = E_{12} \\ \Delta_{\sigma_{11},\sigma_{22}} = E_{13} \\ \Delta_{\sigma_{12},\sigma_{22}} = E_{23} \end{cases} \tag{4.30}$$

Using the standard error propagation theory [40] one can estimate the errors on the computed Twiss parameters at the location (0). Let ζ be the computed parameter i.e. the emittance or the Twiss parameters. Then the error on ζ is given by:

$$\begin{aligned} (\Delta\zeta)^2 = & \left(\frac{\partial\zeta}{\partial\sigma_{11}}\right)^2 (\Delta\sigma_{11})^2 + \left(\frac{\partial\zeta}{\partial\sigma_{12}}\right)^2 (\Delta\sigma_{12})^2 + \left(\frac{\partial\zeta}{\partial\sigma_{22}}\right)^2 (\Delta\sigma_{22})^2 + \\ & + 2\frac{\partial\zeta}{\partial\sigma_{11}}\frac{\partial\zeta}{\partial\sigma_{12}}(\Delta_{\sigma_{11},\sigma_{12}})^2 + 2\frac{\partial\zeta}{\partial\sigma_{11}}\frac{\partial\zeta}{\partial\sigma_{22}}(\Delta_{\sigma_{11},\sigma_{22}})^2 + 2\frac{\partial\zeta}{\partial\sigma_{12}}\frac{\partial\zeta}{\partial\sigma_{22}}(\Delta_{\sigma_{12},\sigma_{22}})^2 \end{aligned} \tag{4.31}$$

The partial derivative in the error propagation formulae are given by:

$$\frac{\partial\tilde{\varepsilon}}{\partial\sigma_{11}} = \frac{\gamma_T}{2}, \frac{\partial\tilde{\varepsilon}}{\partial\sigma_{12}} = \alpha_T, \frac{\partial\tilde{\varepsilon}}{\partial\sigma_{22}} = \frac{\beta_T}{2}, \tag{4.32}$$

$$\begin{aligned} \frac{\partial\beta_T}{\partial\sigma_{11}} = \frac{2 - \beta_T\gamma_T}{2\tilde{\varepsilon}}, \frac{\partial\beta_T}{\partial\sigma_{12}} = -\frac{\beta_T\alpha_T}{\tilde{\varepsilon}}, \frac{\partial\beta_T}{\partial\sigma_{22}} = \frac{\beta_T^2}{2\tilde{\varepsilon}}, \\ \frac{\partial\alpha_T}{\partial\sigma_{11}} = -\frac{\alpha_T\gamma_T}{2\tilde{\varepsilon}}, \frac{\partial\alpha_T}{\partial\sigma_{12}} = -\frac{1 + \alpha_T^2}{\tilde{\varepsilon}}, \frac{\partial\alpha_T}{\partial\sigma_{22}} = -\frac{\beta_T\alpha_T}{2\tilde{\varepsilon}}. \end{aligned} \tag{4.33}$$

Finally after a bit of algebra one can compute the uncertainties on the emittance, and the β_T and α_T parameters:

$$(\Delta_{\tilde{\varepsilon}})^2 = \frac{1}{\tilde{\varepsilon}^2}\Big(\sigma_{12}^2(\Delta_{\sigma_{12}})^2 + \frac{\sigma_{12}^2}{4}(\Delta_{\sigma_{11}})^2 + \frac{\sigma_{11}^2}{4}(\Delta_{\sigma_{22}})^2 - \sigma_{12}\sigma_{11}\Delta_{\sigma_{22}\sigma_{11}} + \frac{\sigma_{11}\sigma_{22}}{2}\Delta_{\sigma_{11}\sigma_{22}} - \sigma_{12}\sigma_{22}\Delta_{\sigma_{11}\sigma_{12}}\Big) \tag{4.34}$$

$$(\Delta_{\beta})^2 = \frac{1}{\tilde{\varepsilon}^6}\Big(\sigma_{12}^2\sigma_{11}^2(\Delta_{\sigma_{12}})^2 + \left(\frac{\sigma_{11}\sigma_{12}}{2} - \sigma_{12}^2\right)^2(\Delta_{\sigma_{11}})^2 + \frac{\sigma_{11}^4}{4}(\Delta_{\sigma_{22}})^2 + \left(\sigma_{12}^2\sigma_{11}^2 - \frac{\sigma_{11}^3\sigma_{11}}{2} - \sigma_{12}^2\right)^2\Delta_{\sigma_{22}\sigma_{11}} + \left(\sigma_{12}^2\sigma_{11}^2\sigma_{22} - 2\sigma_{12}^3\sigma_{11}\right)\Delta_{\sigma_{11}\sigma_{12}} - \sigma_{12}\sigma_{11}^3\Delta_{\sigma_{11}\sigma_{22}}\Big) \tag{4.35}$$

$$(\Delta_{\alpha})^2 = \frac{1}{\tilde{\varepsilon}^6}\Big(\sigma_{22}^2\sigma_{11}^2(\Delta_{\sigma_{12}})^2 + \frac{\sigma_{12}^2\sigma_{11}^2}{4}(\Delta_{\sigma_{11}})^2 + \frac{\sigma_{12}^2\sigma_{22}^2}{4}(\Delta_{\sigma_{22}})^2 - \sigma_{12}\sigma_{11}\sigma_{12}^2\Delta_{\sigma_{12}\sigma_{11}} + \frac{\sigma_{12}^2\sigma_{11}\sigma_{22}}{2}\Delta_{\sigma_{11}\sigma_{22}} - \frac{\sigma_{12}\sigma_{11}^2\sigma_{22}}{2}\Delta_{\sigma_{11}\sigma_{12}}\Big) \tag{4.36}$$

Therefore by building the curvature matrix we can get an estimate of the uncertainties on the computed elements of the Σ-matrix and then propagate these uncertainties on the estimated values for the emittance and Twiss parameters. Lastly the value of $\delta(i)$, the error on beam size measurement, is taken to be equal to the measured resolution of the beam profile measurement system i.e. $\delta(i) = 60\mu m$.

4.4.2 The quadrupole scan method

One way of varying the transfer matrix between a reference point and the measurement is to change the strength of a quadrupole and observe the variation of beam size on an OTR screen upstream. Although this method is generally easy to implement special care must be taken:

- the maximum beam spot size in both direction must be smaller that the dimension of the OTR screen
- the minimum beam size should be chosen to be large with respect to the resolution of the beam size measurement and large enough not to produce any saturation on the CCD camera that is used to measure the beam size.

One question that arises is how to set the optics downstream the quadrupole that is being varied to get the wanted beam size variation on the profile monitor? Such problem has been studied in the case where the quadrupole and the profile monitor are separated by a drift (see reference [34]). In a more general case where the transfer matrix between the quadrupole exit and the profile monitor is R, we can derive a similar criterion on the lattice functions at the profile monitor location: the $\alpha_{x,y}$ and $\beta_{x,y}$ Twiss parameters at the entrance of the quadrupole being varied should be related by:

$$\alpha_x = -\frac{R_{11}}{R_{12}}\beta_x \qquad \alpha_y = -\frac{R_{33}}{R_{34}}\beta_y \tag{4.37}$$

The $\beta_{x,y}$ in the previous relation are the minimum β-function one wishes to achieve at the profile monitor station. The choice of the minimum β-function has two implications.
Let's assume the thin lens approximation to be valid[7] . Then the transfer matrix between the entrance of the quadrupole and the profile monitor is:

$$R = \begin{pmatrix} R_{11} & R_{12} \\ R_{21} & R_{22} \end{pmatrix} \begin{pmatrix} 1 & 0 \\ -1/f & 1 \end{pmatrix} \tag{4.38}$$

Hence the betatron function at the OTR location can be expressed as a function of the initial betatron function at the quadrupole entrance (for instance in the horizontal plane):

$$\beta_x(k) = \frac{R_{12}^2}{f^2}\beta_{x,0} + \frac{R_{12}^2}{\beta_{x,0}} \tag{4.39}$$

where we have use the fact that $\alpha_{x,0} = \beta_{x,0}/L$ when one has taken care of setting the upstream optics to satisfy the relation derived previously in Eqn.(4.37).
Introducing the focal length ($1/f = k_1 l$) and recalling that $R_{12}/\beta_{x,0} = \beta_x(k=0)$ yields:

$$\beta_x(k) = \beta_x(0) + \frac{R_{12}^4 k_1^2 l^2}{\beta_x(0)} \tag{4.40}$$

whose derivative with respect to the quadrupole strength k_1 is:

$$\frac{d\beta_x(k)}{dk} = \frac{2R_{12}^2 k_1^2 l^2}{\beta_x(0)} \tag{4.41}$$

with the same kind of relation in the vertical plane (replacing x index by y and R_{12} by R_{34}). The latter equation shows that the choice of $\beta_{x,0}$, which we have suggested earlier to be as large as possible to reduce the error on the beam size measurement, directly affects the slope of the beam size variation on the profile monitor: a too large $\beta_{x,0}$ will give a "flat looking" variation. Therefore there is an optimum beam value for $\beta_{x,0}$; this optimum should be determined via an iterative process using numerical simulations.

4.4.3 The multi-monitor method

Another way of varying the transfer matrix between the reference point where one wishes to compute the beam parameters and the beam profile measurement station is to measure the beam profile at different position along the beamline which are separated by non-dispersive optics. This method requires at least three monitors but one should use more of them for redundancy. An advantage of this measurement is that no element has to be varied. However to get a precise measurement a dedicated optical lattice setting generally need to be elaborated.
Let analyze quantitatively the method. The beam size on a profile station k and l are related to the Twiss parameters at the reference point by Eqns.(4.24). Indeed, we need to make sure that these two equations are not redundant, namely that:

$$\begin{vmatrix} R_{11,k}^2 & R_{12,k}^2 \\ R_{11,l}^2 & R_{12,l}^2 \end{vmatrix} \neq 0, \begin{vmatrix} R_{11,k}^2 & -2R_{11,k}R_{12,k} \\ R_{11,l}^2 & -2R_{11,l}R_{12,l} \end{vmatrix} \neq 0, \text{and} \begin{vmatrix} -2R_{11,k}R_{12,k} & R_{12,k}^2 \\ -2R_{11,l}R_{12,l} & R_{12,l}^2 \end{vmatrix} \neq 0 \tag{4.42}$$

[7] This is a false statement if we consider the whole range of the magnetic strength for the quadrupoles ($-20 < k_1 < 20$) but it provides easier analytical results and does not change significantly the physics of the present discussion. The treatment of the full problem including the thick lens transfer matrix is done via numerical modeling.

These three determinants yield the same equation (assuming the R_{11} and R_{12} to be different from zero):

$$R_{11,k}R_{12,l} - R_{12,k}R_{11,i} \neq 0 \tag{4.43}$$

which implies, using the general formulation of a beam transfer matrix in term of betatron phase advance $\Delta\mu$ between k and l:

$$\sin(\Delta\mu) \neq 0 \tag{4.44}$$

Hence in order the latter equation to be verified, one must take care to set the optical lattice so that the betatron phase between the viewers being used in the measurement is different from $n\pi$ (with $n \in \mathbf{N}$).
Another care that has to be taken is to make sure that at the profile measurement station the beam is not at a waist; this will enlarge the error bars on the measurement (one should make the beam as large as possible compared to the error on the beam size measurement).

4.4.4 Simulation of Emittance Measurement in the IRFEL

After the decompressor chicane, the beam line consists of a quadrupole triplet and is instrumented with two OTR viewers. For the simulation of the emittance measurement using the quadrupole scan method, we use the OTR monitor located in the dump beamline 3.43 m downstream the exit of the last quadrupole of this triplet quadrupole. Therefore in this case we have investigated whether this quadrupole could be use to vary the transfer matrix while observing beam size variation on the profile monitor. To perform such measurement optimally we need to set the upstream optics to make sure we can have a "right" beam size variation over the quadrupole excitation range. Typically we use the magnetic optics code DIMAD to fit the upstream quadrupoles to satisfy Eqn.(4.37) at the OTR location (such optimization will be discussed in more detail in Chapter 5). After having properly tuned these upstream quadrupoles, we have numerically studied the variation of beam size for two different minimum β-functions at the location of the OTR viewer. A typical beam size variation is presented in figure 4.13. The deduced uncertainties on the emittance for these two different values of the minimum betatron function versus the errors on beam size measurement is plotted in Figure 4.14. From this figure one can obviously notice that the choice of the largest minimum betatron value at the OTR location minimizes the error bars on the deduced emittance (and on the other deduced Twiss parameters). It is seen that 6 m is a reasonable number for which the systematic errors achieved on emittance measurement can be well within the desired 10% level. To fully simulate the whole measurement and benchmark our data analysis algorithm, we propagate using the DIMAD code the expected parameter at the linac exit (as computed with PARMELA) up to the entrance of the varying quadrupole (i.e. last quadrupole of the triplet aforementioned). Then we simulate the measurement: we vary the quadrupole strength and for each setting propagate the parameters up to the location of the OTR monitor where we compute and record the beam size. In table 4.4 we compare the results obtained on the computed beam parameters at the quadrupole entrance face with the DIMAD initial parameters: the results are in excellent agreement. We also compare the error bars obtained with our error analysis with the error bars statistically computed on a set of 200 simulations of the measurement in which the beam size is randomly generated along a normal density centered on the beam size computed with the optics code with a variance equal to the rms resolution (60 μm). The conclusion is that the error propagation agrees with the variances

obtained via the statistical analysis. The fluctuation from measurement to measurement using the Monte Carlo technique is presented in figure 4.15.

When the undulator magnet is installed onto the beamline, the two first triplet are use to match

Parameter	DIMAD	Error Propagation	Monte-Carlo Simulation
$\tilde{\varepsilon}_x$ (mm-mrad)	0.17000	0.16993 ± 0.00479	0.16990 ± 0.00431
β_x (m)	5.56	5.56 ± 0.18	5.56 ± 0.17
α_x	1.39	1.39 ± 0.05	1.39 ± 0.04
$\tilde{\varepsilon}_y$ (mm-mrad)	0.14960	0.14964 ± 0.00449	0.14969 ± 0.00441
β_y (m)	5.56	5.56 ± 0.19	5.56 ± 0.19
α_y	1.39	1.39 ± 0.05	1.39 ± 0.05

Table 4.4: Simulation of the emittance measurement using the quadrupole scan method prior to the first recirculation arc. The parameters presented are all at the entrance face of the quadrupole being used during the measurement.

the lattice function at the middle of the wiggler in such a way to obtain a waist at the undulator center with a value for betatron function of approximately 0.5 meters (depending on the beam energy and the wiggler parameter) in both planes. Such matching is realized by the mean of the two upstream quadrupole triplets that can adjust the four beam parameters (α_x, β_x and α_y, β_y) while keeping the beam envelope within the machine aperture. After the wiggler two other triplets are use to match the beam to the recirculation transport. We have implemented an optics to try to measure emittance in this region: unfortunately we found difficult in simulation to achieve large betatron function on the viewer used in the undulator chamber. This point is illustrated in the table below where, as before, we validate the error propagation for the multi-monitor technique: the error bars are much larger than those generally obtained with quadrupole scan technique.

Parameter	DIMAD	Error Propagation	Monte-Carlo Simulation
$\tilde{\varepsilon}_x$ (mm-mrad)	0.17000	0.17005 ± 0.01233	0.16753 ± 0.01268
β_x (m)	5.48	5.48 ± 0.46	5.58 ± 0.53
α_x	1.25	1.25 ± 0.19	1.27 ± 0.20
$\tilde{\varepsilon}_y$ (mm-mrad)	0.14960	0.14660 ± 0.01186	0.14726 ± 0.01214
β_y (m)	3.09	3.08 ± 0.30	3.17 ± 0.31
α_y	-0.13	-0.13 ± 0.13	-0.15 ± 0.14

Table 4.5: Simulation of emittance measurement using the multi-monitor method in the undulator region. The parameters presented are all at the exit face of last dipole of the decompressor chicane.

4.4.5 Effect of spurious Dispersion on Emittance Measurement

Up to now we have assumed the beam profile measurement, for the subsequent estimation of transverse emittance, is performed in a dispersion free region. Practically this assumption is not a fortiori true: especially after large bending systems such as the recirculation arcs (when set to operate in achromatic mode) in the IRFEL. In such a system because of potential misalignment of magnetic elements, the dispersion may not exactly vanish after the arcs. Hence it is very

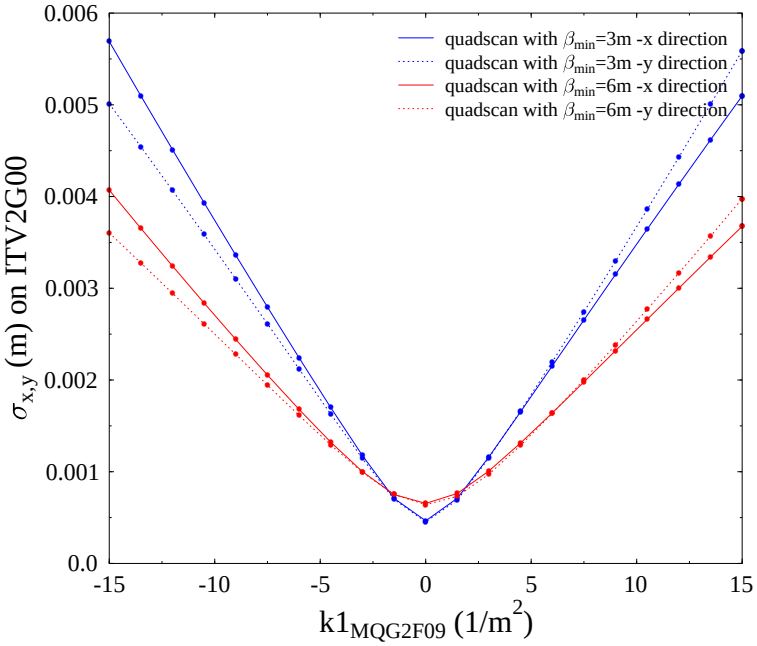

Figure 4.13: Comparison of beam spot size variation versus quadrupole strength for two different setting of the upstream optics to achieve two different minimum betatron value, 3 and 6 m.

important to assess what are the tolerance on the value of this "spurious" dispersion to have an insignificant impact on the transverse measurement performed with beam profile monitor located in these regions. Then prior to measuring emittance, the dispersion should be measured and eventually corrected so that spurious dispersion is within the tolerated value. To establish such criterion, we write the beam rms spot size as $\sigma_x = \sqrt{\beta\tilde{\varepsilon} \times (1+\xi^2)}$ where ξ is a dimensionless constant $(\eta^2(\sigma_E/E)^2)/(\beta\tilde{\varepsilon})$ (σ_E is the rms energy spread). We simulate the beam size at a given beam profile measurement station by using a magnetic optics code and superimpose the effects of spurious dispersion for different values of ξ, and then compute the emittance. In figure 4.16 we present the relative emittance increase due to the dimensionless spurious dispersion ξ. From this figure, we find that in order for the spurious dispersion to have insignificant effect on the emittance measurement, say induce less than 1% emittance growth, we should insure that $\xi < 1/100$. This give an upper limit on the spurious dispersion $\eta < 1/\sqrt{(100)}\sqrt{\beta\tilde{\varepsilon}}/(\sigma_E/E)$, in the most critical case, i.e. assuming an energy spread of $\sigma_E \simeq 0.5\%$ and a betatron beam spot of 1 mm, it gives the condition on the dispersion: $\eta < 6$ cm.

4.4.6 Experimental Method

In the early stage of the IRFEL commissioning we attempted both quadrupole scan and multi-monitor methods to measure the emittance. The latter was somehow difficult to implement especially in the undulator region where we experimentally find it difficult to achieve the proper

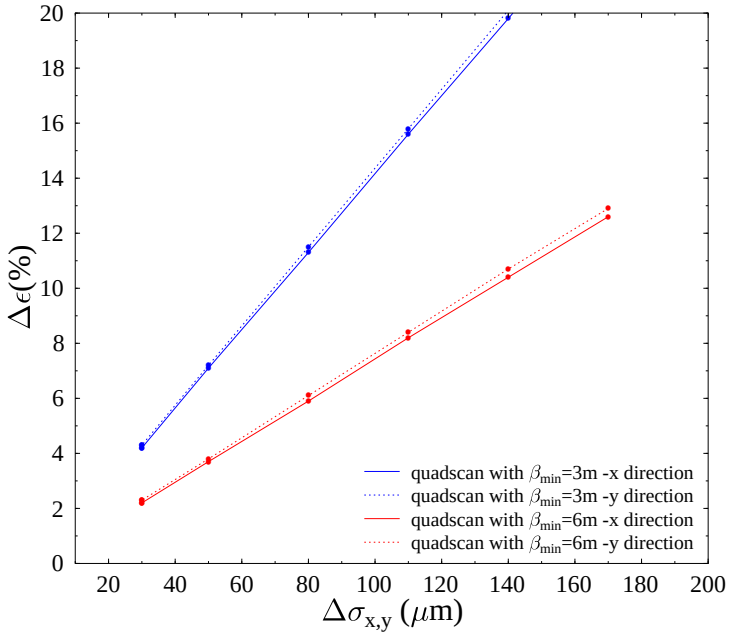

Figure 4.14: Relative error on computed emittance for the two cases presented in figure 4.13 versus the relative error on beam size measurement.

betatron function variation. Because we find we could not reliably set the accelerator optical lattice to achieve desired betatron function variation for optimizing the error bars on the multi-monitor measurements and since we desired to have the same method to measure emittance everywhere in the accelerator, we decided to only use the quadrupole scan technique. We totally automated the emittance measurement by coding the measurement procedure [35], data acquisition and data analysis in a C program with a Tcl/Tk user interface. From this program the user define the quadrupole and viewer she/he desires to use for the measurement and few other parameters. The program then automatically scan the quadrupole strength. For each quadrupole setting, the beam size on the OTR profile monitor, the transfer matrix between the quadrupole entrance and the profile measurement station are computed and stored in a file. Once the program has completed the quadrupole scan, it computes the emittance using the algorithm detailed above. This program can also be used to propagate the beam parameters along the accelerator and observe the beam envelope, useful information e.g. to quantify lattice mismatch.
The program can be divided into three parts: (1) a user interface from which the user enters parameters and read results of data analysis, (2) a machine model, ARTEMIS[8], that is automatically updated to reflect the current accelerator settings (magnet strength, cavity gradient,...); and (3) a control toolbox that contains a series of EPICS-protocol sequences used to control the machine subsystems (i.e. vary quadrupoles, insert transition radiation screen into the beam path,...).
A typical emittance measurement, performed in the backleg transport line for a charge per bunch of 40 pC, using the quadrupole scan method is presented in figure 4.17. It shows the variation of

[8]the on-line Model Server Artemis was implemented in the FEL by Sue Witherspoon and Bruce Bowling

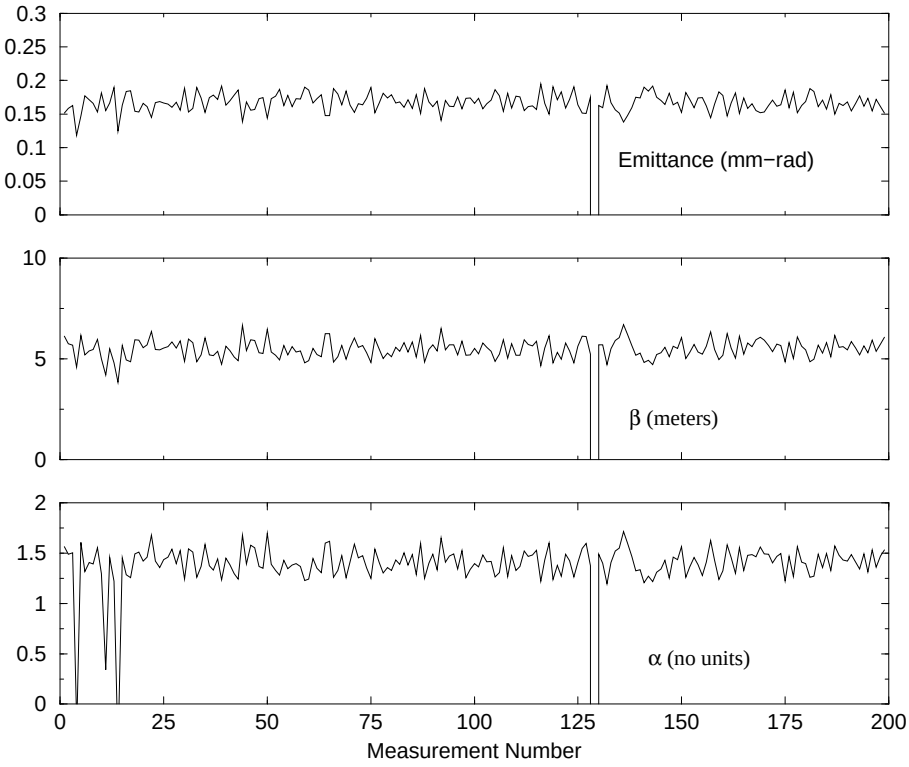

Figure 4.15: Monte-Carlo simulation of 200 emittance measurements. The plots (from top) are the un-normalized rms emittance, the β-function, the α parameter.

beam spot size versus the quadrupole excitation.

4.5 Measurement of Emittance in the Injection Transfer Line

The envelope fitting technique exposed in the previous section relies on the validity of single particle dynamics. In the Injection transfer line, the beam energy is approximately 10 MeV in this regime, the space charge collective force (i.e. Coulombian repulsion between electron in the bunch) are significant for a 60 pC charge per bunch. Therefore, the beam envelope cannot be propagated using the single particle formalism based on transfer matrix. In the case where space charge forces are significant the beam envelope must be described with a differential equation: the Sacherer rms envelope equation [37]. Propagation of the beam through a magnetic element then requires the integration of this equation; generally speaking this integration has to be performed using numerical methods but in some case one can use perturbative theory to find good approximation of the envelope. In any case the envelope fitting are difficult for characterizing, e.g. measuring emittance, of such space-charge-dominated beam. An alternative method is based on the so called phase space sampling techniques [36]. This latter type of measurement can also be used to directly measure the trace-space density.

The technique consists of intercepting the space-charge-dominated beam by a series of apertures 4.18. The beamlet generated by each aperture retains the transverse temperature of the beam. It is drifted through a free space up to a beam profile monitor. The drift length is chosen so

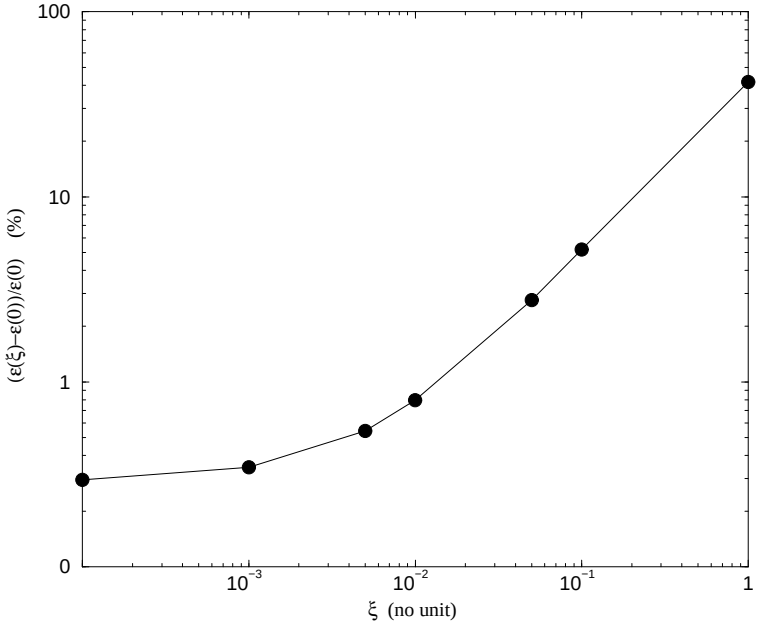

Figure 4.16: Relative emittance error versus dimensionless spurious dispersion contribution to beam size ξ.

that the transverse momentum imparts a significant contribution to the transverse profile. Hence the measure of the beamlet profiles on the uncorrelated transverse momentum spread.
The differences among the various apparatus based on this interceptive technique is the shape of the selecting aperture (hole, slits or matrix of aperture), and the kind of profile monitor used downstream to analyze the beamlets (wire-scanner, fluorescent viewer, optical transition radiation screen).
In the present case, the selecting aperture we chose is composed of parallel slits [38] that samples the beam in the direction we wish to perform the measurement. This choice was essentially done to perform very fast measurement with a simple and robust data reduction algorithm.
Mathematically, the effect of the slits can be seen as a sampling: If before the slits the density in the spatial plane (x, y) is $\int\int \rho_4(x, x', y, y')dx'dy'$, where $\rho_4(x, x', y, y')$ is the four dimensional trace space density, then the projection in the x-x'-plane after the slits is:

$$\sum_{i=1}^{i=n} \int_{x_i - w/2}^{x_i + w/2} dx \rho_2(x, x') \simeq \sum_{i=1}^{i=n} w \rho_2(x_i, x') \tag{4.45}$$

where n is the number of slits.
If the projection is observed after a drift of length L, the multi-beamlet profile is:

$$\Phi(\xi) = \sum_{i=1}^{i=n} w \rho_2(x_i, \xi/L) \tag{4.46}$$

where ξ is the horizontal coordinate in the beamlet observation plane. It is instructive to consider the simple case of a normal distribution in the trace-space:

$$\rho_2(x, x') = \frac{1}{\sqrt{2\pi N}} \exp\left[-\frac{\gamma_T x^2 + 2\alpha_T x x' + \beta_T x'^2}{2\tilde{\varepsilon}^2} \right] \tag{4.47}$$

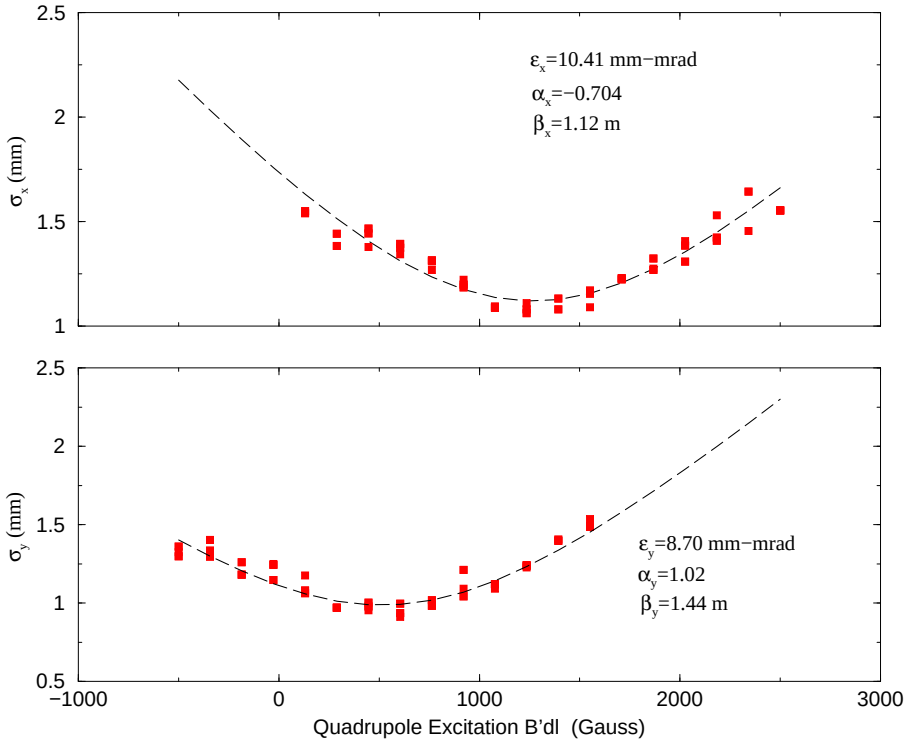

Figure 4.17: An example of transverse emittance measurement in the high energy region of the IRFEL using quadrupole scan method. The two plots present variation of the horizontal (top) and vertical (bottom) rms beam size versus the excitation of the quadrupole. The dashed lines are obtained with the least square fit technique. The reported number are the beam parameters deduced from the fit. The charge per bunch was approximately set to 40 pC.

where N is the number of particles in the beam. For such a distribution, the projection writes:

$$\Phi(\xi) = \frac{Nw}{2\pi}\sum_{i=1}^{i=n} \exp\left[-\frac{4\gamma\alpha^2}{\gamma^2 L^2 \tilde{\varepsilon}}\left(\frac{\gamma^2}{2\alpha}x_i + \xi\right)^2\right] \exp\left[-\frac{1}{\gamma\tilde{\varepsilon}L^2}\xi^2\right] \tag{4.48}$$

Hence each beamlet width yields a measure of the width of the transverse divergence at the corresponding slit (i.e. uncorrelated divergence), whereas the beamlets centroids give information on the slope of the transverse phase space (i.e. the correlated divergence distribution).
As we underlined previously, one advantage of such device is to be able to measure the emittance of a space-charge-dominated beam. In fact, in the Eqn.(4.46) the replacement of the divergence x' by ξ/L is permitted provided the beamlets can be first-order transported. Otherwise the divergence should include the angular spread Ψ_{SC} induced by space-charge force:

$$\xi = Lx' + \int ds \frac{d\Psi_{SC}}{ds}(s) \tag{4.49}$$

If the incoming beam on the multislit mask is emittance-dominated, Ψ_{SC} will be insignificant with respect to x'. However, in the case of a space-charge-dominated incoming beam, the slits width should be optimize so that the beamlets become emittance-dominated.
A criterion to determinate the needed slit width can be derived by introducing the Debye length λ_D, a fundamental parameter in Plasma Physics that can also be by applied to Beam Physics:

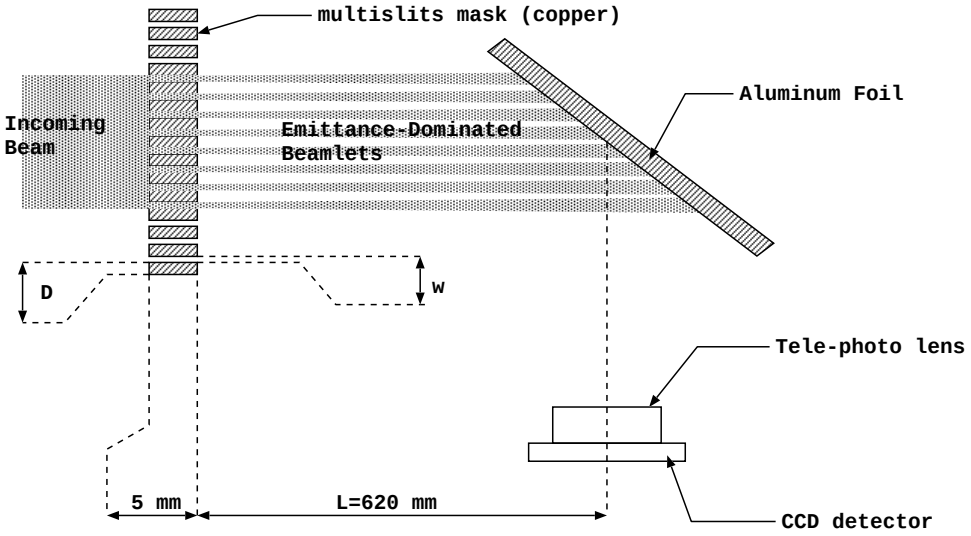

Figure 4.18: Overview of the phase space sampling technique. An incoming A multislit mask intercepts the incoming space-charge-dominated beam. The beamlets issued from the slits are emittance-dominated.

qualitatively, this length characterize the region centered around a test particle in which the potential introduced by this test particle is screened due to reorganization of the neighbor charges. For an electron beam, λ_D writes

$$\lambda_D = \sqrt{\frac{\epsilon_0 \gamma k_B T_b}{e^2 n}} \tag{4.50}$$

where γ is the Lorenz factor, k_B the Boltzman constant, T_b the beam temperature, measured in the beam reference frame, n the particle density and ϵ_0 is the dielectric constant of vacuum. Depending on the magnitude of λ_D versus the inter-distance particles within the beam l_{inter} and the beam size σ, there are two main regimes:

- If $\lambda_D > \sigma$ the Debye screening will be ineffective and single particle dynamics will dominate
- In the case $\lambda_D < \sigma$ the collective effect due to self-field play an important role. Depending on the Debye length compared to the inter-particles distance: If $\lambda_D > l_{inter}$, smooth function for the charge and the self-field may be used; If $\lambda_D \simeq l_{inter}$ then a particle is more sensible to its nearest neighbors than to the collective field of the beam distribution as a whole.

Therefore transverse space-charge contribution is insignificant if $\lambda_D >> \sigma_{eq}$, σ_{eq} being the equivalent beam radius ($\sigma_{eq} = [\sigma_x \sigma_y]^{1/2}$). For the simple case of a K-V distribution the transverse temperature is given by [41]:

$$k_B T_b = \frac{8mc^2 \tilde{\varepsilon}_n^2}{\sigma_{eq}^2} \tag{4.51}$$

Where $\tilde{\varepsilon}_n$ denotes the normalized emittance.
Introducing the Alfvén current $I_A = \frac{4\pi\epsilon_0 mc^3}{e}$, the peak current $I_p = \frac{Ne\beta c}{\sigma_z}$ (with σ_z being the bunch

length and N the number of particles within a bunch $N \simeq n\sigma_{eq}^2\sigma_z$) yields for the expression of the Debye length:

$$\lambda_D^2 = \frac{2\beta\gamma\tilde{\varepsilon}_n^2}{\pi}\frac{I_A}{I_P} \tag{4.52}$$

Hence a measure of the degree of self-field dominance over single particle dynamics is deduced from the ratio $\mathcal{R} = \sigma_{eq}^2/\lambda_D^2$:

$$\mathcal{R} \simeq \frac{I}{2I_A} \times \frac{\sigma^2}{(\beta\gamma)(\tilde{\varepsilon}_n^2)} \tag{4.53}$$

where σ is the beam size (assumed to be round).
Collimating the beam with a slit will scale $\mathcal{R}$ by η, defined as the ratio of the slit rms-width $(\delta/\sqrt{12})$ to the rms-beam size σ:

$$\begin{aligned} \sigma &\longrightarrow \eta\sigma \\ I &\longrightarrow \eta^2 I \\ \varepsilon &\longrightarrow \eta\varepsilon \end{aligned} \tag{4.54}$$

Therefore, in the case of a round beam, and under the assumption $\eta << 1$ the space charge to emittance ratio follow the scaling law:

$$\mathcal{R} \longrightarrow \eta^2\mathcal{R} \tag{4.55}$$

Hence with an estimate of the beam size at the location of the slits, it is straightforward to choose the slits width to minimize the space charge contribution to the beam envelope.

4.5.1 Design of the slits assembly

Overview

The final design of the multislit assembly has two sets of thirteen slits that allow x and y transverse-emittance measurement. When the slits are removed from the beam path, a radio-frequency shielding insures beam-pipe continuity to minimize the wakefield impedance, an important parameter for such high charge (up to 135 pC) ultra-short (< 8 ps) bunch in the injection line. The slits have been machined with a numeric command milling machine, after unsuccessful attempt on traditional milling machine.

Choice of the geometrical parameters

To determine the characteristic parameters for the slit, namely the slits width w, the slits spacing d, and the distance L between the slits assembly and the screen, we writes the three following conditions:

- The Reduction of the Space Charge condition:
  This condition is directly deduced from ratio of space charge term and emittance contribution in the K-V equations exposed previously in this note. If u is the considered direction (u=x or y), the ratio $\mathcal{R}'_u$ after the slits writes:

$$\mathcal{R}'_u = \mathcal{R}_u \times \left(\frac{d}{\sqrt{12}\sigma_u}\right)^3$$

- The non overlapping condition:
  The observed pattern in the screen, as we already show, consists in peaks associated to each slits. We must insure in choosing the drift length L and δ that the peaks do not overlap, i.e.:

$$4\sigma_u L < d$$

- The resolution condition:
  To optimize resolution on the emittance, we must have the same resolution on the spatial axis and on the angular axis. Introducing the transverse resolution of the detector R (which is assumed to be the same in x and y direction), we must satisfy:

$$\frac{\sigma}{d} = \frac{L\sigma'}{R}$$

  This relationship can simplify if we are at a beam waist to:

$$d = \beta \times \frac{R}{L}$$

For a design normalized emittance of about 8 mm-mrad at 135 pC, we determined from the previous set of conditions, the geometric parameters of the multislits should be approximately:

$$w \simeq 50\,\mu\text{m}$$
$$d \simeq 1\,\text{mm}$$
$$L \simeq 55\,\text{cm}$$

In fact due to mechanical constraint $L =$ was set to 620 mm . Also we wish to measure the emittance over a dynamic range going from approximately 3 mm-mrad up to 20 mm-mrad. For this reason we optimized the slits' geometric parameters with the PARMELA code. Using this code we retraced 3000 macroparticles through the whole injector for different set of parameters (w , d, L). From the so generated trace-space at the multislit mask, we generated via a monte-carlo method over 100000 particles and use linear transfer matrix to retrace each of them up to the transition radiation viewer (such large number of particle was needed since the transmission of the multislit mask is only of the order of 5%). A typical simulated OTR-image is shown in Figure 4.19. We used this particle distribution in the *x-y* plane to try to reconstruct the phase space and calculate the transverse emittance using an algorithm that will be detailed later. We gather for the different set we studied, the measured emittance in Table 4.6. From these simulations we retained as design parameters for the apparatus w=75 μm and d=1.5 mm; for these specific parameters we have simulated the error on the computed parameters and insured the emittance and Twiss parameters can be computed within 15% accuracy (assuming 5 beamlets can be generated). We also compare the reconstructed phase-space obtained after simulating the measurement, with the initial phase-space generated with PARMELA in figure 4.20. This reconstructed phase-space iso-contour represents with accuracy the macroparticle phase-space distribution of PARMELA.

$\tilde{\varepsilon}_n$ (mm-mrad)	w=100 μm d=2 mm	w=100 μm d=1.5 mm	w=75 μm d=1.5 mm	w=50 μm d=1.0 mm
3.4354	19.56	14.93	13.27	9.66
6.8709	3.12	20.38	18.26	10.17
20.6127	9.91	7.96	5.79	41.24

Table 4.6: Typical error in percent on the computed emittance for different set of parameters (d,w) and for various emittance.

4.5.2 Mechanical Considerations

In order to avoid using any cooling system, we have opted to make the slits out of copper and have a thermal bridge that quickly dissipates the heat toward the exterior of the vacuum chamber. In order to reduce the deposited power below the damage threshold of 3 W we will use a low duty factor beam mode for emittance measurement, which is possible since the physics of our beam is only dominated by single-bunch effects (bunch spacing is 8.02 m). The multislit mask thickness is a compromise between noise and angular acceptance: if the mask is not thick enough, electrons that go through copper can contribute to the OTR pattern. On the other hand, increasing the thickness would imply more stringent tolerance on the slit alignment with respect to the beam axis.
For 10 MeV electron ($\gamma \simeq 20$), the main process of interaction with matter is ionization, bremsthralung being the second main process. In the case we only consider the ionization process we can have an estimate of the stopping power knowing the $\frac{dE}{dx}$:

$$\mathcal{L}_s = \frac{E}{dE/dx} \tag{4.56}$$

E is the incident kinetic energy in MeV, dE/dx for copper is about 12.5 MeV/cm yielding a stopping power of about 8 mm. Practically we do not need a such thick support because (i) of the energy losses due to bremsthralung production and (ii) the multiple-Coulomb scattering of the electron on the copper nuclei. The latter phenomenon spread the beam angular divergence, it can be quantify using the Molière theory: according to this model, the scattering distribution can be approximate with a normal curve whose standard deviation is given by [42]:

$$\Theta_0 = \frac{13.6}{\beta cp}\sqrt{\frac{X}{X_0}}\left(1 + 0.038 \ln \frac{X}{X_0}\right) \tag{4.57}$$

X is the material thickness, X_0 its radiation length (1.43 mm for copper), and p is the momentum in MeV/c of the incident electrons. A thickness of 5 mm was chosen; this implies $\Theta_0 \simeq 800$ mrad this number is much larger than the angular acceptance of the viewer ($\phi = \frac{15}{620} \simeq$24 mrad). Therefore the electron passing through the copper plate will only contribute in the beamlet analysis plane as a uniform background.
On the other hand, setting the thickness to 5 mm yields an angular alignment tolerance of approximately 1.7 mrad. For this incidence angle, only 10% of the electrons are lost because of edge scattering (see Fig. 4.21). Alignment of the multislit mask within this tolerance can be done easily, furthermore, using downstream magnetic steerers it is also possible to adjust the electron beam incidence angle to correct for eventual misalignment.

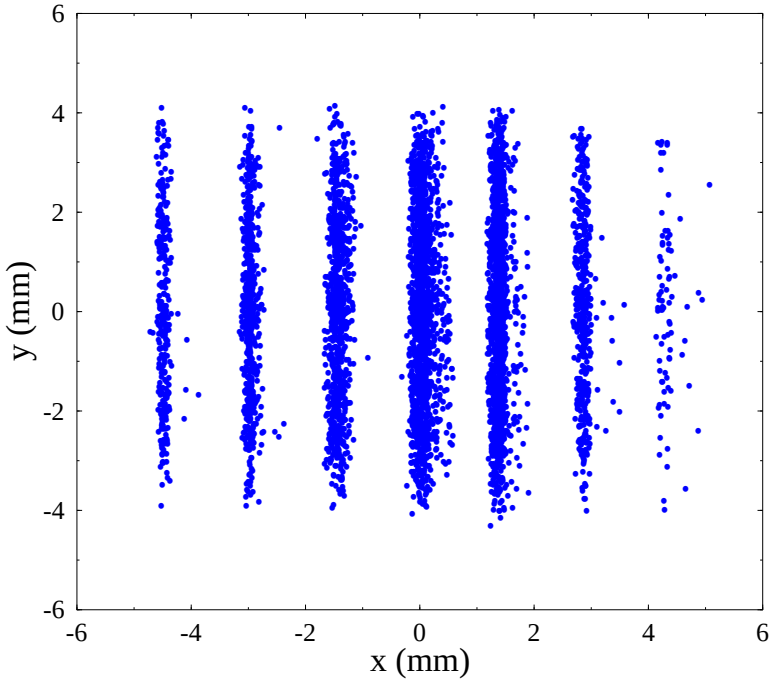

Figure 4.19: Simulated multi-beamlets pattern on the optical transition radiation radiator

4.5.3 Emittance Calculation & Trace-Space Reconstruction

From the OTR image of the multi-beamlet pattern, a projection is generated. This projection consists, as we have previously discussed, in a suite of peaks. Each peak is automatically identified using a "recognition algorithm" [39].
From the projection, the beam average position $\langle x_B \rangle$ can be calculated and used as the reference for x-axis. The beamlets are then referenced to a slit and thereby to a position (with respect to the beam average position) accordingly to:

$$x_i = w \times i - \langle x_B \rangle \tag{4.58}$$

where i is an index that can be positive or negative and identify the slits and w is, as previously, the slits width.
Measuring the average position of each beamlet also give information on the correlated spread in the divergence which in turn give information on the α-Twiss parameter. Form the beamlet distribution $w_{i,j}$ we can deduced the beam divergence distribution x'_j at the specific position x_i using the relation:

$$x'_j = \frac{\xi_j - x_i}{L} - \langle x'_B \rangle \tag{4.59}$$

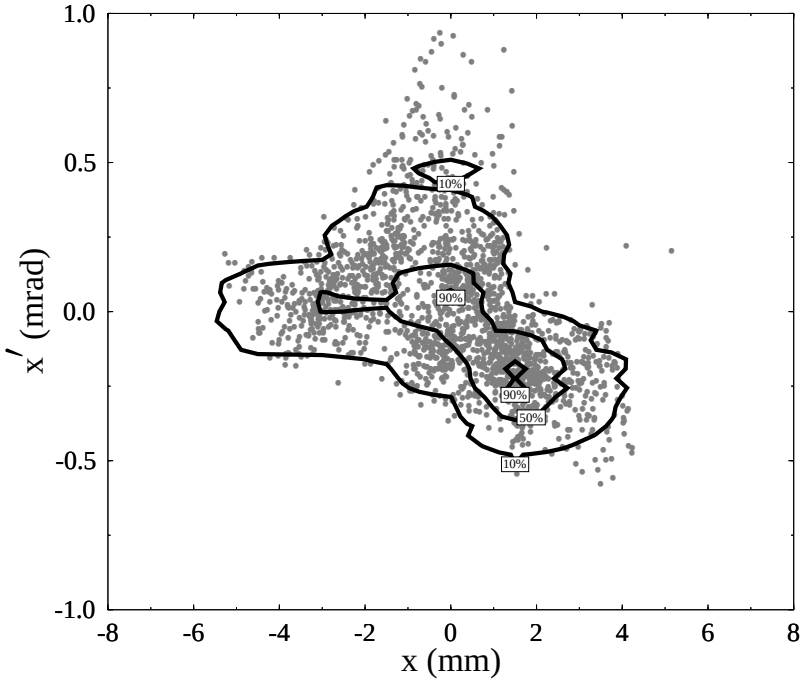

Figure 4.20: Comparison of the expected phase-space, generated via particle retracing (each grey dots represent a macroparticle), with the retrieved phase-space (represented with back line iso-contours) using the simulated beam pattern on the optical transition radiation presented figure 4.19

where $\langle x'_B \rangle$ is the average divergence of the beam computed from the beamlet: $x'_B = \frac{\sum_i \sum_j w_{i,j} x'_j}{\sum_i \sum_j w_{i,j}}$. From all the previous calculations it is then straightforward to compute the emittance and Twiss parameters:

$$\begin{aligned} \langle x^2 \rangle &\simeq \frac{\sum_i x_i^2 \sum_j w_{i,j}}{\sum_i \sum_j w_{i,j}} \\ \langle x'^2 \rangle &= \frac{\sum_i \sum_j x_j'^2 w_{i,j}}{\sum_i \sum_j w_{i,j}} \\ \langle x x' \rangle &\simeq \frac{\sum_i x_i \sum_j x'_j w_{i,j}}{\sum_i \sum_j w_{i,j}} \end{aligned} \tag{4.60}$$

As we already pointed out it is also interesting to have access to the trace-space distribution. The trace-space distribution iso-contour can be deduced from the beamlet profile since this latter corresponds to sample of the distribution in position ($\rho_2(x_i, x')$). Unfortunately under normal operation the number of sample in position does not exceed 5 and therefore some fine detail on the distribution could be missed. Indeed it is possible to move the beam on the multislit mask by means of upstream magnetic steerers, and for each setting of this magnet record the beamlets' projection. In such a case it is possible to fill the trace-space completely; of course this rely on a perfect stability

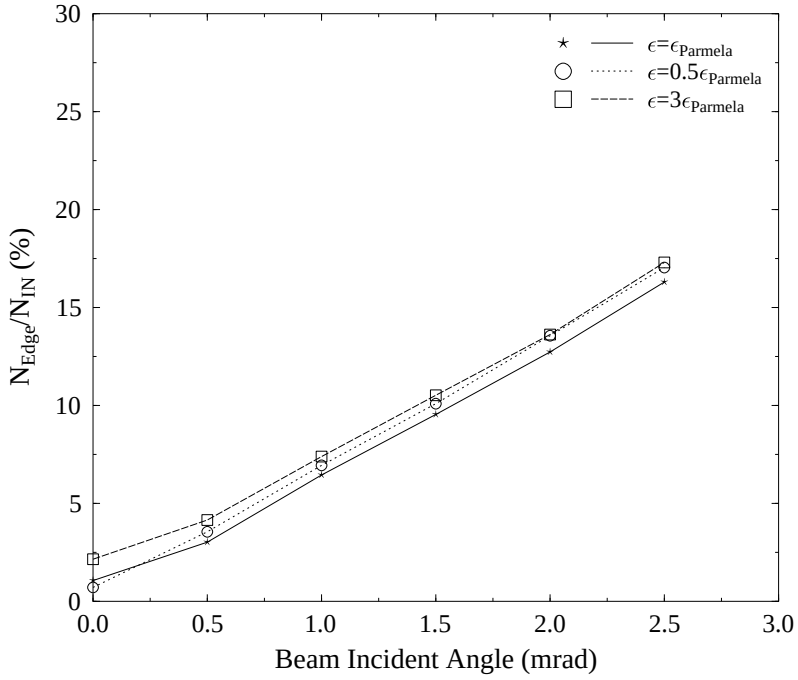

Figure 4.21: Fraction of incident electron that scatters on the slits edge versus the beam incident angle with respect to the normal axis of the multislit mask. The depth of the slits is 5 mm. A misalignment of the mask of 1.2 mrad compare to the beam axis yields approximately the interaction of 10% of the incident electron with the material.

of the electron beam.

The acquired data, in our case a projection that contains the beamlet profiles, is digitized by the frame grabber and then transferred to an IOC on which VxWorks routines have been implemented [39]. After identifying each beamlet profile and the slit it comes from, the code computes the emittance and Twiss parameters. The results can then be accessed from any X-station via the EPICS channel-access protocol. We developed X-window based screens that display emittance, Twiss-parameters and possibly phase-space isocontours. The achieved speeds are, respectively, about 1 and 2 sec for updating parameters and plot refresh, a speed that allows observing the phase space parameters in real time while tuning the injector. Storing raw data and projections is also possible at each stage of the process for more detailed off-line analysis, e.g. using (time and CPU consuming) powerful image processing tools.

$\tilde{\varepsilon}$	$\Delta\tilde{\varepsilon}/\tilde{\varepsilon}$ (%)	$\Delta\beta/\beta$ (%)	$\Delta\alpha/\alpha$ (%)
0.2040	19.9	19.9	20.9
0.3956	9.9	9.9	10.4
1.1597	2.5	2.6	2.6

Table 4.7: Typical systematic error on emittance and Twiss-parameters for the nominal emittance value and two extreme cases.

4.5.4 Error Analysis

Error Propagation

The error propagation is quite tedious to perform analytically since direct calculations require a lot of approximation and assumptions, especially since the trace-space distribution does not a priori follow any kind of analytical function. For these reasons we perform this error propagation numerically. Following previous derivation [45], it is straightforward to compute the systematic error on the rms-emittance as a function of the second-order moments:

$$(\Delta\tilde{\varepsilon})^2 = \frac{1}{\tilde{\varepsilon}^2} \times \left(\langle x x' \rangle^2 \left(\Delta\langle x x' \rangle\right)^2 + \left(\frac{\langle x'^2 \rangle^2}{4} \right)^2 \left(\Delta\langle x' \rangle\right)^2 \left(\frac{\langle x^2 \rangle^2}{4} \right)^2 \left(\Delta\langle x \rangle\right)^2 \right) \tag{4.61}$$

The error on the $\langle x x' \rangle$ is given by:

$$\left(\Delta\langle x x' \rangle\right)^2 = \frac{\sum_i \left[\sum_j w_{i,j}^2 x_i^2 (\Delta\langle x' \rangle)^2 + \sum_j w_{i,j}^2 \langle x' \rangle_i^2 (\Delta x)^2 \right]}{\sum_i \sum_j w_{i,j}} \tag{4.62}$$

Where the uncertainty on the average the divergence is simply $\Delta\langle x' \rangle \simeq \Delta x'$. The error on $\langle x^2 \rangle$ is:

$$\Delta\langle x^2 \rangle = \frac{\sum_i \left[2 \sum_j w_{i,j} \Delta(x'_j) \right]^2}{\sum_i \sum_j w_{i,j}} \tag{4.63}$$

Similarly, the error on $\langle x'^2 \rangle$ writes:

$$\Delta\langle x'^2 \rangle = \frac{\sum_j \left[\sum_i 2 w_{i,j} \Delta x'_j \right]^2}{\sum_i \sum_j w_{i,j}} \tag{4.64}$$

Where the error on the divergence is estimated to $\Delta x' = \frac{1}{L}\sqrt{\delta^2 + \frac{D^2(\Delta L)^2}{L^2}}$ where δ, the resolution of the OTR monitor ($\simeq$60 μm), has been added in quadrature. The uncertainty on the drift length ΔL, is approximately 5 mm. All the previous formulae have been gathered in a program that allows to compute errors on different sets of data. Typical uncertainties associated with the emittance and Twiss parameters are presented on Table 4.7 for the nominal expected emittance and two extreme cases; as expected, this error increases as the emittance value decreases.

Other Source of Errors

As mentioned in reference [44], the slits (directed along y axis) will reduce the x-transverse space-charge field. this effect is due to the fact that when an electron bunch get very close to the slits

(say one bunch length), the transverse self field is short-circuited. This effect is considered to be insignificant in our experiment.
Another source of error is the effect of non-zero space-charge force in the beamlets. Such effect has been studied numerically for the maximum charge per bunch (135 pC) and was observed to enlarge the beamlets width on the OTR-monitor by approximately 12 μm (4-σ). This enlargement is less than the resolution of the monitor and therefore is neglected.

4.5.5 First Experiment in the Injector Test Stand

We chose to commission the multislit assembly in the injector test stand (ITS) of Jefferson Lab since this off-line facility was instrumented with another emittance measurement system that we could use to compare the results obtained with the multislit mask. The configuration consists in a photocathode gun, a solenoid, and a diagnostic beamline than incorporates a transverse emittance measurement based on the one-slit and wire-scanner method [14]. The gun energy can be vary up to 500 keV and the maximum available charge can be set to approximately 135 pC. Since the mask acceptance is ranging from 0.6 mm-mrad to 1.1 mm-mrad (unormalized rms emittance) we had to lower the charge per bunch accordingly to PARMELA numerical simulations to achieve an adequate emittance; initially the charge was vary from 5 pC up to 10 pC to perform our test. The gun energy was arbitrary set to 250 keV.

Preliminary test and cross check with the monoslit method

As mentioned above, the injector test stand is equipped with one-slit and wire-scanner apparatus to perform very accurate emittance measurement for a wide range of charge. The technique is, as the multislits, based on phase space sampling method: a movable slit selects a position and the generated emittance-dominated beamlet is analyzed downstream by the mean of a wire scanner profile monitor. The advantage of this "one slit and collector" technique is its ability to resolve the phase space distribution for a wide dynamical range in emittance by adjusting the slits positions steps. Such system has been successfully used to fully characterize the emittance of the beam produced out of the photoemission gun. Unfortunately this method is time consuming: the time required to perform one emittance measurement is typically 45 mins and therefore rely on the assumption of perfect beam stability over this time. During our tests we find the beam not so stable over this large time.
For a first test, we set the charge to 10 pC and acted on the solenoid strength (the only parameter on which we can play on-line) to try to illuminate with the electron beam as many slits as we could. Unfortunately because of technical problem we were only able to illuminate up to four slits. A typical beamlets profile obtained performing our tests is presented in figure 4.22 along with a typical reconstruction of trace-space whose iso-contour density plot is pictured in figure 4.23.
The table 4.8 presents the results of our cross check between the two methods. Both technique agrees at the 15 percent level.

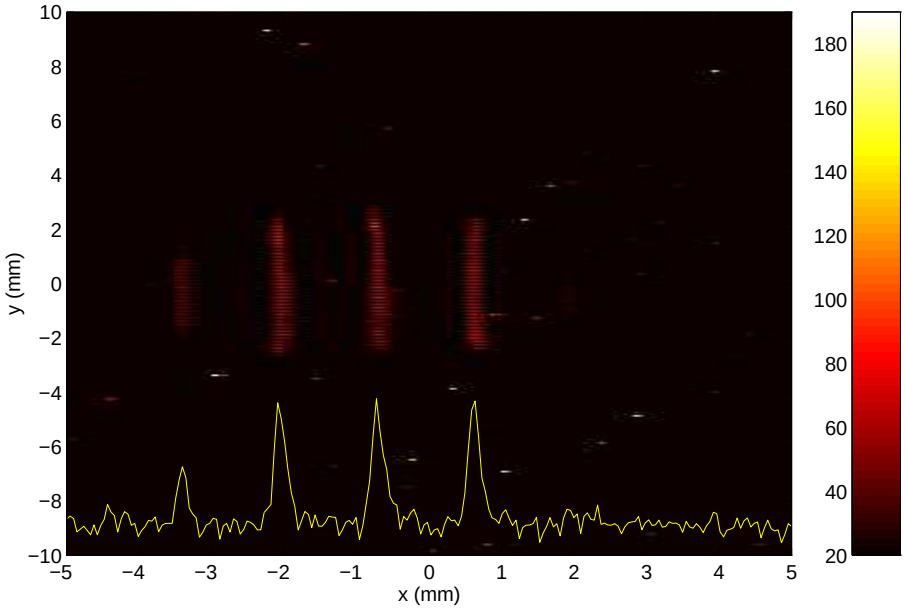

Figure 4.22: An example of 2D beam distribution on the analyzer screen downstream the multislit mask. The projection onto the x-axis is also displayed.

$\tilde{\varepsilon}_x$ (mm-mrad) multi slit method	$\tilde{\varepsilon}_x$ (mm-mrad) one-slit-one harp method	Difference (%)
0.5594	0.4859	15
0.5607	0.5070	11
0.4669	0.5071	8

Table 4.8: Comparison of the rms transverse emittance measurement performed with the multislits and the one-slit and one-harp techniques.

Measurement of Emittance in the Injector Test Stand

We then varied the solenoid strength from 237.5 G up to 307.5 G to see how was evolving the emittance value for different settings of the first solenoid. The emittance presents a gap at values around 280 G (see Fig. 4.24) as observed in numerical simulation. The β-function presents as expected a minimum corresponding to the beam waist. Charge was varied using the laser attenuator and the bunch charge was measured using a beam dumped equipped with a Faraday cup. As it can be seen in figure 4.25 below, the emittance was found to be dependent on the macropulse width. In fact this was due to problem with the optical switch of the photocathode laser yielding a light leak creating low emittance "ghost pulses": extinction ratio (ratio between the intensity of the light at the output of the switch when it is close or open) was not optimized and then even when closed, the number of photon was still high enough to produced unwanted electrons (see our comment in Chapter 1). The number of produced electrons depends on the selected width for the macropulse.

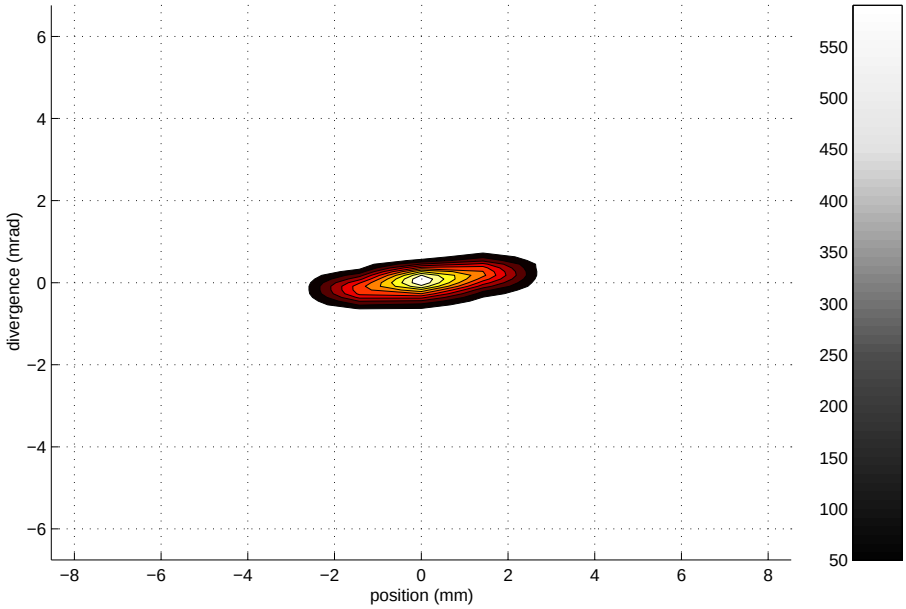

Figure 4.23: An example of reconstructed phase space iso-contour density.

4.6 Summary

In this chapter we have presented the techniques we have developed to perform emittance measurement in the injector transfer line, a region where the beam is still in the space charge regime, and in the 38+ MeV linac and recirculation region. We have shown that under the expected experimental condition both measurement could be performed with systematic error of the order of 10%.

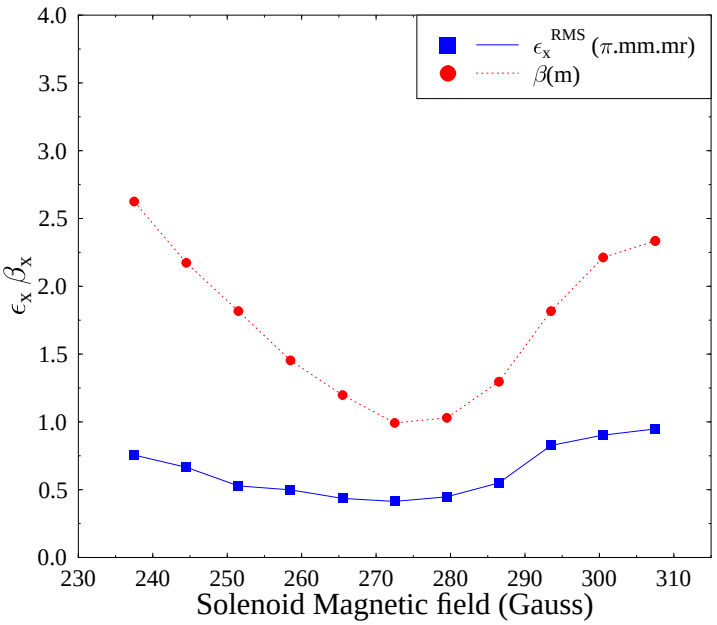

Figure 4.24: Emittance and betatron function versus the solenoid excitation.

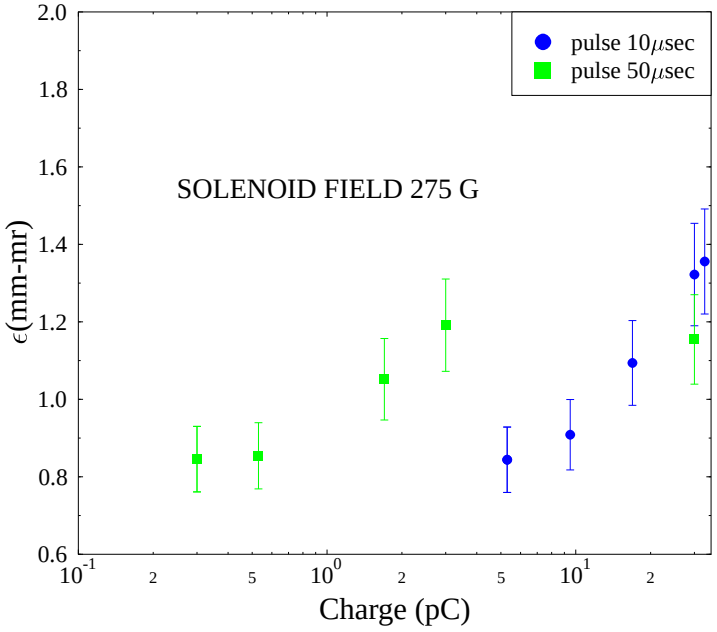

Figure 4.25: Emittance as a function of the charge per bunch for two different macropulse width (10 μsec and 50 μsec).

Chapter 5

Longitudinal Phase Space Characterization

5.1 Introduction

As mentioned earlier, in Chapter 2, the FEL gain strongly depends on the bunch length and energy spread achieved in the vicinity of the undulator magnet. Hence it is of prime importance to properly instrument the driver-accelerator in order to measure these quantities at critical point of the bunching stage.
The bunching process, along the beam transport, is controlled by several elements: a warm buncher cavity, SRF-cavities located in the injector and in the main linac, and the injection and by-pass chicanes. In order to make sure the bunching process is performing adequately, it is worthwhile to have many longitudinal diagnostics that can provide information on how the bunching is performing. Also they can be useful to identify at which stage the bunch dynamics is not as expected and therefore can allow to isolate a problem or monitor drifts in the system. For such a purpose several diagnostics have been developed. These diagnostics include frequency domain methods, which consists in estimating the bunch properties by detecting coherent radiation emitted from the bunch, and time-based methods.
Along with bunch length measurement, the longitudinal phase space emittance can be estimated, under certain conditions, provided one can measure the intrinsic energy spread.
Both measurements are described in this chapter, after discussing the longitudinal phase space manipulation in the driver accelerator.

5.2 The Longitudinal Phase Space Manipulation in the IRFEL

In the IRFEL, bunch formation starts at the electrons' emission from the photocathode which is illuminated by a driver-laser whose optical pulse is approximately 47 psec (FWHM), as measured by autocorrelation technique [1]. Therefore at the cathode surface, the electrons are gathered in bunch of approximately 47 psec (FWHM), if we ignore the bunch lengthening due to the GaAs wafer time

[1] M. D. Shinn, private communication

response. The evolution of the longitudinal phase space from the electron bunch emission up to the end of the magnetic decompressor is best described in terms of sequences of PARMELA runs shown in figure 5.1. In the following we only concentrate on the case of 60 pC charge per bunch with lasing turned off.

1. The length of the electron bunch after emission via photoelectric effect and acceleration to 350 keV in the DC-gun structure is approximately 15 ps (RMS) (see Fig. 5.1(A)).

2. The first element that significantly affects the longitudinal bunch distribution is the buncher cavity. This cavity is operated at zero-crossing so that the average arrival time of the bunch coincides with a zero accelerating field. The electrons arriving sooner (i.e. that belong to the bunch head) are decelerated whereas the late electrons (i.e. that are located in bunch tail) are accelerated (see Fig. 5.1(B)). Hence the principal effect of this cavity is to provide an energy ramp across the bunch. This energy modulation translates as the bunch propagates though a drift space to a "bunching" of the electrons: because of the electrons' average energy of approximately 350 keV, which make them nonrelativistic, their propagation in a drift space of appropriate length will bunch the electrons (mathematically this traduces to the nonzero value of the momentum compaction of a drift space of length L: $R_{56} = -L/\gamma^2$).

3. After drifting through a longitudinally free space, the bunch enters the first accelerating five-cell CEBAF-type SRF-cavity with a nominal average accelerating gradient of 11 MV/m. The cavity is operated for maximum energy gain (which does not mean, because of the non-relativistic nature of the electron, that the bunch is injected in phase with the maximum accelerating electric field). There is a strong compression occurring in the first two cells of the cavity (that acts as a capture section), then the bunch length is frozen and remains constant up to the cavity exit while the relative energy spread is greatly reduced.

4. Approximately 7 cm after the exit of the previous cavity, the bunch enters a second SRF-cavity with a nominal average accelerating gradient of 9 MV/m. This cavity is operated off the maximum energy gain phase, so that it provides further bunch compression. Indeed the choice of the phase is made to impress the longitudinal phase space with the proper slope needed to match the slope desired at the entrance of the upstream achromatic chicane for optimum bunching through this chicane. At the cavity exit, the parameters are: 1.2 ps for the bunch length, 4% for the relative energy spread and approximately 10 MeV for the beam average energy.

5. The electrons then drift through an achromatic three-bend chicane. This latter can reduce the bunch length by means of magnetic compression that is based on the fact that path length inside bends is energy dependent.

6. Then the bunch is injected in the SRF linac. The gradient of each cavity and the overall phase of the linac is adjusted to give precisely the desired energy (which will determine the FEL wavelength) and to adjust the incoming bunch length and energy spread in the compressor chicane.

7. The compressor chicane will compress the bunch down to 120 μm (RMS) to achieve the minimum bunch length at the wiggler location.

8. After the wiggler a second chicane that acts as a decompressor chicane lengthens the bunch length.

9. The beam is then recirculated.

The beam dynamics in the recirculation will be described later. In the present chapter we only concentrate on the beam parameters in the undulator vicinity, which are of importance to startup of the FEL process and quantify few of its properties.

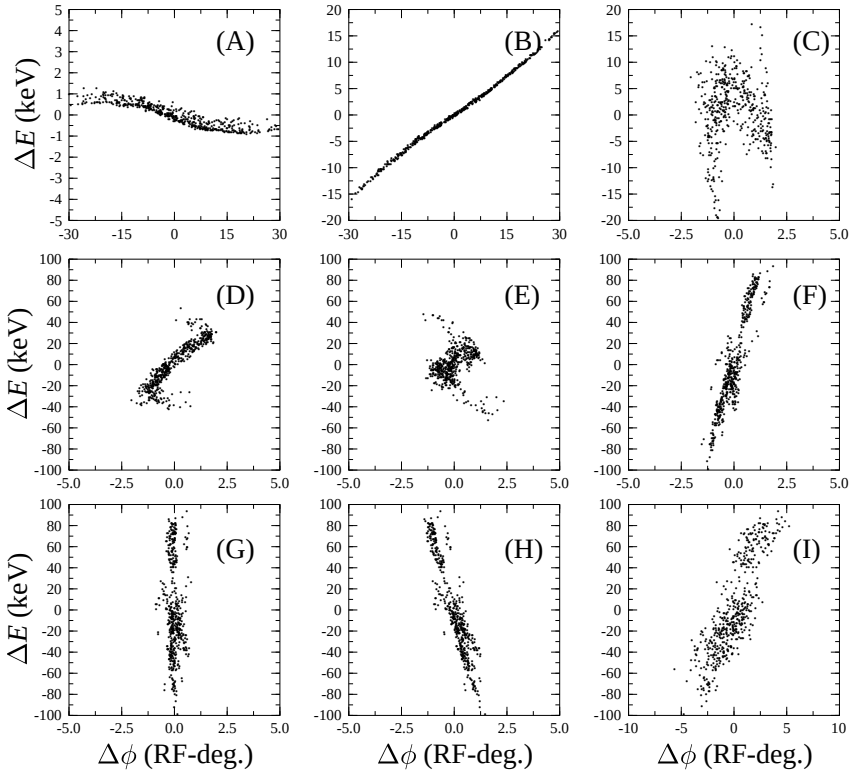

Figure 5.1: Sequences of PARMELA runs demonstrating the bunching process in the IR FEL. The longitudinal phase space is plotted at the exit of the gun **(A)**, the buncher **(B)**, the SRF-cavity #1 **(C)**, the SRF-cavity #2 **(D)**, the achromatic chicane **(E)**, the SRF-linac **(F)**, the bunch compressor chicane **(G)**, the bunch decompressor chicane **(H)**, the arc # 1 **(I)**. Note that electrons with positive $\Delta\phi$ belong to the bunch tail while the one with negative $\Delta\phi$ are in the bunch head.

5.3 Theory of Bunch Length Measurement using Frequency Domain

We presented in Chapter 2 the formalism associated to the emission of electromagnetic waves by a multi-particle distribution. We have seen that the total spectral angular power emitted ($d^2P/(d\omega d\Omega)$) by such system has a contribution that is proportional to N^2, where N is the number of electrons in the multi-particle system. This contribution is also proportional to the so called bunch form factor (BFF) $f(\omega, \widehat{n})$ that in turn can be written as the product of two factors named the spatial and angular BFF. In the next section we study both BFFs and show how it is possible from the latter to extract information on the longitudinal bunch distribution.

The Angular BFF

The second term in Eqn.(2.5) in Chapter 2 is the dependence of the coherent emission with respect to the angular beam properties. It is interesting to note that this term is wavelength independent and therefore is not going to influence the spectrum of the radiation: it acts as a multiplicative factor that can reduce the total power emitted by a bunched beam. Its expression from Eqn.(1.5) is:

$$\tilde{A}(\widehat{n}) \stackrel{\text{def}}{=} |\int A(\overrightarrow{\beta})\psi(\overrightarrow{\beta})d\overrightarrow{\beta}|^2 \tag{5.1}$$

It is relatively difficult to evaluate this factor for an arbitrary bunch distribution. However under the assumption of transverse cylindrically symmetric bunches, and introducing the angles $\zeta = \angle(\widehat{n}, \widehat{\beta})$, $\phi = \angle(\widehat{n}_{yz}, \widehat{z})$, $\psi = \angle(\widehat{n}, d\widehat{z})$, and $\theta = \angle(\widehat{n}_{xy}, d\widehat{z})$ it reduces to [2]:

$$\tilde{A}(\theta) = |\int d\psi \int d\phi A(\psi) \frac{\cos\theta \sin\psi \cos\phi - \sin\theta \cos\psi}{\sin\zeta}|^2 \tag{5.2}$$

which in turn can be expressed as a complete elliptic integral (extended from Ref. [2]) if we assume the angular distribution writes as a Gaussian distribution: $A(\psi) = 1/\sqrt{2\pi\sigma'^2} \times \exp(-\psi^2/(2\sigma'^2)$

$$\tilde{A}(\theta) = |\frac{\theta^2}{\sigma'^2} \int_0^{\pi/(2\theta)} x[(1-x)\mathrm{K}(\frac{2x^{1/2}}{1+x}) + (1+x)\mathrm{E}(\frac{2x^{1/2}}{1+x})] \exp[-\frac{\theta^2}{2\sigma'^2}x^2]|^2 dx \tag{5.3}$$

where the complete elliptic integral of the first kind, $\mathrm{K}(u)$, and second kind, $\mathrm{E}(u)$, have been introduced[2]. The numerical integration of Eqn.(5.3) is presented for different RMS width of the angular distribution in figure 5.2. It is noticed that typically this integral is unity in the case where the beam divergence σ' is much smaller than the angle of observation. In the case of transition radiation, the spectral power has its maximum at angles of the order of $\theta \simeq 1/\gamma$ and since the RMS divergence is of the order of $\sigma' \simeq 1$ mrad, we satisfy the relation $\sigma' \ll \theta \simeq 1/\gamma$ for the nominal energy of 38 MeV (i.e. $\gamma \simeq 77$). Henceforth we will assume, except when explicitly mentioned, that this factor is always unity for our typical beam parameters.

The Spatial BFF

The Eqn.(2.5) is written in a vector form. We will work in Cartesian coordinates to make this equation more explicit. If $\widehat{n}_{yz}$ is the projection of the $\widehat{n}$ unity vector in the (y,z) plane, let $\theta = \angle(\widehat{n}, \widehat{z})$ and $\phi = \angle(\widehat{n}_{yz}, \widehat{x})$ then the argument of the exponential function in Eqn.(2.5) writes $\widehat{n}\overrightarrow{X} = (x\sin\theta\sin\phi + y\sin\theta\cos\phi + z\cos\theta)$, and this equation rewrites:

$$\tilde{S}(\omega, \widehat{n}) \stackrel{\text{def}}{=} |\int S_x(x)S_y(y)S_z(z) \exp\left(-\frac{i\omega}{c}(x\sin\theta\sin\phi + y\sin\theta\cos\phi + z\cos\theta)\right) \tag{5.4}$$

where we have assumed we could factor the 3D-spatial beam density distribution S as the product of the 1D projections S_x, S_y and S_z.
In order to use frequency-domain analysis to deduce information on the bunch longitudinal distribution, it is necessary that the ω-dependence come only from longitudinal coordinate z. From the

[2]The elliptic integral of the first and second kind are respectively defined as $\mathrm{K}(u) = \int_0^{\pi/2}[1-u^2\sin^2(\xi)]^{-1/2}d\xi$ and $\mathrm{E}(u) = \int_0^{\pi/2}[1-u^2\sin^2(\xi)]^{1/2}d\xi$

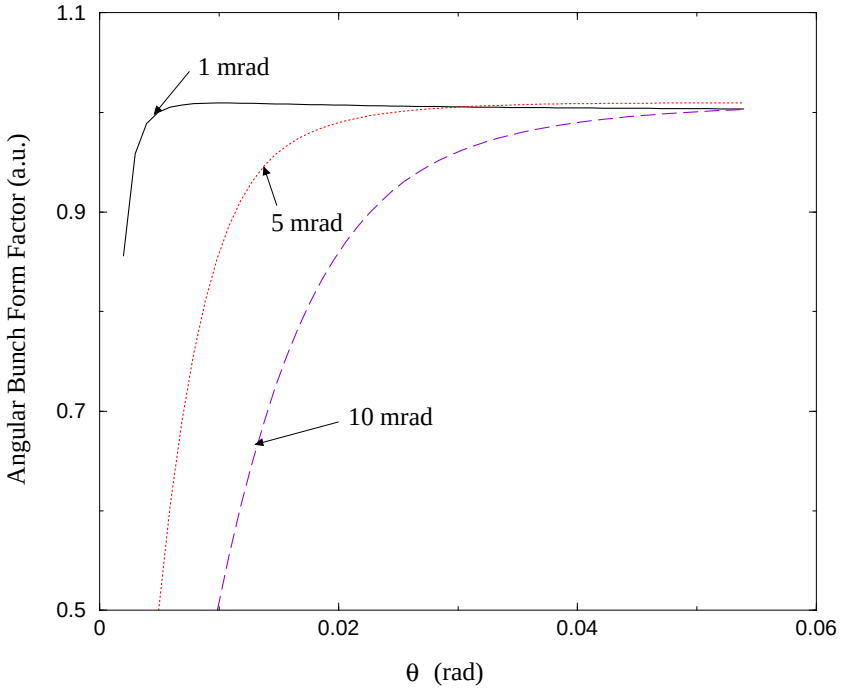

Figure 5.2: Angular BFF for three different value of the RMS beam divergence.

latter equation, we can define the effective coordinates $x_{eff} = x \sin\theta \sin\phi$, $y_{eff} = y \sin\theta \cos\phi$ and $z_{eff} = z \cos\theta$; and derive a criterion on the rms beam size to ensure the wavelength dependence is mainly due to the longitudinal distribution:

$$z_{eff} \gg \left[x_{eff}^2 + y_{eff}^2\right]^{1/2} \tag{5.5}$$

or

$$z \gg \tan\theta \left[x^2 \sin^2\phi + y^2 \cos^2\phi\right]^{1/2} \tag{5.6}$$

which can be expressed in term of RMS quantities without loss of generality:

$$\sigma_z \gg \tan\theta \left[\sigma_x^2 \sin^2\phi + \sigma_y^2 \cos^2\phi\right]^{1/2} \tag{5.7}$$

If this latter criterion is fulfilled we can use the line charge approximation, i.e., treat a bunch as a line with a 1D charge distribution. In such case, analysis of the coherent emission of the bunch reveals information on the bunch longitudinal distribution and is not contaminated by the transverse effect aforementioned, and we can write the BFF as it is generally written in the literature:

$$\tilde{S}(\lambda) = \left| \int_{-\infty}^{+\infty} S_z(z) \exp\left(-2i\pi\sigma z\right) dz \right|^2 \tag{5.8}$$

where as before $S_z(z)$ is the longitudinal bunch density along the longitudinal axis z moving along with the bunch. We have introduced the wavenumber $\sigma = 1/\lambda = \omega/(2\pi c)$ for convenience.
The computation of the BFF for a normal distribution or a square distribution is simple; the results are presented in Fig. 5.3 where we have assumed the bunch is a continuum and its RMS extent is 300 μm. For both types of distribution, the BFFs suddenly take off at wavelength of the order of

the bunch length. Hence measuring the coherent radiation power at wavelength comparable to the bunch length, i.e. where the coherent enhancement occurs, can provide information on the bunch structure and length. Also we can notice that the square distribution, and generally all type of distribution with sharp edge, induces BFF with low wavelength (high frequency) components. It

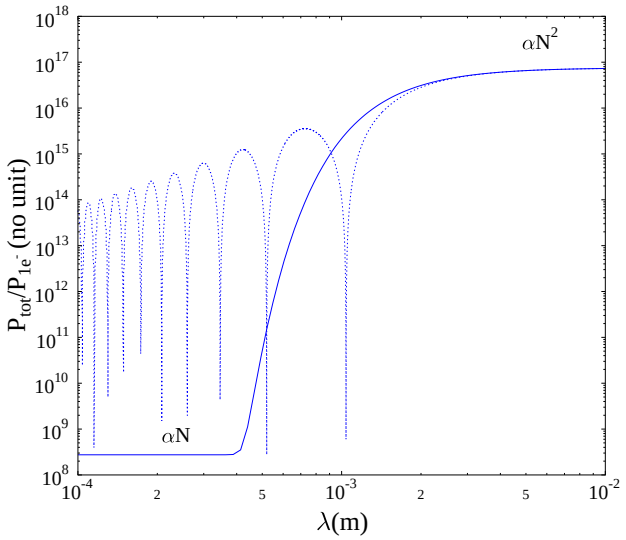

Figure 5.3: Bunch form factor computed for a 300 μm (RMS) square (**dash line**) and gaussian (**solid line**) bunches.

is interesting to numerically compute the BFF using a Monte-Carlo simulation technique, for a finite number of macro-particles in the bunch. In figure 5.4 we present computation of bunch form factor for 10^6 macro-particles. In the case of the bunch charge we are interested in i.e. 60 pC, the macro-particle represents 375 electrons. The choice to simulate only 10^6 macro-particle instead of the whole number of electron i.e. 3.75×10^8 was imposed by the desire to economize CPU time and expedite simulations. The Monte-Carlo generated distribution can be written as a Klimontovich distribution:

$$S(z) = \sum_{i=1}^{i=N} \delta(z - z_i) \tag{5.9}$$

and the associated bunch form factor, under the line charge assumption, reduces to a sum:

$$\tilde{S}(\lambda) = \sum_{i=1}^{i=N} \left(|\sin \frac{2\pi z_i}{\lambda}|^2 + |\cos \frac{2\pi z_i}{\lambda}|^2 \right) \tag{5.10}$$

We see in figure 5.4 that because of the finite number of particles, the bunch distribution and the BFF cannot be treated as continuum. These features should be kept in mind even if in the following we will assume the bunch distribution to be continuum.

If one uses standard beam parameters experimentally achieved in the IRFEL accelerator, i.e. transverse beam size of approximately 1 mm, minimum bunch length of 140 μm, Eqn.(5.7) is not a fortiori

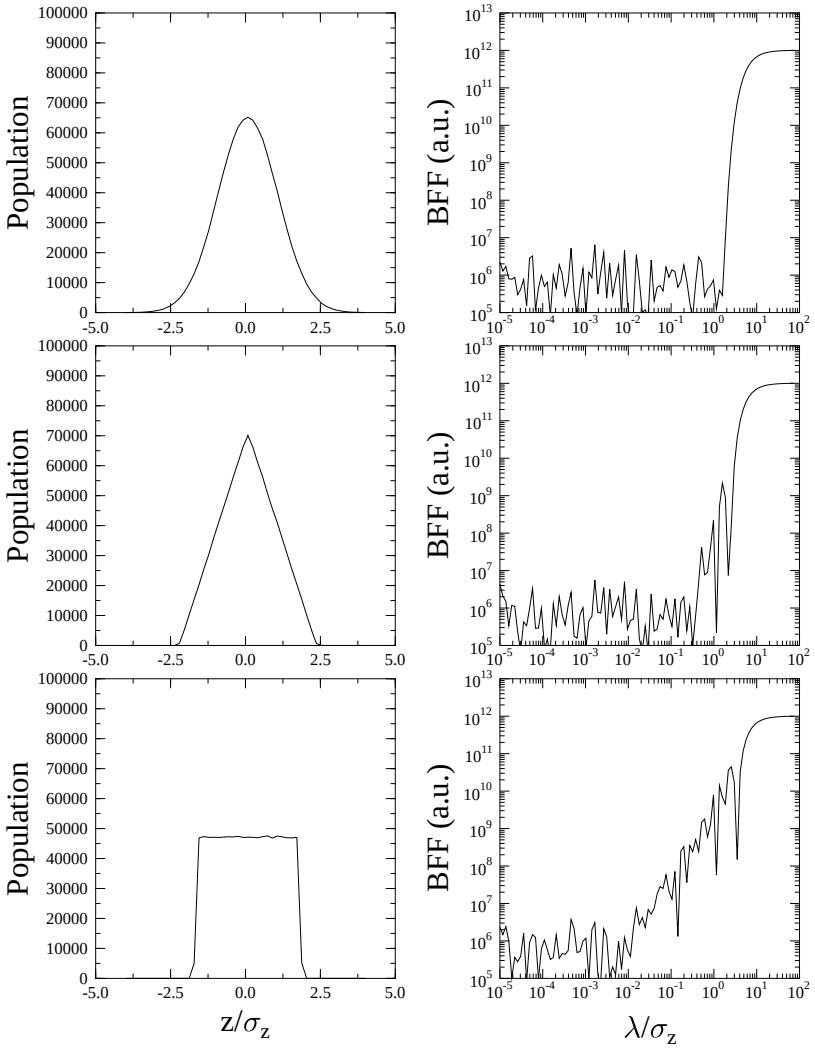

Figure 5.4: Monte-Carlo simulated bunch form factor (**right**) with 10^6 macroparticle for three types of bunch longitudinal distribution (**left**).

satisfied: transverse effect can yield non-negligible contribution to the bunch form factor. Fortunately we are also helped by the directionality of the radiation: in the case of both transition and synchrotron radiation most of the power resides in a cone that is of the order of $1/\gamma$: In the FEL coherent radiation setup the collecting optics has an angular acceptance of 0.3 rad. We study the effect of transverse beam spot size numerically by performing the integration:

$$\Delta P(\omega) = \int_{0.9\omega}^{1.1\omega} d\omega \int d\Omega \frac{d^2 P_{1e^-}(\omega)}{d\omega d\Omega} \tag{5.11}$$

For simplicity, let's assume that the bunch is cylindrically-symmetric i.e. $\sigma_x = \sigma_y \stackrel{def}{=} \sigma_r$. The results of the numerical integration of Eqn.(5.11) is depicted in Fig. 5.5 where we compare the effect of the transverse beam size on the bunch form factor. The total TR and SR power spectral density is computed for three typical bunch shape: a line charge bunch ($\sigma_r = 0$), an ellipsoidal bunch ($\sigma_r = 10\sigma_z$), and a "pancake" bunch ($\sigma_z = 0$). Beam size significantly affects the region of coherent enhancement in the BFF: if one use the thereby computed BFF to retrieve the bunch length, the

transverse beam size effect leads to an underestimate of the bunch length by a approximately a factor of 2. However, the effect of the beam spot size is very small on the CSR and CTR spectrum. In the case of ellipsoidal bunch, i.e. the worst case that can happen in the IR FEL, the error is at the 10% level.

Hence, we will assume the measurement of CTR or CSR in the IR FEL is directly related to the

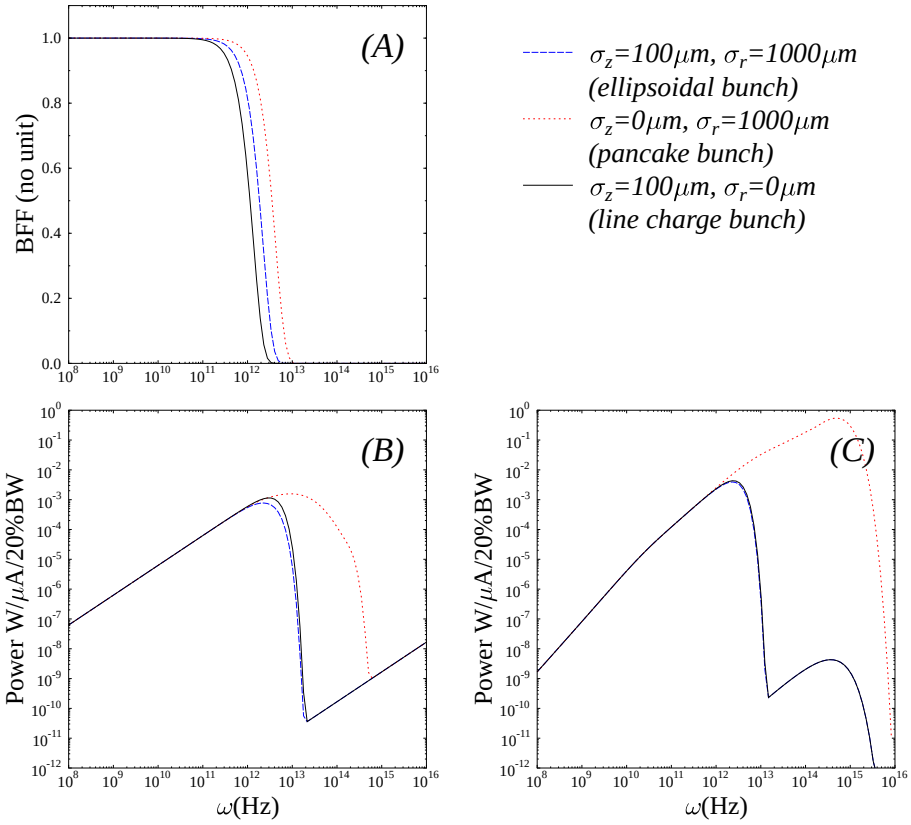

Figure 5.5: Effect of transverse beam size on the 3D-BFF. For three different type of bunch (ellipsoidal, pancake and line charge bunch), the BFF (**A**), the CTR (**B**) and CSR (**C**) power spectrum are numerically computed. The power spectrum are computed assuming an angular acceptance of 0.3 rad and are given for a 20% frequency bandwidth.

longitudinal bunch distribution, without any "contamination" coming from the transverse beam size effect or from the angular bunch form factor.

5.3.1 The use of the BFF to compute and monitor the bunch length

Under the "line charge" assumption mentioned earlier, the BFF only depends on the bunch length. In this section, we derive a simple relation, without making any assumptions on the bunch density function, that allows one to compute the rms bunch length from the bunch form factor. Let's start with the BFF definition, by introducing the wavelength number $\sigma = 1/\lambda$ for convenience, and by replacing the exponential function in the Fourier transform by its Taylor expansion:

$$\exp(\alpha) = \sum_{n=0}^{\infty} \frac{\alpha^n}{n!} \tag{5.12}$$

The equation 5.8 yields:

$$f(\sigma) = |\int_{-\infty}^{+\infty} \sum_{n=0}^{\infty} \frac{(2i\pi\sigma z)^n}{n!} \rho(z)dz|^2 = |\sum_{n=0}^{\infty} \frac{(2i\pi\sigma)^n}{n!} \int_{-\infty}^{+\infty} z^n S(z)dz|^2 \tag{5.13}$$

Defining the n-order moment ν_n as

$$\nu_n = \int_{-\infty}^{+\infty} z^n S(z)dz \tag{5.14}$$

Eqn. (5.13) becomes:

$$\tilde{S}_z(\sigma) = |\sum_{n=0}^{\infty} \frac{(2i\pi\sigma)^n}{n!} \nu_n|^2 \tag{5.15}$$

In case we are at high σ we can approximate the series by its first three terms only. In such case, the previous equation reduces to:

$$\begin{aligned} \tilde{S}_z(\sigma) &= |1 + 2i\pi\sigma\nu_1 + \frac{(2i\pi\sigma)^2}{2}\nu_2 + \mathcal{O}(\sigma^3)|^2 \\ &= 1 - 4\pi^2\sigma^2\Sigma^2 + \mathcal{O}(\sigma^3) \end{aligned} \tag{5.16}$$

where we have introduced the variance $\Sigma^2 = \nu_2 - \nu_1^2 (\stackrel{def}{=} \sigma_z)$.
From Eqn. (5.16) we note that it is straight forward to extract the bunch length, Σ, by fitting the bunch form factor with a parabolic function at high frequency. This result is a generalization of the gaussian distribution $\exp(-z^2/(2\Sigma^2))$ case: for such a distribution the form factor writes $\exp(-4\pi^2\sigma^2\Sigma^2)$ whose Taylor expansion at small frequency is also given by Eqn. (5.16). It is very informative to develop the BFF to higher order to see whether we can extract information on the higher moments of the bunch longitudinal distribution. Performing such derivation yields the general form of the BFF [46] (with $\zeta = 2\pi\sigma$):

$$\begin{aligned} \tilde{S}_z(\sigma) &= |\sum_{n=0}^{\infty} \frac{(-1)^n\zeta^{2n}}{(2n)!}\nu_{2n} + i\sum_{n=0}^{\infty} \frac{(-1)^n\zeta^{2n+1}}{(2n+1)!}\nu_{2n+1}|^2 \\ &= \left(\sum_{n=0}^{\infty} \frac{(-1)^n\nu_{2n}\zeta_{2n}}{(2n)!}\right)^2 + \left(\sum_{n=0}^{\infty} \frac{(-1)^n\nu_{2n+1}\zeta_{2n+1}}{(2n+1)!}\right)^2 \\ &= \sum_{n=0}^{\infty} \frac{\zeta^{4n}}{((2n)!)^2}\nu_{2n}^2 + 2\sum_{n=0}^{\infty}\sum_{m<n} \frac{(-1)^{n+m}\zeta^{2(n+m)}}{(2n)!(2m)!}\nu_{2n}\nu_{2m} + \\ &\quad + \sum_{n=0}^{\infty} \frac{\zeta^{4n+2}}{((2n+1)!)^2}\nu_{2n+1}^2 + 2\sum_{n=0}^{\infty}\sum_{m<n} \frac{(-1)^{n+m+2}\zeta^{2(n+m+1)}}{(2n+1)!(2m+1)!}\nu_{2n+1}\nu_{2m+1} \end{aligned} \tag{5.17}$$

From Eqn. (5.17) it is possible to obtain a system of n equations with $2n$ unknowns. Fitting the bunch form factor with high degree polynomial only allows to determine unambiguously the variance of the bunch distribution; it does not give access to higher-order moments (but only to combination of these moments). This indetermination is in fact related to the measurement, a

power measurement, yielding the loss of phase information.
We have also noticed from experiment using a particle pushing code that the fine structure of the BFF is affected differently depending on how the bunching process is performed. For instance in figure 5.6 we plot the BFF computed from numerical simulation for different settings of radio-frequency elements that play a key role in the bunching process. Though the bunch length does not vary significantly, we can notice that each element affects the BFF at different wavelength. Such features can be experimentally used to determine which element is not operated at its nominal operation point (e.g. because of drift,...). Before its application we will need to perform experimental parametric studies by systematically varying each RF-elements.

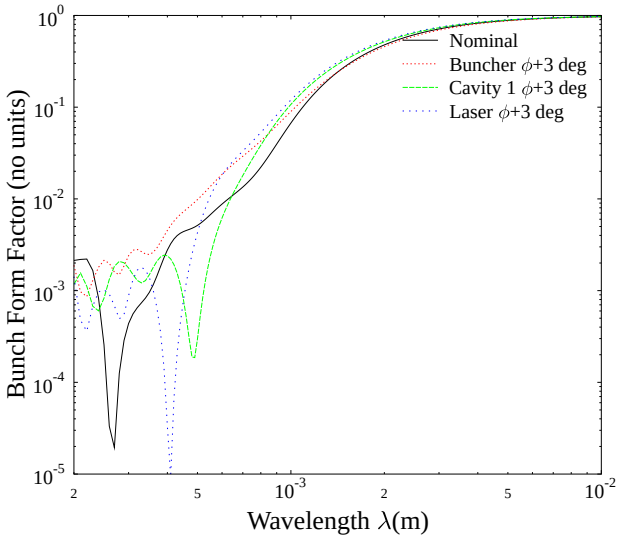

Figure 5.6: Effect of different key elements in the bunching process of the electrons on the BFF. The BFF corresponding to the nominal settings for the RF elements (solid line) is compared with the cases where the buncher (dotted line), the first cavity in the injector (grey line) and the photocathode drive laser (dotted line) are operated +3 deg off their nominal settings.

5.3.2 Retrieval of the Bunch Distribution by Hilbert Transforming the BFF

As we mentioned earlier, the only observable we can measure is the power of the coherent radiation i.e. the square amplitude of the electric field; all the phase information is lost. However, it is still possible to get some insight on the phase information using the so-called dispersion relations [3] that are commonly used in Solid State Physics *e.g.* for reconstructing the imaginary part of the refractive index of a material from from knowledge of the real part. This technique has been first applied to the present problem by Lai et al. [48]; however in the literature there is no clear derivation that proves the use of the dispersion relation for retrieving the phase of the BFF is legitimate. We

[3] Also referred as Kramers-Kronig's relations

present an outline of this proof below, and a detailed proof in Appendix C. From the definition of the bunch form factor we can write:

$$\tilde{S}(\sigma) = \breve{S}\ (\sigma)\ \breve{S}^{*}\ (\sigma) \tag{5.18}$$

σ is the wave number and $\breve{S}\ (\sigma)$ is the Fourier transform of the bunch longitudinal distribution; it can be written as:

$$\breve{S}\ (\sigma) = \sqrt{\tilde{S}(\sigma)} \times \exp(i\psi(\sigma)) \tag{5.19}$$

where $\psi(\sigma)$ is the phase associated to the Fourier transform. The method is discussed in standard mathematics textbooks (see for instance [50]) and can be applied to $S(\sigma)$ to calculate its imaginary part knowing its real part because $S(\sigma)$ is a square integrable function. In the present case, the problem is slightly different: we know the modulus of $S(\sigma)$ and need to compute the phase. By taking the logarithm of the latter equation, we come back to the determination of the imaginary part of the function $\log[S(\sigma)]$ from the knowledge of its real part $\log[|S(\sigma)|]$:

$$\log(\breve{S}\ (\sigma)) = \log(\sqrt{\tilde{S}(\sigma)}) + i\psi(\sigma) = 1/2 \times \log(|\tilde{S}(\sigma)|) + i\psi(\sigma) \tag{5.20}$$

Now, $\log(\breve{S}\ (\sigma))$ is not square integrable and the Cauchy integral on $\log(\breve{S}\ (\sigma))$ does not converge ($\zeta = \sigma + i\sigma'$ is the complex wavenumber):

$$\oint \frac{\log(\breve{S}\ (\zeta)) - \log(\breve{S}\ (\zeta))}{\zeta - \sigma} \overset{|\zeta| \to \infty}{\longrightarrow} \int_0^{\pi} \frac{\log(\breve{S}\ (\zeta))}{\zeta} \to -\infty \tag{5.21}$$

Let's introduce the function $\Sigma(\zeta)$ defined as:

$$\Sigma(\zeta) \overset{\text{def}}{=} \frac{\log[\breve{S}\ (\zeta)] - \log[\breve{S}\ (\sigma)]}{\zeta - \sigma} \tag{5.22}$$

$\Sigma(\zeta)$ is not singular at $\zeta = \sigma$ and is square integrable. We can then derive a set of "modified" dispersion relations for $\breve{S}$ (see Appendix C for a detailed derivation), and finally the phase of $\breve{S}$ takes the form:

$$\psi(\sigma) = \psi(\sigma_0) - \frac{1}{\pi}(\sigma - \sigma_0)\mathcal{P}\int_{-\infty}^{+\infty} \frac{\log[|\ \breve{S}\ (\zeta)|] - \log[|\ \breve{S}\ (\sigma)|]}{(\zeta - \sigma)(\zeta - \sigma_0)} d\zeta \tag{5.23}$$

where $\mathcal{P}$ designates the Cauchy principal value for the integral.
Letting $\sigma_0 = 0$ and using the fact $\breve{S}\ (\zeta) = \breve{S}\ (-\zeta)$ we finally find:

$$\psi(\sigma) = \psi(0) - \frac{2\sigma}{\pi}\mathcal{P}\int_0^{+\infty} \frac{\log[|\ \breve{S}\ (\zeta)|]}{\zeta^2 - \sigma^2} d\zeta \tag{5.24}$$

This latter equation is widely known, in the literature, and is sometimes referred as dispersion relation. Once the phase $\psi(\sigma)$ is computed we can recover the initial distribution by using the inverse Fourier transform:

$$S(z) = \int_0^{\infty} \breve{S}\ (\sigma) \cos(2\pi\sigma z - \psi(\sigma))\, d\sigma \tag{5.25}$$

Two facts should be emphased about Eqn.(5.24) (1) the $\psi(0)$ term is unknown and is assumed to be zero, and (2) this equation is applicable provided $\log[S(\sigma)]$ is analytic in the upper half-part of the complex plane. If it has singularities then, in virtue of the residue theorem, there are other contribution to the phase that must be considered. In the following we will not consider such cases by assuming the standard bunch distribution is analytic in the upper half-plane (a fully detailed discussion is provided in Appendix C).

5.4 Observation of Coherent Transition Radiation

In the early stage of the IRFEL commissioning, the experimental setup described in figure 5.12 was used to image the CTR beam emission source produced by the electron beam as it passes through an aluminum foil onto a Golay cell detector. The Golay cell (see Fig. 5.7(A)) is a thermal detector with a nearly uniform energy response from the ultraviolet up to the microwave region. The detector consists of a gas-filled cell enclosed by two membranes. The incoming radiation is absorbed by a thin aluminum layer deposited on the "input" membrane. The aluminum film thickness is chosen so that the corresponding surface impedance yields the maximum absorption of radiation over a broad range of wavelengths. The absorbed radiation heats the gas which in turn increases the pressure inside the cell and distorts the second (flexible) membrane. The distortion is sensed by a photodetector cell that detects a light beam reflected from the membrane. This effect is amplified by two large grids arranged so that initially, i.e. when no radiation is detected, the lines of one grid are imaged on the space of the second grid resulting in no light detection by the photodetector. When the membrane is distorted, the image of the first grid shifts, allowing significantly more light to reach the photodetector. This grid system is in fact a mechanical means of enhancing the effect of small displacements of the membrane. The output analog signal from the photodetector in the Golay cell setup is electronically processed as described in Fig. 5.7(B): First, it is amplified by a factor 10 using a simple operational amplifier located in the accelerator tunnel enclosure, then the signal is brought in the service building located upstairs the tunnel where it is shaped using a noise filter. Afterward, it is fed into a Analog to Digital Converter (ADC) where it is digitized, at a sample rate equal to the beam macropulse repetition rate. The digital signal is broadcast via a VME input/output controller (IOC) to the Ethernet network so that it can be accessed from any work station communicating to the control system.

It is possible to verify the nonlinearity of the radiation versus the bunch charge as pictured in

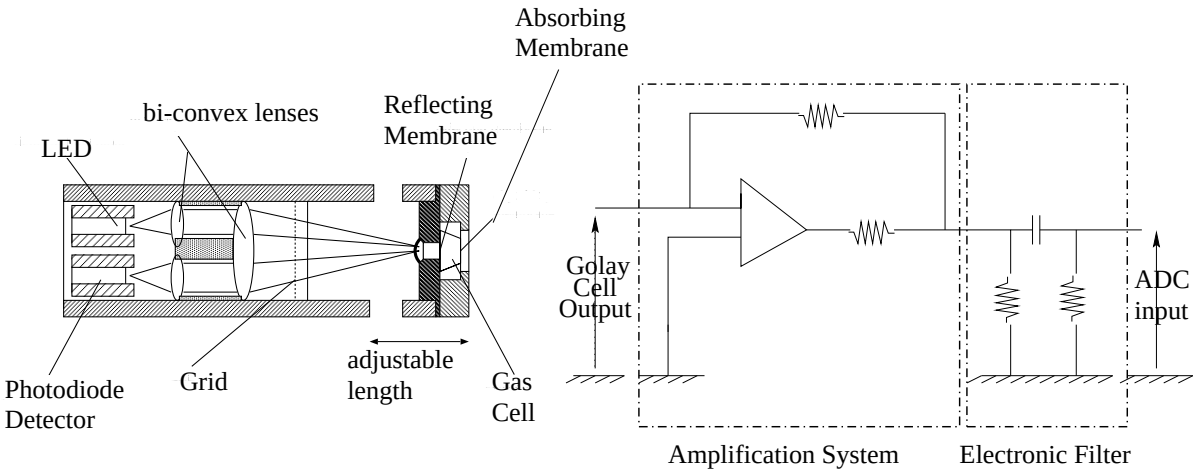

Figure 5.7: Simplified schematics of a Golay cell (**A**) and the associated signal acquisition electronics (**B**).

figure 5.8. The quadratic dependence of the CTR signal versus the charge per bunch is not very pronounced compared to the one measured in the CEBAF accelerator [20] for example. This is

due to the method we use to vary the charge: we use a rotational polarizer to attenuate or increase the drive laser power on the photocathode that also significantly affects the beam dynamics in the machine (especially in the low energy region where the beam dynamics is strongly dependent, via space charge forces, on the charge). Therefore varying the charge also affects the bunch length, and therefore the CTR signal since it is dependent on both the charge and the bunch length. By contrast in the CEBAF machine, varying a slit aperture opening in a chopper cavity varies the charge per bunch. For all the practical slits openings, the beam is never space-charge dominated and so the slit opening does not significantly affect the bunching process.

Figure 5.9 depicts the dependence of the CTR signal versus the overall phase of the main linac:

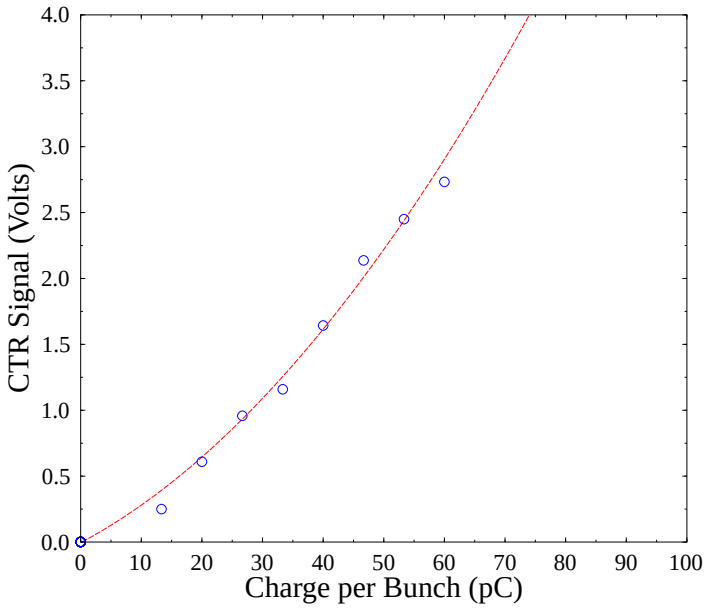

Figure 5.8: Scaling of coherent transition radiation power versus charge per bunch. The charge per bunch is changed by varying the intensity of the photocathode drive laser. The circles are the experimental data point and the dash line is the result of a quadratic interpolation of the experimental point.

during this experiment the machine settings were kept constant and only the linac "gang" phase [4] was varied. The maximum acceleration phase, determined experimentally by maximizing the energy, is -4 deg and the expected phase for maximum bunching (i.e. minimum bunch length) is approximately 6 deg which is in good agreement with the phase value for which the maximum CTR signal is observed in figure 5.9 ($\simeq$6.3 deg).

A last experiment consisted of varying the beam spot size on the TR radiator and each time recording the CTR signal. The variation of this signal versus the equivalent beam radius we define as $\sqrt{\sigma_x \sigma_y}$ is presented in figure 5.10. At this point it is difficult to tell whether the decrease of total power detected is due to the spatial or the angular BFF.

[4] the "gang phase" knob allows to shift all the accelerating cavities in the linac by the same phase compare to the other radio-frequency elements in the IRFEL (see Appendix D)

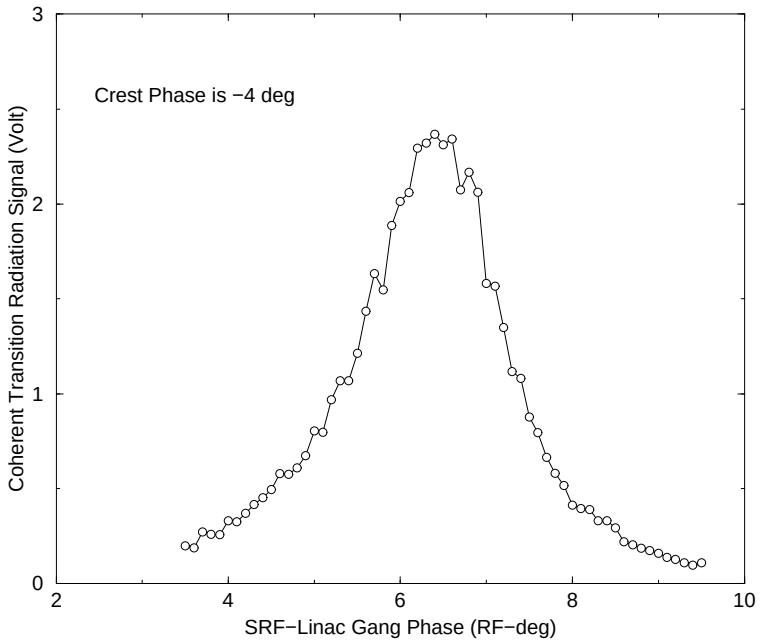

Figure 5.9: CTR signal versus the SRF linac overall phase. As the linac phase is varied the bunch length at the undulator vicinity is changed.

5.5 The Michelson Polarizing Interferometer

5.5.1 Overview of the experimental setup

One way of accessing the frequency spectrum of an electron bunch longitudinal distribution is to perform an interferometric measurement. In addition to providing the energy spectrum of the radiation emitted, it can also give an estimate of the bunch length directly from the interferogram. Such estimates must be taken with care as we will see in the following. We equipped the IRFEL accelerator with two "polarizing" Michelson interferometer built by the Department of Physics and Astronomy of the University of Georgia. The location of the devices are:

- the injector front end, to verify the bunching process in the injector is correct,
- the wiggler insertion region, to check the bunch length is adequate to get the FEL lasing.

The adjective "polarizing" refers to the nature of the beam splitter used in the interferometer: it is a dichroic polarizer that has a preferred direction. It reflects the polarization of the incoming field that is parallel to this preferred direction and transmits its orthogonal component.
Because electrons in an accelerator are randomly distributed from bunch to bunch, autocorrelation of radiation at wavelength smaller than the bunch length will not provide any information on the bunch structure. Hence the wavelength of observation must be chosen to be comparable or larger than the bunch length: this is the regime of coherent emission and this insures bunch-to-bunch coherence of the radiation.
In the IRFEL, this interferometer is used to measure the autocorrelation function of coherent

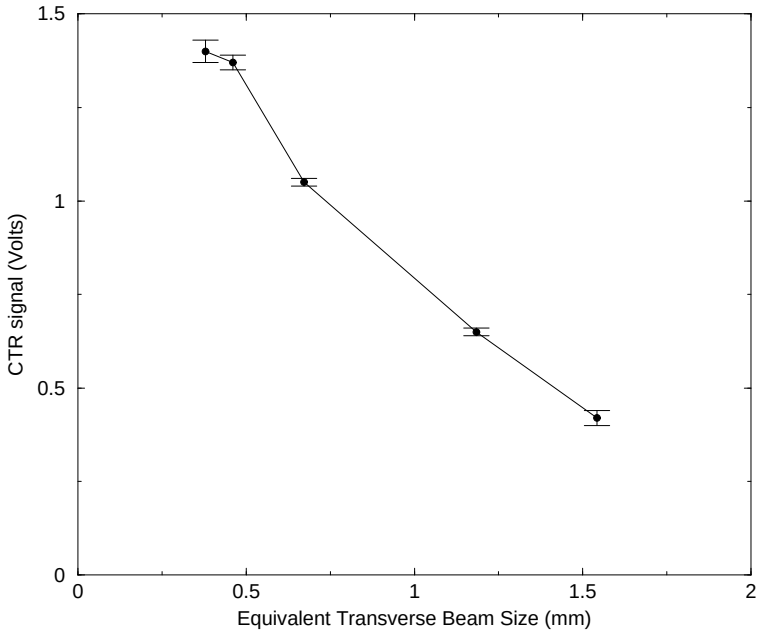

Figure 5.10: CTR signal versus beam equivalent transverse spot size $\sqrt{\sigma_x \sigma_y}$. The error bars correspond to the variance of five consecutive measurements.

transition radiation (CTR) pulses emitted as the electron bunches pass through a 0.8 μm thick, and 50.8 mm diameter aluminum foil. Though the use of CTR is a destructive measurement as we have previously discussed, it was preferred to CSR because the TR power spectrum is frequency independent in the region of interest whereas the CSR spectrum depends on the frequency ($\propto \omega^{3/2}$) and therefore is somewhat more difficult to analyze.
The backward CTR emitted from the foil directly shines out of the vacuum chamber through an optical window located at 90 deg with respect to the beam trajectory. This optical window is made of single crystal quartz so that it can transmit far infrared radiation without significant losses. The window thickness is 4.826 mm. After the window, a plano-convex lens with a focal length in the FIR domain of 125 mm is used to collimate the CTR beam to parallel rays (the lens is approximately located 125 mm far from the point of emission on the foil). The collimated beam is sent to the Michelson polarimeter via one planar mirror M_0 (see Fig.5.11). The optical beamline and the interferometer can be filled with nitrogen so that the measurement is not contaminated by water absorption in the microwave region of the spectrum. In the polarimeter components are: two beam splitters, two planar mirrors, one off-axis parabolic reflector, and a Golay cell detector:

- The beam splitters are made of parallel tungsten wires of 20 μm diameter spaced by 50 μm. Being metallic, the tungsten wires provide high conductivity for electric fields parallel to the wires. Such fields produce electric currents in the wires, and the energy of the fields is converted to energy of the current. The latter is then converted to heat, because of the small but significant electrical resistance of the wires. Hence to obey the boundary condition at the wire, the field parallel to the wires is reflected. However, because of the non-conducting spaces between the wires, no current can flow perpendicular to them. Hence the electric field component perpendicular to the wires produce no currents and lose no energy, therefore it is transmitted.

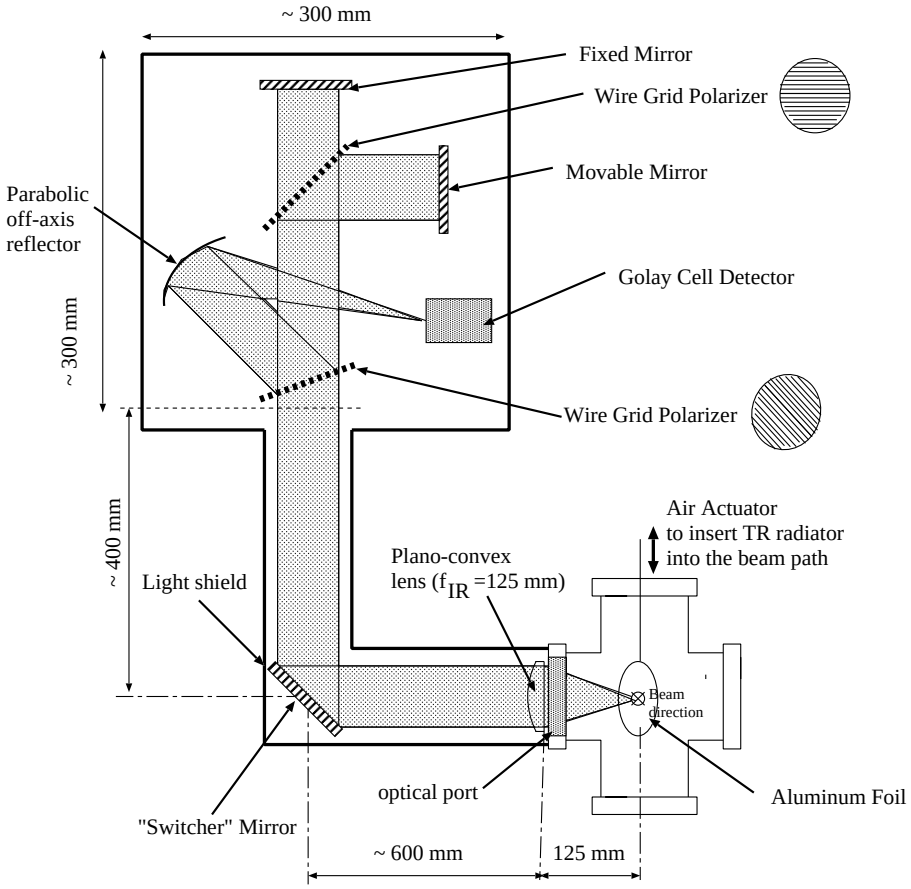

Figure 5.11: Overview of the optics to guide the coherent transition radiation emitted from an aluminum foil to the entrance of the interferometer.

- The planar mirrors are standard optical circular mirrors of 50.8 mm diameter. The movable mirror (M_1) is mounted on a micropositioner that can translate by 1 μm steps. Two picomotors are also mounted on the mirror gimbal mounts that can be used remotely to adjust the horizontal and vertical inclination of the mirror to make sure it is coplanar with the image of the fixed mirror (M_2) through the beam splitter.
- The parabolic reflector is used to focus an incoming collimated beam onto the detector sensitive area. It is an-off axis gold-sputtered reflector with a focal length of 10 cm.
- The Golay cell (see Fig. 5.7) and its acquisition system have been described previously.

5.5.2 Theory of Operation

The polarizing interferometer is depicted in Fig 5.12: Let's first analyze how a polarizing interferometer works in the simplistic (usual) case of a plane TEM wave. Afterward, we will refine this analysis including the effect due to TR electric field.

- Let $\vec{E}(t)$ be the electric field incoming into the interferometer. When this field enters the

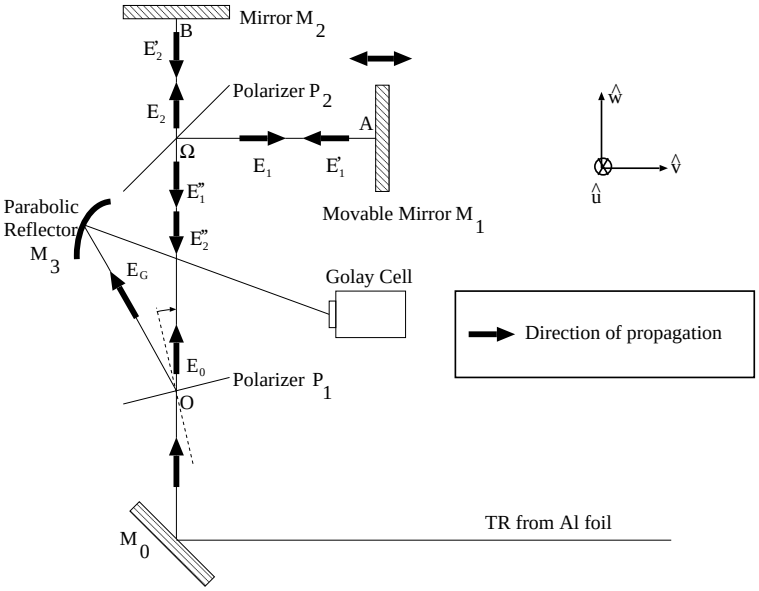

Figure 5.12: Simplified schematics of the Michelson polarizing interferometer.

Michelson interferometer it first encounters a polarizer P_1 whose wires are oriented at 45 deg with respect to the horizontal plane. The effect of this polarizer is only to transmit the field polarization whose direction is parallel to the wires. Therefore in the standard horizontal-vertical, $\widehat{u}$ and $\widehat{v}$, coordinate system (see figure 5.11 for detail), the electric field after the polarizer can be written as:

$$\overrightarrow{E_0}(t) = \frac{\widehat{u}+\widehat{v}}{\sqrt{2}} E_0(t) \tag{5.26}$$

- Then a second polarizer P_2, located at approximately 130 mm from P_1,that plays the role of beam splitter, intercepts the optical beam. Since its wires are horizontal, the horizontal polarization of the electric field get reflected in the variable length arm (1) ($\overrightarrow{E_1}$) whereas the vertical polarization is transmitted to the fixed arm (2), ($\overrightarrow{E_2}$).

- In the variable length arm (1): the reflected field writes:

$$\overrightarrow{E_1}(t) = \frac{R}{\sqrt{2}} E_0(t)\widehat{u} \tag{5.27}$$

and propagates up to the mobile mirror M_1 where it is reflected. The reflected field $\overrightarrow{E_1'}$ is (the reflection introduces a factor $\exp(-i\pi)$:

$$\overrightarrow{E_1'}(t) = -\frac{R}{\sqrt{2}} E_0(t+\tau)\widehat{u} \tag{5.28}$$

where τ is a time delay introduced by the mirror. By convention, $\tau = 0$ when the mirror M_1 is at the same distance from the beam splitter as M_2. The electric field $\overrightarrow{E_1'}$ back-propagates to the beam splitter and is reflected a second time on P_2. Finally at the exit of the arm (1) the electric field writes:

$$\overrightarrow{E_1''}(t) = \frac{R^2}{\sqrt{2}} E_0(t+\tau)\widehat{u} \tag{5.29}$$

- In the fixed length arm (2): the transmitted field writes:

$$\overrightarrow{E_2'}(t) = \frac{T}{\sqrt{2}} E_0(t)\widehat{v} \tag{5.30}$$

and propagates up to the fixed mirror M_2 where it is reflected. The field $\overrightarrow{E_2'}$ after reflection writes:

$$\overrightarrow{E_2'}(t) = -\frac{T}{\sqrt{2}} E_0(t)\widehat{v} \tag{5.31}$$

The electric field $\overrightarrow{E_2'}$ back-propagates to the beam splitter and is transmitted a second time through P_2. Finally, at the exit of the arm (2), the resulting electric field is:

$$\overrightarrow{E_2''}(t) = -\frac{T^2}{\sqrt{2}} E_0(t)\widehat{v} \tag{5.32}$$

- After re-combination of the electric field issued from the two arms of the interferometer, the total electric field writes:

$$E_0'(t) = \frac{1}{\sqrt{2}}\left(-R^2 E_0(t+\tau)\widehat{u} - T^2 E_0(t)\widehat{v}\right) \tag{5.33}$$

This field is the total electric field incident on the P_1 polarizer. This polarizer reflects electric field with component $\propto (\widehat{u}-\widehat{v})/\sqrt{2}$ and transmit the components $\propto (\widehat{u}+\widehat{v})/\sqrt{2}$. Hence only the latter polarization component is transmitted to the Golay cell after reflection and focusing on the off-axis parabolic mirror; it takes the form:

$$E_G(t) = \frac{R}{2\sqrt{2}}\left(R^2 E_0(t+\tau) - T^2 E_0(t)\right) \tag{5.34}$$

If we assume the polarizer to be perfect conductor, then $R^2 = T^2 = 1/2$ and the field detected reduced to:

$$E_G(t) = \frac{R}{2\sqrt{2}}\left[E_0(t+\tau) + E_0(t)\right] \tag{5.35}$$

Indeed the Golay cell is sensitive to the average power $\langle |E_g(t)|^2\rangle_t$ which is:

$$I(\tau) \propto 2\langle |E_0(t)|^2\rangle_t - \left[E_0(t)E_0^*(t+\tau) + E_0^*(t)E_0(t+\tau)\right] \tag{5.36}$$

which can be expressed in the integral form:

$$I(\tau) \propto \underbrace{2\int_{-\infty}^{+\infty} |E_0(t)|^2 dt}_{\text{baseline}} - \underbrace{2\Re\left[\int_{-\infty}^{+\infty} E_0(t)E_0^*(t+\tau)dt\right]}_{\text{autocorrelation: } \Gamma(\tau)} \tag{5.37}$$

It is important to insist that in virtue of the superposition principle, the electric field is proportional to the longitudinal bunch distribution and therefore measuring the properties of this radiation electric field will provide information on the electron bunch. The "autocorrelation" term gives the information on the bunch structure, it can be written as:

$$\Gamma(\tau) = \frac{1}{2}\left(I(\tau) - \lim_{|\tau|\to\infty} I(\tau)\right) \tag{5.38}$$

In the following we will replace the time delay, τ, by an optical path difference (OPD), δ,$(= c\tau)$. Finally it is interesting to note that Fourier-transforming Eqn.(5.37) gives:

$$I(\tau) \propto 2\int_{-\infty}^{+\infty} |\widetilde{E_0}(\omega)|^2 d\omega - 2\Re\left[\int_{-\infty}^{+\infty} \widetilde{E_0}(\omega)\widetilde{E_0}^*(\omega)e^{i\omega\tau}d\omega\right] \tag{5.39}$$

Therefore the autocorrelation part can be written (since $\widetilde{E}(\omega) = \widetilde{E}^*(-\omega)$):

$$\Gamma(\tau) = \int |\widetilde{E_0}(\omega)|^2 e^{i\omega\tau}d\omega \tag{5.40}$$

which mean that the autocorrelation is the Fourier transform of the energy spectrum of the incoming radiation. This result in fact constitutes the well-known Wiener-Kintchine theorem in signal processing.
In the previous explanation we assumed the electric field was a TEM plane wave, i.e. we assumed it had the form:

$$E(z) = E_0 e^{-ikz}$$

Such field has a planar front and the field value is constant in the plane. In the case of TR, such description is not *a fortiori* a good description. The electric field associated with TR in the time domain writes [7]:

$$\overrightarrow{E}(t,\theta,r) = \frac{2\beta N e S(t)}{r(1-\beta^2\cos^2\theta)}\widehat{\theta}\exp(-ikr) \tag{5.41}$$

where $S(t = z/c)$ is the longitudinal density of the bunch, and r is the distance from the point of emission (or its image). So it deviates from the previous assumptions:

1. It is not a plane wave because of the phasor dependence $\exp(-ikr)$. The use of the plano-convex lens however makes the wave front planar to first order and under the Fresnel approximation; under such an approximation, the phasor is multiplied by the phasor introduced by the plano-convex lens of focal length f: $\exp(-ik(x^2+y^2)^2(1/f)/2)$, the resulting phasor is $\exp(-ikz)$ (which is a planar wave front).

2. It is not a TEM wave, for a given wavefront plane (after the plano-convex lens) the field is still not constant in the within front.

Henceforth we assume the wavefront to be a plane wave after the plano-convex lens, a valid assumption under the Fresnel approximation. However we shall consider the case where the lens do not perfectly image the TR source at infinity. Then the variable r in the Eqn.(5.41), is the distance between the point of observation and the position of the TR source through the plano-convex lens. In such case, the autocorrelation writes:

$$I(\tau) \propto \langle|\frac{S(t+\tau)}{r_1} - \frac{S(t)}{r_2}|^2\rangle\widehat{\theta} \tag{5.42}$$

where r_1 and r_2 are respectively the distance between the image of the TR source and the mirrors M_1 and M_2; the angle vector $\widehat{\theta}$ is assumed to have the same direction for both field, a valid assumption under the Fresnel approximation.

With $r_1 = r + c\tau$ ($\tau = \delta/c$ where δ is the mirrors relative position), $r_2 = r$, Eqn.(5.42) takes the form:

$$I(\tau) \propto \frac{1}{r + c\tau}\left(\Gamma(0) - \Gamma(\tau) + \frac{c\tau}{r}\left(\Gamma(0) - \Gamma(\tau)\right)\right) \tag{5.43}$$

It is important to note that the quantity δ, in the above equation, is of the order of the bunch length (i.e. at maximum $500\,\mu$m for the present case). A 10% error in the location of the focal plane with respect of the point of emission will result in a value of r, the distance between TR image and the fixed mirror, of the order of 1 m; hence replacing $r + c\tau$ in Eqn.(5.43) with r is a 5×10^{-4} effect. Therefore, without introducing significant error the intensity on the detector can be written as for a TEM wave, that is $I(\tau) \propto (\Gamma(0) - \Gamma(\tau))$; and the standard analysis presented above can be used to extract information from a transition radiation interferogram.

5.5.3 Relating an Interferogram Measurement to a Bunch Length Measurement

By measuring the full-width half-maximum (FWHM) of the autocorrelation, one can very easily get an estimate of the bunch length. Let's analyze how the FWHM is related to the RMS values of two typical particle distributions: a normal distribution that is characterized by its rms value (variance) σ_z and a square distribution whose characteristic length is its full width w. Table 5.1 relates FWHM, RMS and equivalent length for these distributions.

Distribution	**Equ. Length**	**RMS**	**FWHM**
Gaussian	$\sqrt{2\pi}\sigma_z$	σ_z	$2\sigma_z\sqrt{\ln(2)}$
Square	w	$w/\sqrt{12}$	w

Table 5.1: Relationships between "equivalent", "RMS" and "FWHM" lengths for a gaussian and square longitudinal bunch density.

Case of a Gaussian distribution:

$S(z) = 1/\sqrt{2\pi\sigma_z^2}\exp\left(z^2/(2\sigma_z)\right)$. For such distribution, the autocorrelation is $\Gamma(\delta) = 1/(2\sqrt{\pi}\sigma_z)\exp\left(\delta^2/(4\sigma_z^2)\right)$. Hence the RMS value of the convolution is $\sqrt{2}$ times the RMS value of the distribution. Using Table 5.1, we deduce that

$$\mathrm{FWHM}_{\mathrm{autocor}} = \sqrt{8\ln(2)}\sigma_z \tag{5.44}$$

Case of a Square distribution:

We write this distribution as:

$$S(z) = \begin{cases} (1/w) & \text{if } -w/2 < \delta < w/2 \\ 0 & \text{elsewhere} \end{cases} \tag{5.45}$$

Its autocorrelation is:

$$S(z) = \begin{cases} (1/w^2)[-\delta + w] & \text{if } -w < \delta < 0 \\ (1/w^2)[\delta + w] & \text{if } 0 < \delta < w \\ 0 & \text{elsewhere} \end{cases} \tag{5.46}$$

The FWHM of the autocorrelation is exactly the width w of the distribution.

$$\text{FWHM}_{\text{autocor}} = w \tag{5.47}$$

Arbitrary Distribution:

Contrary to a typical circular accelerator in which damping and statistical fluctuations lead to a gaussian phase space corresponding to thermal equilibrium, there is no reason in linear accelerators to invoke the gaussian assumption. Hence it is not rigorous to perform some kind of fit with a normal distribution. The philosophies we use to get an estimate of the bunch length are as follows: (1) We can give an estimate of limits for the bunch length by assuming the bunch length is a comprise between the bunch length given by the gaussian and square-like distribution; (2) we can also use multiple particle numerical simulation code to obtain a model for the numerical distribution and use this distribution to relate numerically the coefficient that relates the FWHM of the autocorrelation with the RMS value of this numerical distribution; (3) finally, we can also estimate the bunch distribution, solving the phase retrieval problem exposed previously, and directly compute its RMS value.

5.5.4 Extracting the bunch form factor

The derivation of the bunch form factor from the energy frequency spectrum is a nontrivial problem: there are limiting factors that must be taken into consideration due to the finite bandwidth of some "optical" components in the interferometer.
A first limitation comes from the detector itself: because of the finite diameter of the Golay cell entrance window of approximately 5 mm diameter, it acts as a low frequency filter via diffraction effects. Typically such effects can be simply estimated using the theory of Franhaufer diffraction of plane wave by a circular aperture. This would yield a transmission factor for the Golay cell having the dependence: $\propto \int d\theta [\mathrm{J}_1(2\pi\sigma a \sin\theta)/\sin\theta]^2$. This factor is plotted in figure 5.13 as $T[E]_{gc}$. The cut-off wavenumber is estimated to be approximately $\sigma \simeq 8\,\mathrm{cm}^{-1}$ (i.e. frequency $\simeq 0.1$ THz).
On the other hand, there is a high frequency cut off that is induced by the grid polarizers. Typically such polarizers do not work when the wavelength of the incoming field is greater that the wire spacing ($50\,\mu$m). The reflection coefficients for both the electric component parallel and orthogonal to the wires are given by [51]:

$$R[E_{||}]_{wg}(\sigma) = \frac{1}{1 + \left(2d\sigma \log \frac{d}{2\pi a}\right)^2}, \text{ and } .R[E_{\perp}]_{wg}(\sigma) = \frac{\left(\frac{2\pi^2 a^2 \sigma}{d}\right)^2}{1 + \left(\frac{2\pi^2 a^2 \sigma}{d}\right)^2} \tag{5.48}$$

where a is the wire radius, and d the distance between the wire centers. Using the plot of these reflection coefficients presented in Fig.5.13, we estimate the bandwidth of the autocorrelator to be approximately $8\,\mathrm{cm}^{-1} < \sigma < 500\,\mathrm{cm}^{-1}$.

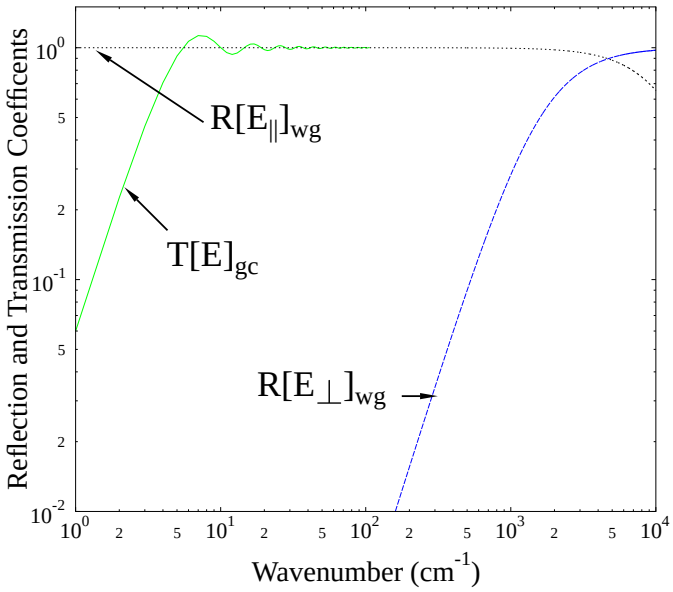

Figure 5.13: Limitation of some optical components in the Michelson polarizing interferometer. $R[E_{\|}]_{wg}$ is the reflection coefficient of the wire grid for the electric field component parallel to the wires, $R[E_{\perp}]_{wg}$ is the reflection coefficient of the wire grid for the component perpendicular to the wires, and $T[E]_{gc}$ is the transmission coefficient of the Golay cell entrance window.

The energy spectrum can be derived by Fourier transforming the autocorrelation deduced from the interferogram. However, we cannot perform an exact Fourier transform and have to use standard Fast Fourier Transform algorithm (FFT) [47] because of the sampled nature of the experimental data. Since the Fourier transform of a sampled function with sampling interval δt is a $1/\delta t$-periodic function, the frequency resolution will be of the order of $1/(2N\delta t)$ if N is the number of samplings acquired. Again note that $\delta t = \delta/c$ is related to the OPD and therefore, for an interferogram acquired with mirror steps of Δ, the frequency spectrum resolution is $1/(4N\Delta)$.

5.5.5 Experimental Results Using an Autocorrelation Technique

A first set of measurements was performed in the period prior first lasing of the IRFEL. Typically, it was found that the Golay cell could easily detect, with a fairly good signal over noise, the coherent transition radiation power generated as the electron beam was in low duty cycle mode (the so-called tune-up mode); signals with amplitude of the order of 1 V were seen in this case.

Autocorrelation measurement

Figure. 5.14(A) and (B) depicts two autocorrelation measurements performed the same day, it corresponds to the longitudinal phase space setup used for the first FEL light generation. The difference between Figures (A) and (B) comes from the ghostpulse background. In (B) the ghostpulse was not cautiously minimized by properly setting the electro-optics crystal of the photocathode drive laser whereas in (A) ,such operation was properly performed. Figure. 5.14(C) which represent the algebraic difference between the two measurements, shows that the only difference between the two aforementioned measurements resides in the presence of a DC offset for the case where the ghostpulse is not minimized. Therefore the autocorrelation itself is not at all contaminated by the ghostpulse.

From these interferograms we can also notice other features: (1) The autocorrelation is not symmetric and does not vanish when the path length in the two arms are identical. This fault was initially thought to be due to a non perfect orthogonality between the two mirrors in the two arms; we tried to correct for it by installing piezoelectric picomotors on the movable mirror so that its tilt can be adjusted remotely while performing a measurement. Unfortunately we never managed to get the interferogram to vanish at this location. (2) There are secondary bumps located at approximately $\pm 1800\,\mu$m that probably corresponds to reflections in the system (the distance $1800 \times 2 = 3600\,\mu$m corresponds to the distance between the optical vacuum window and the plano-convex lens).

In Fig. 5.15(A) we present a fine scan (mirror step size for the displacement is $5\,\mu$m) of the central peak of the interferogram shown in Fig. 5.14(A). From this peak we can deduce the rms width ($\simeq 110\,\mu$m) and also distinguish whether the core of the beam longitudinal distribution is a gaussian-like or square-like bunch distribution. For such a purpose we have plotted on the same figure the equivalent gaussian and square distribution that have the same FWHM and the same integral. Neither of these standard distributions really fit the interferogram core. However a distribution that consists of the sum of the two previous distributions better matches the interferogram core.

Dependence of the interferogram on the beam transverse size on the TR screen

A second set of experiments we performed was to study how sensitive the bunch length measurement was with respect to the beam transverse size on the TR radiator. The procedure consisted in varying an upstream quadrupole triplet to vary the beam spot size at the point of bunch length measurement. For each setting of the triplet we measured, at the same time, the beam transverse spot size and then the bunch length. For such purpose we can direct the transition radiation to the interferometer or a CCD camera by moving the "switcher mirror". The images recorded by the CCD camera are processed accordingly to the description of Chapter 3 and the beam transverse profile and rms width are then computed. The results of the measurements for five different settings of the upstream optics are presented in figure 5.16 while the FWHM of the interferogram along with the corresponding transverse beam sizes are gathered in Tab. 5.5.5.

Case	Interferogram	σ_x	σ_y	$\sqrt{\sigma_x \sigma_y}$
	FWHM (μm)	(mm)	(mm)	(mm)
(a)	200	0.4215	0.3415	0.3794
(b)	240	0.5316	0.3987	0.4604
(c)	240	0.7843	0.5763	0.6723
(d)	320	1.2554	1.1164	1.1839
(e)	280	1.4667	1.6240	1.5433

Table 5.2: Measured bunch length and transverse beam dimension for the cases reported in Fig. 5.16.

Computation of the longitudinal bunch distribution

Using the methodology previously exposed, we have developed an off-line analysis code that allows the computation of the bunch longitudinal distribution.
Because the experimentally obtained interferogram is not perfectly symmetric, its Fourier transform, i.e. the energy spectrum, will not be real. Hence the first step consists of symmetrizing the Fourier transform. We have implemented three methods: we can either use only the left part of the interferogram, or the right part; we can also symmetrize the interferogram by computing the average of the left and right part of the interferogram. The autocorrelations so-obtained and their corresponding Fourier transforms are presented respectively in Fig. 5.17-A and Fig. 5.17-B. We can notice that there is not much difference between the computed spectra. The method we will use henceforth is the "average" method.

Moreover, the interferogram (and therefore the autocorrelation) can be measured for arbitrary mirror displacement. However the information contained at large displacement might not be relevant to compute the energy spectrum. To verify such assumption, we have used different length of the central part of autocorrelation presented in figure 5.14: we used 64, 128, 256, and 512 points; note that because we used an FFT algorithm that employs a radix-2 algorithm, the number of points in the sequence must be a power of 2. From our previous discussion we noticed that the step size in the Fourier plane (i.e. the energy spectrum) increases inversely to the number of points in the standard plane (i.e., the interferogram). Therefore a naive argument would be, for a given mirror displacement step, to measure the interferogram over a large range. Practically there are two arguments against this fact: (1) the measurement can take up to one hours (depending on the mirror displacement step size) and (2) for large values of the displacement the two TR pulses associated with the electron bunch do not overlap anymore and therefore the interferogram does not provide any information for the power spectrum (i.e. the autocorrelation is theoretically zero). From figure 5.18 we see that indeed there is a compromise on the number of points; if this number is too small, the fine structure of the spectrum is lost and the reconstructed bunch distribution is smoothed. On the opposite, if the number of points is too large, because points corresponding to large displacements consists only of noise, this noise propagates on the spectrum and a great detail of fake structure appears. A proper choice is to "manually" cut *ad viso* the autocorrelation at the point it seems to vanish. In our case typical values are ± 1.5 mm.

Experimentally we can clearly distinguish, for a wavenumber of approximately $10\,\mathrm{cm}^{-1}$, the low frequency cut off induced by the finite aperture size of the Golay cell detector entrance window. This low frequency part of the spectrum must somehow be reconstructed, otherwise the experimentally computed energy spectrum cannot be used to recover the bunch longitudinal distribution. For such a purpose we extrapolate this low frequency region of the spectrum using the fact that

for large frequency (i.e. low wavelength), the bunch form factor has a quadratic dependence on the frequency; the CTR spectrum has the same dependence. Hence, using the general polynomial expansion of the BFF derived in this chapter, the spectrum can be extrapolated using the equation: $I(\sigma) = a_0 + a_2\sigma^2 + \mathcal{O}(\sigma^3)$. The point of attachment of this parabola is chosen to be in the neighborhood of the low frequency cut off. The coefficient a_2 and a_0 are computed by using the continuity conditions at the cut off point: we assume both the spectrum and its local derivative with respect to wavelength are continuous. In figure 5.19 we perform different low frequency extrapolations of the energy spectrum by varying the parameter a_2 and using only the continuity of the spectrum at the cut-off point to compute the coefficient a_0. The influence of these different extrapolations on the recovered longitudinal bunch distribution is shown in figure 5.20. It is interesting to note that one way to reject unphysical distribution is to reject all the parabolic extrapolations that give a significant number of negative values in the bunch longitudinal distributions.

5.6 Zerophasing Technique for Bunch Length Measurement

5.6.1 Basis of the Method

The so-called zerophasing (or backphasing) technique has proven to be a very powerful method. It has been demonstrated to resolve bunch length in the subpicosecond regime [52]. Therefore we investigated the possibility of its application to measure the bunch length in the IRFEL accelerator. The zerophasing method uses RF accelerating cavities phased ± 90 degrees off crest i.e. in such a way that the bunch centroid coincides with a zero accelerating electric field. Hence the cavities induce a longitudinally dependent energy ramp along the bunch. Then, by means of a spectrometer, the energy distribution is mapped into the transverse direction, and the beam transverse density is measured with a beam profile station located in the dispersive region. Therefore to implement this method we only need accelerating cavities and spectrometers. There are two spectrometers readily available to perform such measurements: we can use the energy recovery dump line or the first 4-bend chicane. Preliminary considerations have shown that the latter is not easily workable: the dispersion in the chicane at the beam profile measurement station is about 2 times less than the one at the OTR profile monitor located in the energy recovery dump.
Despite the fact that the energy recovery dump has been chosen as a spectrometer, it is not an optimum choice: the maximum beam energy that can be deflected into the dump is about 24 MeV [5] which implies that the four last cavities of the cryomodule must be turned off and/or used as zerophasing cavities. The non-zerophased cavities are operated under their nominal settings (accelerating gradient 7.33 MV/m, phase -9.6 deg) giving a beam energy of 23.74 MeV. At such an intermediate energy, the dynamics of 60 pC bunches is not emittance dominated, requiring a study of space charge effects on the measurement.
In the FEL, the energy recovery dump line consists of a quadrupole and an OTR profile monitor. The dispersion at the OTR location when the quadrupole is turned off is expected to be η=75 cm; this latter value can be reduced, if needed, using the upstream quadrupole.
It should be stressed that the measured bunch length is the bunch length at the exit of the fourth cavity i.e. in the middle of the SRF-linac (the PARMELA predicted bunch length and phase space slope at this location are 370 μm and -48.74 MeV/m respectively).

Following notation of Reference [52], we write the horizontal position x on the beam profile

[5] Private communication from R. Legg, January 1998

measurement station of one electron with longitudinal position z with respect to the bunch center as:

$$x = x_\beta + \left(\frac{2\pi e V_{RF}}{\lambda_{RF}} + \frac{dE}{dz}\right)\frac{\eta}{E_0} z \stackrel{\text{def}}{=} x_\beta + (C_0 + C_1)z \tag{5.49}$$

where C_0 is the contribution from RF-induced energy spread and C_1 is the sum of initial intrinsic energy spread and the space charge energy spread induced as the beam drifts. x_β, V_{RF}, λ_{RF}, η and E_0 are respectively the pure betatron contribution to the position, the total accelerating voltage of the cavities used during the measurement (i.e. operated at zero-crossing), the RF-wavelength (for 1497 MHz it is 20.05 cm), the dispersion at the beam profile measurement location, and the average beam energy at the entrance of the first cavity operated at zero-crossing. $\frac{dE}{dz}$ is the longitudinal phase slope; it can be expressed using the beam matrix element as $\frac{dE}{dz} = -\sigma_{56}/(\sigma_z^2)$ where σ_{56} is the energy position correlation i.e. $\sigma_{56} = -\langle zE \rangle$.

Let σ_x^0, $\sigma_x^\pm$, be the beam sizes measured after the spectrometer dipole on the OTR profile monitor, with the cavities respectively turned off and turned on at their ± 90 deg zero-crossing point. Since the beam profile on the profile monitor is the convolution of pure betatron contribution i.e. transverse and longitudinal phase space, these beam sizes can be expressed as:

$$(\sigma_x^0)^2 = \sigma_\beta^2 + C_1^2 \sigma_z^2 \tag{5.50}$$

$$(\sigma_x^\pm)^2 = \sigma_\beta^2 + (C_1 \pm C_0)^2 \sigma_z^2 \tag{5.51}$$

σ_β is the horizontal betatron contribution to the beam spot size.

Because the sign of the product $2C_0C_1$ is alternated as the cavities are operated at ± 90 deg, this quantity can be eliminated and by computing the pure dispersive contribution due to the energy spread induced by the cavities at ± 90 deg i.e.[6] $(X_{RMS}^\pm)^2 = (\sigma_x^\pm)^2 - (\sigma_x^0)^2$, it is straightforward to deduce an analytical expression for the bunch length:

$$\sigma_z = \frac{\left[(X_{RMS}^+)^2 + (X_{RMS}^-)^2\right]^{1/2}}{\sqrt{2}|C_0|} \tag{5.52}$$

Finally we can also estimate the coefficient C_1, which can provide information on the phase space slope, using the formula:

$$C_1 = \frac{|C_0|}{2}\frac{(X_{RMS}^+)^2 - (X_{RMS}^-)^2}{(X_{RMS}^+)^2 + (X_{RMS}^-)^2} \tag{5.53}$$

Note that in the case of small energy spread these formulae reduce to the one derived in reference [52].
From Eqn.(5.53) the longitudinal phase space slope is:

$$\frac{dE}{dz} = \frac{\pi V_{RF}}{\lambda_{RF}}\frac{(X_{RMS}^+)^2 - (X_{RMS}^-)^2}{(X_{RMS}^+)^2 + (X_{RMS}^-)^2} \tag{5.54}$$

In summary, the measurement of bunch length (and potentially phase space slope) reduces to three beam profile measurements for three different settings of the zerophasing cavities (± 90 deg, and 0 deg).

[6] The beam transverse density at the profile measurement station is a convolution of the betatron distribution with the energy distribution. The rms value of a function $g = f * h$ ($*$ is the convolution product) is $\langle g^2 \rangle = \langle f^2 \rangle + \langle h^2 \rangle$

Transverse Space Charge Effects

As a first approximation, we can estimate transverse space charge using the K-V envelope equations by calculating the ratio of the emittance term with the space-charge term (we assume the beam is cylindrical-symmetric):

$$R = \frac{1}{4}\frac{I_p}{I_0}\frac{2}{(\beta\gamma)^3}\left(\frac{\sigma_x}{\epsilon_x}\right)^2 \tag{5.55}$$

where I_p is the peak current, I_0 the Alfvèn current (17000 A for electrons), β and γ are the usual relativistic factors. For the expected values obtained via numerical simulation we estimated R to be approximately 0.6 at the cavity #5 exit. Therefore space charge and emittance terms are of the same order in driving the transverse beam envelope.
In equation 5.51, one must insist that σ_β contains the transverse space charge effect. In order to validate the derived equations to compute the bunch length and phase space slope, we must make sure that σ_β, as it is implicitly assumed in the previous section, remains the same as the zerophasing cavities phased are turned on and phased at their two zero crossing[7]. We have verified such assumption using the PARMELA code: the beam envelopes along the beamline are plotted in figure 5.22 for different cases (different number of zero-phasing cavities used): each case is treated with the PARMELA space charge routine turned on and off. The effect on the beam size before the spectrometer, in all the cases, remains the same and increases the beam rms size by approximately 36 μm. Therefore the transverse space charge contribution to the beam size on the OTR is included in σ_β which is measured when the cavities are turned off. Also it remains the same as the cavities are turned with their phase set at $\pm$90 deg. Hence the transverse space charge contribution is indeed deconvolved unambiguously when one uses the Eqn.(5.52) to compute the bunch length.

Longitudinal Space Charge Effect

The longitudinal space charge tends to induce bunch lengthening which in turn rotates the longitudinal phase space. Hence one way of assessing the associated effect is to study how the phase space slope evolves as the cavities are zero-phased. One can conceive that because of the space charge the slope at the dipole entrance is approximately:

$$\frac{dE}{dz} = \left[\frac{dE}{dz}\right]_{init} + \left[\frac{dE}{dz}\right]_{SC} \tag{5.56}$$

where $\left[\frac{dE}{dz}\right]_{init}$ is the phase space slope upstream the first zerophasing cavity, and $\left[\frac{dE}{dz}\right]_{SC}$ represents the space charge induced phase space rotation.
Again we need to justify that $|C_1|$ remains the same as the zerophasing cavities settings are changed: namely we must make sure that the space charge induced slope is the same in the different cases. This can be understood since the zerophasing cavities are not providing energy. We have checked this using PARMELA: the slope evolution for the different cases of zerophasing are presented in figure 5.24. For each case we compare the slope computed with the space charge routine turned

[7] There is another effect that can significantly affect the transverse beam size on the profile monitor: the cavity focusing effect. Such effect is investigated later in this dissertation and was anyway found to be very small for the purpose of the present discussion; therefore we ignore it for sake of simplicity.

# zero. cav	1	2	3	4
C_0	3.7028	7.4057	11.1085	14.8114
C_1	1.1656	1.0873	1.0056	0.8991
Slope (Mev/m)	36.1706	33.7412	31.2067	27.9008
X^+_{RMS} (mm)	1.8434	3.2860	4.7258	6.1368
X^-_{RMS} (mm)	0.8789	2.4282	3.9352	5.4319
σ_z (mm)	0.3900	0.3901	0.3915	0.3913

Table 5.3: rms beam horizontal size simulated with the PARMELA particle pushing code on the energy recovery transfer line profile measurement station.

on and off. It is noticed that the variation of the slope due to space charge is the same for all the cases and we have estimated this variation for the normalized slope $\frac{d\delta}{dz}$ to 0.54 %/m.

5.6.2 Numerical Simulation of the Method

We have numerically performed a bunch length measurement for the nominal settings using the relations derived above. We have done such measurement using 1, 2, 3, and 4 zerophasing cavities to check the constancy of the method. Table 1 summarizes the results we obtained. For the nominal bunch length of 370 μm the computed bunch length is always overestimated by about 20 μm. On the other hand the coefficient C_1 is dependent on the number of cavities (in fact on the drift distance). The beam size measured at the OTR location are shown in figure 5.25, for the two zero-phasing values $\pm$90deg, versus the number of zero-phasing cavities. In the figure we also simulate the measurement with the PARMELA space-charge routine turned off to verify again our previous statement that we could unambiguously deconvolve transverse space charge effect contribution to the beam size. In figure 5.26, we present the beam distribution in the transverse plane along with the horizontal beam projection, in the case where four cavities are used as zerophasing cavities.

5.6.3 Experimental Results

During the early stage of the commissioning of the linac, we attempted a bunch length measurement using the zerophasing method. We tried to zerophase different numbers of cavities and since the bunch length was larger than expected we needed only to use two cavities.
During our experiment, the gradient of the two zerophasing cavities was set to 7.33 MV/m, the total energy of the incoming beam was estimated to be 23.75 MeV; with such value the constant C_0 defined in Eqn.(5.49) is approximately $C_0 \simeq 7.19$.
The rms size of the horizontal projection of the beam spots, presented in fig. 5.27, recorded during the zerophasing experiment are respectively: $\sigma_x^0 \simeq 3.5$ mm, $\sigma_x^{-90} \simeq 5.8$ mm and $\sigma_x^{+90} \simeq 4.0$ mm; these values yield $X^-_{RMS} \simeq 1.9$ mm and $X^+_{RMS} \simeq 4.7$ mm.
Using Eqn.(5.52) we get an rms bunch length estimate of $\sigma_z \simeq 488 \pm 112\,\mu$m and the longitudinal phase space slope $\frac{dE}{dz} \simeq -82$ MeV/m. Both of these values are in disagreement with the parameters predicted with PARMELA. These discrepancies were not relevant at the time the measurement was performed: the injector beam dynamics was not yet fully understood and the settings not optimized. Also note that the error bar on the bunch length measurement is obtained using the

error propagation [8] theory applied on Eqn.(5.49), assuming an uncertainty of 10% on η, V_{RF}, and the beam sizes measurement, and a relative error of 2% on the beam energy inferred from the dipole magnet strength.

5.7 Intrinsic Energy Spread Measurement

5.7.1 Method

The estimation of the beam energy spread is performed by measuring transverse beam profile in a plane where there is significant dispersion. In the case of the IRFEL, several locations can be used to measure the energy spread. Typical high-dispersion point are, symmetry points of the chicane and various location in the recirculation arc. In the plane where dispersion occurs, i.e. in the horizontal plane in our case, the rms beam size is written:

$$\sigma_x = \left[(\eta\delta)^2 + \beta\tilde{\varepsilon}\right]^{1/2} \tag{5.57}$$

This commonly used relation is valid as long as nonlinearities in the transport is negligible. Typically, for the nominal energy (without lasing) spread in the IRFEL (0.2% RMS) it can be used. From Eqn.(5.57) we see that to deduce the energy spread we must know the dispersion function, η, but also the betatron contribution $\beta\tilde{\varepsilon}$ to the beam size. Though the former can be easily measured or estimated via magnetic optics code, the latter requires an emittance measurement (in a dispersion free region) and the propagation of the Twiss parameters to the dispersive region where energy spread is to be measured. Indeed we can avoid the emittance measurement[9] by varying the strength of an upstream quadrupole while observing the beam size on the dispersive location, until the beam size is minimum. At that point the betatron term contribution to the beam size is the smallest possible. In figure 5.28, we present the beam size variation for two scenarii of energy spread (i.e. the case were the laser is off i.e. $\sigma_\delta \simeq 0.2\%$ and on i.e. $\sigma_\delta \simeq 2\%$). For the lowest energy spread the minimum beam rms size simulated with DIMAD is comparable to the quantity $\eta\delta$. However for larger energy spread, we observe discrepancies between the value computed from DIMAD and the one derived from Eqn.(5.57). This disagreement comes from the non-negligible nonlinear dispersion at the location of the beam size measurement which renders Eqn.(5.57) difficult to use (because it only contains linear dispersion): Let $x_{0,0}$, $x'_{0,0}$ be the position and divergence of an electron at the entrance of a magnetic system, with a zero-energy spread, and let $x_{0,\delta}$, $x'_{0,\delta}$ be the same coordinates associated to an electron with an energy spread δ. Inside the bending system that generates energy spread, we will have:

$$\begin{aligned} x_{f,0} &= R_{11}x_{0,0} + R_{12}x'_{0,0} \\ x_{f,\delta} &= R_{11}x_{0,\delta} + R_{12}x'_{0,\delta} + R_{16}\delta + T_{166}\delta^2 \end{aligned} \tag{5.58}$$

[8] The systematic error, $\Delta\sigma_z$, on the bunch length computation is:

$$(\Delta\sigma_z)^2 = \frac{\lambda_{RF}^2\left[(X^+_{RMS})^2 + (X^-_{RMS})^2\right]}{8\eta^2\pi^2V_{RF}^2}(\Delta E_0)^2 + \frac{E_0^2\lambda_{RF}^2\left[(X^+_{RMS})^2 + (X^-_{RMS})^2\right]}{8\eta^4\pi^2V_{RF}^2}(\Delta\eta)^2 +$$
$$\frac{E_0^2\lambda_{RF}^2\left[(X^+_{RMS})^2 + (X^-_{RMS})^2\right]}{8\eta^2\pi^2V_{RF}^4}(\Delta V_{RF})^2 + \frac{E_0^2\lambda_{RF}^2\left[16(\sigma_x^0)^2(\Delta\sigma_x^0)^2 + 4(\sigma_x^-)^2(\Delta\sigma_x^-)^2 + 4(\sigma_x^+)^2(\Delta\sigma_x^+)^2\right]}{32\eta^2\pi^2V_{RF}^2\left[(X^+_{RMS})^2 + (X^-_{RMS})^2\right]}$$

[9] Suggestion from D.R. Douglas

$$= \quad x_{f,0} + R_{16}\delta + T_{166}\delta^2$$

Therefore we can define an orbit offset with respect to the "reference orbit", i.e. the orbit of the electron with no energy offset $\delta = 0$, as:

$$\Delta x \stackrel{def}{=} x_{f,\delta} - x_{f,0} = R_{12}x'_{0,\delta} + R_{16}\delta + T_{166}\delta^2 \tag{5.59}$$

Hence the energy spread can be expressed as a function of Δx by solving the second degree equation in δ and taking the physical solution:

$$\delta = -\frac{R_{16}}{2T_{166}}\left[1 - \left(1 + 4\frac{T_{166}}{R_{16}^2}(\Delta x)^2\right)^{1/2}\right] \tag{5.60}$$

In the case of practical value in the bending systems of the IRFEL, a third-order Taylor expansion is largely sufficient, therefore the energy offset of an electron at position Δx with respect to the reference orbit is:

$$\delta = -\frac{\Delta x}{R_{16}} + \frac{T_{166}(\Delta x)^2}{R_{16}^3} - \frac{2T_{166}(\Delta x)^3}{R_{16}^5} \tag{5.61}$$

As an example we shall consider an energy-spread measurement performed using a beam profile monitor located in the center of one of the by-pass chicanes: Using the second order magnetic optics code DIMAD, we computed transfer the matrix elements to be $R_{16} \simeq -42$ cm and $T_{166} \simeq 45$ cm.

5.8 Estimate of Longitudinal Emittance in the Undulator Vicinity

An important parameter to permit the laser to turn on, as we will discuss in detail in Chapter 6, is the longitudinal emittance. We define it as:

$$\tilde{\varepsilon}_{\phi\delta} = \sqrt{\langle\phi^2\rangle\langle\delta^2\rangle - \langle\phi\delta\rangle^2} \tag{5.62}$$

where ϕ is the longitudinal coordinate expressed in units of RF-degree and δ is the momentum spread.

At the undulator location, the longitudinal phase space is at a longitudinal waist i.e. the correlation coefficient $\langle\phi\delta\rangle$ vanishes and therefore the emittance is simply the product of rms bunch length and energy spread. At the undulator location we can measure the bunch length using CTR methods (see fig. 5.29). However an energy spread measurement can be performed only in a high dispersion point i.e. in the middle of one of chicane thanks to an OTR profile monitor (see fig. 5.29). It is therefore important to check how the measured energy spread relates to the energy spread at the bunch length measurement station. Under the validity of linear transfer matrix formalism, it is clear that energy spread should be the same over the whole region provided the FEL is turned off. However, we must be cautious about the applicability of linear optics: there are a few effects that can significantly spoil the energy spread. The principal effects are the longitudinal space charge force and wakefield effects. The former has been studied by performing numerical simulations using the code PARMELA. As pictured in figure 5.30, where we compare the longitudinal phase space at the wiggler insertion and the one at one potential point of measurement, namely the downstream chicane midpoint, the energy distribution change is insignificant. The degradation of energy spread

induced by space charge is not a concern in the present discussion.

The second mechanism that can potentially deteriorate the beam energy spread is due to wakefield generation as the beam encounters discontinuities in the vacuum chamber. Between the point of bunch length measurement and the energy spread measurement station, the largest discontinuity is introduced by the beam pipe size variation close the wiggler magnet: there is a transition between the standard beam vacuum chamber, that has a circular section of 50.8 mm diameter, and the undulator vacuum chamber which has a rectangular section of $48\times9\,\mathrm{mm}^2$.
Wakefield forces are due to the change in boundary conditions surrounding a particle, which obligate the Coulomb field to reorganize. An electron in the head of the bunch can cause an electric field at the location where the boundary condition changes. An electron behind can interact with this electric field and thereby modify its orbit. Typically wakefields are described by wake functions. For an electron traversing a structure with an offset (x, y), with its velocity parallel to z, the wake function writes:

$$\overrightarrow{W}(x,y,s) = \frac{1}{e}\int_{-\infty}^{\infty} dz \left(\overrightarrow{E}(x,y,z,t) + c\hat{z} \wedge \overrightarrow{B}(x,y,z,t)\right) \tag{5.63}$$

If we assume all the electrons are centered in the structure, i.e. $x = y = 0$, the principal effect of wakefield is to introduce energy variation along the bunch which in turn can spoil the rms energy spread. The rms energy spread induced by this effect is purely coming from the longitudinal wakefield, $W_{||}$; it writes:

$$\sigma_{\delta,\mathrm{wake}} = e^2\left[\int_{-\infty}^{\infty} ds\Lambda(s)W_{||}^2(s) - k_{||}^2\right]^{1/2} \tag{5.64}$$

where $\Lambda(s)$ is the bunch distribution function, and $k_{||} \overset{\mathrm{def}}{=} -1/e\int_{-\infty}^{\infty} W_{||}(s)\Lambda(s)ds$ is the total loss factor.
In the present case the computation of the wakefield is estimated by using a 2D code TBCI which also assumes the bunch is a rigid line charge distributed along a gaussian distribution. The expected energy spread increase to the wakefield effect is presented in figure 5.31: it is noticed that the associated energy spread is, in the worst case 25 times less than the beam intrinsic rms energy spread (of typically 50 keV at 38 MeV as achieved in numerical simulations). Hence it is not expected to have a significant contribution since the total energy spread is the quadratic sum of the intrinsic and wakefield induced energy spread. Moreover the step transition between the wiggler and the circular vacuum chamber has been smoothed by introducing a "trumpet" shaped copper piece.

Hence under the assumption that there is no mechanism to spoil significantly the energy spread of the beam, when the longitudinal envelope is at a waist close to the undulator location (.e. $\langle\delta z\rangle \simeq 0$), the longitudinal emittance reduces to $\tilde{\varepsilon}_z \simeq \sigma_z\sigma_\delta$ (where σ_z is the bunch length measured in the undulator vicinity and σ_δ is the energy spread measured in one of the high dispersion locations in the chicanes). Typical bunch length and energy spread measured during the commissioning of the IRFEL, in the period just prior to first laser light production, are respectively $\sigma_z = 110 \pm 30\,\mu$m and $\sigma_\delta = 0.25 \pm 0.05\,\%$ which yield a longitudinal emittance of approximately 18.8 ± 5.5 deg-keV. This is much larger than the expected value from the PARMELA code (11.7 deg-keV) but still within the specification 33 deg-keV.

5.8.1 Conclusion

In this chapter we have developed techniques to measure bunch length. Theses techniques include both a frequency-based method that consists of measuring the energy spectrum of coherent transition (and potentially synchrotron) radiation, and a time-based method. Both techniques are capable of resolving picosecond-time-scale bunch lengths. Along with bunchlength measurement, some insights on the longitudinal phase space can be obtained by measuring the energy spread from which, knowing the bunch length, the longitudinal emittance can be computed.

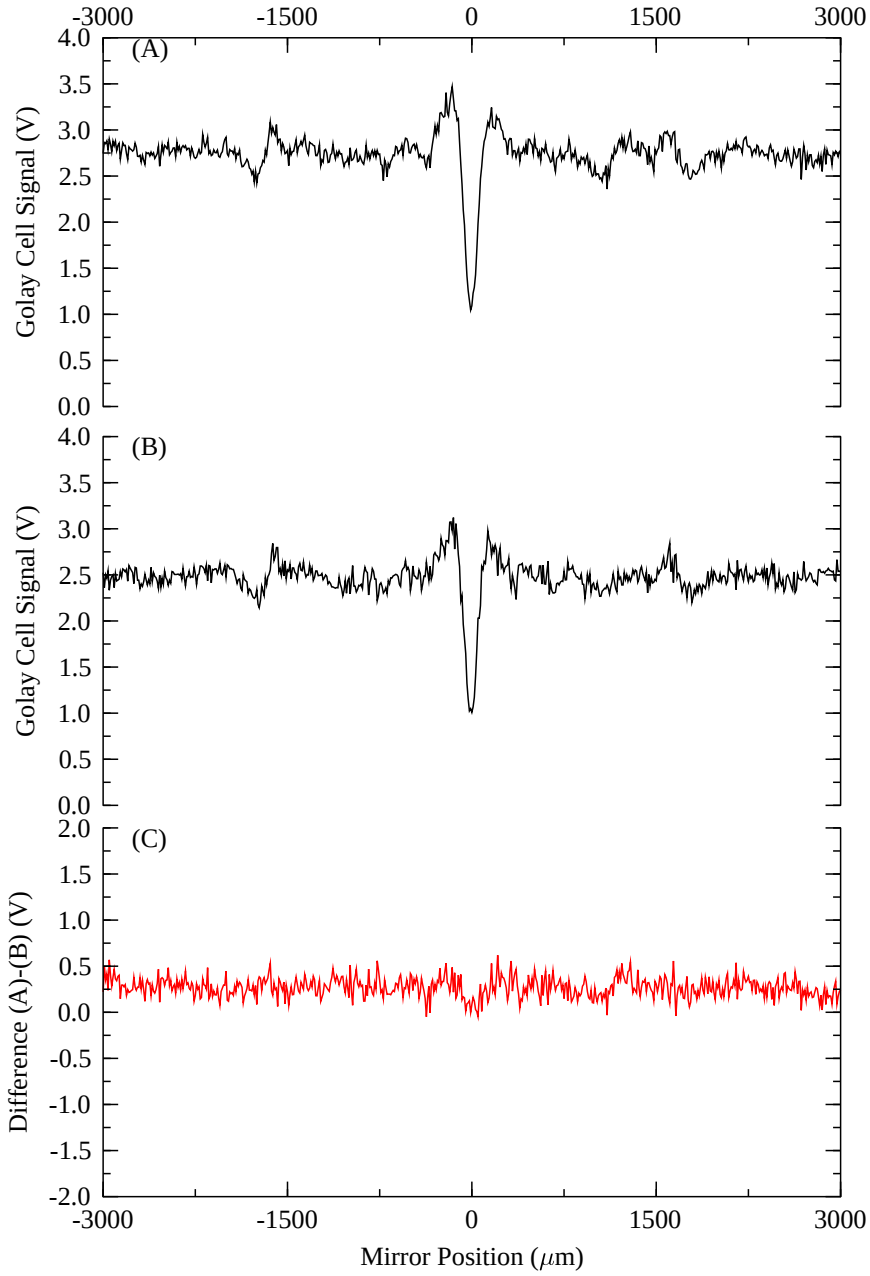

Figure 5.14: Complete interferograms taken few minutes apart: In **(A)**, the ghost-pulse was not totally suppressed while in **(B)** it was. **(C)** gives the difference between the two previous plots **(A)**-**(B)**

.

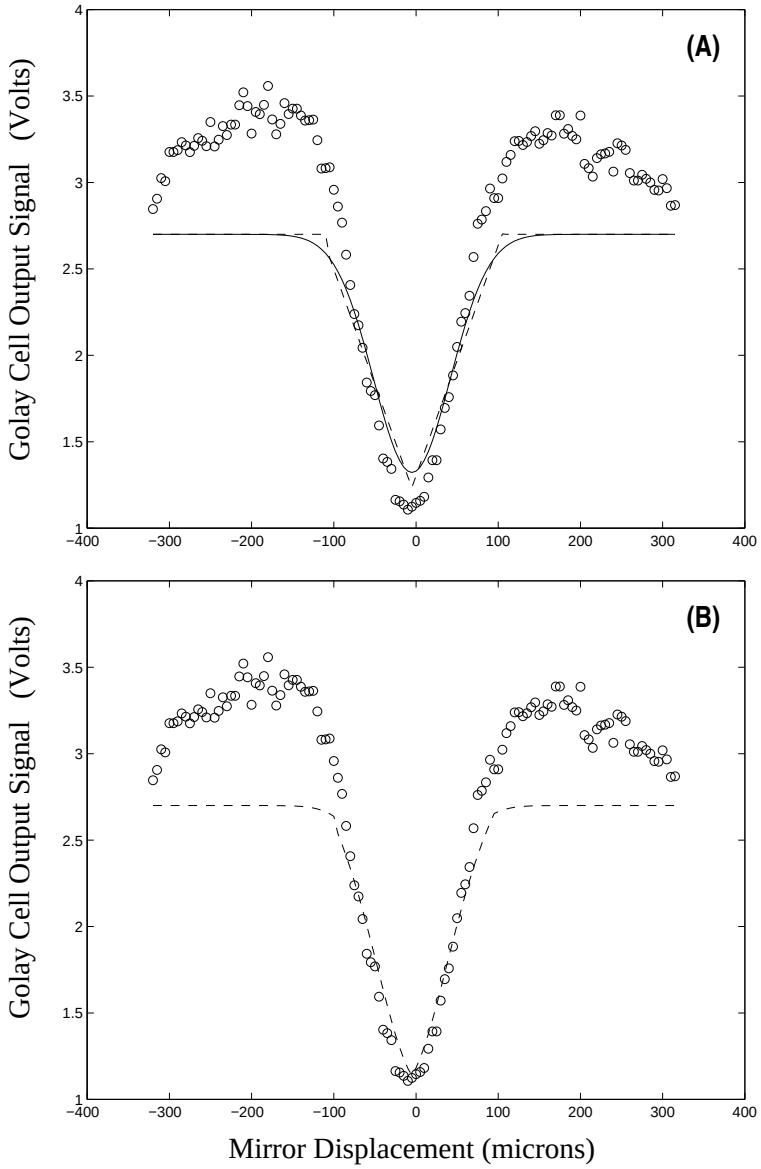

Figure 5.15: Fine scan of the central part of the interferogram presented in Fig. 5.14(A). The experimental interferogram (circle) is compared with an interferogram generated from a gaussian distribution (solid line) and a square distribution (dash line) both of these distribution have the same FWHM **(A)**. The interferogram is compared with an interferogram of the sum of a square and gaussian distribution both having a FWHM of 110 μm **(B)**. The baseline is 2.7 V.

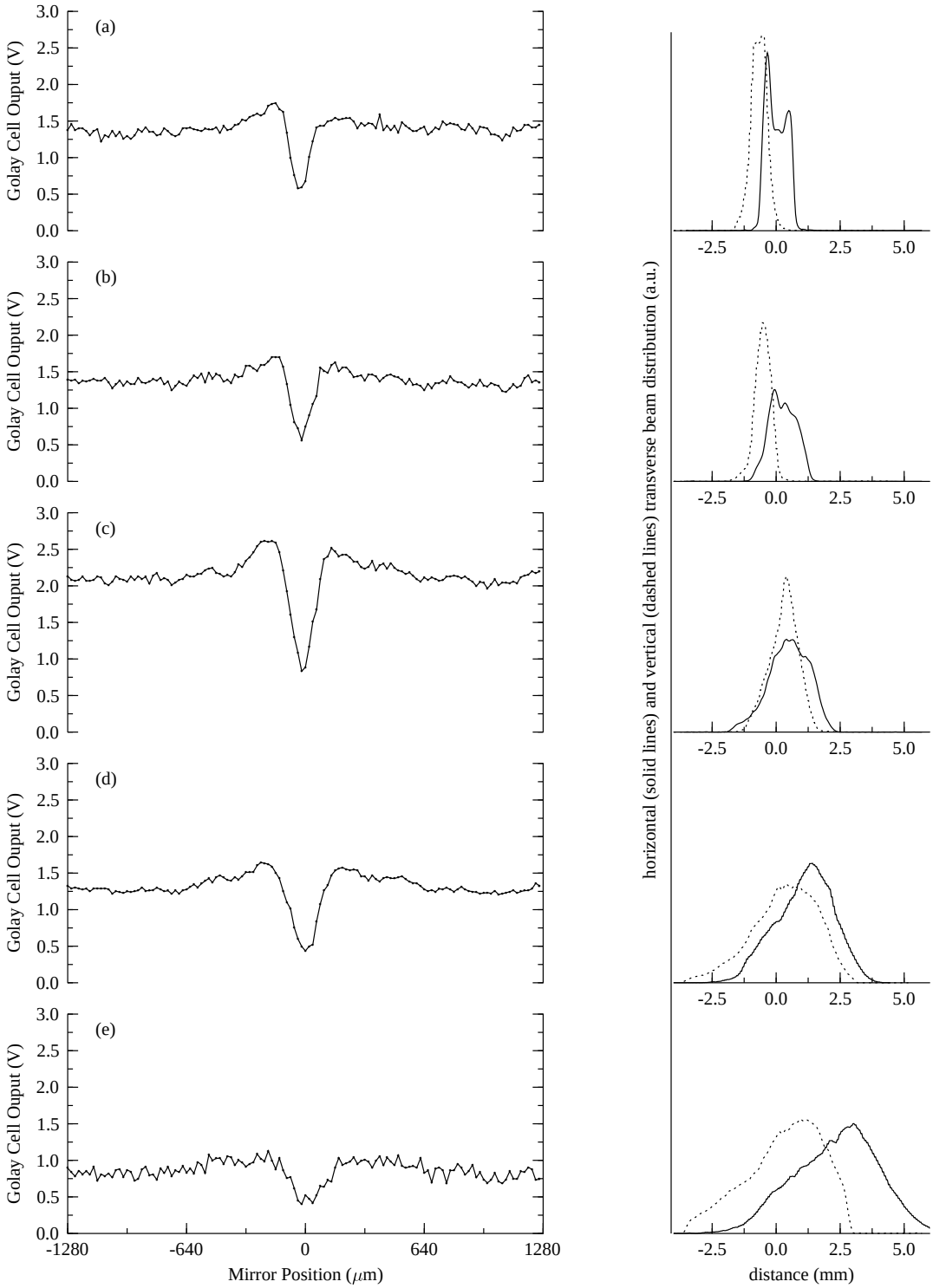

Figure 5.16: Interferogram measured for different transverse beam size on the TR radiator. The left plots are the measured interferograms whereas the right plots show the beam transverse (horizontal and vertical) distributions.

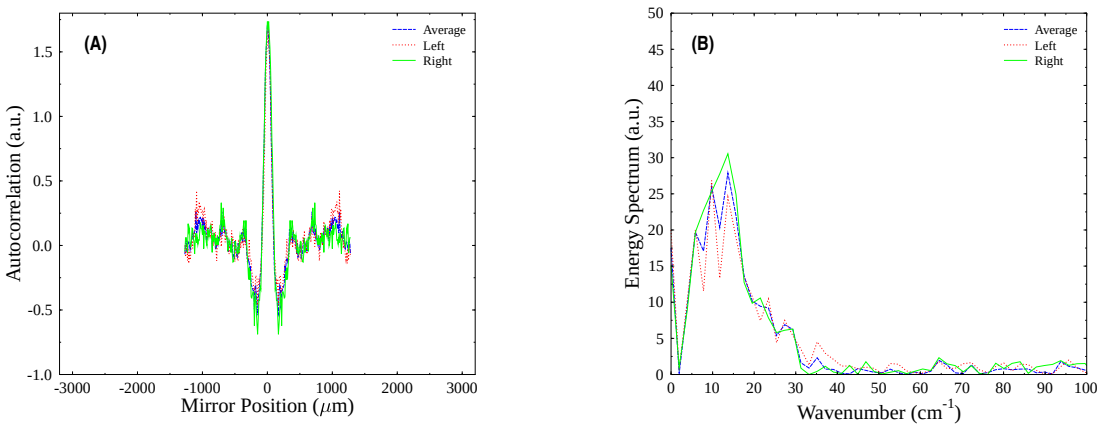

Figure 5.17: Symmetrization of the autocorrelation by different methods **(A)** (see text for detail) along with the corresponding power spectrum **(B)**.

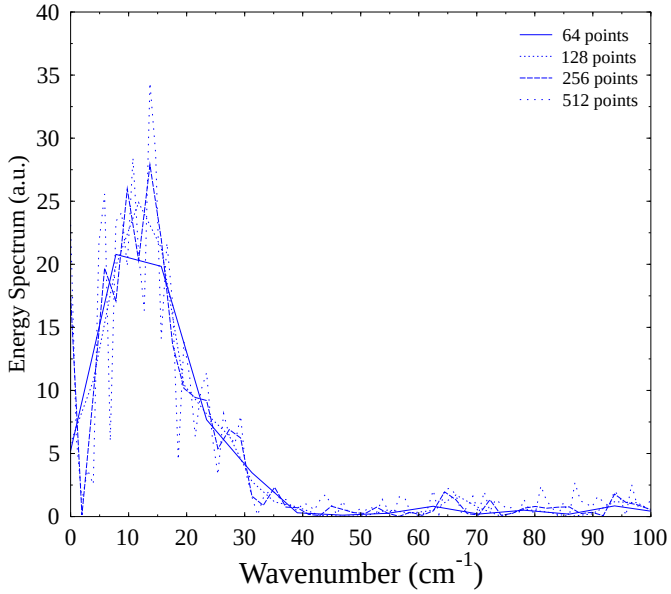

Figure 5.18: Energy spectrum obtained by considering different numbers of data points from the autocorrelation. The numbers are all powers of two, as required by the FFT algorithm we used.

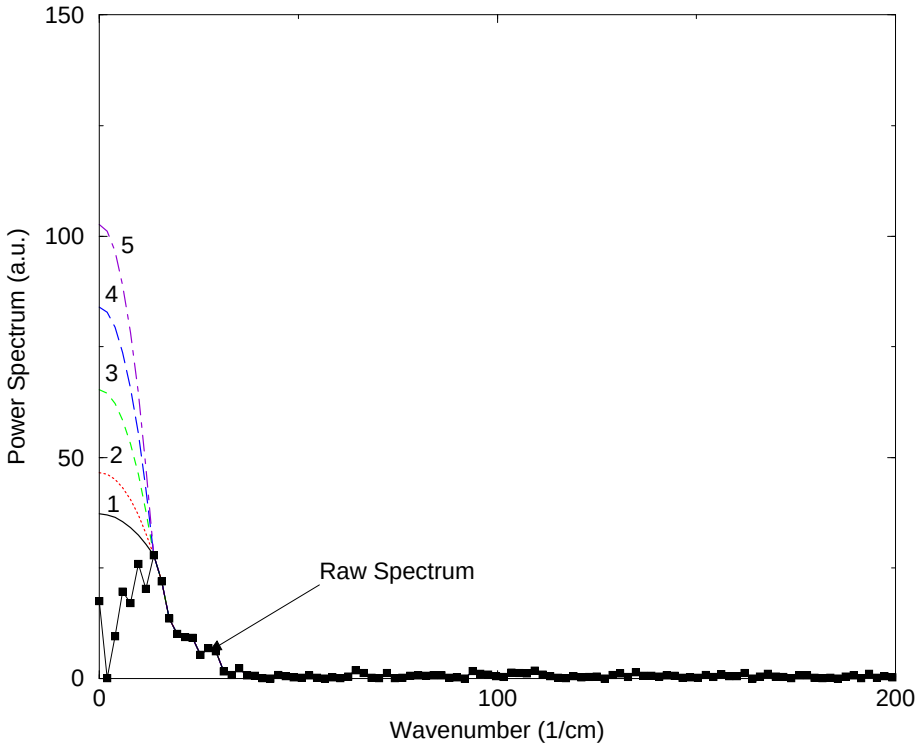

Figure 5.19: Energy spectrum obtained by Fourier transforming an autocorrelation with 256 data points (solid line with squares) and the different low frequency extrapolations considered.

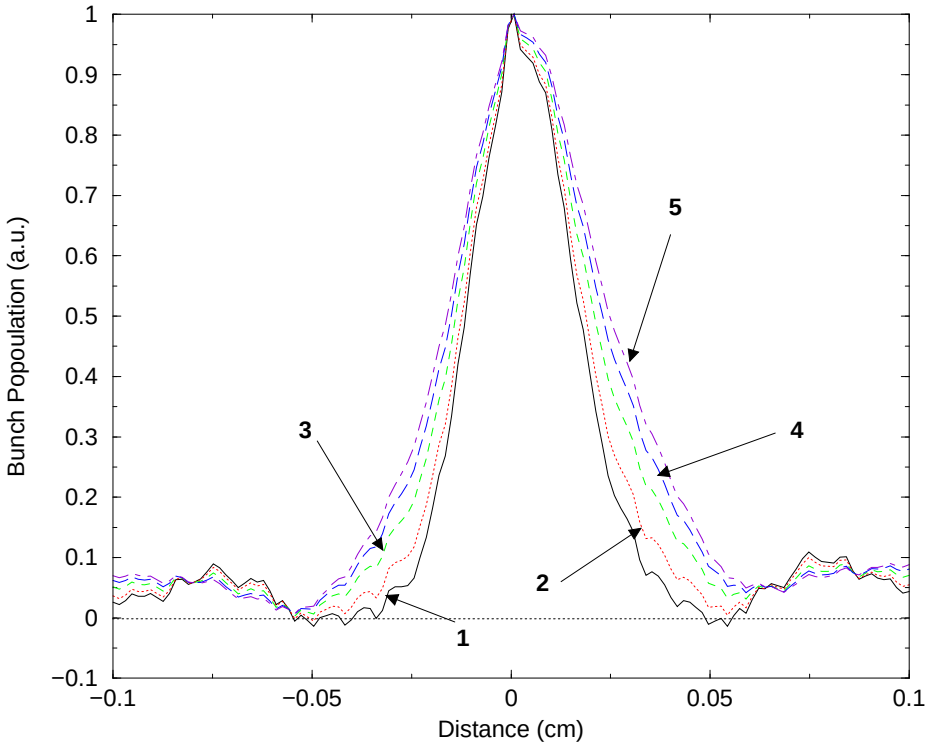

Figure 5.20: Recovered longitudinal bunch distribution for the different extrapolation of the power spectrum shown in figure 5.19.

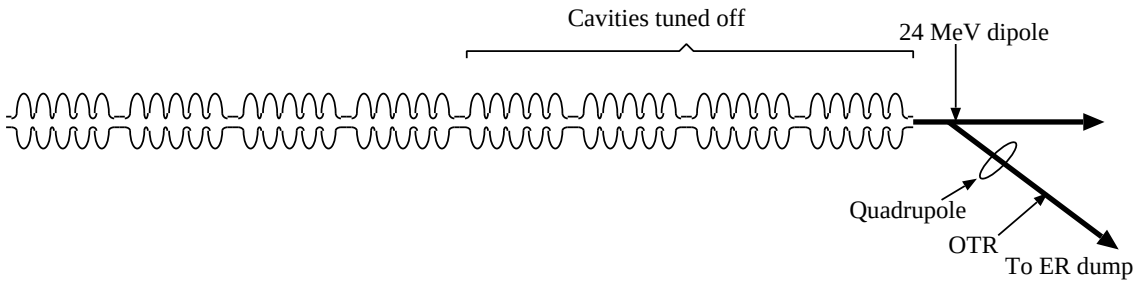

Figure 5.21: Experimental setup to measure bunch length with zerophasing method in the IR-FEL driver accelerator

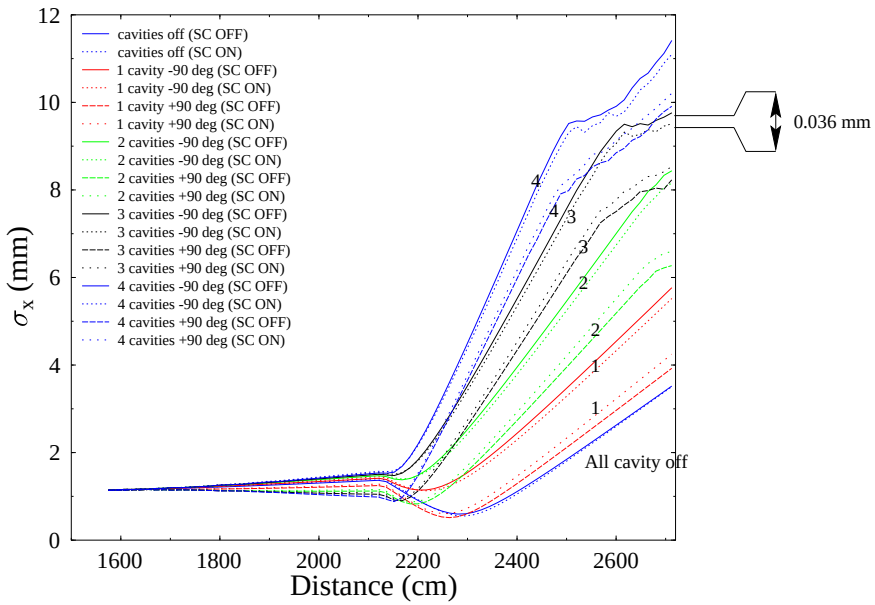

Figure 5.22: Horizontal beam envelope evolution from the exit of the four cavities in the cryomodule up to the beam profile station in the spectrometer transport line for different numbers of zerophasing cavities. For each case, the space charge routine in PARMELA is turned on and off.

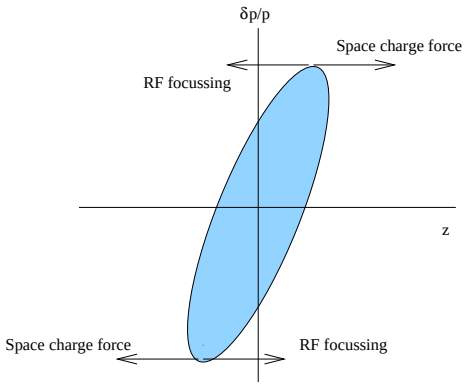

Figure 5.23: pictural effect of longitudinal space charge force on the phase space distribution.

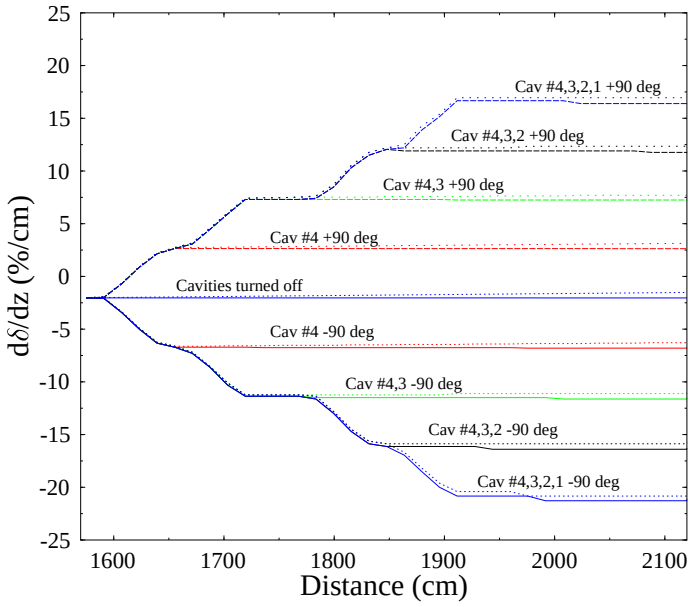

Figure 5.24: Longitudinal phase space slope evolution along the drift between the entrance of the first zero-phasing cavity up to the entrance plane of the spectrometer dipole. The number of cavities used for the zero phasing is indicated below each curve. The slope is normalized to the initial energy. For each case the simulation is performed with the space charge routine in PARMELA turned on (upper curve) and off (lower curve).

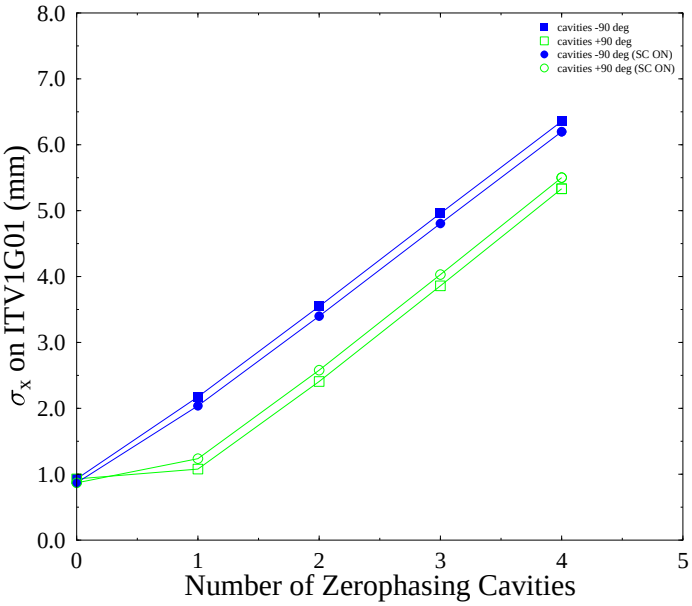

Figure 5.25: RMS horizontal beam size at the profile measurement station versus number of zerophasing cavities

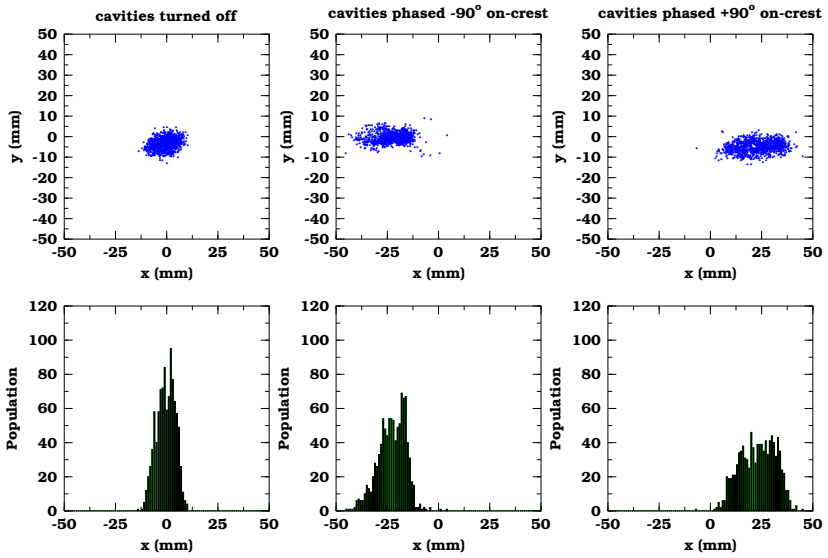

Figure 5.26: Beam spot on the dispersive OTR monitor for the three phases of the zero-phazing measurement.

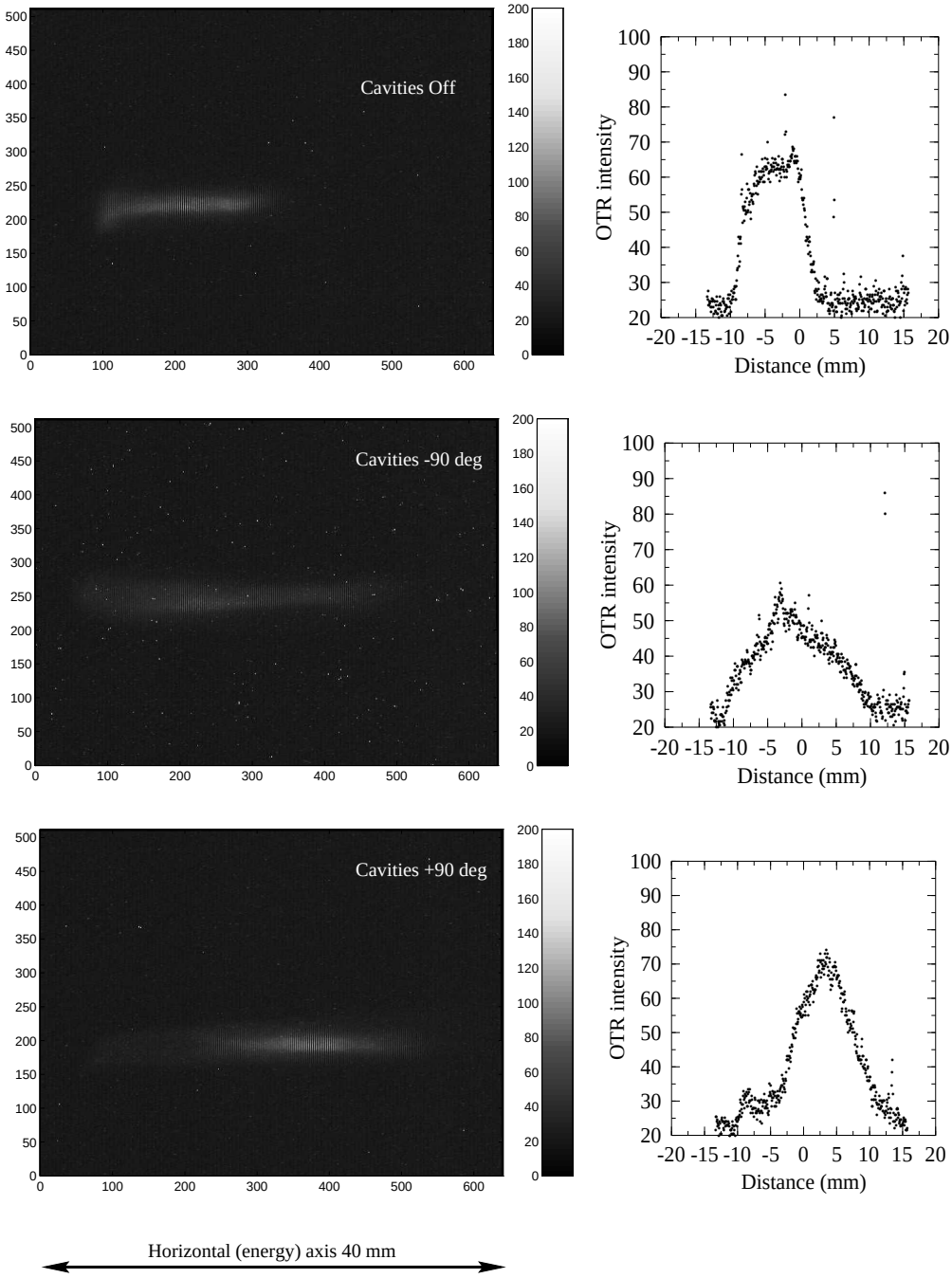

Figure 5.27: Typical zerophasing based measurement. The 2D false color image represents the beam spot measured on the dispersive viewer in the spectrometer line whereas the right plot is the projection onto the horizontal axis. Measurement for the case where all the "zerophasing" cavities are off (top line), are phased -90 deg w.r.t. the maximum acceleration phase (middle line) and are phased +90 deg w.r.t. the maximum acceleration phase (bottom line).

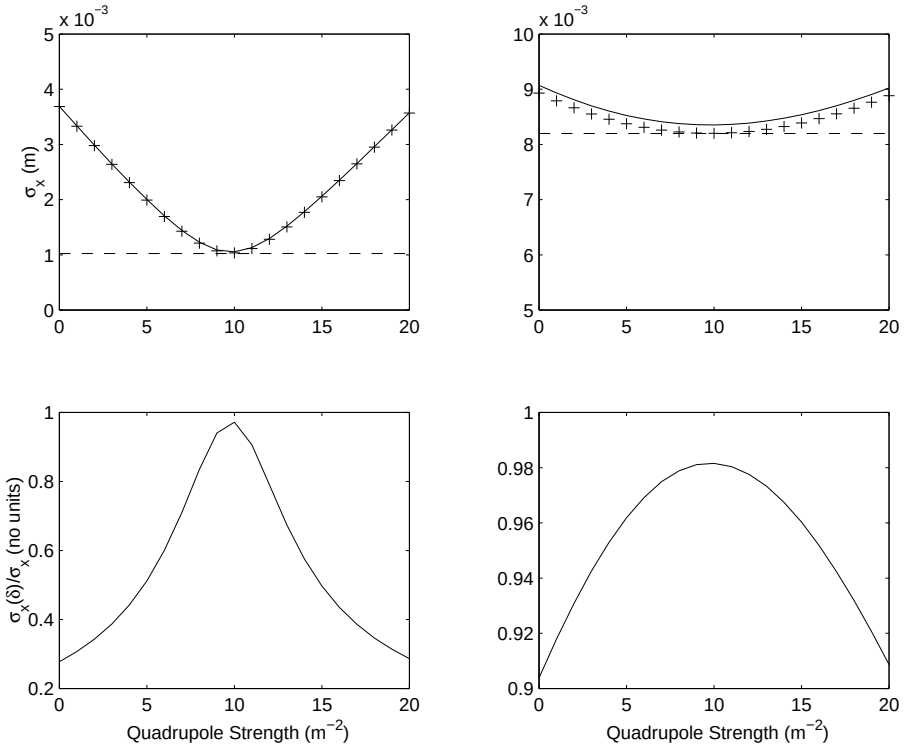

Figure 5.28: Comparison for $\delta = 0.2\%$ (**top left**) and for $\delta = 2\%$ (**top right**) of the beam rms size variation in the center of the bunch compressor versus the excitation of an upstream quadrupole using DIMAD simulation (solid lines), using Eqn.(5.57) (crosses). The dashed line on these plots is the beam size contribution due to dispersion only $\delta\eta$. The bottom plots present the ratio of the beam size contribution due to dispersion only with the total beam size for $\delta = 0.2\%$ (**bottom left**) and $\delta = 2\%$ (**bottom right**)

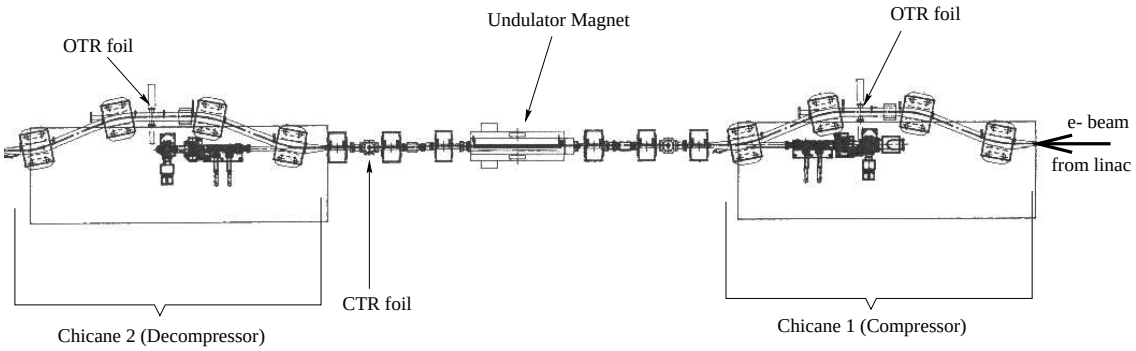

Figure 5.29: Schematics of the available diagnostics in the undulator region for measuring the longitudinal emittance.

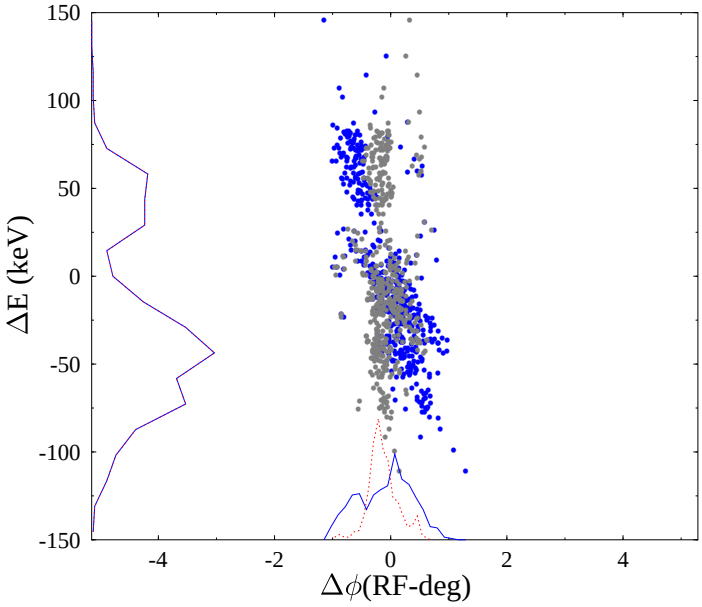

Figure 5.30: Comparison of the longitudinal phase space at the CTR foil (grey dots) and the decompressor mid-point (black dots). The energy distribution are exactly the same while the bunch length at the CTR foil is smaller (dashed lines) than at the chicane mid-point (solid lines).

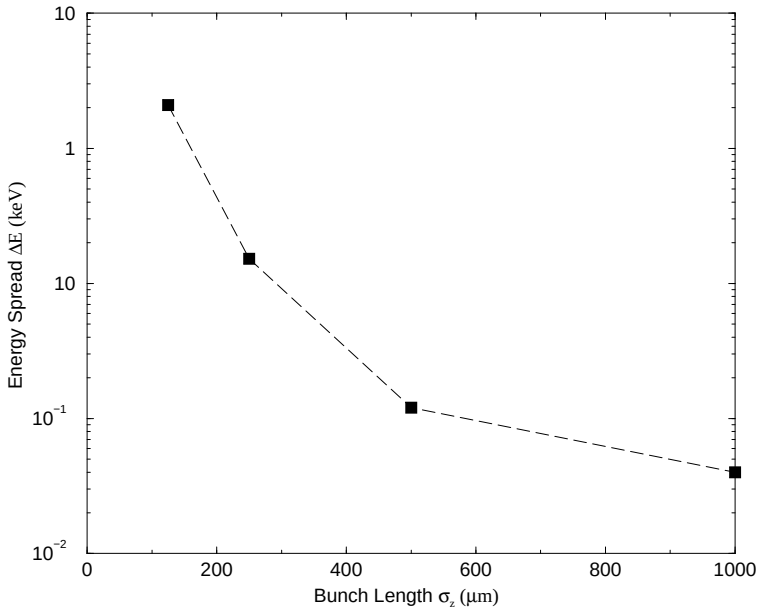

Figure 5.31: rms energy spread induced by wakefields generated as a 60 pC bunch of electron travels through the vacuum chamber transition at the undulator location.

Chapter 6

Beam Dynamics Studies

In the present Chapter we would like to present few applications of the diagnostics we have previously described. Essentially, to the present date, these instruments have been helpful in trying to optimize and understand the photoinjector. They have been used to optimize the bunching scheme, and verify that the beam parameters close to the undulator insertion are within the specified values. Recently we started to study transverse emittance growth to assess if we could relocated the undulator in the back leg transport as it is presently envisioned for the IRFEL Upgrade.

6.1 Study of the Photoinjector

The beam generation and low energy transport is probably one of the most crucial issue for the driver-accelerator; every care must be taken to prevent any beam degradation and insure the beam parameters remain within the specified values. Since the injector transports low energy, high charge bunches, effects such as space charge have to be taken into account.
A few features of the DC photoemission-based injector, especially the beam generation using the GaAs photocathode, have been described in Chapter 1. Here we shall only concentrate on the beam transport from the gun exit up to the front end.
The injector beam linepro is pictured in fig. 6.1; it can be divided into three main regions:

1. The 350 keV transport line that consists of two solenoid lenses and a warm buncher cavity,
2. The high gradient accelerating structure, composed of two CEBAF-type superconducting cavities capable of accelerating the beam up to a total energy of approximately 10 MeV,
3. The 10 MeV region that can be subdivided into two parts: a quadrupole telescope that is used to match the transverse phase space into the main linac and an achromatic injection chicane that consists of three bends arranged in a "staircase" configuration.

In this section we will study each region, try to provide a simple model of beam evolution, we will compare with simulations, and when possible, benchmark with experimental results and provide tentative explanation of discrepancies. However, we will not describe the photoemission process and acceleration in the gun chamber since it has been treated in Reference [14].

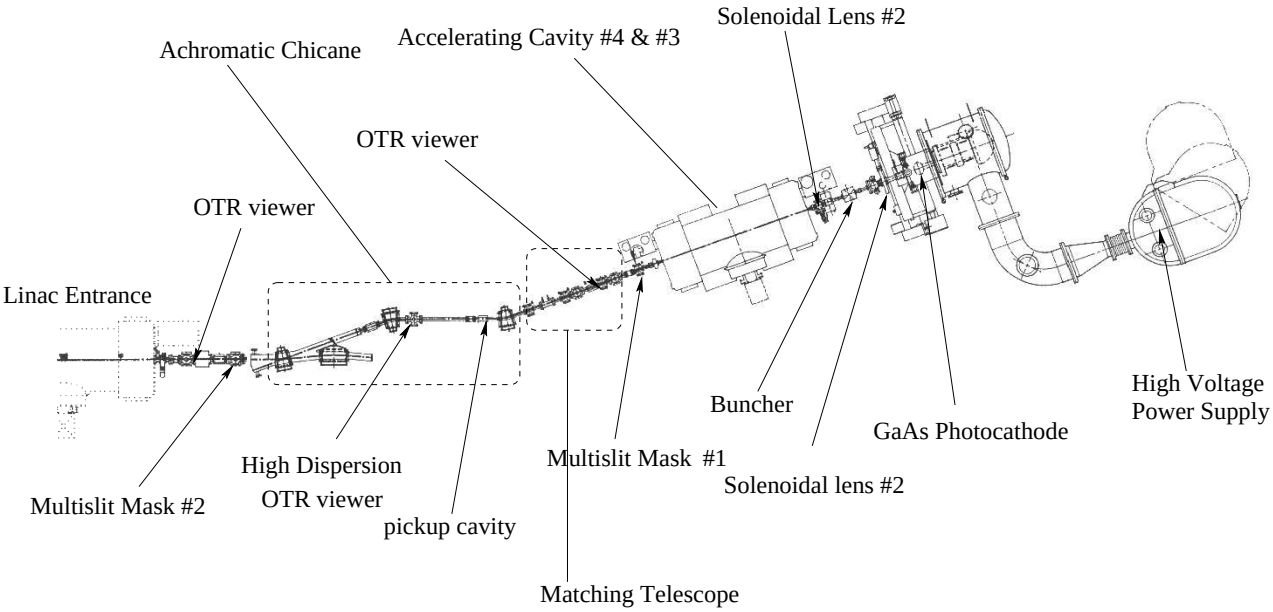

Figure 6.1: Simplified schematic of the IRFEL photoinjector (see text for explanation).

6.1.1 Introduction

The numerical model

The injector has been subject to extensive integrated modeling using several codes. The PARMELA particle pushing code is used as skeleton for the simulation [53], the electrostatic field in the gun and in the solenoid lenses are computed with the POISSON code, whereas the electromagnetic field in the RF cavities are obtained from a 3D model using the MAFIA family code. The injector parameters have been set after many iterative optimization runs using PARMELA. The resulting rms beam transverse and longitudinal envelopes throughout the injector transport, optimized for a gun voltage of 350 keV are presented in figure 6.2.

6.1.2 The 350 keV region

The beam is generated with a DC photocathode gun aforementioned. The accelerating voltage between the photocathode and the anode can reach 500 kV. Ideally one would like to maintain the highest accelerating voltage to minimize the space-charge-induced emittance growth since this force is proportional to $1/\gamma^2$. Unfortunately because we encountered technical difficulties (e.g. field emission of the cathode support) during the gun commissioning, we had to operate the gun with a lower accelerating voltage of 350 keV (and sometime 330 keV). It was assessed via numerical modeling that even with this lower accelerating voltage, we could still find adequate settings to provide the required beam parameters at the undulator location. As a bunch is emitted and accelerated in the gun, its rms transverse (i.e. radial) beam size is strongly diverging and the bunch is elongating as pictured in figure 6.2. To correct for the strong divergence and collect all particle of the bunch, a solenoid lens has been located immediately downstream the anode plate.

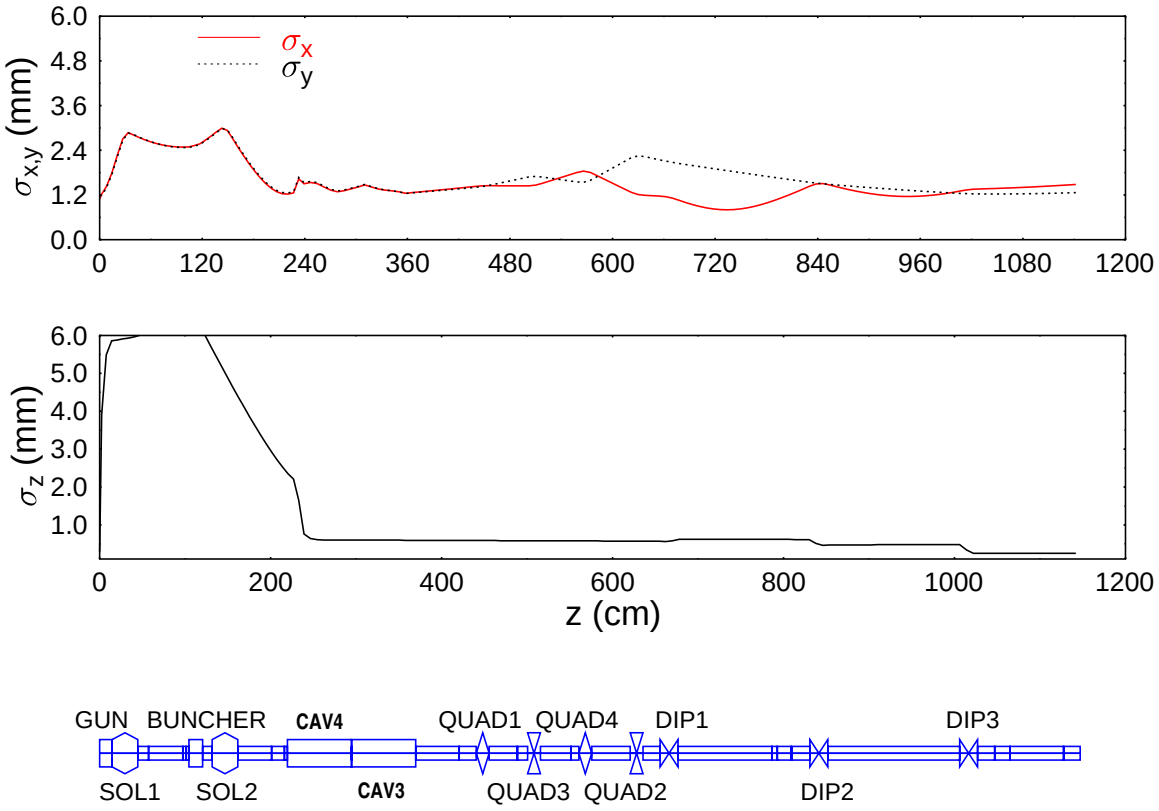

Figure 6.2: RMS transverse (σ_x and σ_y) and longitudinal (σ_z) beam sizes along the injector. The bottom schematics locates the optical elements along the beam line (the gun accelerating voltage is 350 keV).

This solenoid, that will be referred henceforth as the "emittance solenoid", because of its impact on the beam emittance, should be operated with the optimum magnetic field to minimize space-charge-induced emittance growth and make sure there is no beam loss downstream due to scraping on the vacuum chambers. Typically the optimum magnetic field depends on the charge per bunch and electron energy (i.e. accelerating voltage of the gun). Generally the gun along with this first solenoid are referred as the beam generation line[1]. Usually, this region is entirely simulated with numerical methods: the magnetostatic field 2D map in the gun and in the solenoid [2] are computed with magnetostatic solver code such as POISSON and PARMELA is used to simulate photoemission of electron macroparticles and track them along this generation line.
In the following we are going to provide analytic description of the evolution of the beam parameters along the 350 keV transport beam line. This analytic description is based on coupled differential

[1] this generation line as been the subject of a PhD thesis see Reference [14]
[2] The gun and the solenoid are cylindrically symmetric elements

equation that require some initial conditions, that we will take to be at the emittance solenoid exit. Let σ_r and σ_z be respectively the rms transverse and longitudinal beam envelope. It is well know (e.g. see reference [54]) that one can describes the evolution of the beam envelope via the so-called coupled rms envelope equation that write (extended from reference [54]):

$$\frac{\partial^2\sigma_r(s)}{\partial s^2} + k_0^2\sigma_r(s) - \frac{3}{10\sqrt{5}}\frac{Nr_c}{\beta_0^2\gamma_0^3}\frac{1}{\sigma_r(s)\sigma_z(s)}\left(1 - \frac{g}{2}\frac{\sigma_r^2}{\gamma_0^2\sigma_z^2}\right) - \frac{\tilde{\varepsilon}_r^2}{\sigma_r^3} = 0 \tag{6.1}$$

$$\frac{\partial^2\sigma_z(s)}{\partial s^2} + k_0^2\sigma_r(s) - \frac{3}{10\sqrt{5}}\frac{Nr_c}{\beta_0^2\gamma_0^5}\frac{g}{\sigma_z(s)^2} - \frac{\tilde{\varepsilon}_z(s)^2}{\sigma_z(s)^3} = 0$$

where $g = g(\sigma_z/\sigma_r, b/\sigma_r)$ a function of the beam rms size and the vacuum pipe diameter b, describes the effect of the bunch interaction with its image on the beam line vacuum chamber; $r_c = e^2/(4\pi\epsilon_0 mc^3)$ is the classical radius of an electron and γ_0 is the bunch reduced energy (from now on we will assume an energy of 350 keV, i.e. β_0=0.8048 and γ_0=1.6849. To convince ourselves on the necessity of using the above equation system, we can study the dependence of the "space charge over emittance ratio". For the longitudinal direction we define this ratio as:

$$R_r \stackrel{def}{=} \frac{3}{10\sqrt{5}}\frac{Nr_c}{\gamma_0^3}\frac{g\sigma_z}{(\tilde{\varepsilon}_r^n)^2} \tag{6.2}$$

The same kind of factor can be defined for the transverse direction:

$$R_z \stackrel{def}{=} \frac{3}{10\sqrt{5}}\frac{Nr_c}{\gamma_0}\frac{\sigma_r^2}{(\tilde{\varepsilon}_z^n)^2\sigma_z}\left(1 - \frac{g}{2}\frac{\sigma_r^2}{\gamma_0^2\sigma_z^2}\right) \tag{6.3}$$

The evolution of these ratios along the beam line using rms envelope numerically computed with PARMELA are shown in figure 6.3. In the 350 keV line it is seen that space charge contribution in the envelope equation can be a factor 100 larger than the emittance term contribution. Even in the 10 MeV region, there is still a predominance of space charge term by a factor 10 except in the bunching chicane where dispersion increase transverse beam size and therefore locally reduce space charge force. On the other hand, the longitudinal ratio is significantly larger than unity only in the 350 keV region. It is strongly damped as the beam is accelerated in the 10 MeV structure and downstream the cryounit the longitudinal envelope equation is only driven by the emittance term. To apply the rms envelope equation to the different elements we can use the following steps:

- for a drift space, the external focusing parameters, k_r and k_z are set to zero.
- the buncher cavity is modeled as a "slope impulse": $z' \stackrel{buncher}{\rightarrow} z' + \frac{2\pi}{\lambda_{RF}}\frac{eV}{mc^2\beta^2\gamma^3}\sigma_z$
- the solenoid external focusing parameter is estimated using the relation $k_0 = \frac{eB_0}{2mc\beta\gamma}$ where B_0 is the integrated magnetic field, which we have estimated using a POISSON generated magnetic field profile.

6.1.3 The high gradient structure

In this section we would like to discuss few interesting effects induced on the transverse beam dynamics by the CEBAF-type accelerating cavities. The discussion will enable the reader to understand experimental results presented in the next section.

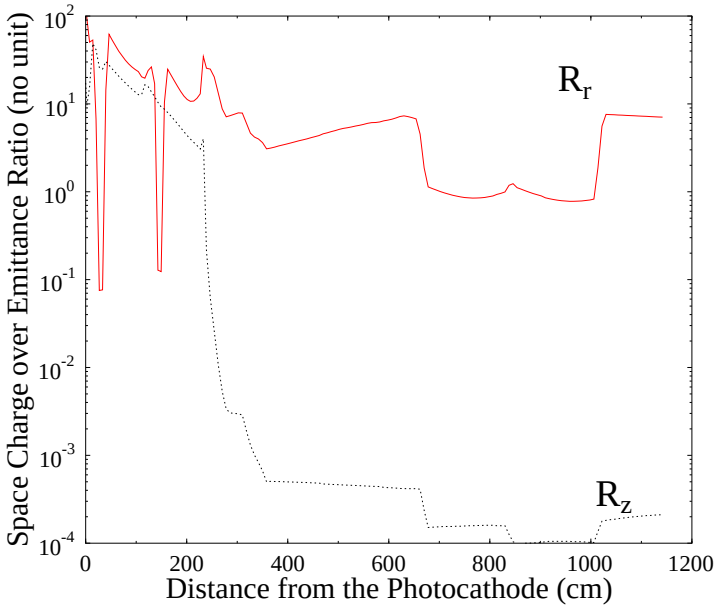

Figure 6.3: "space charge over emittance ratio for the transverse (R_r) and longitudinal (R_z) direction.

Energy Gain

The acceleration in accelerating cavities is provided by the longitudinal component of the electric field of the fundamental mode. Such field can be written approximately:

$$E_z = E_0 \cos(kz)\cos(\omega t + \phi) = \frac{E_0}{2}\left(\cos(\omega t + \phi - kz) + \cos(\omega t + \phi + kz)\right) \tag{6.4}$$

E_0 is the peak field, z is the position with respect to the cavity center, and ϕ is the offset phase between the particle and the RF-wave. Because of their energy at the first cavity entrance, 350 keV, the electrons are not relativistic and therefore one electron is not going to keep the same relative phase with respect to the RF-wave, such effect is named phase slippage. Let's define the phase $\Psi(z)$ as:

$$\Psi(z) \stackrel{def}{=} \omega t - kz - \phi = k\int_0^z \left(\frac{\gamma}{\sqrt{\gamma^2 - 1}} - 1\right) dz + \phi \tag{6.5}$$

Moreover the normalized energy gain is:

$$\frac{d\gamma(z)}{dz} = \left(\frac{eE_0}{2mc^2} - 1\right)\left(\cos(\Psi(z) + 2kz) + \cos(\Psi(z))\right) \tag{6.6}$$

The Eqns.(6.5) and (6.6) together form a coupled differential equation system that can be solved numerically using standard technique. Figures 6.4 presents the energy gain in the two cavity with

an electron beam of initial energy of 350 keV. It is notably seen that maximum energy gain provided by the first cavity (cavity #4) is not obtained by injecting the bunch with a relative phase $\phi = 0$ w.r.t. the RF-wave. This fact is a consequence of phase slippage between the RF wave and the bunch which is not yet relativistic. In fact to obtain the maximum possible energy at the exit of cavity #4, one needs to inject the bunch with $\phi \simeq -40$ deg.

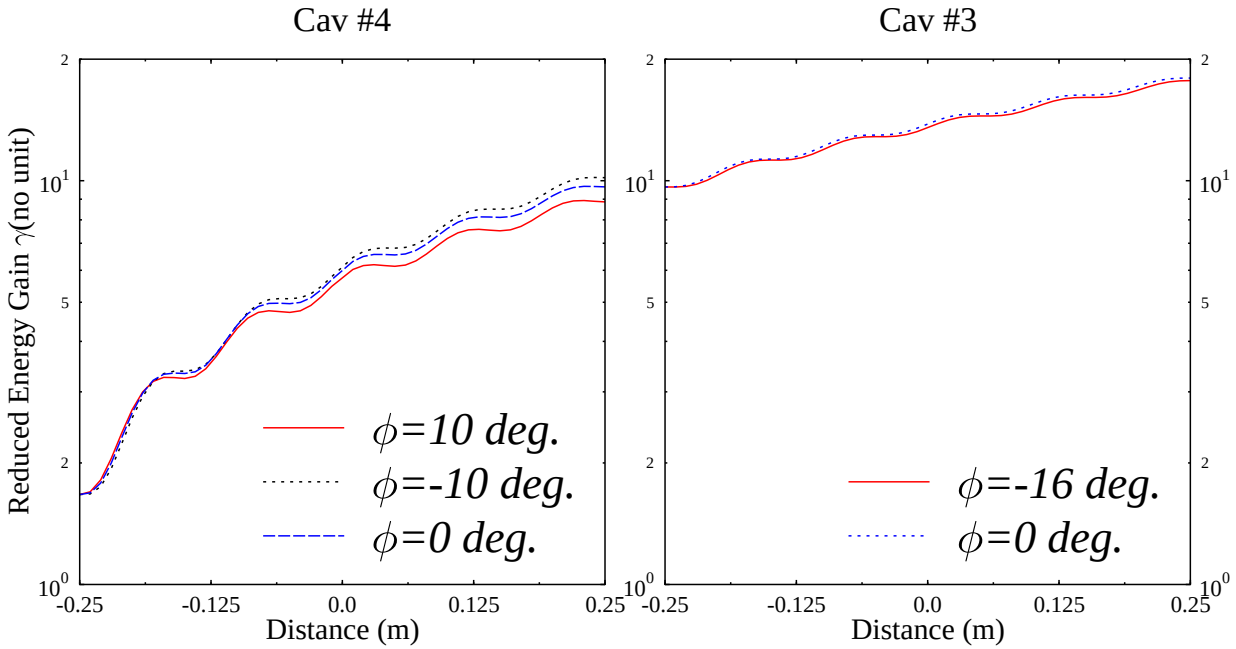

Figure 6.4: Reduced energy gain, γ, along the first (cavity #4) and second (cavity #3) cryounit cavity.

Radio-Frequency induced Focusing

The fundamental mode longitudinal accelerating field also induces, by virtue of Maxwell's equations, a radial electric component that writes:

$$E_r(z) = -\frac{r(z)}{2}\frac{d}{dz}E_z \tag{6.7}$$

This radial field together combined with the equation of motion $\partial_t p = eE_r$ yields a transverse equation of motion, e.g. for the horizontal plane:

$$\frac{d^2x(z)}{dz^2} + \frac{\gamma'(z)}{\gamma(z)}\frac{dx(z)}{dz} + \frac{d^2\gamma(z)}{dz^2}x(z) = 0 \tag{6.8}$$

This equation can be solved numerically, but some approximated solution have been derived by Chambers [58, 57], for pure π-mode accelerating cavities, and are in very good agreement with the

numerical solution [56]. This approximate solution is written in term of transfer matrix (e.g. in the x-x' phase space) as:

$$M = \begin{pmatrix} \cos(\alpha) - \sqrt{2}\cos(\phi)\sin(\alpha) & \sqrt{8}\frac{\gamma_i}{\gamma'}\cos(\phi)\sin(\alpha) \\ -\frac{\gamma'}{\gamma_i}\left(\frac{\cos(\phi)}{\sqrt{2}} + \frac{1}{\sqrt{8}\cos(\phi)}\right)\sin(\alpha) & \frac{\gamma_i}{\gamma_f}\left(\cos(\alpha) + \sqrt{2}\cos(\phi)\sin\alpha\right) \end{pmatrix} \tag{6.9}$$

where $\gamma_{i,f}$ are the initial and final reduced Lorentz factors, the angle α is $\alpha = \frac{1}{\sqrt{8}\cos(\phi)}\ln(\gamma_f/\gamma_i)$ and ϕ is, as usual, the phase of the injection of the particle with respect to the on-crest phase. γ' is the averaged (over the RF structure) energy gradient: $\gamma' = \frac{eG}{mc^2}\cos(\phi)$. The focal length can be estimated in a straight forward fashion: using first order matrix formalism, the σ_{11} beam matrix elements at the exit of the cavity of the cavity are related to the beam matrix element at the cavity entrance by:

$$\sigma_{11}^{(f)} = m_{11}^2\sigma_{11}^{(0)},\ \sigma_{12}^{(f)} = -m_{11}m_{21}\sigma_{11}^{(0)},\ \sigma_{22}^{(f)} = -m_{21}^2\sigma_{11}^{(0)} \tag{6.10}$$

After a drift along a distance l, the beam size writes:

$$\sigma_{11}^{ff} = \sigma_{11}^{(f)} - 2l\sigma_{12}^{(f)} + l^2\sigma_{22}^{(f)} \tag{6.11}$$

Since the focal length is defined by the length f where we have $d\sigma_{11}^{(ff)}/dl = 0$, it yields:

$$f \overset{def}{=} \frac{\sigma_{11}^{(f)}}{\sigma_{22}^{(f)}} = -\frac{m_{11}}{m_{12}}\frac{\cos\alpha - \sqrt{2}\cos\phi\sin\alpha}{-\frac{\gamma'}{\gamma_f}\left(\frac{\sin\phi}{\sqrt{2}} + \sqrt{\frac{1}{8}}\frac{1}{\cos\phi}\right)\sin\alpha} \tag{6.12}$$

Unfortunately this model is derived assuming perfect axi-symmetric RF structure which is generally not the case: in the CEBAF-type cavities, for instance, there are asymmetries in the vicinity of the high order mode (HOM) and the forward power (FP) couplers. These asymmetries, in turn, induced transverse electromagnetic fields. Thus it requires a complete 3D model to accurately study the effect of these couplers on the beam dynamics. Such a 3D model is readily available and has been implemented in the Jefferson Lab version of PARMELA using 3D electromagnetic field map generated with the eigensolver MAFIA [64]. In order to characterize the focusing effect of the cavity we generate a hallow sheet beam in the $x-y$ spatial coordinate space with zero divergence (i.e. $x' = y' = 0$ for all macroparticle in the beam). The properties of this kind of beam has a beam size that is equal to the hallow radius, and zero-emittance. After the accelerating cavities the parameter σ_{11}^f and σ_{22}^f are computed and the focal length is deduced using the equation 6.12. The results computed for the two cavities in the injector, taking into account non-relativistic effect, are presented in figure 6.5.

Radio-Frequency induced Steering

In a similar fashion we have studied, for the injector cavities, the RF-kick effect on the beam centroid. The kick imparted due to the presence of transverse field in the accelerating structure versus the phase of the electron bunch with respect to the RF-wave are plotted in figure 6.6.

The RF-induced kick due to the presence of the forward power and High order mode couplers can yield emittance dilution via two effects: the head tail effect and the skew coupling. The former is

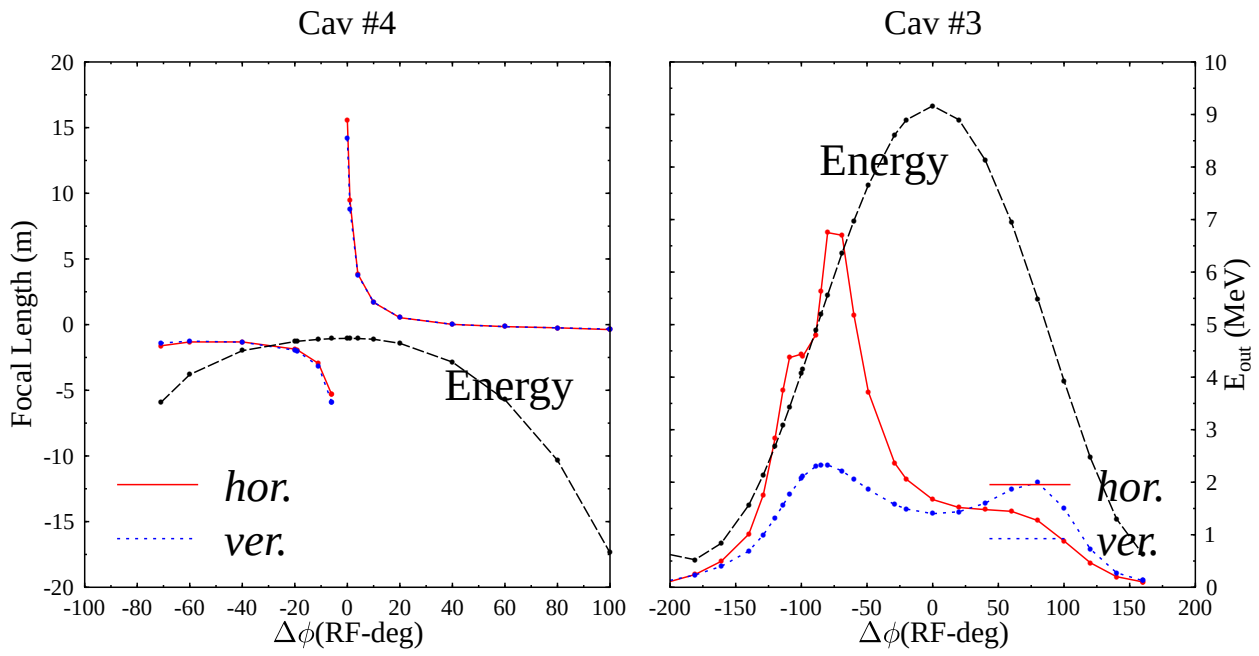

Figure 6.5: Focal length of the first (cavity #4) and second (cavity #3) cryounit cavities versus $\Delta\phi$, the phase difference w.r.t. the maximum energy phase (so-called "crest phase")

due to the fact that the kick is dependent on the particle position inside the bunch, and therefore yields a differential motion between the head and the tail of the bunch. This in turn reults in an increase of the bunch (projected) emittance. It is straight forward to estimate the emittance growth due to this effect: it depends on the bunch length and the beam parameters at the location of the considered coupler. The general expression for the emittance growth is [62]:

$$\delta\tilde{\varepsilon}_x \simeq \frac{\sigma_z}{2\tilde{\varepsilon}_{x0}}\left(A\sigma_x^2 + B\sigma_x'^2\right) \tag{6.13}$$

where $\tilde{\varepsilon}_0$ is the initial emittance, σ_z, σ_x and σ_x' are respectively the rms beam size and divergence at the coupler location, and A and B accounts for the steering effects of the cavity, these latter two terms can be estimated using tracking code. The other contribution that can spoil the transverse emittance is the skew coupling effect induced by the skew quadrupole moment of the electric field in the cavity: it introduces a coupling between the vertical and horizontal transverse plane. Generally the corresponding effect on emittance growth is smaller than the head-tail effect induced dilution and it can be reduced with a proper correction scheme [62]; this latter effect will be ignored in the forthcoming discussion.

6.1.4 The 10 MeV Region

As previously mentioned, we have instrumented the 10 MeV region with a variety of diagnostics devices: beam density monitors, emittance measurement devices, a time-of-flight pickup and a

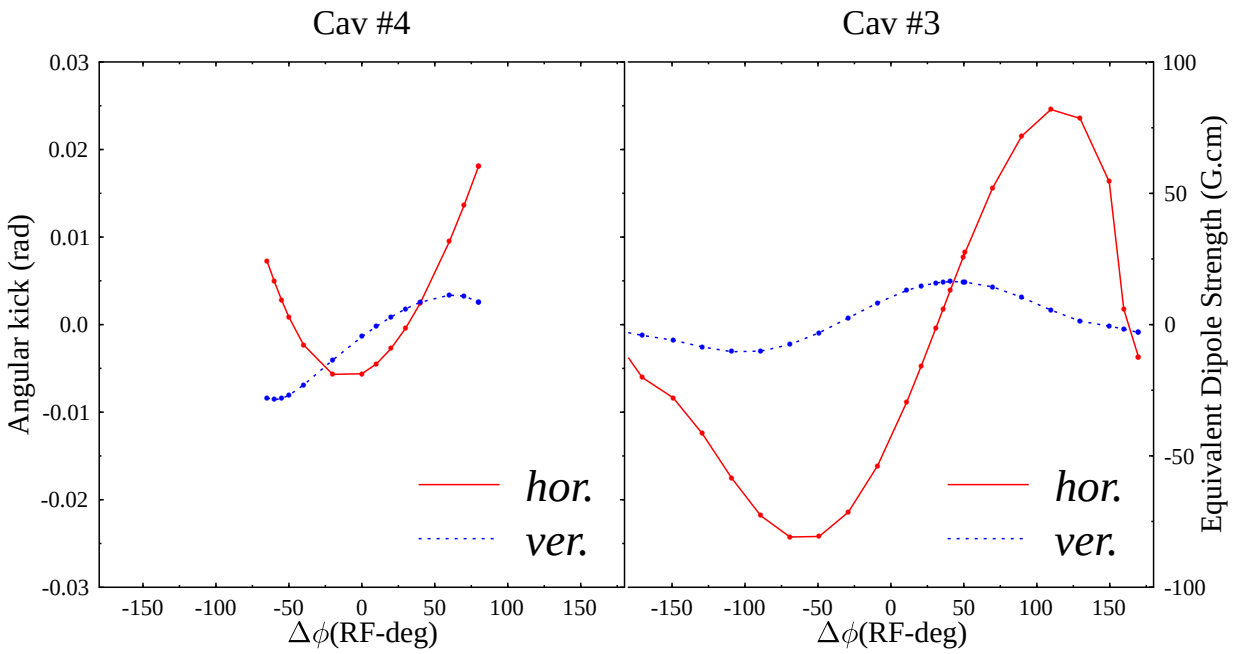

Figure 6.6: Steering effect due to FP and HOM coupler in the cryounit versus $\Delta\phi$, the phase difference w.r.t. the maximum energy phase (so-called "crest phase").

electromagnetic beam position monitor. Therefore, we can try to compare the experimental measurements with numerical simulations and attempt to explain potential discrepancies and try to refine the model to incorporate the effects that may account for these discrepancies.

Transverse Beam Properties

As a first qualitative observation, we measured beam density profile on the OTR density monitor located just downstream the accelerating structure. A comparison of the measured and expected beam density is shown in figure 6.7. The beam shape are quite similar, and rms value are in agreement at the 30% level: $\sigma_x^{simu} \simeq \sigma_y^{simu} = 1.47$mm, and $\sigma_x^{exp} = 1.77$, and $\sigma_y^{exp} = 1.60$ mm. However first measurements of transverse emittance based on the phase space sampling method utilizing the multislits mask revealed emittance 70% larger than simulated. Many parametric studies where conducted to determine if this emittance growth could be minimized by use of available parameters: the magnetic field in the first and second solenoids, and the buncher gradient. Most of our effort concentrated on the solenoid lenses and the buncher gradient, also this latter knob is difficult to adjust because it also affect the bunching scheme and some other adjustment (accelerating cavities and phases along the linac) are then needed to preserve an ultrashort bunch length in the main linac at the undulator location. An example of parametric study of the transverse emittance versus the "emittance" solenoid magnetic field is presented in figure 6.8. This figure clearly reveals the injector emittances are degraded compared to the one predicted via numerical modeling. One hypothetic explanation of such a disagreement is a the misalignment of the cryounit with respect to the

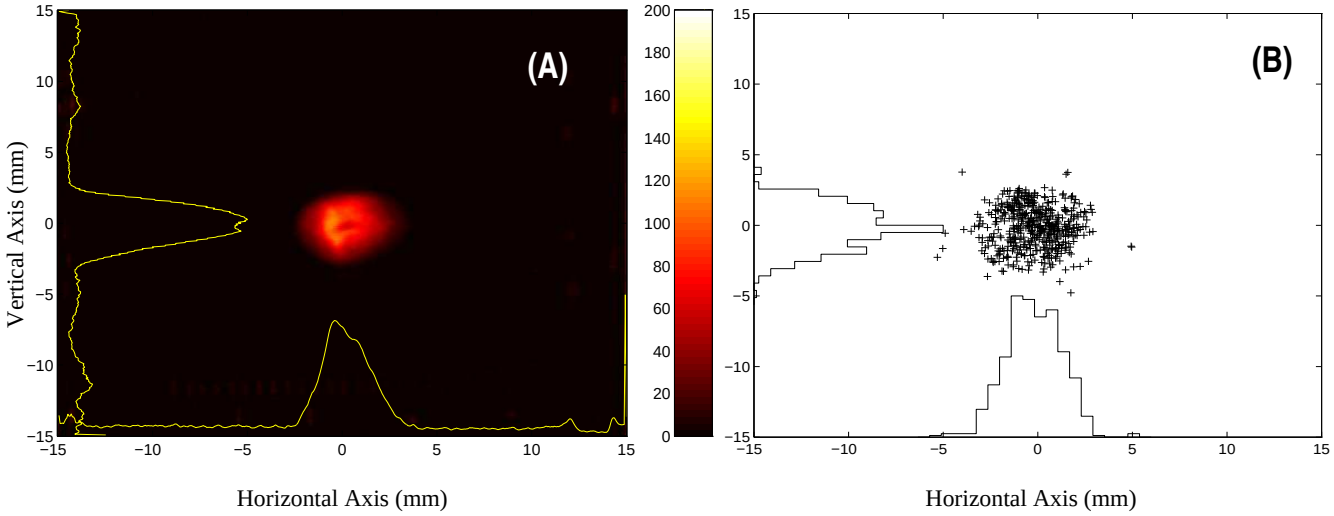

Figure 6.7: Comparison of the transverse beam density measured at the exit of the accelerating structure (A) with particle pushing numerical simulation (B).

beam axis. Such hypothesis has been inferred from other observations during the commissioning of the injector including a noxious orbit that could not be straightened[3] out. In the figure 6.8, the misalignment curve was generated by steering the beam by 50mrad upstream the cryomodule. In our desire to obtain a more realistic model of the IRFEL electron beam transport, we included the misalignment in PARMELA and get emittance values closer to what we experimentally measured.

Energy Spread

The energy spread can be estimated by measuring the horizontal beam profile at the high dispersion OTR (see figure 6.1). At this location the dispersion is computed to be $\eta \simeq 42$ cm and therefore a measurement of the rms horizontal beam size gives access to the quantity:

$$\sigma_x = \sqrt{\beta_x \tilde{\varepsilon}_x + \left(\eta \frac{\sigma E}{E}\right)^2} \tag{6.14}$$

Using the routinely measured rms horizontal emittance ($\tilde{\varepsilon}_x$ $\simeq$5-6 mm-mrad and beta function $\beta_x \leq 5$ m) we deduce that the dispersive contribution to the beam horizontal size is dominant, this latter statement is indeed also verified via numerical simulation using the code PARMELA. In figure 6.9 we present the effect of the buncher electric field on the beam OTR image recorded on the high dispersion OTR density monitor. From these images we compute the rms values for the horizontal (energy axis) projection and compare their values with the one expected from numerical simulation in figure 6.10. The agreement is seen to be reasonable, i.e. within 30%, except for large buncher voltage, though in this range we believe the beam was scraping on the beam line vacuum chamber upstream the location of the measurement.

[3] Unfortunately because of time constraints this problem was not addressed

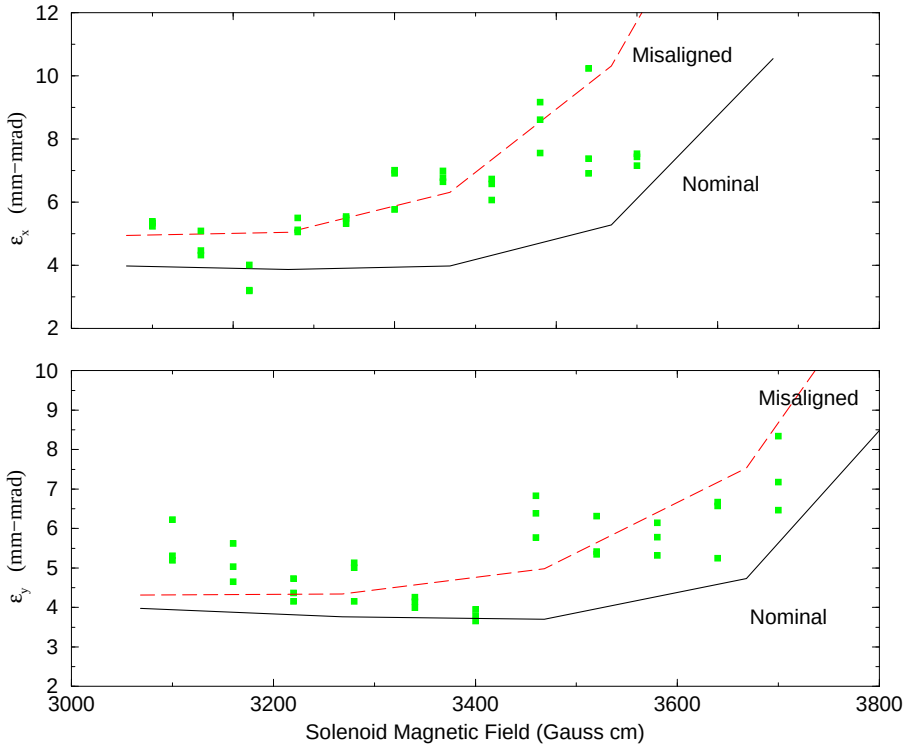

Figure 6.8: Measured (squares) and predicted transverse emittances (solid and dash lines) at the cryounit exit versus the emittance solenoid magnetic field.

Phase-Phase Correlation Measurement

Similarly to the bunch compression efficiency diagnostics described in the Chapter 3, the injector is instrumented with a pickup cavity that can be used to measure the time of arrival of a bunch and consequently determine phase-phase correlation by modulating the RF-phase of the photocathode drive laser. Unfortunately in the case of the FEL injector, the pickup cavity is located in a dispersive region which renders the time-of-flight (TOF) dependent on other parameters [4], in particular to RF-induced steering which, in turn, depends on the injection of the bunches with respect to the RF accelerating field in the cryounit. Hence at the pickup cavity location, the TOF of the bunch centroid emitted at the photocathode surface with initial phase ϕ_i with respect to the "zero-crossing" bunch (i.e. the bunch for which the TOF is zero by definition) is:

$$\phi_f = \phi_{RF} + R_{55}^{i\to f}\phi_i + R_{56}^{i\to f}\delta_i \tag{6.15}$$

where ϕ_{RF} is the TOF contribution due to the RF-induced steering: $\phi_{RF} = R_{51}^{c\to f}x_c + R_{52}^{c\to f}x'_c$; c, i, and f are respectively the location of the cryounit exit, the photocathode surface, and the pickup cavity.

The RF steering is due to (1) the RF transverse equation of motion in an accelerating cavity, and (2) the forward power and high order mode coupler induced kicks. To quantify the contribution of the RF-steering in the phase-phase correlation measurement, we have compared phase-phase correlation maps generated via numerical simulation using PARMELA with two distinct models of

[4] The necessity of studying carefully this point was brought to my attention by D. R. Douglas

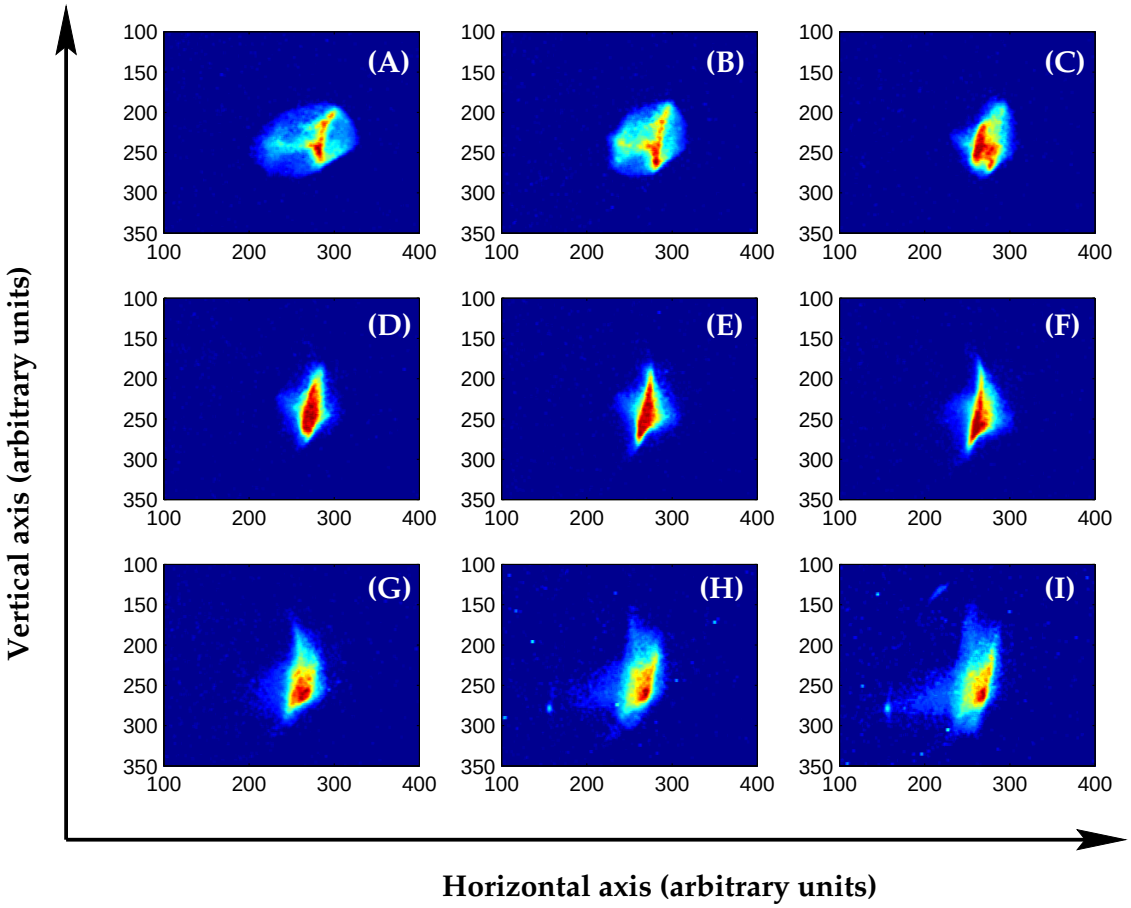

Figure 6.9: Beam density measured on the high dispersion OTR monitor for nine different bunch gradient settings (the images (A) to (I) corresponds to the points presented in fig. 6.10 starting from the low gradient values)

the CEBAF cavity: a 3D MAFIA model (which includes the coupler-induced effects) and a 2D-cylindrical symmetric SUPERFISH model. The results are presented in figure 6.11, which shows that there is not significant difference between the generated transfer maps except some broadening in the case the of the map generated from the 3D MAFIA model (which incorporates the RF-kick due to couplers). In the same figure we also compare the phase-phase correlation pattern generated if the cavity was located downstream the cryounit after a drift of similar length to its present location in the injector chicane; since the calculation corresponds to a dispersion-free drift, this transfer map gives insights on the effects of the ϕ_{RF} in the above equation. We can clearly observe that this effect does not wash out the TOF variation due to energy changes; small effects are observable only for large photocathode drive laser phase. Despite the fact that the effect is small, it prevents us from extracting quantitative information from the map (i.e. by performing nonlinear fits as in Chapter 3). In fact, we can use a similar technique to the one already in use in the CEBAF accelerator [22] that consists of comparing the phase-phase pattern experimentally measured with one numerically generated for an ideal setup.

An application of this type of measurement was to find the proper operating point of the buncher

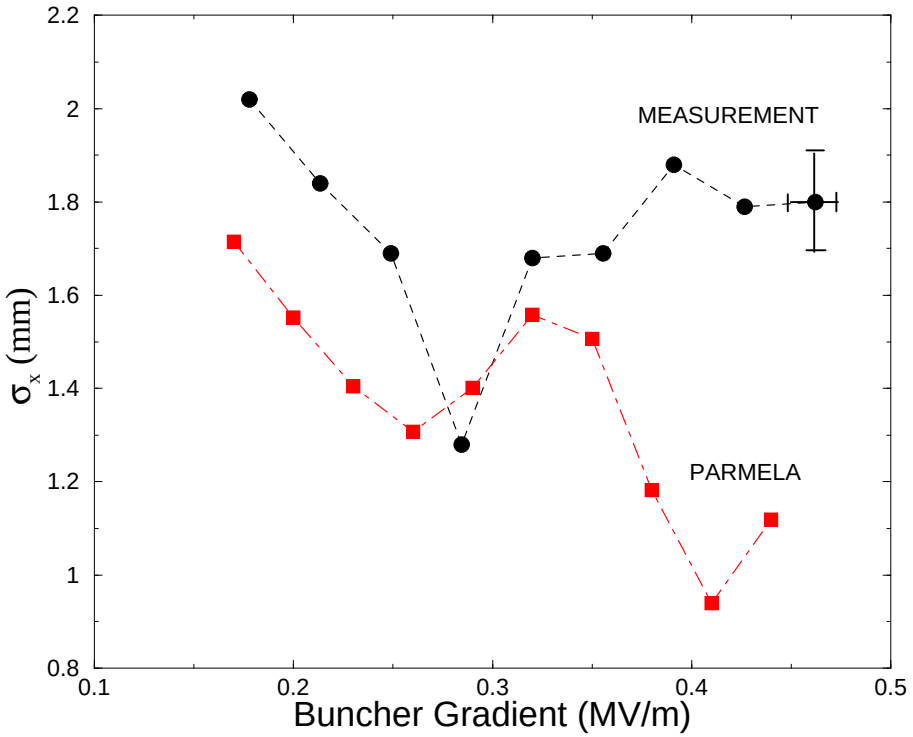

Figure 6.10: Comparison of the rms transverse horizontal beam size measured in the high dispersion OTR monitor with the one expected from PARMELA.

cavity electric field: devising a "good" bunching scheme in the injector is a three parameters problem with one possible measurement: the phase-phase correlation pattern. The three unknowns are the buncher, cavity #4, and cavity #3 gradients (at the time of the measurement their gradients were not precisely calibrated). Since the cavity's control electronics and software are identical, and because cavity #4 is operated at a gradient 30% higher than cavity #3, we estimated the gradient with the help of PARMELA: using this code we have varied the gradient of the two cryounit cavities (keeping cavity #4 at a gradient 1.3 times higher than cavity #3) until the simulated energy at the injector front end matched the experimentally estimated kinetic energy of 9.56 MeV (inferred from the strength of the injection chicane dipoles); during the simulations the cavity #4 was set to operate on crest while the cavity #3 was -20 deg off-crest to reflect the experimental operating points at that time). The buncher was operated at a gradient of 0.32 MV/m. The so-generated model is henceforth termed as "ideal" injector.

First series of measurements performed

We have investigated the buncher effect on the 320 kV gun setup[5] after the injector RF-phases were properly reset. The optimized phase are gathered in Table 6.1.4. The buncher gradient was initially set to 0.28MV/m, and we investigated the effect on the "R_{55}" transfer map pattern by systematically varying the buncher gradient. The recorded patterns are presented in figure 6.12 along with the pattern generated with PARMELA for the ideal injector. From this figure we decided

[5] At the time of the present experiment we were limited to this voltage; higher voltage would induce arcing in the gun chamber which in turn will remove the cesium from the photocathode wafer.

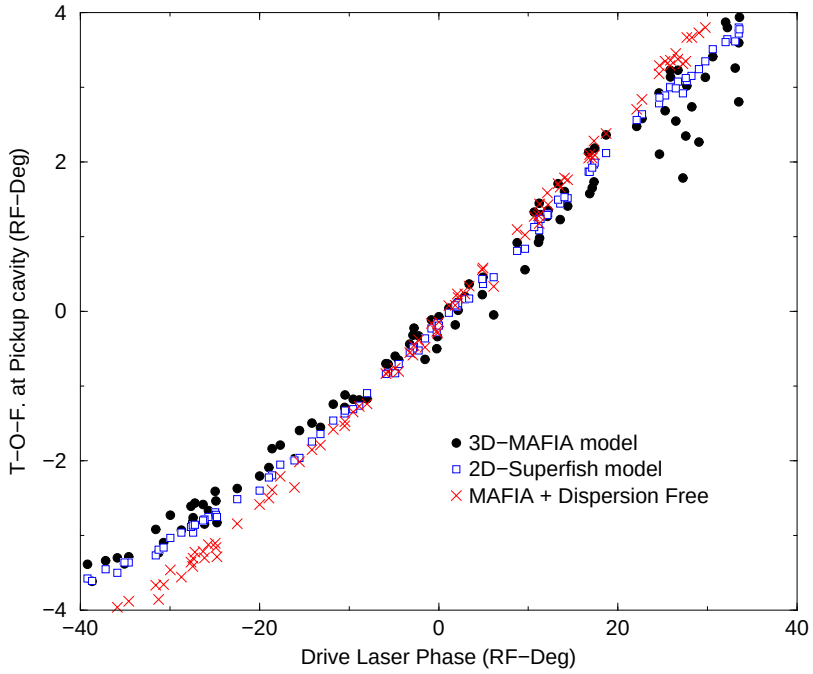

Figure 6.11: "R_{55}" transfer map generated with PARMELA for (1) different cavity model (3D mafia and 2D superfish) at the pickup cavity located in the injection chicane and (2) for the case where the pickup cavity is located downstream the cryounit after a drift in a dispersion-free region.

Elements	Phase	Gradient
Laser	reference phase	N/A
Buncher	zero-crossing	0.28 MV/m
Cavity #4	on-crest	11.8 MV/m
Cavity #3	-20 deg off-crest	9.10 MV/m

Table 6.1: Nominal injector settings before the first series measurement.

to operate the buncher at 0.32MV/m since it provides a pattern very close to the simulated one.

It is seen from the figure 6.10 that the "best" buncher gradient devised by matching the experimental phase-phase correlation pattern with the simulated one occurs for a buncher gradient of approximately 0.32MV/m; such a gradient does not correspond to the minimum energy spread on the dispersive viewer.

Second series of measurements performed

A second series of measurement was performed after the FEL photon beam was optimized for 60 pC/bunch [6]. The value for the phases and gradients recorded before the measurement, after the FEL was optimized, are gathered in table 6.2. The phase-phase pattern measured is compared in figure 6.13 with the "ideal" one obtained by numerical simulations. The agreement between the measurement and simulation is excellent. This agreement validates the method for setting up the longitudinal dynamics manipulation in the IRFEL injector. Basically the technique consists of

[6] this optimization consisted of maximizing the output FEL power by varying the buncher gradient

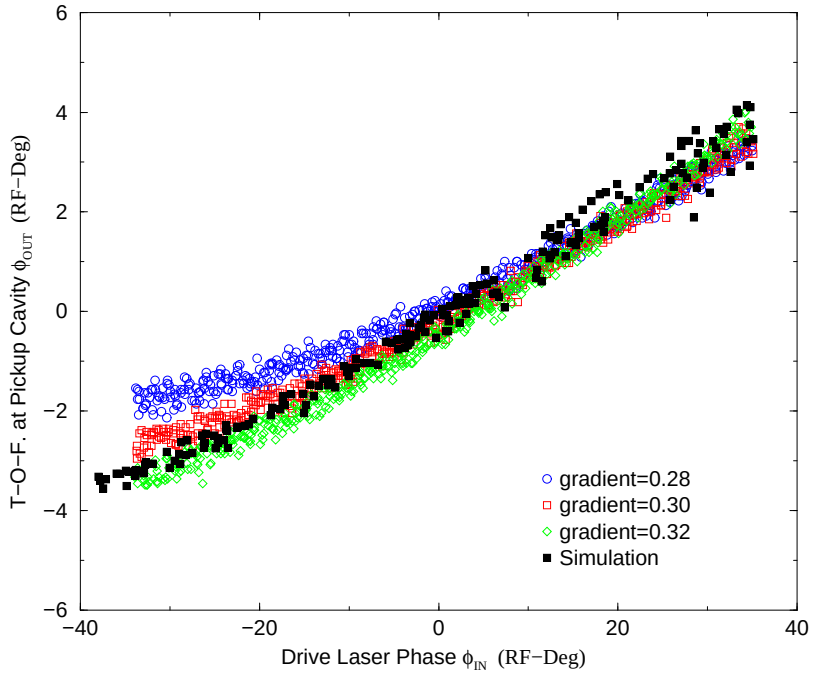

Figure 6.12: "R_{55}" transfer map for different experimental operating points of the buncher gradient. The measurements are also compared with the "ideal" injector devised from numerical simulations. (First series of measurement)

Elements	Phase	Gradient
Laser	reference phase	N/A
Buncher	zero-crossing	0.32 Mv/m
Cavity #4	on-crest	11.8 MV/m
Cavity #3	-20 deg off-crest	9.10 MV/m

Table 6.2: Nominal injector settings before the second series of measurement.

reproducing the "optimum" correlation pattern by only playing with the buncher gradient.

6.2 Bunch Compression Studies in the Linac

Up to now we have only mentioned the compressor chicane, without much discussion. This chicane consists of four rectangular-edge dipole-magnets arranged symmetrically. Though its purpose is to bypass the optical cavity of the FEL, it also serves as a bunch compressor using the standard magnetic compression scheme. Again, a simple way of demonstrating the principle is to propagate the generalized moments of the longitudinal distribution across the chicane. Let R be the 2×2 longitudinal transfer matrix of the chicane and let see how $\langle z^2 \rangle$ propagate from the chicane entrance

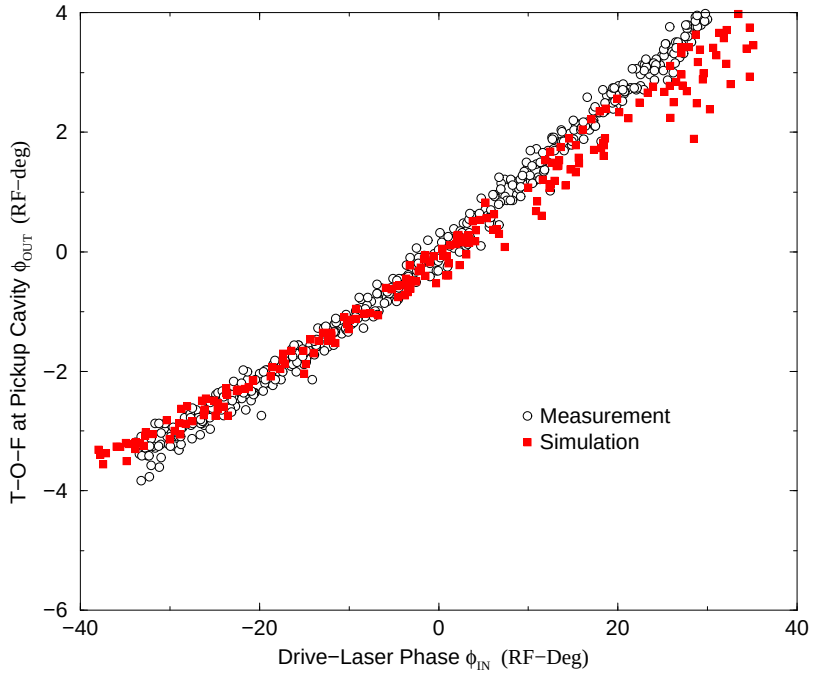

Figure 6.13: Comparison of the measured R_{55} pattern after the FEL was optimized with the "ideal" R_{55} pattern generated with PARMELA (using the second setup).

(position i) to its exit (position f):

$$\langle z^2\rangle_f = R_{55}^2\langle z^2\rangle_i + 2R_{55}R_{56}\langle z\delta\rangle_i + R_{56}^2\langle\delta^2\rangle_i = R_{55}^2\langle z^2\rangle_i + 2R_{55}R_{56}\langle z\delta\rangle_i + R_{56}^2\frac{\tilde{\varepsilon}_z^2 + \langle z\delta\rangle_i^2}{\langle z^2\rangle_i} \quad (6.16)$$

where we have used the definition of rms longitudinal emittance to write the far right expression. In the present configuration, the parameter at the entrance of the chicane are set by the linac; which indeed essentially modify the correlation term $\langle z\delta\rangle_i$. Hence, under the assumption that the bunch is not significantly varying with the linac set point, the minimum bunch length is given by the condition $\partial\langle z^2\rangle_f/\partial\langle z\delta\rangle_i = 0$, which gives the relation $\langle z\delta\rangle_i/\langle z^2\rangle_i = -1/R_{56}$; by definition we introduce the longitudinal phase space slope $(dE/dz)_i = \langle z\delta\rangle_i/\langle z^2\rangle_i$; therefore the "matching" condition for achieving minimal bunch length after the compressor system is $(dE/dz)_i = -1/R_{56}$. By setting the linac phase and accelerating gradient such that the aforementioned matching condition is fulfilled, and because of the initial emittance, the minimum bunch length achieved, via numerical simulations, at the undulator location is about 140 μm (rms). The evolution of the bunch length computed according to PARMELA from the photocathode surface up to the exit of the second chicane is presented in figure 6.14. Experimentally the typical bunch length measured in the undulator vicinity is approximately 100 μm (rms), an example of reconstructed bunch shape (using the inverse Hilbert transform technique detailed in Chapter 5) is compared with a beam profile generated with PARMELA in figure 6.15(C). Within the level of accuracy[7], we have good agreement. By varying the phase of the linac (thereby changing the quantity $\langle z\delta\rangle_i$) we can vary the bunch length; we present the result of such an experiment in figure 6.15(B) along with results from numerical simulation (in

[7](1) we only used 500 macroparticles in the numerical simulation, (2) the Hilbert transformation, as we have seen do not give a unique longitudinal distribution, and there are a lot of assumptions that have to be considered (e.g. extrapolation of the CTR spectrum at low frequency,...)

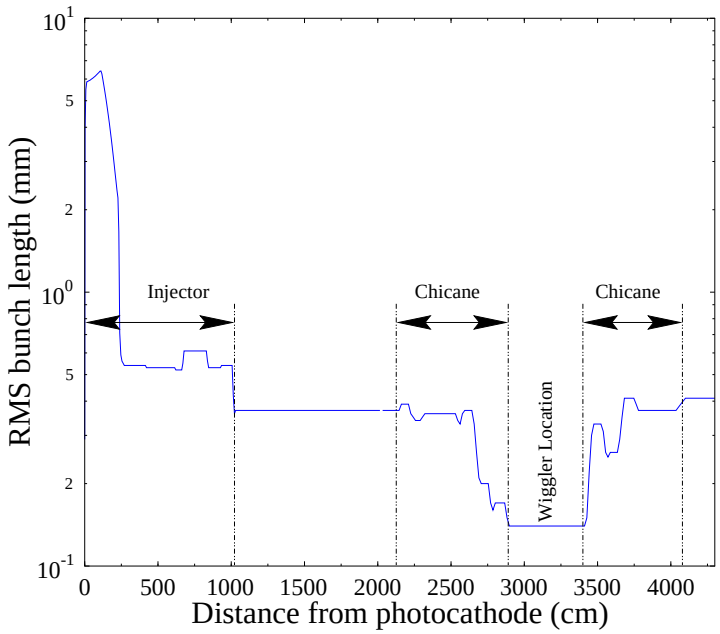

Figure 6.14: rms bunch length evolution along the IRFEL from the photocathode up to the exit of the second chicane.

plot (B)); for completeness we also include in figure 6.15(D) the total CTR power detected. We find that the bunchlength predicted via numerical modeling has a less pronounced variation compared to the measured variation.

6.3 Beam Parameters Measurement Prior to "First lasing"

As we mentioned in the very beginning of this report, one motivation, for operational purpose, of the diagnostics developed herein is to verify the electron beam quality is within the specifications to enable the FEL to lase. In the early stage of the commissioning of the IRFEL, the undulator magnet was removed, the main reason being that during this "tuning period" we could have damaged the undulator because of radiation showers induced as the electron beam "scrapes" on the vacuum chamber. In table 6.3 we present some of the beam parameters required along with the experimentally achieved and the numerically expected values. It is seen that we have achieved sufficient beam quality to enable the FEL to operate however the achieved parameters are somewhat larger than the one that could be theoretically reached as predicted from numerical modeling, except for the bunch length. With the above parameters first light was achieved at low duty cycle within a couple of hours after we installed the undulator magnet, and two days later we were able to operate the FEL with an output power of 150 W (cw), thereby demonstrating the quality of the electron beam. On the Beam Physics point of view it is interesting to try to understand the discrepancies between the numerical model and the achieved parameter.

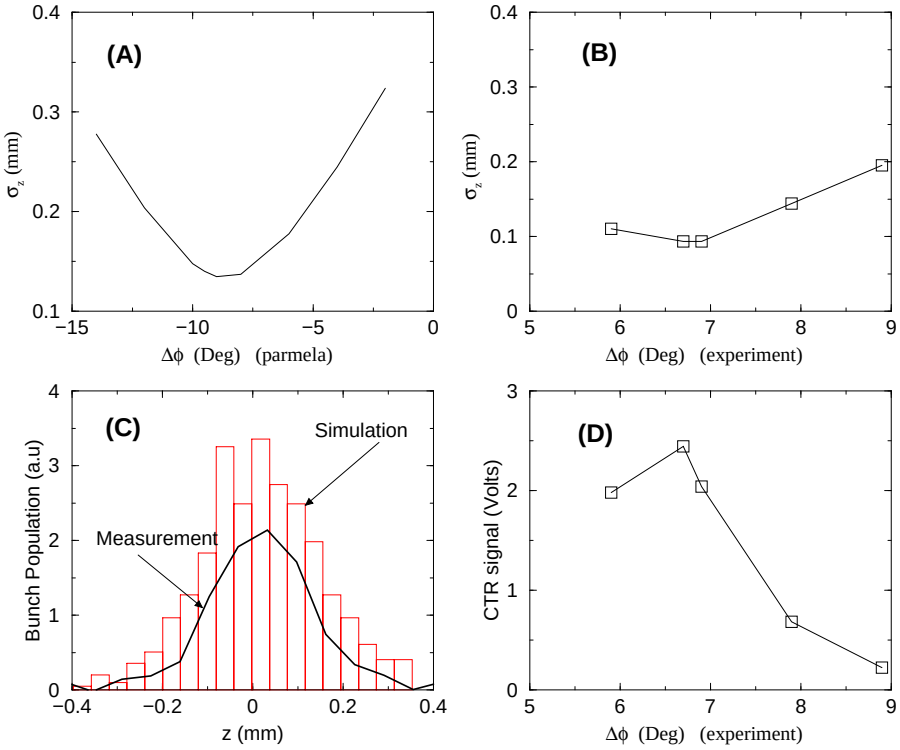

Figure 6.15: Variation of the bunch length versus the linac accelerating phase per PARMELA simulation **(A)** and measured **(B)** ["measured" means the bunch distribution was recovered from the CTR autocorrelation using the technique mentioned in Chapter 5]. Comparison between the experimental and simulated bunch longitudinal distribution **(C)**. Total CTR power signal measured during plot (B) experiment **(D)**.

6.4 Study of Potential Emittance Growth

In this last section we would like to report on an attempt to measure emittance (and to a lesser extent energy spread) degradation in the bending system of the IRFEL. For such a purposes we need to consider in the few following sections what are the mechanisms that can lead to an increase of the emittance. It seems we can divide such mechanism into two categories: the first one are due to the lattice (betatron mismatch, filamentation, chromaticity); the second type are due to bunch self interaction (because of Coulomb field or radiation field).
A growth of emittance comes from an increase of one of the position and/or divergence, i.e. x or x' in the x-x' phase space. Let's start with an initial emittance at the entrance of a beam line section $\tilde{\varepsilon}_0$: [8]

$$\tilde{\varepsilon}_0 = \left(\langle x_0^2 \rangle \langle x_0'^2 \rangle - \langle x_0 x_0' \rangle^2 \right)^{1/2} \tag{6.17}$$

If we assume, that due to perturbation in the beam line section, the position and divergence of a particle change accordingly to:

$$\begin{aligned} x_0 &\rightarrow x_0 + \delta x \\ x_0' &\rightarrow x_0' + \delta x' \end{aligned} \tag{6.18}$$

[8] We voluntary omit the subscript $_x$ for the emittance.in this section

Parameter	Required	Achieved	Expected
Emittances (mm-mrad)	$\tilde{\varepsilon}_{x,y} < 8.7$	$\tilde{\varepsilon}_x \simeq 7.5$	$\tilde{\varepsilon}_x = 5.16$
		$\tilde{\varepsilon}_y \simeq 7.1$	$\tilde{\varepsilon}_y = 3.77$
Bunch Length (mm)	$\sigma_z < 0.3$	0.110	0.137
Energy Spread (%)	$\delta E/E < 0.2$	0.25	0.140
Longitudinal Emittance (deg-keV)	< 33	18.8	11.7
Charge/Bunch (pC)	$Q = 60$	> 60	–
Kinetic Energy (MeV)	$E = 38$	> 38	–

Table 6.3: Comparison of the achieved, required and simulated beam parameters (the beam parameters are specified for a charge per bunch of 60 pC).

then, at the beam line section exit, we can compute the emittance as:

$$\tilde{\varepsilon} = \left(\langle (x_0 + \delta x)^2 \rangle \langle (x_0' + \delta x')^2 \rangle - \langle (x_0 + \delta x)(x_0' + \delta x') \rangle^2 \right)^{1/2} \tag{6.19}$$

Which, expressed as a function of the initial parameters, takes the form:

$$\tilde{\varepsilon}^2 = \tilde{\varepsilon}_0^2 + \left(\langle \delta x^2 \rangle \langle \delta x'^2 \rangle - \langle \delta x \delta x' \rangle \right) + \langle x_0^2 \rangle \langle \delta x'^2 \rangle + \langle x_0'^2 \rangle \langle \delta x^2 \rangle - 2 \langle x_0 x_0' \rangle \langle \delta x \delta x' \rangle + \text{ cross terms} \tag{6.20}$$

6.4.1 Chromaticity

Because a bunch does not consist in a mono-energetic distribution of electron, i.e. it has an energy spread σE, and since focusing in the optical lattice also depend on momentum it can spoil the transverse emittance. To quantify the lattice effect on the transverse phase space, one generally defines the so-called chromaticity. For a beam line section it is defined as the ratio of betatron phase advance $\Delta\mu$ change with the given energy change, ΔE:

$$\xi_{x,y} = \frac{\Delta \mu_{x,y}}{2\pi \Delta E} \tag{6.21}$$

Therefore, even under the linear optics approximation, the transfer matrix in the TRANSPORT code formalism is dependent on $\delta = \Delta E/E$. Because of this dependence there is potential emittance variation that can be generated.
The technique we used to study the chromatic aberrations consisted of raytracing a few points on the initial beam ellipse in the transverse phase space at the cryomodule exit. This raytracing is performed for a variety of energy spread with a span of $\pm 1\%$ and was computed with the TLIE code using expansion of the transfer map up to the third order. The results for two different locations along the beam line (after the decompressor chicane and in the middle of the backleg transfer line) are presented in figure 6.16. The phase space distortion is very small; to further quantify this statement we studied the emittance growth due to this effect in the backleg transfer line; for such a purpose we tracked an initial Gaussian distribution in the 6-D phase space and vary the rms relative energy spread of the distribution in the longitudinal plane. The result is presented in fig 6.17. For the nominal (measured) rms relative energy spread of 0.25% the emittance growth due to chromaticity is less than 2%, even in the case of energy spread of the order of 1% (which can be reached depending on the linac accelerating phase) the expected growth is approximately 5%. Hence it seems in the IRFEL emittance growth due to chromatic aberration is not a concern.

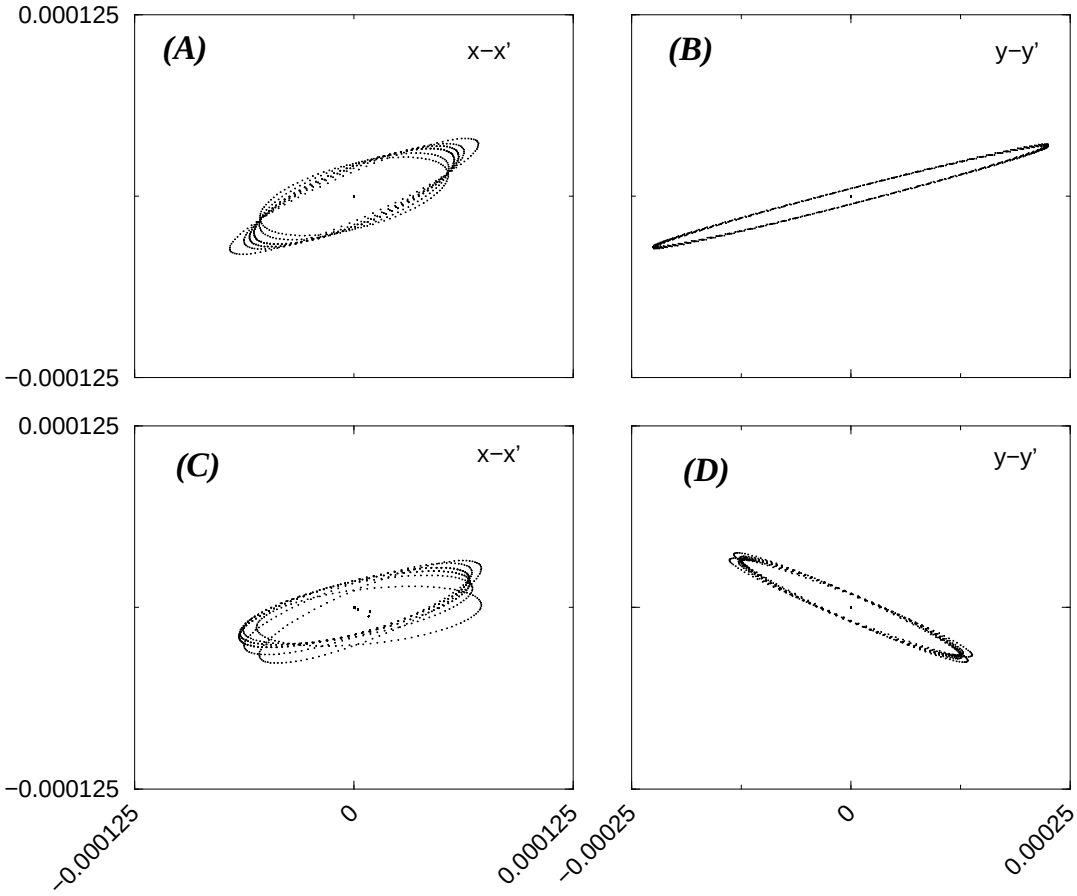

Figure 6.16: Phase space distortion due to chromatic aberration at the decompressor chicane exit (top plots) and the arc 1 exit (bottom plots).

6.4.2 RF-effects

In the high energy region, we have investigated the change in parameters due to variation of accelerating phase since we will attempt to measure the transverse horizontal emittance versus the linac gang phase[9]. The simulations were performed with PARMELA; and the results showing the dependence of the beam parameters versus the linac phase are presented in figure 6.18; the linac energy during these simulations was set to 38 MeV and the gang phase that provide minimum bunch length at the undulator location is $\Delta\phi \simeq -9.5$ deg. Both horizontal and vertical emittances at the linac exit do not depend on the accelerating phase.

6.4.3 Energy Spread induced in a Dispersive region

The general class of effects that can lead to energy spread are bunch self interaction via self field (space charge) or radiation field (wakefield due to vacuum chamber irregularities, synchrotron radiation). We have already briefly considered longitudinal wakefield at the end of Chapter 5 and

[9] A reminder that in Appendix D we provide a schematics of the RF-control system

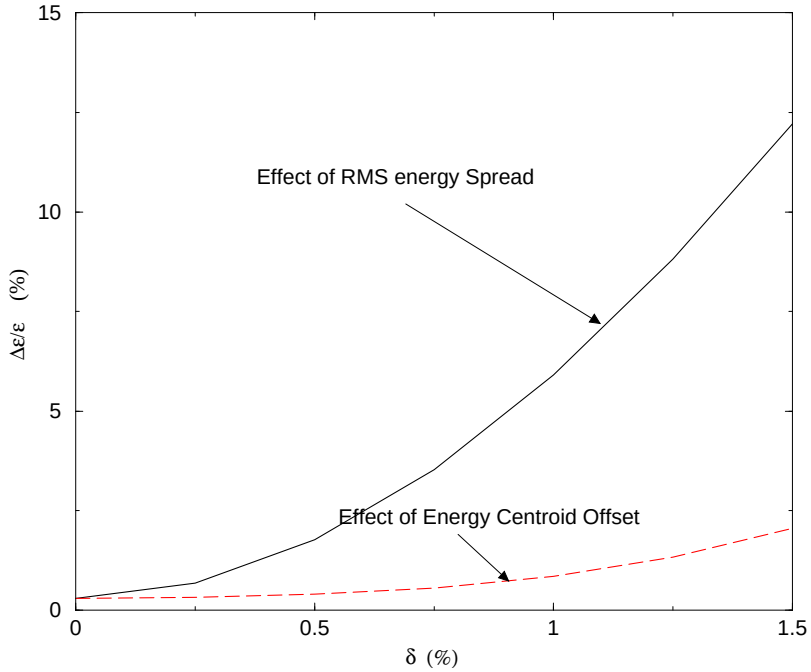

Figure 6.17: Emittance growth due to chromatic aberration versus the momentum spread and energy offset of the beam.

have show that it is very small for our beam parameters. In fact all the beamline components have been specified in such a way that the total longitudinal loss factor is within some impedance budget so that the potential beam degradation is very small [65].
In this section we would like to show how energy spread generated in a dispersive region (i.e. a bends system) can couple to the transverse plane and yield emittance degradation. The linearized equation of motion of an electron in a bend, assuming no external focusing and no coupling between the two transverse phase spaces, for the bending plane (the x-x' plane in the case of the IRFEL) is [59]:

$$\frac{d^2x}{ds^2} + \frac{x}{\rho_x^2} = \frac{\delta}{\rho_x} \tag{6.22}$$

where s is the longitudinal position referred w.r.t. the entrance of the bending system, ρ_x is the radius of curvature of the trajectory and δ is the relative energy offset w.r.t. the reference orbit.
Let's assume, for simplicity, that the mechanism generates an energy spread that is only dependent on the curvilinear coordinate s[10], i.e. $\delta = \delta(0) + \delta(s)$. Under such an assumption, the latter equation takes the form:

$$\frac{d^2x}{ds^2} + \frac{x}{\rho_x^2} = \frac{\delta(0) + \delta(s)}{\rho_x} \tag{6.23}$$

[10]generally speaking the mechanism is also dependent on time, for a complete treatment see [69]

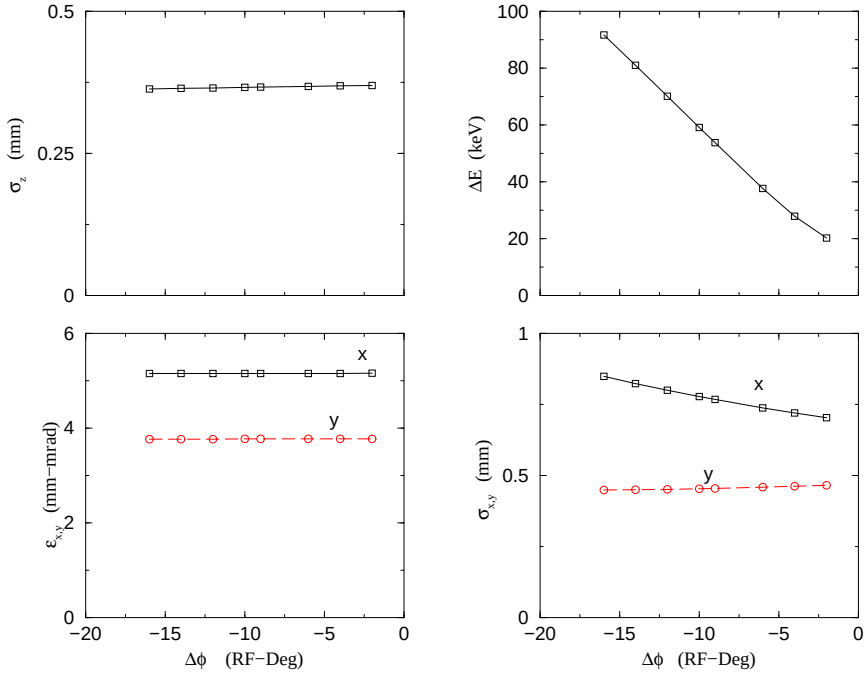

Figure 6.18: Evolution of beam parameters (bunch length σ_z, rms energy spread ΔE, transverse emittances $\tilde{\varepsilon}_{x,y}$, and rms beam sizes $\sigma_{x,y}$) versus the operating accelerating phase of the linac.

which can be solved using the standard Green function perturbative technique [59][11] The solution of the above equation is:

$$x(s) = \cos(s/\rho_x)x(0) + \rho_x \sin(s/\rho_x)x'(0) + \rho_x(1-\cos(s/\rho_x))\delta(0) + \int_0^s -\rho_x \sin(\tilde{s}/\rho_x)\delta(\tilde{s})d\tilde{s}$$

$$x'(s) = -1/\rho_x \sin(s/\rho_x)x(0) + \cos(s/\rho_x)x'(0) + \cos(s/\rho_x)\delta(0) + \int_0^s \cos(\tilde{s}/\rho_x)\delta(\tilde{s})d\tilde{s} \quad (6.24)$$

the latter equation clearly shows that, compared to the constant energy spread equation, there is an increment in angle and position of:

$$\Delta x(s) = \int_0^s -\rho_x \sin(\tilde{s}/\rho_x)\delta(\tilde{s})d\tilde{s}$$

$$\Delta x'(s) = \int_0^s \cos(\tilde{s}/\rho_x)\delta(\tilde{s}) \quad (6.25)$$

To compute the emittance growth we need to compute the second order moments ($\langle x^2 \rangle$, $\langle x'^2 \rangle$ and $\langle xx' \rangle$) and substitute them in the eqn.(6.20). It is interesting to note that in the case of an achromatic bending system, the achromatic character is broken because of Eqn.(6.25). Another interesting point is that depending on the bending system design, one can conceive a way of making the above integral very small (or ideally zero) so that the net emittance growth is negligible. Such a method has been discussed in detail in references [60] and [61].

[11] If we consider the right hand side of the previous equation as a perturbation term $p(t,s)$ the solution of this equation writes $x(t) = \int_0^t p(\tilde{t})d\tilde{t}G(t,\tilde{t})$ where $G(t,\tilde{t})$ is a Green's function that can be constructed from the two principal solutions ($S(t)$ and $C(t)$) accordingly to:

$$G(t,\tilde{t}) = S(t)C(\tilde{t}) - C(t)S(\tilde{t})$$

6.4.4 Bunch Self Interaction via Coherent Synchrotron Radiation

CSR is a long standing topic in several subjects, especially in Accelerator Physics. The first comprehensive study was performed by J.S. Nodvick and D.S. Saxon [4] in 1954. These authors studied the interaction of charged particle moving on a curved path between to perfectly conducting plane and showed how CSR emission could be partially suppress at a given wavelength by the means of the two conducting plane that act as a shielding. Indeed, to the best of our knowledge, CSR effect on the Beam Dynamics, and CSR emission, have never been observed in storage ring or circular accelerator. It is a consequence of the generally long bunch that are circulating in such accelerator: as we will see in this chapter, CSR emission occurs at wavelength comparable to the bunch length. Therefore, for bunch length of the order of centimeters (as it is current in circular accelerator), the emission of CSR should occur in the microwave region: unfortunately, the size of the vacuum beam pipe chamber, which serve as a waveguide for the CSR propagation, are also of the order of centimeters and so is their cut off wavelength. Therefore the CSR emission is "shielded" by the beam pipe, i.e. it does not propagate. In fact, only very recently, CSR emission in the far field region, and in the far-infra-red wavelength has been observed in a 100 MeV linear accelerator of the Tohoku University by T. Nagazato [66]. This group showed experimentally how it was possible to infer the bunch length and bunch structure using the frequency spectrum of CSR, using the same technique we presented in Chapter 4 for the transition radiation. They also demonstrate the possible shielding of CSR emission using two parallel conducting plane with variable gap [67]. However the anticipated effects of CSR on the Beam Dynamics, i.e. transverse emittance dilution, has never been observed up to now.

A simple model: steady state in free space

We outline in the present section a simple picture of the CSR phenomenon. For such a purpose we start with the Liénard-Wietchert retarded electric field [8]:

$$\overrightarrow{E} = e\left[\frac{\hat{n}-\overrightarrow{\beta}}{\gamma^2(1-\hat{n}.\overrightarrow{\beta})^3R^2}\right]_{\text{ret}} + \frac{e}{c}\left[\frac{\hat{n}\wedge(\hat{n}-\overrightarrow{\beta})\wedge\overrightarrow{\dot{\beta}}}{(1-\hat{n}\,\overrightarrow{\beta})^3R}\right]_{\text{ret}} \tag{6.26}$$

$\overrightarrow{R}$ is a vector from S' to S, and $1-\hat{n}\,\overrightarrow{\beta} = 1-\beta\cos(\Delta\theta/2)$ and $\Delta\theta = \angle(\overrightarrow{OS'},\overrightarrow{OS})$ (see figure 6.19). The subscript $_{ret}$ means that the quantities inside the brackets must be evaluated at the retarded time t'. Because of causality the retarded t' and present t times are related by $t = t' + R(t')/c$ or equivalently by $\Delta\theta = \Delta\phi - 2\beta\rho\sin(\Delta\phi/2)$ with $\Delta\phi$ being the angle between the two electrons in the moving frame, ρ the radius of curvature, and $\Delta\theta$ the angle between them in the laboratory frame.

The problem has been treated in several references (e.g. Ref.[69]), it first consists of calculating the electric field emitted at the retarded time and location S' at the present time and location S. This electric field induces an energy change on S, $V(s-s')$, that depends on the relative positions, s and s', of the two particles. In essence CSR is very similar to wakefield: it yields an energy redistribution along the bunch. The energy change of a reference particle S is given by the superposition of the radiation force of all the back particles:

$$\frac{dE}{d(ct)} = \int_{-\infty}^{s}\Lambda(s')V(s-s')ds' \tag{6.27}$$

In the case of a rigid line charge with a Gaussian distribution $\Lambda(s) = N/\sqrt{2\pi\sigma_z^2}\exp\left[-s^2/(2\sigma_z^2)\right]$, one obtains for the energy change [68]:

$$\frac{dE}{d(ct)} = \frac{2Ne^2}{(2\pi)^{1/2}3^{1/3}\rho^{2/3}\sigma_z^{4/3}}F(s/\sigma_z) \tag{6.28}$$

with the function[12] F defined as $F(\xi) = \int_{-\infty}^{\xi}\frac{d\xi'}{(\xi-\xi')^{1/3}}\frac{d}{d\xi'}e^{-\xi'^2/2}$ A plot of this energy change is presented in figure 6.20 along with simulation results using a modified version of PARMELA that includes a simple model for CSR bunch self interaction (see Appendix B). Contrary to standard wakefield where the trailing electrons in the bunch generally lose energy, CSR effects yield an energy gain for electrons located in the head of the bunch.

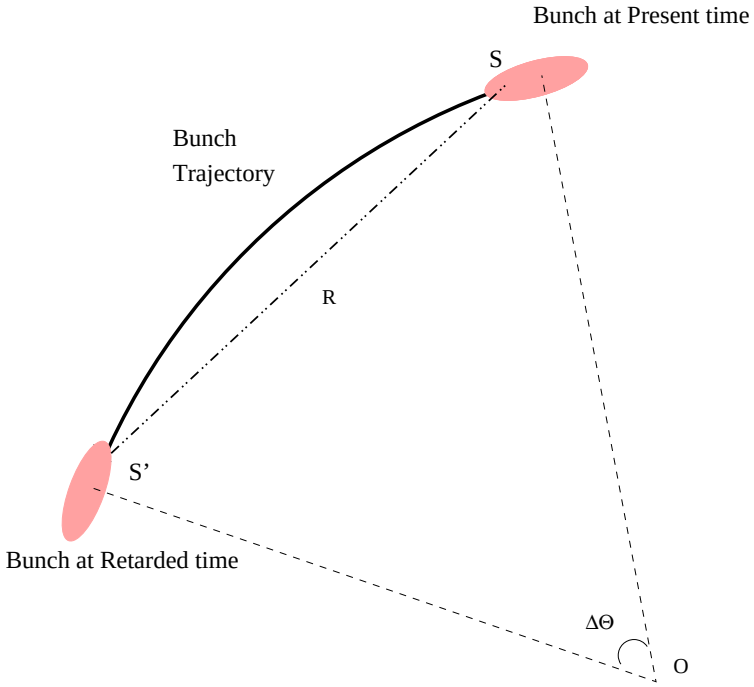

Figure 6.19: Schematics of CSR self interaction of a bunch.

Limitations of the previous model

The model of CSR bunch self interaction briefly outlined in the previous section is oversimplified in two ways: (1) it assumes the bunch has been orbiting on a circular path for ever (steady state assumption) and (2) it assume the bunch is in free space. Both of this assumptions are not true in practice: (1) an accelerator (even circular) consists of straight sections joined by bending elements therefore a more realistic picture of CSR should include the transient CSR, i.e. the passage from the straight section to the bend section. (2) the bunch propagates in metallic (e.g. stainless steel) vacuum chambers and therefore CSR can be shielded (i.e. not allow to propagate because of the cut-off frequency associated with the geometric parameters of the vacuum chamber).

[12] sometime termed as "overtake" function

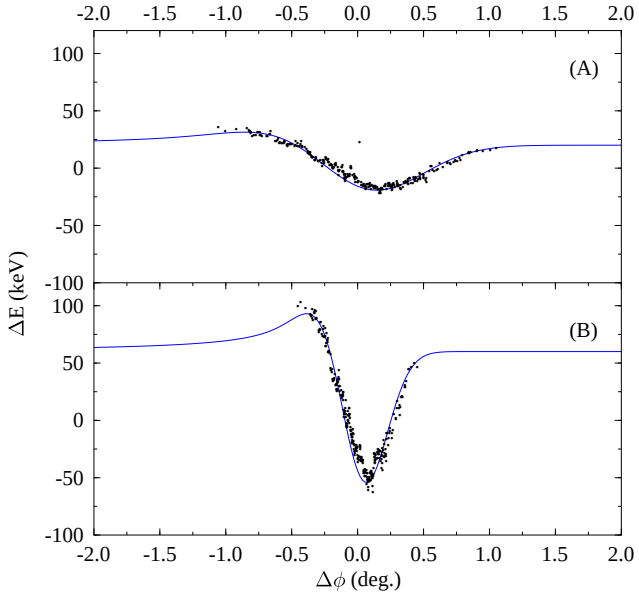

Figure 6.20: Analytical computation for CSR-induced energy loss along a gaussian bunch and prediction using a simple numerical model in a modified version of the sc parmela code for 200 μm **(A)** and 100 μm **(B)**. The system considered is a simple achromatic chicane (macroparticle with $\Delta\phi > 0$ are in the bunch tail).

6.5 Preliminary Experimental Results on Emittance and Energy Spread Measurements

The primary purpose of the experiment that was attempted in the IRFEL is to measure whether the transverse horizontal emittance is significantly degraded after the recirculation arc 1. The reason is to confirm the viability of the envisioned Upgrade IRFEL in which several wigglers will be located in the backleg transport.
Another motivation was to try to setup the IRFEL optics so that we could generate emittance degradation and perform some parametric studies.
The experimental setup to measure emittance follows our discussion of Chapter 3.

The experiment was attempted in two series of runs. During the first run, we varied the linac accelerating phase and measured the emittance before and after the arc 1. In the second series of run, because the emittance was found to be large (technical problem with the injector), we concentrated on measuring the energy spread measurement only.

6.5.1 Emittance Measurement

A first experiment consisted in varying the bunch length at the undulator location and measuring the horizontal emittance after the decompressor chicane. A typical plot obtained is presented in figure 6.21. The emittance seems to go through a maximum for a minimum bunch length in the undulator vicinity (as inferred from the maximum CTR signal). From a simplistic model implemented in PARMELA we found that at such point the emittance increases compared to the case where CSR is not included in the calculation is approximately 10%. At the time of the measurement we operated the gun with a very poor photocathode and could not extract more that 20 pC charge per bunch, a too low charge to unambiguously measure potential effects from CSR bunch self interaction, if those are present. A fully self-consistent code, written by R. Li of Jefferson Lab [70], ran for 60 pC and a nominal emittance of approximately 7 mm-mrad yielded a 20% increase in emittance[13].

We also attempted to compare the transverse horizontal emittance before and after the arc 1. In the case corresponding to the nominal operation of the linac, which corresponds to a minimum bunch length in the undulator vicinity, no emittance growth was observed within the error bars (transverse horizontal emittances measured were approximately 18 mm-mrad normalized at 38 MeV).

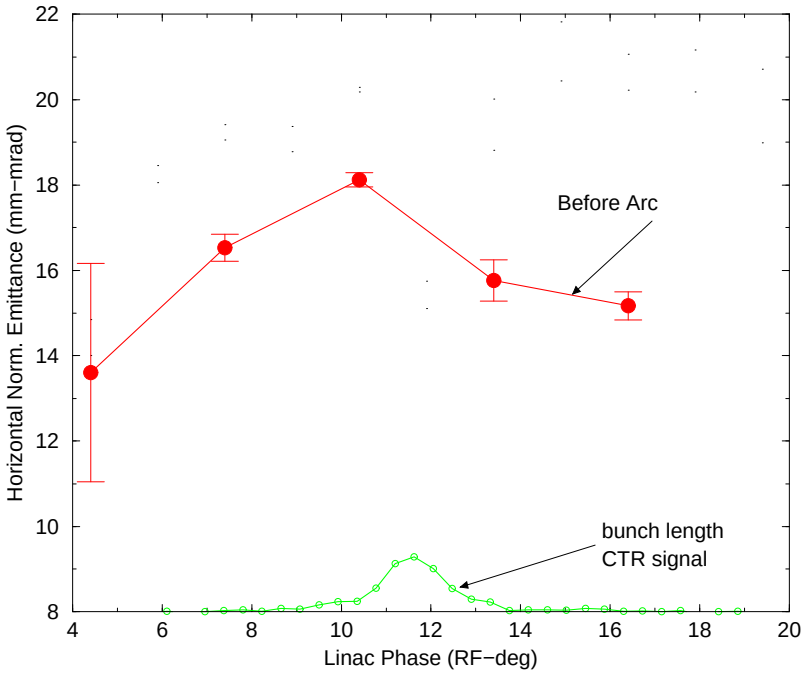

Figure 6.21: Transverse Horizontal emittance and total power CTR signal measured as a function of the linac gang phase.

[13] R. Li, private communication, this increase was noticed to be very dependent on the optical lattice setup. Unfortunately no parametric study has been completed to the present date

6.5.2 Energy Spread Measurement

In the second series of run, we were able to extract high charge per bunch from the photocathode (typically 60 pC) but we were never able to establish sufficiently low transverse emittance in the IRFEL [14] to provide a low enough signal-to-noise to see definitively a potential emittance growth at the arc exit. In the case of energy spread, it was generally difficult to convince ourselves that we had removed all transverse effects of transport from the viewer images, something that needs to be done to be sure only energy spread is being observed on the viewers. However, for a few select cases corresponding to short bunchlengths close to the undulator, we believe we have good data, and within the resolution of these measurements, they show no increase in energy spread as pictured in figure 6.22. This result is consistent with simulation performed with the JLab self consistent code which indicates the energy spread increase between the compressor chicane midpoint and the arc1 exit should be of the order of 5% [15].

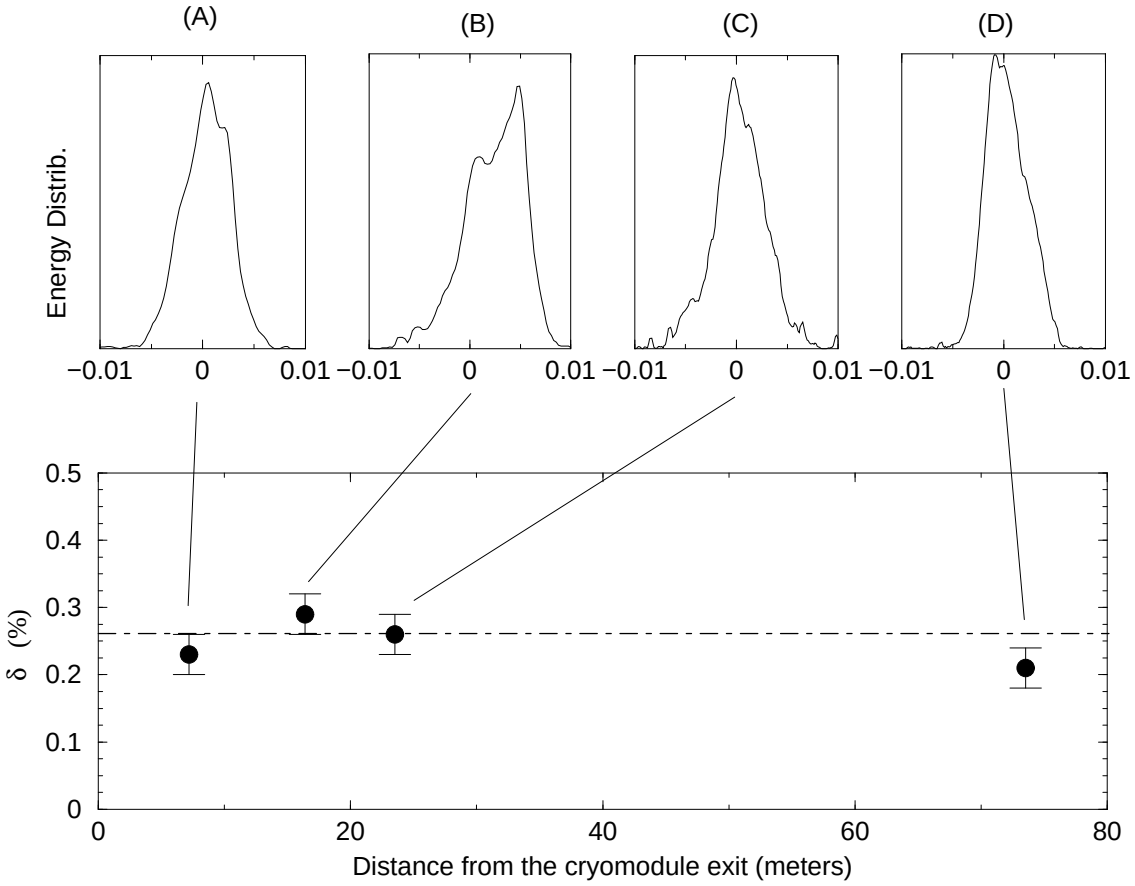

Figure 6.22: Energy distribution measured along the beam line, at the chicane midpoint (A) and (B) and entrance of the arcs (C) and (D) [the horizontal axis of these plot represent the relative energy spread (no units)]. The bottom plot presents the rms relative energy spread computed from the distributions.

[14] the reason is still not understood at the present time

[15] R. Li, private communication

6.5.3 Conclusion

Our experiment on CSR was not very successful because of bad beam quality during the period we tried to performed the measurements. However a preliminary conclusion would indicate that CSR is not a significant effect in the IRFEL, in the sense that no tremendous growth of the transverse emittance or the energy spread was observed even at 60 pC. Only one measurement has been performed and there might be optical lattice setups that may provide a larger energy spread and emittance growth. At minimum we can conclude that with the nominal setup of the IRFEL accelerator neither significant emittance dilution nor energy spread generation were measured. In the future, once the beam dynamics in the machine is fully optimized, one should try to transport higher charge (e.g. the full 135 pC required for the Upgrade IRFEL), and attempt to generate and measure beam degradation due to bends.

Chapter 7

Conclusion

The work presented in the present report describes in detail the implementation of different types of diagnostics for a relatively high brightness electron beam and the applications of these diagnostics to study some beam dynamics problems. This work had a significant contribution in the success of commissioning, understanding and operating the first high average power (kW-level) infra-red free electron laser oscillator that has been built at Thomas Jefferson National Accelerator Facility.

The recirculator transverse response functions, the lattice dispersion, and the longitudinal transfer functions R_{56} and R_{55} (along with nonlinearities) have been measured and compared with a magnetic optics code such as DIMAD and particle pushing code such as PARMELA.

We have implemented two transverse phase space characterization techniques to study the phase space density of the electron beam as it is still in the space-charge dominated regime, but also in the emittance dominated regime. The former technique based on transverse phase space sampling using a multislit mask has allowed some preliminary parametric studies of the phase space of 60 pC charge per bunch beam produced at the front end of a 10 MeV photoinjector and has been capable to resolve emittance as low as 1 mm-mrad in a test injector stand.

Along with the transverse phase space, a full six-dimensional characterization of the phase space has been attempted by measuring both bunch length and energy spread of the electron beam. Because of the ultra-short beam required to drive a free-electron laser (typically <0.5 picosecond rms bunch length), we have instrumented the driver-accelerator with Michelson interferometers that detect coherent transition radiation produced by the bunched electron beam. This interferometer has also been used to perform parametric study of the bunch length evolution versus some radio-frequency element that play a key role in the bunching scheme.

Finally a full model based on multiparticle simulation of the IRFEL has been elaborated and compared when possible with experiments. A tentative experiment to measure energy spread generation in the recirculation arc of the driver accelerator, along with emittance dilution has been performed. The results yields the observation of emittance growth that is correlated with bunch length in the

undulator vicinity. We have not managed, up to the present date, to unambiguously demonstrate whether this effect was due to coherent synchrotron radiation. A second series of runs were performed, where we concentrated on the measurement of energy spread along the transport channel, resulting in no observation, within the precision of the measurement, of energy spread generation (also this data were taken for one operating point of the linac only).

We can conclude, at a minimum, that it should be possible set up a beam that will transport around the Bates arc without significant growth in energy spread (which translates to no significant growth in emittance), and therefore for the FEL Upgrade it seems reasonable to plan on putting the FEL systems in the back leg transfer line - a bunch charge of 135 pC (versus the 60 pC used for the measurement reported in this report) would roughly double the effect provided all else were equal, but then it still would not be significant. Once the lattice design of the IRFEL Upgrade has matured, then one should be able to use the IR Demo to set up a beam at the entrance to the first Bates bend that mimics the IRFEL Upgrade beam parameters, and try to perform the same type of measurements (emittance and energy spread) the 135 pC case.

Bibliography

[1] C.L. Bohn and S.V. Benson, "Radiofrequency Superconductivity Applied to free-electron lasers", *Part. Acc.*, **69**, pp. 623-635 (1998)

[2] Y. Shibata, T. Takahashi, T. Kanai, K. Ishi, and M. Ikezawa, "Diagnostics of an electron beam of a linear accelerator using coeherent radiation", *Phys. Rev.*, **E50** num. 2, pp. 1479-1484 (1994)

[3] C. Hirschmugl, M. Sagurton, and G. Williams, "Multiparticle coherence calculations for synchrotron-radiation emission", *Phys. Rev.*, **A44** num. 2, pp. 1316-1320 (1991)

[4] Nodvick and Saxon, "Multiparticle coherence calculations for synchrotron-radiation emission", *Phys. Rev.*, **A44** num. 2, pp. 1316-1320 (1991)

[5] I. M. Frank, "Transition Radiation and Optical Properties of Matter", *Sov. Phys. Uspekhi*, **8** num. 5, pp. 729-742 (1966)

[6] L. Wartsky, "Etude du Rayonnement de transition optique produit par des electrons d'energie 30 à 70 MeV. Application aux diagnostics de faisceaux de particules chargées", Ph. D Thesis, Université d'Orsay, France

[7] M. L. Ter-Mikaelian, *High Energy Electromagnetic Processes in Condensed Media*, Wiley-Interscience, New York (1972)

[8] J. D. Jackson, *Classical Electrodynamics*, Wiley Edt, New York (1975)

[9] A. Hofmann, "Theory of Synchrotron Radiation", report SSRL ACD-NOTE 38, Stanford University, CA (1986)

[10] M. Sands, "The Physics of Electron Storage Rings, An Introduction", report SLAC-121, Stanford (1970) (also published as report US-28, and University of California, Santa Cruz, CA (1970))

[11] G. Dattoli, and A. Torre, "Free-Electron Laser Theory", report CERN 89-03, CERN, Geneva, Switzerland (1989) Stanford (1986)

[12] S.V. Benson, "Tunable Free-Electron Lasers", in *Tunable Lasers Handbook*, Academic Press Inc., pp. 443-469 (1995)

[13] S.V. Benson and M.D. Shinn, "Drive Laser for a DC photocathode gun", *Proc. Part. Acc. Conf.'95* IEEE catalog #97CH35843, pp. 1052-1054, Dallas (1995)

[14] D. A. Engwall, "High Brightness Electron Beams from a DC, High-Voltage, GaAs Photoemission Gun", Ph. D Thesis, University of Illinois at Urbana-Champaign (1998)

[15] C.L. Bohn, S. Benson, G. Biallas, I. Campisi, D. Douglas, R. Evans, J. Fugitt, R. Hill, K. Jordan, G.A. Krafft, R. Li, L. Merminga, G. Neil, P. Piot, J. Preble, M. Shinn, T. Siggins, R. Walker, and B. Yunn, "Performance of the Accelerator Driver of the Jefferson Laboratory's free-electron laser", to appear in *Proc. Part. Acc. Conf.'99*, New York (1999)

[16] D.R. Douglas, "Lattice Design for a High-Power Infrared FEL", *Proc. Part. Acc. Conf.'97* IEEE catalog #97CH36167, pp. 1351-1355, Vancouver (1997)

[17] J. B. Flanz, and C. P. Sargent, "Operation of an Isochronous Beam Recirculation System", *Nucl. Instr. Meth.*, **A241**, pp. 325-333 (1985)

[18] D.R. Douglas, "Lattice Issues Affecting Longitudinal Phase Space Management During Energy Recovery, Or, Why the FEL Needs Sextupoles", report TN-98-025, Jefferson Lab, Newport News VA, USA (1997)

[19] C. R. Carman, and J.-L. Pellegrin, "The Beam Positions of the Spear Storage Ring", preprint SLAC-PUB-1227 (A), SLAC, Stanford University CA-USA (1973)

[20] G. A. Krafft, M. Crofford, D. R. Douglas, S. L. Harwood, R. Kazimi, R. Legg, W. Oren, K. Tremblay, and D. X. Wang, "Measuring and adjusting the pathlength at CEBAF", *Proc. Part. Acc. Conf.'95*, pp 2429-2431 (1995)

[21] D. Hardy, J. Tang, R. Legg, M Tiefenback, M. Crofford, and G. A. Krafft, "Automated path length and M_{56} measurement at Jefferson Lab", *Proc. Part. Acc. Conf.'97* IEEE catalog #97CH36167, pp. 1351-1355, Vancouver (1997)

[22] G. A. Krafft, "Correcting M56 and T556 to obtain short bunches at CEBAF", AIP Conference Proceedings **367**, E. Blum and A. Sievers Ed., pp 257-265 (1996)

[23] J. van Zeijts, TLIE version 2.03 private communication; for a description of of the code see J. van Zeijts and F. Neri, "The arbitrary order design code Tlie 1.0", *Proc. of the Int. Workshop on Nonlinear Problems in Accelerator Physics*, pp. 135-145, Inst. of Physics Conf. Series **131**, Edited by M. Berz, S. Matin, & K. Ziegler (1992)

[24] T. Powers L. Doolittle, R. Ursic, and J. Wagner, "Design, Commissioning and Operational Results of Wide Dynamic Range BPM Switched Electrode Electronics", AIP Conference Proceedings **390**, A.H. Lumpkin and C. E. Eyberger Ed., pp 257-265 (1996)

[25] P. Piot, G. A. Krafft, K. Jordan, A. Grippo, and J. Song, "Performance of the Electron Beam Diagnostics at the Jefferson Lab's High Power FEL", to appear in *Proc. Part. Acc. Conf.'99*, New York (1999)

[26] C. Lejeune and J. Aubert, "Emittance and Brightness: Definitions and Measurements", in *Applied Charged Particle Optics*, A. Septier Ed., Advances in Electron Physics, Supp. **13A**, pp. 159-259 (1980)

[27] P. Lapostolle, "Quelques effets essentiels de la charge d'espace dans les faisceaux continus", report CERN/DI 70-36, CERN, Geneva, Switzerland (1970)

[28] R. Abbott, S. V. Benson, M. Crofford, D. Douglas, R. Gonzales, R. Kazimi, D. Kehne, G.A. Krafft, P. Liger, H. Liu, D. Machie, C.K. Sinclair, "Design, Commissionning, and Operation of the upgraded CEBAF injector", *Proc. International Linear Accelerator Conference*, pp 777-779, Tsukuba (1994)

[29] J.-C. Denard, C. Bochetta, G. Traomba, "Design Considerations Related to the Thermal Load of the Fluorescent Screen Monitors", Internal Note ST/m-TN-91/14, Sincrotrone Triestre, Società consortile per azioni, Triestre, Italia (1991)

[30] E. Keil, E. Zeitler, und W. Zinn, "Zur Einfach- und Mehrfachstreuung geladener Teilchen", *Z. Naturforschg.* **15a**, pp 1031-1038 (1960)

[31] S. Leisegang, *Z. Phys.* **132**, pp 183-187 (1952)

[32] P. Piot, J.-C. Denard, P. Adderley, K. Capek and E. Feldl, "High Power CW Beam Profile Monitor at CEBAF", AIP Conference Proceedings **390**, A.H. Lumpkin and C. E. Eyberger Ed., pp 298-305, (1996)

[33] V. A. Lebedev "Diffraction-limited resolution of the optical transition radiation monitor", *Nucl. Instr. Meth.*, **A372**, pp. 344-348 (1996)

[34] D. Douglas, "An observation point for measurement of the 45 MeV emittance in the Front End Test", report TN-90-265, Jefferson Lab, Newport News VA, USA (1990)

[35] P. Piot, "A Tcl/Tk Package for Collecting and Analyzing Beam Tranverse Density Measurements using OTR in the IRFEL", report TN-99-031, Jefferson Lab, Newport News VA, USA (1999)

[36] P. Piot, G.A. Krafft, R. Li, J.Song, "Real-Time Transverse Emittance Measurement", pp. 684-689, *Proc. International Linear Accelerator Conference*, Chicago (1998)

[37] F. J. Sacherer, "rms envelope equations with space charge", report CERN/SI/Int. DL/70-12, CERN Geneva Swizerland (1970)

[38] M. Crescenti and U. Raich, "Second European Workshop on Beam Diagnostics and Instrumentations for Particle Accelerator" DESY M 95-07, pp 66-68 (1995)

[39] J. Song, P.Piot, R. Li, et al. "Real-Time Phase Space Monitor", *Nucl. Instr. Meth.*, **A407**, pp. 343-349 (1998)

[40] P. Bevington, *Data Reduction and Error Analysis for the Physical Sciences*, Mc Graw-Hill Book (1969)

[41] J. D. Lawson, *The Physics of Charged-Particle Beams*, 2nd Edition, International Series of Monographs on Physics **75**, Oxford Science Publications (1988)

[42] D. E. Groom, "Passage of particles trough matter", *Eur. Phys. Jour.* **C3** num (1-4), pp. 144-151 (1998)

[43] E. C. Reichenbach, S. K. Park, R. Narayanswamy, "Characterizing digital image acquisition devices", *Opt. Eng.* **30** (2), pp 170-177 (1991)

[44] M. G. Tiefenback, "Space-Charge Limits on the transport of Ion Beams in a long alternating gradient system", Ph. D. Thesis, Lawrence Berkley Laboratory, University of California, report LBL-22465 (1986)

[45] B. M. Dunham, D. Douglas, R. Legg, and B. Bowling, "Analysis of Emittance Measurement Using Single and Multiple Harps", report TN-96-014, Jefferson Lab, Newport News VA, USA (1996)

[46] P. Piot, and G.A. Krafft, "Monitoring Longitudinal Phase Space of a Charged-Particle Beam with a Multifrequency Coherent Radiation Device", report TN-97-030, Jefferson Lab, Newport News VA, USA (1997)

[47] W. H. Press, S. A. Teukolsky, W. T. Vetterling, and B. P. Fannery, *Numerical Recipes in C: The Art of Scientific Computing*, 2nd Edition, Cambridge University Press (1992)

[48] R. Lai, and A. J. Sievers, "Phase problem associated with the determination of the longitudinal shape of a charged particle bunch from its coherent far-ir spectrum", *Phys. Rev.*, **E52** num. 2, pp. 45764579 (1995)

[49] R. E. Burge, M. A. Fiddy, A. H. Greenway, and G. Ross, "The Phase Problem", *Proc. R. Soc. Lond.* A.**350**, pp. 191-212 (1976)

[50] N. Levinson, and R. Redheffer, *Complexe Variable*, Holden-Day Inc., San Fransisco, Cambridge, London and Amsterdam (1970)

[51] T. Larsen, "A Survey of the Theory of Wire Grids", *IRE Trans. Micr. Theo. & Tech.*, pp. 191-201 (1962)

[52] D. X. Wang, G. A. Krafft, and C. K. Sinclair, "Measurement of femtosecond electron bunches using a rf zero-phasing method", *Phys. Rev.*, **E57** num. 2, pp. 2283-2286 (1998)

[53] H. Liu, et al., *Nucl. Instr. and Meth.* **A358**,pp 475-478 (1995)

[54] M. Reiser, *Theory and Design of charged particle beams*, John Wiley & Sons, (1994)

[55] P. Piot, G. Biallas, C. L. Bohn, D. R. Douglas, D. Engwall, K. Jordan, D. Kehne, G. A. Krafft, R. Legg, L. Merminga, J. Preble, T. Siggins, and B. C. Byunn, "Experimental Results from an Injector for an IR FEL", *Proc. Euro. Part. Acc. Conf.'98*, pp. 1447-1449 (1998)

[56] P. Piot, G. A. Krafft, "Transverse RF-focussing in JLAB RF Cavity", *Proc. Euro. Part. Acc. Conf.'98*, pp. 1327-1330 (1998)

[57] J. B. Rosenzweig, and L. Serafini, "Transverse particle motion in radio-frequency linear accelerator", *Phys. Rev.*, **E49** num. 2, pp. 1599-1602 (1994)

[58] E. Chambers, unpublished work, SLAC, Standford University (1965)

[59] H. Wiedemann, *Particle Accelerator Physics II*, Springer-Verlag Berlin Heidelberg (1995)

[60] P. Emma, and R. Brikmann,"Emittance Dilution Trough Coherent Energy Spread Generation in Bending System", *Proc. Part. Acc. Conf.'97*, pp. 1679-1681 (1997)

[61] P. G. O'Shea, "Reversible and irreversible emittance growth", *Phys. Rev.*, **E57** num. 1, pp. 1081-1087 (1998)

[62] Z. Li, "Beam Dynamics in the CEBAF Superconducting Cavities", PhD thesis, College of William & Mary VA-USA (1995)

[63] A. W. Chao, *Physics of Collective Beam Instabilities in High Energy Accelerators*, John Wiley & Sons, (1993)

[64] Z. Li, "Beam Dynamics in the CEBAF Superconducting Cavities", *Proc. Part. Acc. Conf.'93* IEEE catalog #93CH3279-7, pp. 179-182, Chicago (1993)

[65] B. C. Yunn, "Impedances in the IRFEL", report TN-96-049, Jefferson Lab, Newport News VA, USA (1996)

[66] T. Nagazato, et al., "Observation of Coherent Synchrotron Radiation", *Phys. Rev. Let.*, **63** num. 12, pp. 1245-1248 (1989)

[67] R. Kato, et al. "Suppression and enhancement of coherent synchrotron radiation in the presence of two parallel conducting plates", *Phys. Rev.* **E57**, num 3, pp 3454-3460 (1998).

[68] E. L. Saldin, E. A. Schneidmiller, M. V. Yurkov, report TESLA-FEL 96-14, Deutsches Elektronen-Synchrotron-DESY, Hamburg (Deutchland)

[69] R. Li, C.L. Bohn, and J. Bisognano, "Shielded transient self-interaction of a bunch entering a circle from a straight path", report TN-97-048, Jefferson Lab, Newport News VA, USA (1997)

[70] R. Li, "Self Consistent Simulation of CSR", *Proc. Euro. Part. Acc. Conf.'98*, pp. 1230-1232 (1998)

Appendix A

Abbreviations

- **BFF :** bunch form factor.
- **BPM :** beam position monitor.
- **CCD :** charge coupled device.
- **CSR :** coherent synchrotron radiation.
- **CTR :** coherent transition radiation.
- **CW :** continuous wave.
- **FFT :** fast fourier transform.
- **FWHM :** full width half maximum.
- **FP coupler :** forward power coupler (on accelerating cavities).
- **HF :** high-frequency.
- **HOM coupler :** high order mode coupler (on accelerating cavities).
- **IRFEL :** infrared free-electron laser.
- **ISR :** incoherent synchrotron radiation.
- **ODP :** optical path difference.
- **OTR :** optical transition radiation.
- **RF :** radio-frequency.
- **RMS :** root mean square.
- **SC :** space charge.
- **SR :** synchrotron radiation.
- **SRF :** superconducting radio-frequency.

- **TEM :** transverse electric magnetic.
- **TOF :** time of flight.
- **TR :** transition radiation.

Appendix B

Beam Dynamics: Notes & Tools

B.1 Linear and Second Order Transport: Convention

B.1.1 Transfer Matrix

In the present report we work in the coordinate system $(x, x', y, y', \phi, \delta)$ where:

- x, y, ϕ are the coordinate in the standard 3D position space (note that $\phi = 2\pi z/\lambda_{RF}$ represents the longitudinal position of the particle in unit of the RF wavelength of the accelerator (within a factor 2π))
- x' and y' are the divergence in the transverse plane
- δ is the relative energy offset of the particle with a reference particle (which is in the present report coincident with the energy average of the bunch).

To propagate a vector $\overrightarrow{r}_{in}$ along a section of beam line, we use, provided the second-order approximation of the equation of motion is applicable:

$$r_{out,i} = \sum_j R_{ij} r_{in,j} + \sum_k \sum_{j>k} T_{ijk} r_{in,j} r_{in,k} + \mathcal{O}(r^3) \tag{B.1}$$

R_{ij} is the first order matrix and T_{ijk} are the second order terms.

B.1.2 Beam Matrix

The beam or Σ matrix, e.g. for the x-x' phase space is defined as follows:

$$\Sigma_x \stackrel{\text{def}}{=} \Sigma_{1|2} \stackrel{\text{def}}{=} \begin{pmatrix} \sigma_{11} & \sigma_{12} \\ \sigma_{12} & \sigma_{22} \end{pmatrix} = \begin{pmatrix} \langle x^2 \rangle & \langle x x' \rangle \\ \langle x x' \rangle & \langle x'^2 \rangle \end{pmatrix} \tag{B.2}$$

The same matrix can be defined for the y-y' phase spaces ($\Sigma_{3|4}$) or ϕ-δ longitudinal phase spaces ($\Sigma_{5|6}$). we have the following definitions/properties:

- the transverse rms emittance is the determinant $\det(\Sigma_z)$
- We define the slope of the phase space as: $dx/dx' = \langle x x' \rangle / \langle x'^2 \rangle$

B.2 A note on space charge

We have already mentioned that charged particle beam are subject to space charge force that originates from Coulomb repulsion between electrons within a bunch. Space charge tends to induce emittance growth. In this section, we would like to show that these forces are only a concern for low energy beam, in our case ($Q \simeq 60$ pC the space charge collective effect is only important in the injector beamline. For such a purpose we consider a very simple model of a uniformly charged beam or radius a and longitudinal charge density $\lambda(z)$ [1]. For such a simple case the electric and magnetic fields inside the beam, and in the beam reference frame, can easily be computed from the Maxwell equation and are (for $r < a$) (in the bunch frame):

$$E'_r(z) = \frac{1}{4\pi\epsilon_0} 2Q\lambda(z)\frac{r}{a^2} \tag{B.3}$$

The longitudinal field can also be computed considering the beam inside a pure metallic cylindrical pipe of radius b is:

$$E'_z = \frac{Q}{4\pi\epsilon_0}\frac{1}{\gamma^2} g(a', b')\frac{\lambda}{l'} \tag{B.4}$$

where $g(a, b)$ is a geometric factor that will be discussed later.
The electromagnetic field in Eqns.(B.3) and (B.4) are valid in the moving frame. The can be transformed in the laboratory frame using the Lorentz transformation:

$$E_r = \gamma E'_r,\ E_z = \gamma E'_z \tag{B.5}$$

Furthermore in the laboratory frame, the beam radius and length are related to their equivalent in the bunch frame by $l = \gamma l'$ and $a = a'$. Hence in the laboratory frame, these field dependance are:

$$E_r \propto 1/\gamma, \text{ and, } E_z \propto 1/\gamma^2 \tag{B.6}$$

which in turn yield the following dependance for the forces:

$$F_x = e(E_x - \beta c B_y) = \frac{e}{\gamma} \propto 1/\gamma^2, \text{ and, } F_z = eE_z \propto 1/\gamma^2 \tag{B.7}$$

Therefore we find, using this simple uniform beam model, that the space-charge induced defocusing force damps as $1/\gamma^2$ and eventually because negligible for high enough energy beam. Indeed we will derive a criterion, in the next section, from the rms beam envelope equation to determine when the space charge effect is not a concern.

[1] A. W. Chao, *Physics of Collective Beam Instabilities in High Energy Accelerators*, John Wiley & Sons, (1993)

B.3 The Simulation Tools

B.3.1 DIMAD

The program DIMAD [2] studies particle behavior in circular machines and in beam lines. The trajectories of the relativistic particles are computed according to the second order matrix formalism. It does not provide synchrotron motion analysis but can simulate it. The program provides the user with the possibility of defining arbitrary elements to tailor the program to specific uses. DIMAD, like its predecessor DIMAT, is the result of many years of experimenting with several different charged particle computer codes.

B.3.2 TLIE

TLIE [3] is a general 6D relativistic design code with a MAD compatible input language. The particularity of TLIE is its ability to compute transfer map at an arbitrary order and not only up to second order like DIMAD. The Physics behind this code is based on the use of the Lie Algebra operator to propagate transfert map along a beamline section. A Lie algebra is an algebra (i.e. a vector space with a product $\bullet$ verifying the properties (1) $\alpha(x \bullet y) = (\alpha x) \bullet y = x \bullet (\alpha y)$ and (2) $y\bullet(x_1+x_2) = y\bullet x_1+y\bullet x_2$) that also verifies the Jocobi identity: $x\bullet(y\bullet z)+y\bullet(z\bullet x)+z\bullet(x\bullet y) = 0$. The Lie algebra operator used in Beam Dynamics is the Poisson bracket defined as: $[f,g] = \sum_i \frac{\partial f}{\partial q_i}\frac{\partial g}{\partial p_i} - \frac{\partial g}{\partial q_i}\frac{\partial f}{\partial p_i}$ where g and f are functions of the generalized variables p_i and q_i. The reason for such a choice is the fact that with the help of the canonical Hamilton equations, we can write for a function $f(p_i, q_i)$:

$$\frac{df}{dt} = \frac{\partial f}{\partial t} + [f, H] \tag{B.8}$$

where H is the Hamiltonian that governs the evolution of the distribution f in the conjugate space (p_i, q_i). In standard notation, the Poisson bracket operator is often written $: f : g = [f, g]$ where $: f :$ is a Lie operator. To illustrate how the TLIE code works, let's assume, for the time being, that f is not an explicit function of time i.e. $\frac{\partial f}{\partial t} = 0$ in Eqn.(B.8). Then Eqn.(B.8) becomes: $\frac{df}{dt} = [f, H] =: f : H = - : H : f$, and using purely symbolic equation we have in term of operator: $\frac{d}{dt} = - : H :$ so the Lie operator $: H :$ reduces to a simple time derivative. The solution of this differential equation is $e^{-:H:}f$ where the exponentiation of Lie operator is defined as the series $e^{:H:}f = f + [H, f] + 1/2[H, [H, f]] + ...$
The beauty of Lie Algebra technique resides in that the computation of the function f at a time $t = t_0 + \tau$, knowing the function f at time t_0, just consists of computing $f_t = e^{-\tau:H:}f_{t_0}$; such calculation can be carried at any order by computing the Poisson bracket series at the desired order, this is the principle on which TLIE is based: the hamiltonian H along with the corresponding operator $e^{:H:}$ are computed for each beam line piece and are concatened using the Campbell-Baker-Hausdorff theorem, that states $e^{:H^{A\to C}:} = e^{:H^{A\to B}:}e^{:H^{B\to C}:}$, to obtain the Lie operator for a whole beam line section [A,C].

---

[2] R. Sevranckx, K. L. Brown, L. Scachinger, and D. Douglas, "Users Guide to the Program DIMAD", SLAC REPORT 285 SLAC - Stanford University CA-USA (1985)

[3] The code was written by Johannes van Zeijts and Filippo Neri

B.3.3 PARMELA

Features of Jefferson Lab Version

"Phase and Radial Motion in Electron Linear Accelerators." It is a versatile multi-particle code that transforms the beam, represented by a collection of macroparticles, through a user-specified linac and/or transport system. It includes a 2-D space-charge calculation and an optional 3-D point-to-point space-charge calculation. PARMELA integrates the particle trajectories through the fields. This approach is especially important for electrons where some of the approximations used by other codes (e.g. the "drift-kick" method commonly used for low-energy protons) would not hold. PARMELA works equally well for either electrons or ions. PARMELA can read field distributions generated by either FISH for rf problems or POISSON for magnet problems.

Modified Space charge algorithm

At Jefferson Lab, a modified version of PARMELA has been produced by H. Liu. It incorporates a 3D point-by-point space charge algorithm from K.T. Mc. Donald [4]. An outline of the algorithm is as follows. PARMELA use a two-step method to generate a space charge impulse on each macroparticle: (!) it determines the net electromagnetic space charge field at the location of each macroparticle due to all other macroparticle, (2) apply the space charge impulse to each macroparticle. Then track the macroparticle through a slice (width defined by the user) of the beam line (for simple element the tracking is performed using second order transfer matrix, but the user can if desired define the 3D map of the electromagnetic field. In such case the equation of motion is integrated in each slice). This space point-by-point algorithm is very simple but because of the $1/r^2$ dependence (which can lead to singularity or numerical noise) it must be implemented carefully. For instance in the eventuality two macroparticles come very close to each other the charge of the macroparticles in the algorithm is reduced. The algorithm to reduce the macroparticle charge is discussed in detail elsewhere [5]

A simple model for Coherent Synchrotron Radiation

The implementation of the CSR interaction into the PARMELA code closely follows the method described by Carlsten [6]where the electric field generated at a retarded angle ζ' by a line i of uniform charge Q_i and length δ_i orbiting on a circular trajectory of radius R_i detected at the present time by an observer electron j derived and expressed as:

$$E_{i,j} = \frac{Q_i}{\delta_i}\left[\frac{1}{r(1-\overrightarrow{\beta_i}\widehat{n}_{ij})}\left[\frac{1}{\gamma_i^2} - \beta_i^2\frac{x_j}{R_i} + \beta_i^2(1-\cos(\zeta'))\right]\right]_{\zeta_r}^{\zeta_f} \tag{B.9}$$

[4]K. T. Mc Donald, *IEEE Trans. Elect. Dev.* **35** p 2052 (1988)

[5]H. Liu,"Concept of Variable Particle Size Factor for a Point-by-Point Space Charge Algorithm", CEBAF report TN-94-040, Jefferson Lab, Newport News, VA-USA (1994)

[6]B. E. Carlsten,"Calculation of the noninertial space-charge force and the coherent synchrotron radiation force for short electron bunches in circular motion using the retarded Green's function technique" *Phys. Rev* **E54** num 1, pp 838-845 (1996)

where β_i, γ_i are the usual Lorentz factors for the orbiting line i, $\widehat{n}_{ij}$ is the normed vector along the direction from the line center and the observer electron. The quantity in bracket must be evaluated for the present angles ζ_{ij}^r (resp. ζ_{ij}^f) that corresponds to the angle between the rear (resp. front) of the line charge and the observer electron. The retarded angle ζ' is related to the present angle ζ by a transcend equation derived from geometrical consideration. For instance for the line charge i and the observer j we have:

$$\beta_i^2 R_i^2 (\zeta' - \zeta)^2 = \rho_j^2 + 2R_i(R_i + x_j)(1 - \cos(\zeta')) \tag{B.10}$$

where ρ_j is the total transverse displacement of the observer electron with respect to the trajectory of the line charge.
The denominator of Eqn.(B.9) can also be expressed as a function of the retarded time using geometrical consideration.

The extension to a bunch of electron described by a macroparticle model is straight forward: the line charge can be replaced by a macroparticle which carry, as in PARMELA, a uniform charge. Therefore the total electric field produced by the bunch of macroparticle at a retarded time on an observer macroparticle at the present time simply writes as the sum:

$$E_j^{\text{total}} = \sum_{i=1}^{N} E_{i,j} \tag{B.11}$$

where N is the number of macroparticle in the model.
In fact this "point by point" type macroparticle algorithm has already been implemented in the JLab PARMELA version to simulate macropaticle interaction via space-charge force. Hence we can easily modify the existing algorithm to simulate CSR self interaction.
The retarded angle is evaluated as described by Carlsten using an iterative process to solve the transcendent equation Eqn.(B.10). The model described in the previous section as been implemented in the JLab version of PARMELA (both a HP9000 and a Cray C90 versions). Pratically, when the bunch enters a bend in which the user wish to include CSR interaction, the radius of the trajectory of each macroparticle is ealuated and then, based on geometrical consideration, all the parameter in Eqn.(B.9) are computed and the field due to bunch on a macroparticle is evaluated. This operation is performed for each macroparticle and therefore a large number of iteration is needed. Typical CPU time needed to run one FEL chicane is approximately 1hr wall clock. A block diagram of the PARMELA code is presented in Fig. B.1. The modification performed are shown in grey: firstly we have introduced a new card `BENDCSR` which follow the same syntax as the `BEND` card. This card must be used to indicate the bending magnet where the user wish to simulate CSR interaction. Secondly, we have modified the program `PARMDYN` so that when the electrons are in the `BENDCSR` card the subroutine `csr` is called.

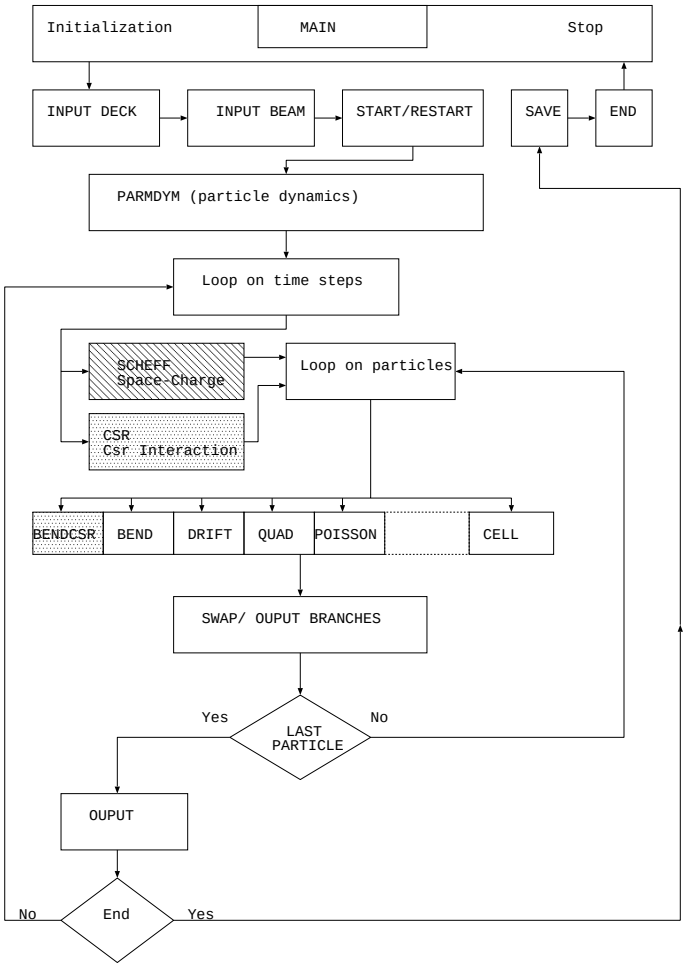

Figure B.1: Parmela simplified algorithm.

Appendix C

Dispersion Relations for Bunched Beam Distributions

C.0.4 Introduction

Dispersion relations to compute the phase associated to the electric field generated via coherent emission from a bunched electron beam have been used by many authors. However we believe the mathematical proof is not always properly derived: these dispersion relations are applied to functions which cannot be expressed as Cauchy integrals. In the present addendum we present a derivation of such relations and discuss the fact that these dispersion relation do not a fortiori give the phase, but only one term contributing to the phase (depending on the bunch longitudinal distribution properties).

C.0.5 Background

There are many ways electrons can emit radiation as their environment is modified. It has been shown in the case of bunched electron beam that if the emitted radiation is observed at wavelength comparable or larger that the bunch length, the electrons in the bunch emit coherently. In such a case, the spectrum of the radiation writes as:

$$E_{\text{total}}(\omega) = \sqrt{N(N-1)}\sqrt{|\breve{S}(\omega)|}E_{1\text{e-}}(\omega) \tag{C.1}$$

where $\breve{S}(\omega)$ is the Fourier transform of the longitudinal distribution $S(t)$. The problem that has been studied is to use the power spectrum, which is proportional to the modulus of the Fourier transform of the electric field, to compute the bunch form factor phase.
In the many papers, the function $\log(\breve{S}(\omega))$ is defined and the complex part of this function (which is the phase of $\breve{S}(\omega)$) is calculated using the standard dispersion relations. However we shall see below that $\log \breve{S}(\omega)$ does not have the "right" properties and cannot be generally written as a Cauchy integral and more care should be used when trying to recover the imaginary part of the $\log \breve{S}(\omega)$ function.

C.0.6 The Dispersion Relations for $\breve{S}(\omega)$

When $S(t)$, the bunch distribution has the "right" properties, its Fourier transform has some interesting properties: its imaginary and real part are Hilbert conjugate, i.e. they are related via Hilbert transformation. The "right" properties $S(t)$ must satisfy are as follows:

- $\int_0^{+\infty} S(t)dt < \infty$ i.e. the integral converge,
- $\lim_{t\to\infty} S(t) = 0$ and $S(t) \to 0$ faster than $1/t$,
- $S(t) = 0\ \forall t < 0$.

The last item insure $S(t)$ is a causal function and the two other are equivalent to $S(t) \in \mathcal{L}^2$, the ensemble of square integrable functions. The bunch distribution indeed satisfies all of the above items. Moreover because of item (1) its Fourier transform is bounded.

Let's extend the Fourier transform into the complex plane. Let $\xi = \omega + i\omega'$ be the complex frequency then the Fourier transform writes:

$$\breve{S}(\xi) = \int_0^{\infty} S(t)e^{i\xi t}dt = \int_0^{\infty} e^{i\omega t}e^{-\omega' t}dt \tag{C.2}$$

If we only consider the upper half-plane $\breve{S}(\xi)$ is analytic since in this region of the complex plane the function $\exp(-\omega' t)$ is a purely decaying function (because of causality $t \geq 0$). Because of analyticity we can write $\breve{S}(\xi)$ as a Cauchy integral:

$$\breve{S}(\xi) = \frac{1}{i\pi}\mathcal{P}\int_{-\infty}^{+\infty} \frac{\breve{S}(\alpha)}{\alpha - \xi}d\alpha \tag{C.3}$$

from which, after identifying $\breve{S}(\xi) = \Re[\breve{S}(\xi)] + i\Im[\breve{S}(\xi)]$ and using the fact that $S(-\xi) = S(\xi)$, we get the standard dispersion relations:

$$\begin{aligned} \Re[\breve{S}(\xi)] &= \frac{2}{\pi}\mathcal{P}\int_0^{\infty} \frac{\Im[\breve{S}(\alpha)]}{\xi - \alpha}d\alpha \\ \Im[\breve{S}(\xi)] &= -\frac{2}{\pi}\mathcal{P}\int_0^{\infty} \frac{\Re[\breve{S}(\alpha)]}{\xi - \alpha}d\alpha \end{aligned} \tag{C.4}$$

C.0.7 The Dispersion Relations for $\log[\breve{S}(\omega)]$

When detecting the power spectrum of coherent radiation emitted by a bunched beam with an infrared detector we only have access to the modulus of $\breve{S}(\omega)$ (see Chapter 5 of this report). A natural choice is to define the function $\Sigma \stackrel{\text{def}}{=} \log[\breve{S}(\omega)]$ whose real and imaginary part are the modulus and phase of $\breve{S}(\omega)$ [1] . Such function has been defined by several authors and the

[1] we write $\breve{S}(\omega) = |\breve{S}(\omega)|\exp(-i\Psi(\omega))$

dispersion relations have been applied to this function to retrieve its imaginary part (i.e. the phase of $\breve{S}\ (\omega)$).
Unfortunately $\log[\breve{S}\ (\omega)]$ cannot be expressed as a Cauchy integral because $\log[\breve{S}\ (\omega)]$ is not an analytic in the full upper half-plane. Moreover:

$$\oint \frac{\log[\tilde{S}(\xi)]}{\xi-\alpha} \overset{|\xi|\to\infty}{\longrightarrow} \int_0^{\pi} \frac{\log[\tilde{S}(\xi)]}{\xi} \neq 0 \tag{C.5}$$

Obviously $\log[\breve{S}\ S(\xi)]$ is not a "good" function! A commonly used ruse is to define the function

$$\Sigma(\xi) \overset{\text{def}}{=} \frac{\log\ \breve{S}\ (\xi) - \log\ \breve{S}\ (\alpha)}{\xi-\alpha} \tag{C.6}$$

where α is an arbitrary point of the upper half-plane where $\log[\tilde{S}]$ is analytic (note that $\Sigma(\xi)$ is not singular at $\xi=\alpha$).
The dispersion relations applied to $\Sigma(\xi)$ yields:

$$i\pi\Sigma(\xi) = \mathcal{P}\int_{-\infty}^{+\infty} \frac{\Sigma(x)dx}{x-\xi} \tag{C.7}$$

Using Eqn.(C.6) we get:

$$i\pi \log[\breve{S}\ (\xi)] = i\pi \log[\breve{S}\ (\alpha)] + (\xi-\alpha)\left[\mathcal{P}\int_{-\infty}^{+\infty} \frac{\log[\breve{S}\ (x)]dx}{(x-\xi)(x-\alpha)} - \mathcal{P}\int_{-\infty}^{+\infty} \frac{\log[\breve{S}\ (\alpha)]dx}{(x-\xi)(x-\alpha)}\right] \tag{C.8}$$

which expands to:

$$\begin{aligned} i\pi \log[\breve{S}\ (\xi)] = i\pi \log[\breve{S}\ (\alpha)] + (\xi-\alpha)\Bigg[\mathcal{P}\int_{-\infty}^{+\infty} \frac{\log[\breve{S}\ (x)]dx}{(x-\xi)(x-\alpha)} - \log[\breve{S}\ (\alpha)]\mathcal{P}\int_{-\infty}^{+\infty} \frac{dx}{x-\xi} \\ + \log[\breve{S}\ (\alpha)]\mathcal{P}\int_{-\infty}^{+\infty} \frac{dx}{x-\alpha}\Bigg] \end{aligned} \tag{C.9}$$

The two far RHS terms are zero, so that we finally get:

$$\log[\breve{S}\ (\xi)] = \log[\breve{S}\ (\alpha)] + \frac{\xi-\alpha}{i\pi}\mathcal{P}\int_{-\infty}^{+\infty} \frac{\log[\breve{S}\ (x)]dx}{(x-\xi)(x-\alpha)} \tag{C.10}$$

By identifying the real and imaginary parts we obtain the dispersion relations for $\log[\breve{S}\ (\xi)]$ which relate $\log[|\ \breve{S}\ (\xi)|]$ to the phase of $\breve{S}\ (\xi)$, $\Psi(\xi)$:

$$\begin{aligned} \log[|\ \breve{S}\ (\xi)|] &= \log[|\ \breve{S}\ (\alpha)|] + \frac{\xi-\alpha}{\pi}\mathcal{P}\int_{-\infty}^{+\infty} \frac{\Psi(x)dx}{(x-\xi)(x-\alpha)} \\ \Psi(\xi) &= \Psi(\alpha) - \frac{1}{\pi}(\xi-\alpha)\mathcal{P}\int_{-\infty}^{+\infty} \frac{\log|\ \breve{S}\ (x)| - \log|\ \breve{S}\ (\xi)|}{(x-\xi)(x-\alpha)}dx \end{aligned} \tag{C.11}$$

which after taking into account the symmetry of $\breve{S}$ ($\breve{S}\ (\xi) = \breve{S}\ (-\xi)$ yields for $\alpha=0$:

$$\Psi(\xi) = \Psi(0) - \frac{2\xi}{\pi}\mathcal{P}\int_0^{\infty} \frac{\log|\ \breve{S}\ (x)|dx}{x^2-\xi^2} \tag{C.12}$$

$\Psi(0)$ can be estimated because the Fourier transform at $\omega = 0$ is the integral of $S(t)$; it gives $\breve{S}\ (0) = 1 \in R$, since $S(t)$ is a real function normalized to unity; therefore $\Psi(0) = 0$. So finally we have:

$$\Psi(\xi) = -\frac{2\xi}{\pi}\mathcal{P}\int_0^\infty \frac{\log|\ \breve{S}\ (x)|dx}{x^2 - \xi^2} \tag{C.13}$$

However it should be noted that we have assumed from the beginning that $\breve{S}\ (\xi)$ is analytic in the upper plane. Unfortunately it does not imply $\log[\breve{S}\ (\xi)]$ has the same region of analyticity; in particular the point where $\breve{S}\ (\xi) = 0$ will give singularity on $\Sigma(\xi)$ which in turn must be taken into account in the phase by, when writing $\Sigma(\xi)$ as a Cauchy integral, taking in account the contribution to the integral via the residue theorem.

In the figure (figure C.1) below we present results for a simple bi-modal distribution that consists of a sum of two normal distributions: we have generated three types of distribution (a) (c) and (e) and for each of them we compare the phase calculated directly from the computation of the Fourier transform of the distribution with the phase retrieve using Eqn.(C.13). On this very simple example we notice that this equation does not a fortiori reproduce the veritable phase of the Fourier transform of the distribution.

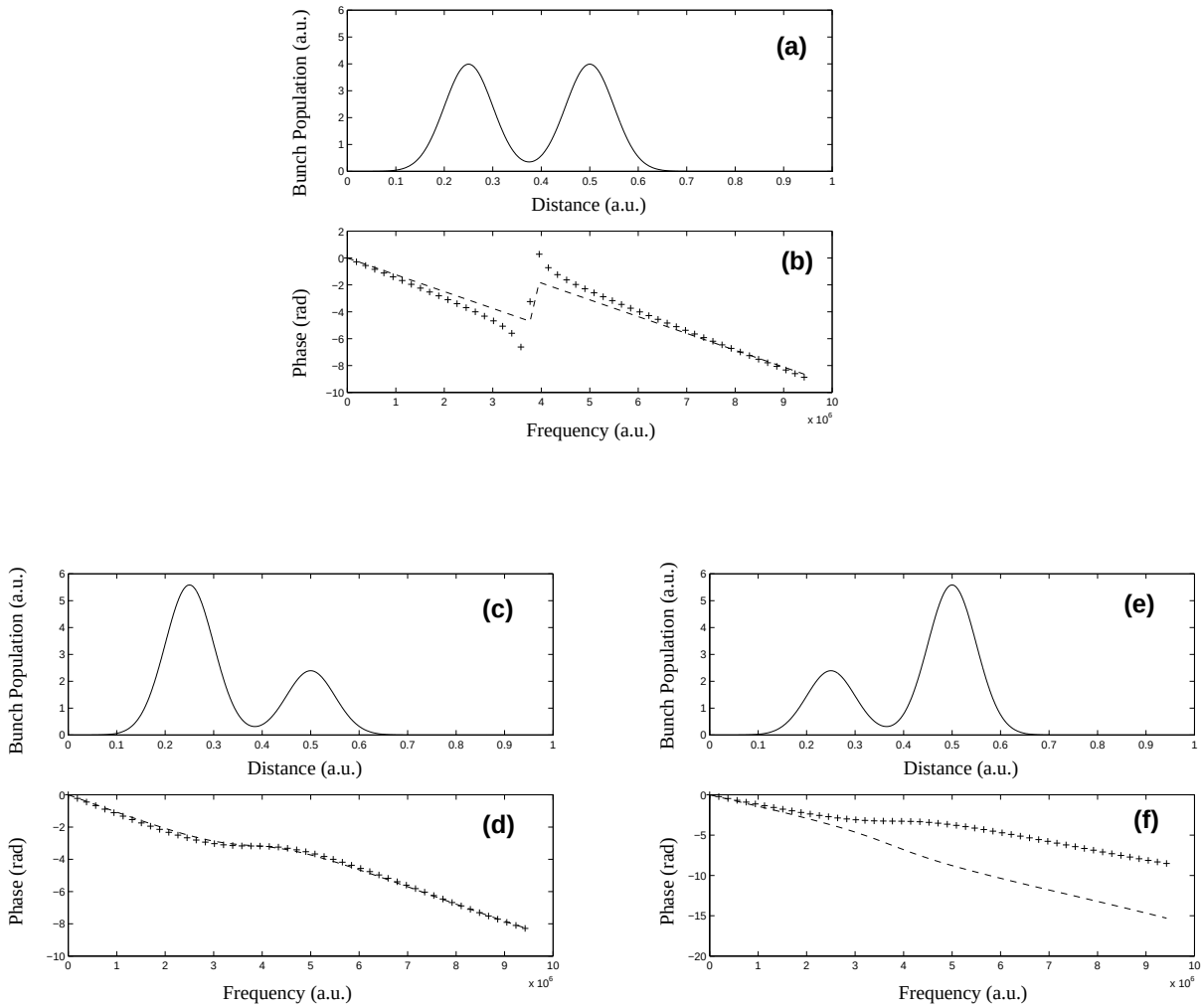

Figure C.1: Example of phase retrieval for a bi-gaussian-like bunch distribution. Three type of bi-modal distributions (a), (c) and (e) are presented along with the exact phase of their Fourier transform (dash lines on plot (b), (d), and (f)) and the recovered phase using the dispersion relation (crosses) on the same former plots.

Appendix D

The Radio-Frequency Control System

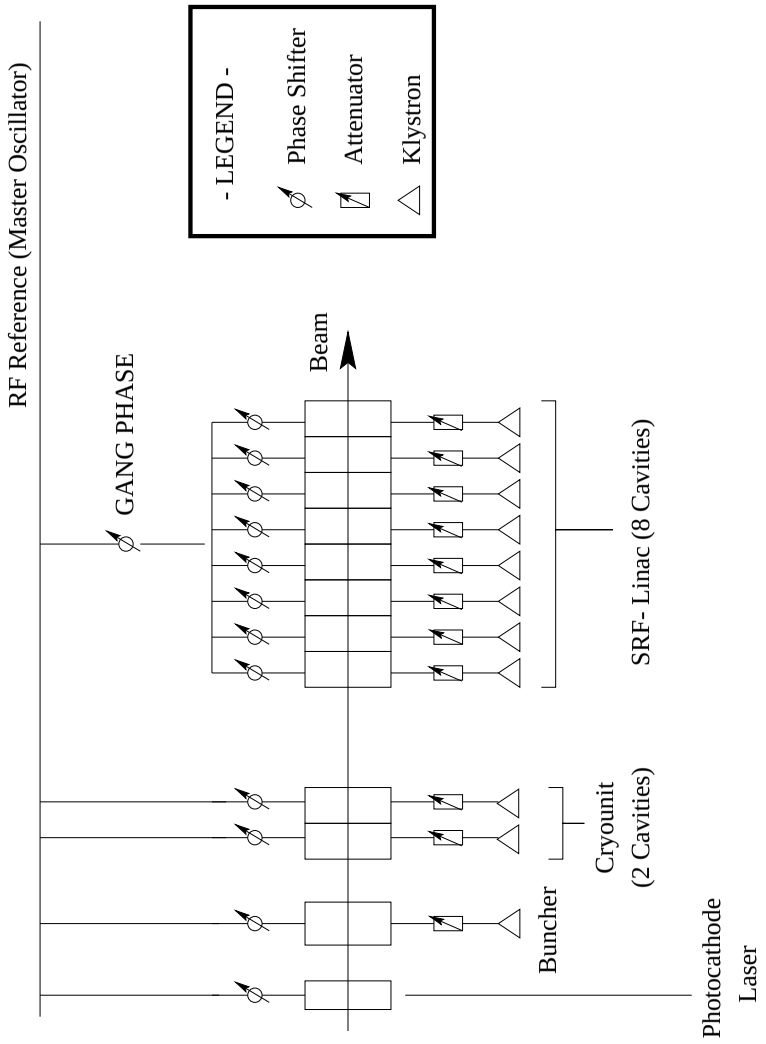

Figure D.1: Overview of the RF-control system for the IRFEL.